Spinal cord pathology in CLN1 disease
A novel therapeutic target

Nelvagal, Hemanth Ramesh

Awarding institution:
King's College London

Spinal cord pathology in CLN1 disease:

A novel therapeutic target.

Thesis submitted for the degree of

Doctor of Philosophy

Hemanth Ramesh Nelvagal

Department of Basic & Clinical Neuroscience

Institute of Psychiatry, Psychology and Neuroscience

King's College London

2016

Abstract

The neuronal ceroid lipofuscinoses (NCLs) are a group of up to 14 inherited progressive neurodegenerative lysosomal storage disorders affecting children and young adults. Together, they are the most common pediatric neurodegenerative storage disorders. Symptoms include loss of vision, epileptic seizures and the loss of cognitive and motor function. A lack of any effective therapies means that all forms are fatal. CLN1 disease or Infantile NCL is one of the most rapidly progressing forms of the disease and is caused by a deficiency of the lysosomal enzyme palmitoyl protein thioesterase – 1 (PPT1). Ppt1 deficient (*Ppt1*$^{-/-}$) mice recapitulate features of the human disease and have proved to be a useful tool in characterizing disease progression and pathology in the brain. However, these pathological changes fail to fully explain the sensorimotor deficits seen in this mouse model as well as in human CLN1 disease. Along with the limited success of various brain directed therapies, this led us to analyze the spinal cord. Our analysis revealed unexpectedly profound and rapidly progressing disease pathology in the spinal cords of these mice, which occurs earlier than similar events in the brain. This included regional atrophy, neuroinflammation, and significant neuron loss at all levels of the cord as well as novel phenotypes indicating a postnatal developmental delay and significant white matter pathology. Automated gait analysis also showed novel early phenotypes in these mice including an increased dependence on the forelimbs for locomotion. Similar spinal cord pathology was also demonstrated in human INCL autopsy samples as well as in mouse models of the other major forms of NCL. Targeting the spinal cords of *Ppt1*$^{-/-}$mice with enzyme replacement therapy (ERT) and gene therapy significantly improved disease pathology, motor function and lifespan in these mice, demonstrating the clinical significance of spinal cord pathology in these mice. Furthermore, combining intracranial and intrathecal gene therapy showed a synergistic effect, showing the greatest improvements for any CLN1 disease therapy to date. Taken together, these findings highlight the spinal cord as not only being significantly affected in CLN1 disease, but also as a novel and effective therapeutic target.

Statement of Originality

The genotyping, breeding and maintenance of *Ppt1*$^{-/-}$ and control C57BL/6 mice for automated gait analysis (Chapter 4) were carried out in the Biological Services Unit (BSU) of the James Black Center at the Institute of Psychiatry, Psychology and Neuroscience (IoPPN), King's College London (KCL) by Hemanth Ramesh Nelvagal.

The generation, processing and analysis of *Thy1-YFP/Ppt1*$^{-/-}$ mouse spinal cords (Chapter 3.9), administration of intrathecal and intracerebral injections and the analysis of rotarod function and survival for the gene therapy study (Chapter 5.3), as well as harvesting the *Ppt1*$^{-/-}$ and control mouse tissue for histological analysis for the analysis of the spinal cord pathology (Chapter 3) and the gene therapy study (Chapter 5.3) were all performed by our collaborators, Dr. Charles Shyng and Dr. Joshua Dearborn from the laboratory of Professor Mark Sands at the University of Washington Medical School, St. Louis, MO, USA .

Sectioning of 1µm semi-thin spinal cord sections for the analysis of white matter pathology (Chapter 3.9) was performed by Patricia Mavrogianis at the laboratory of Dr. Peter Gann, University of Illinois, College of Medicine, IL, USA.

Similarly, administration of intrathecal injections and *Ppt1*$^{-/-}$ and control mouse tissue for the Enzyme Replacement Therapy (ERT) study (Chapter 5.2) were supplied by Dr. Jui-Yun Lu from the laboratory of Professor Sandra Hofmann at University of Texas Southwestern Medical Centre, Dallas, TX, USA.

All other histological processing, staining and analysis of tissue presented in this thesis, as well as the gait analysis in *Ppt1*$^{-/-}$ and control (C57BL/6) mice was performed by Hemanth Ramesh Nelvagal at the Pediatric Storage Disorders Laboratory (PSDL), IoPPN under the supervision of Professor Jonathan D. Cooper, Dr. Brenda Williams and Dr. Sandrine Thuret; with the exception of the data for peripheral lymphocyte infiltration as well as microglial activation in the

white matter (Chapter 3.11), which were generated by Sioned R. Williams as part of her research project for the intercalated BSc Neuroscience programme at KCL.

All procedures were carried out according to the Animals (Scientific) Procedures Act, 1986 (UK), NIH guidelines and Institutional Animal Care and Use Committee (IACUC) guidelines (USA) at the respective institutions.

Publications arising from this thesis

Lu JY, **Nelvagal HR**, Wang L, Birnbaum SG, Cooper JD and Hofmann SL (2015). "Intrathecal enzyme replacement therapy improves motor function and survival in a preclinical mouse model of infantile neuronal ceroid lipofuscinosis." Mol Genet Metab **116**(1-2): 98-105.

Cooper JD, Brooks HR, **Nelvagal HR** (2015) "Quantifying storage material accumulation in tissue sections." Methods Cell Biol 126**:** 349-356

Cooper JD, Tarczyluk MA, **Nelvagal HR** (2015) "Towards a new understanding of NCL pathogenesis." Biochim Biophys Acta 1852**:** 2256-2261

Shyng C*, **Nelvagal HR***, Dearborn JT, Tyynelä J, Schmidt R, Sands MS, Cooper JD (2017) "Profound spinal cord pathology in CLN1 disease: a novel and effective therapeutic target." Submitted to PNAS, February 2017. (* Co-first authors)

Acknowledgements

I have been fortunate to have the help and support of some wonderful people during my PhD. I would therefore be amiss if I didn't thank them here and to say well done for putting up with me!

I would like to express my utmost gratitude to my supervisor, Professor Jonathan Cooper, without whom I would not be here. Thank you for being a mentor and a friend in equal measure, for turning this *Padawan* clinician to the dark side and for showing me that, despite its ups and downs, science could truly be rewarding. I would like to thank my second supervisors Dr. Brenda Williams for her support, guidance, comforting presence and belief in my ability, and Dr. Sandrine Thuret for her timely advice and for giving me the courage to think independently. I would also like to thank Dr. Deepak Srivastava, for always being happy to talk about life, science and everything in between. This work would not have been possible without having wonderful collaborators in Professor Mark Sands, Dr. Charlie "Chuckles" Shyng and Professor Sandra Hofmann, who have been helpful at every stage. I am also grateful to Dr. James Gray for showing me how to use the *CatWalk XT* system. I wish to also thank the King's College London graduate school for funding this PhD.

My PhD would not have been possible or indeed quite as enjoyable without the help of the PSDL lab members past and present, with special thanks to Dr. Greg "Cultural Awareness Officer" Anderson, Dr. Jenny Lange for our wonderful coffee chats that encompassed middle earth and the laboratory equally, Dr. Marta Tarczyluk-Wells for always being there to help and to have a great time (!), Dr. Yewande Pearse for always having a smile on her face and a kind word to say and Tina Harris for being an inspiration to us all. Many thanks also to Dr. Helen Brooks, Marc "*Spoon!*" Goldfinger, Usama "Dockhand" Saleem, Dr. Martin Egeland, Charlott Repschlager, Ana Assis Gomes, and Sioned Williams for making the PSDL an amazing place to work! There are many friends at the IoPPN and away that have made working and living fun: Ewelina L, Sarmi S, Rob "The

Grumpy Bear" C, Marie-C C, Fabio V, Rodrigo RD, Luís T, Alistair B, Karan "The Man" Sood, Vinay K, Felix MZ and Button!

I would like to thank my mother for always telling me to dream big, my father for showing me that I'd need hard work to achieve this and both for giving me the opportunity to find my way. I would like to dedicate this thesis to my grandparents Dr. N. Sundar, Dr. Kasturi Sundar and Gomathy Doreswamy, whose perseverance in the face of adversity in their lives has been the single greatest inspiration in mine.

A special thank you to Marion Bonneau for always giving me a reason to smile, for giving me the strength to keep going and always supporting me. You are amazing!

Lastly, to the families, thank you for inspiring us everyday and for the privilege to work towards cures for the NCLs.

"We are visitors on this planet. We are here for one hundred years at the very most. During that period, we must try to do something good, something useful, with our lives. If you contribute to other people's happiness, you will find the true meaning of life."

- H.H the 14th Dalai Lama

Table of Contents

List of Figures

List of Tables

List of abbreviations

AAV	Adeno-associated virus
ABC	Avidin biotin complex
AD	Alzheimer disease
AFSM	Autofluorescent storage material
ALS	Amyotrophic lateral sclerosis
ANCL	Adult neuronal ceroid lipofuscinosis
APP	Amyloid-β precursor protein
BBB	Blood brain barrier
BMT	Bone marrow transplantation
BOS	Base of support
CB	Calbindin
ChAT	Choline acetyltransferase
CNCL	Congenital neuronal ceroid lipofuscinosis
CNS	Central Nervous System
CoE	Coefficient of Error
CR	Calretinin
CSF	Cerebrospinal fluid
CTSD	Cathepsin D
DAB	3,3'-diaminobenzidine
DH	Dorsal Horn of spinal cord gray matter
DPX	p-xylene-bis (pyridinium bromide)
DRG	Dorsal root ganglion
ERT	Enzyme replacement therapy
GABA	Gamma-aminobutyric acid
GAD65	Glutamic acid decarboxylase
GFAP	DNAJ homolog subfamily C member 5
GM	Gray matter
HD	Huntington disease
HSCT	Hematopoietic stem cell transplantation
Hu-CNS SC	Human central nervous system derived stem cells
IACUC	Institutional animal care and use committee

IC	Intracranial
IF	Immunofluorescence
IGF IIr	Insulin-like growth factor II receptor
IHC	Immunohistochemistry
IMS	Industrial methylated spirit
INCL	Infantile neuronal ceroid lipofuscinosis
IT	Intrathecal
JNCL	Juvenile neuronal ceroid lipofuscinosis
LAMP1	Lysosomal associated membrane protein-1
LF	Left front paw
LFB	Luxol fast blue
LGnD	Dorsal Lateral Geniculate Body of Thalamus
LH	Left hind paw
LINCL	Late infantile neuronal ceroid lipofuscinosis
LSD	Lysosomal storage disorder
M1	Primary motor cortex
M6P	Mannose-6-phosphate
MBP	Myelin basic protein
MDB	Myelin dense bodies
MPS	Mucopolysaccharidosis
NAC	N-acetyl cysteine
NCL	Neuronal ceroid lipofuscinosis
NF	Neurofilament-H 200kD
NMD	Nonsense mediated decay
PBS	Phosphate buffered saline
PD	Parkinson disease
PFA	Paraformaldehyde
PNS	Peripheral nervous system
PPT1	Palmitoyl protein thioesterase-1
PTC	Premature termination codon
RER	Rough endoplasmic reticulum
RF	Right front paw
RH	Right hind paw

S1BF	Primary somatosensory barrel field of cortex
SC	Spinal cord
SEM	Standard error of the mean
TBS	Tris buffered saline
TBSAF	Tris buffered saline- antifreeze
TGN	Trans Golgi network
YFP	Yellow fluorescent protein
TNF-α	Tumor necrosis factor- α
TPP1	Tripeptidyl peptidase I
UPR	Unfolded protein response
VAMP2	Vesicle associated membrane protein-2
VH	Ventral horn of spinal cord
VPM/VPL	Ventral posterior medial/lateral nuclei of the thalamus
WM	White matter
WT	Wildtype

Chapter 1. General Introduction

The neuronal ceroid lipofuscinoses (NCLs) are a group of up to 14 lysosomal storage disorders (LSDs) that mainly affect children and young adults (Bennett & Rakheja, 2013; Mole & Cotman, 2015; Santavuori, 1988). Together, they are considered the most common pediatric neurodegenerative storage disorders, having a worldwide incidence of approximately 1 in 100,000 live births, and a particularly high incidence of up to 1 in 12,500 live births in Scandinavia (Goebel, 1995; Haltia, 2006; Jalanko & Braulke, 2009; Schulz et al, 2013). They are each caused by monogenetic recessive mutations in their respective "*CLN*" genes that impact the function of the endosomal-lysosomal system (Cotman et al, 2013; Mole & Cotman, 2015; Schultz et al, 2011).

The NCLs are classified together based on shared clinical features including visual impairment leading to blindness, epileptic seizures, cognitive impairment and sensorimotor deficits (which is an umbrella term used here to describe deficits affecting the sensory and motor systems) (Dolisca et al, 2013; Schulz et al, 2013; Williams et al, 2006), as well as neuropathological features such as the pathognomic accumulation of autofluorescent storage material, early glial cell activation and the progressive and widespread loss of neurons (Carcel-Trullols et al, 2015; Cooper et al, 2015). All forms of NCLs are fatal and there is currently no effective therapy available (Cotman et al, 2013; Geraets et al, 2016).

Infantile NCL (INCL) or classic CLN1 disease is one of the most severe and rapidly progressing forms of NCL (Hawkins-Salsbury et al, 2013; Santavuori et al, 1974). It is caused by mutations in the *CLN1* gene that codes for the lysosomal enzyme palmitoyl protein thioesterase-1 (PPT1) (Vesa et al, 1995). Children affected with CLN1 disease begin to show symptoms as early as 6-24 months of age including a rapid loss of motor function with hyperkinesias, loss of visual acuity and cognitive abilities, and a greatly reduced life expectancy of between 9 and 13 years (Dolisca et al, 2013; Schulz et al, 2013; Williams et al, 2006). Ppt1 deficient (*Ppt1*$^{-/-}$) mice recapitulate most phenotypic characteristics of the human disease and have been crucial for understanding functional deficits, as well as defining the pathology present in the forebrain and cerebellum (Bible et al, 2004; Griffey et al, 2006; Gupta et al, 2001; Kielar et al, 2007). However, these findings have

not been able to completely explain the sensorimotor deficits seen in these mice (Dearborn et al, 2015; Gupta et al, 2001). Furthermore, various forebrain-directed experimental therapies have only met with limited success (Hu et al, 2012; Macauley et al, 2012; Tamaki et al, 2009; Wei et al, 2011). While most studies characterizing the pathology in CLN1 disease focused on the brain and cerebellum (Bible et al, 2004; Kielar et al, 2007; Macauley et al, 2009), recent studies have indicated the presence of pathology outside the central nervous system (Galvin et al, 2008), and the original study of human pathology in INCL briefly mentioned presence of pathology in the spinal cord (Haltia et al, 1973a; Santavuori et al, 1974).

The research presented in this thesis therefore aims to a) determine and characterize the extent and nature of spinal cord pathology in murine and human INCL, b) relate abnormalities in the gait of Ppt1 deficient (*Ppt1*$^{-/-}$) mice to this pathology, and c) whether pathology in this region of the central nervous system (CNS) can be alleviated with experimental therapies targeted to the spinal cord.

1.1 The lysosome: structure and function

a) Structure

The lysosome is a cellular organelle first described by de Duve and colleagues in 1955 (Appelmans & De Duve, 1955; De Duve et al, 1955). They are bound by a lipid bilayer membrane and contain over 60 hydrolytic enzymes in an acidic lumen (pH 4.5-5.0). The lysosomal membrane contains various proteins that are involved with transporting molecules across this membrane, regulating the pH of its lumen and the fusion of the lysosome with other cellular compartments (Novikoff et al, 1973; Parkinson-Lawrence et al, 2010; Saftig & Klumperman, 2009; Xu & Ren, 2015).

The lysosome is formed by the fusion of clathrin-coated transport vesicles from the trans-Golgi network (TGN) with late endosomes that form as a result of endocytosis (Luzio et al, 2007; Luzio et al, 2000; Saftig & Klumperman, 2009). Many different soluble hydrolase enzymes are contained in the lysosomal lumen including peptidases, sulphatases, glycosidases, phosphateses, nucleases and

lipases that help to degrade a wide range of substrates (Braulke & Bonifacino, 2009). After protein synthesis, hydrolases destined for the lysosome undergo post-translational modifications including being tagged with mannose oligosaccharide side chains and linked with mannose-6-phosphate residues (M-6-P) in the rough endoplasmic reticulum (RER) (Helenius & Aebi, 2001; Kornfeld, 1992), as part of a highly regulated process. These hydrolases are then transported to the Golgi apparatus, where they are recognized by mannose-6-phosphate/ insulin-like growth factor II receptors (M6P/IGF IIr) or other pathways, and this enzyme-receptor complex is coated with clathrin to be transported across the TGN to the pre-lysosomal compartment or to the endosome (Braulke & Bonifacino, 2009; Ghosh et al, 2003; Saraste & Kuismanen, 1992). Fusion with the late endosome results in lowering of the luminal pH, which in turn causes the enzymes to dissociate from the M6P receptors, which are recycled to the Golgi apparatus (Luzio et al, 2007; Seaman, 2004). Lysosomal membrane proteins arrive at the endosome independent of the M6P pathway, either directly after protein synthesis or indirectly after being transported to the plasma membrane and being internalized during the formation of early endosomes (Braulke & Bonifacino, 2009; Kornfeld & Mellman, 1989; Luzio et al, 2000).

Molecules to be degraded in the lysosome may reach the lysosome from the extracellular or intracellular space (Zhang et al, 2009). Molecules in the extracellular space may be internalized by means of receptor-mediated endocytosis (Doherty & McMahon, 2009; Goldstein et al, 1985) or by phagocytosis (Flannagan et al, 2012). Intracellular molecules reach the lysosome either as a result of autophagy, resulting in a double membrane bound autophagosome (Levine & Klionsky, 2004; Stromhaug & Klionsky, 2001), or directly from the endoplasmic reticulum (Braakman & Bulleid, 2011).

b) Function

The lysosome was initially thought to be solely concerned with the waste disposal and recycling of endogenous and internalized molecules (Kornfeld & Mellman, 1989). This role as being the terminal degradative compartment in a cell has been described in great detail (Boya, 2012; Luzio et al, 2007; Saftig & Klumperman, 2009; Xu & Ren, 2015). However, further studies of lysosomal function over the last 60 years have also revealed it to have other crucial roles to play in cellular homeostasis and repair, recycling of cell membrane receptors, cholesterol homeostasis, antigen presentation, cell signaling, inactivation of pathogens and mediating cell death (Boya, 2012; Saftig & Klumperman, 2009).

In the nervous system, lysosomes have been shown to be critical to the development of neurons by regulating axon and dendrite growth, neurite arborization and axon pruning (Sann et al, 2009; Song et al, 2008). They also help regulate synaptic endocytosis and are essential for normal neuronal functioning and cell signaling (Lasiecka & Winckler, 2011; Murthy & Stevens, 1998; Nixon & Cataldo, 1995), as well as being involved in regulating neuronal cell death (Terman et al, 2010; Yamashima & Oikawa, 2009).

The complexity of lysosomal cellular functions as well as the highly polarized nature of neurons means that lysosomal dysfunction has a major impact on neuronal function (Wong & Cuervo, 2010; Zhang et al, 2009).

1.2 Lysosomal storage disorders (LSDs)

Following the discovery of the lysosome (Appelmans & De Duve, 1955; De Duve et al, 1955), Hers and colleagues properly developed the concept of lysosomal storage diseases with the identification of Pompe disease (Hers, 1965), despite the fact that many similar disorders had been described even before the discovery of the lysosome itself (Klein & Futerman, 2013).

LSDs are a group of around at least 50 heterogeneous diseases caused by mutations in genes that code either for lysosomal proteins or proteins involved in lysosomal biogenesis that lead to reduced or nonexistent functioning of these

proteins, and the characteristic accumulation of undegraded storage material (Ballabio & Gieselmann, 2009; Cox & Cachon-Gonzalez, 2012; Futerman & van Meer, 2004; Vitner et al, 2010; Walkley, 2009). LSDs have a combined incidence of approximately 1:5000-1:7000 live births worldwide (Fuller et al, 2006; Kingma et al, 2015; Klein & Futerman, 2013) and are most commonly autosomal recessively inherited (Winchester et al, 2000) with the exception of Fabry disease (Desnick et al, 1989) and Hunter syndrome (Mucopolysaccharidosis (MPS) type II) (Hopwood et al, 1993), which are X-linked, as well as the inherited adult form of NCL (CLN4), which shows an autosomal dominant inheritance (Nijssen et al, 2003; Noskova et al, 2011).

While most LSDs present clinically as diseases of childhood (Wraith, 2002; Wraith, 2004), there are some that have a later age of onset (Nijssen et al, 2003; Nixon et al, 2008; Shapiro et al, 2008; Spada et al, 2006). Typically, children are born healthy, with the exception of those diseases with storage material deposition in the bone and cartilage (e.g. Mucopolysaccharidosis) (Klein & Futerman, 2013; Platt et al, 2012; Wraith, 2004). After initially meeting developmental milestones, there is a period of decelerated development or decline (Beck, 2001; Wenger et al, 2003; Wraith, 2004). While some LSDs affect non-neuronal tissues, such as macrophages in Type 1 Gaucher disease (Hollak et al, 1997; van Breemen et al, 2007), the vast majority of LSDs present with CNS pathology (Ballabio & Gieselmann, 2009; Wraith, 2004). This neuropathology is typified by specific temporal and spatial patterns of glial activation and neuron loss, and the accumulation of large amounts of storage material within different cell types, although the links between these events is unclear and may vary between LSDs (Platt et al, 2012; Vitner et al, 2010). Glial cell activation, which is a common feature in LSDs, may potentially have a negative impact upon neuronal function and therefore contribute to disease progression (Chen et al, 2007; Di Malta et al, 2012; Ohmi et al, 2003; Pressey et al, 2012; Vitner et al, 2012).

While the primary defects in LSDs may originate in the proteins of the lysosomal-endosomal system resulting in lysosomal dysfunction and the accumulation of undegraded metabolites, these alone do not necessarily lead to cell death (Klein

& Futerman, 2013; Vitner et al, 2010; Winchester et al, 2000). Various other cellular pathogenic mechanisms have been shown to occur in most LSDs, such as altered calcium homeostasis, oxidative stress, ER stress, increased autophagy, autoimmune responses and inflammation that affect other cell organelles and therefore exert a greater deleterious effect upon cell function (Platt et al, 2012; Vitner et al, 2010). Therefore, despite differing in the primary genetic defect, LSDs show some degree of overlap in their pathological features, although the nature and timing of these events may differ markedly. This has therapeutic implications, as therapies that target shared pathological mechanisms can theoretically be effective in multiple LSDs (Vitner et al, 2010; Walkley, 2009), but this is likely limited to the downstream pathological cascade rather than the primary genetic defect.

These potentially common pathogenic cascades may not only link lysosomal dysfunction and its cellular sequelae to LSDs, but also to the development and/or progression of various neurodegenerative disorders in which protein aggregation due to impaired autophagy is observed, such as Alzheimer disease (AD), Parkinson disease (PD), Huntington disease (HD), fronto-temporal dementia (FTD) and amyotrophic lateral sclerosis (ALS) (Filimonenko et al, 2007; Garcia-Arencibia et al, 2010; Lee et al, 2007; Nixon & Cataldo, 2006; Nixon & Yang, 2011; Otomo et al, 2012; Pan et al, 2008; Wong & Cuervo, 2010). Therefore, despite different primary genetic causes, these more common neurodegenerative diseases may also share some common pathogenic pathways with LSDs that are downstream of the primary defect, and therefore may also potentially be amenable to some therapies targeting these downstream effects.

1.3 Neuronal ceroid lipofuscinoses (NCLs) or Batten disease.

a) History and classification

The NCLs are a group of up to 14 genetically and pathologically distinct LSDs (Bennett & Rakheja, 2013; Kohlschutter & Schulz, 2009; Kollmann et al, 2013; Mole & Cotman, 2015). Together, they are the most common inherited neurodegenerative storage disorders of childhood (Goebel, 1995; Haltia, 2006; Schulz et al, 2013).

While first described by Dr. Otto Stengel in a small Norwegian mining community in 1826 (Brean, 2004), this group of diseases was initially named after Dr. Frederick Batten who reported cases of Juvenile NCL in England in the early 20th century (Batten, 1903; Batten & Mayou, 1915; Zeman & Dyken, 1969). The NCLs were initially classified along with another LSD, Tay-Sachs disease (GM2-gangliosidosis Type A) as "amaurotic familial idiocies" due to having a similar clinical presentation of marked familial incidence, blindness and progressive mental deterioration (Haltia & Goebel, 2013). However, with time it became evident from the varying age of onset and differing biochemical properties that these diseases were a distinct group of LSDs, and were named the "neuronal ceroid lipofuscinoses" for the dense storage material that resembled ceroid and lipofuscin that accumulated within most cells in the body (Seehafer & Pearce, 2006; Zeman & Donahue, 1963; Zeman & Dyken, 1969).

These NCLs were initially classified based on their age of onset: infantile (Haltia-Santavuori disease), late infantile (Jansky-Bielschowsky disease), juvenile (Batten-Spielmeyer-Vogt disease), and adult (Kufs disease) (Getty & Pearce, 2011; Siintola et al, 2006). With the addition of congenital NCLs (Norman & Wood, 1941; Sandbank, 1968), as well as many atypical or variant forms of NCL, this classification was seen to be insufficient (Mole et al, 2011). With advances in molecular genetics, the primary genetic defects of the different forms of NCL have been identified, allowing for the NCLs to be classified based on their affected *CLN* gene and age of onset of the disease (Kollmann et al, 2013; Mole & Cotman, 2015; Williams & Mole, 2012) (Table 1.1). The NCLs can also be broadly divided based on the gene product into two categories – those that code for lysosomal enzymes (e.g. CLN1, CLN2, CLN10 etc.) and those that code for transmembrane proteins (e.g. CLN3, CLN6, CLN7, CLN8 etc.) (Kollmann et al, 2013). This is useful to determine which therapeutic approach may theoretically be applicable in each form of NCL. (Cooper et al, 2015)

Name	Age of onset	Gene affected	Type of protein
CLN1	Infantile NCL (INCL)	*CLN1/PPT1*	Lysosomal hydrolase (Palmitoyl thioesterase)
CLN2	Late Infantile NCL (LINCL)	*CLN2/TPP1*	Lysosomal hydrolase (Serine Protease)
CLN3	Juvenile NCL (JNCL)	*CLN3*	Transmembrane lysosomal protein (modulation of vesicular trafficking and fusion)
CLN4	Adult autosomal dominant NCL (ANCL, Parry Disease)	*CLN4/DNAJC5*	Cytoplasmic protein in cellular membranes (Hsc70 co-chaperone, involved in exocytosis and endocytosis)
CLN5	Variant LINCL (vLINCL)	*CLN5*	Soluble lysosomal protein
CLN6	vLINCL or Adult Kufs type A	*CLN6*	Transmembrane endoplasmic reticulum protein
CLN7	vLINCL	*CLN7/MFSD8*	Transmembrane lysosomal protein
CLN8	vLINCL (Northern epilepsy)	*CLN8*	Transmembrane endoplasmic reticulum protein
CLN9	*Juvenile NCL (**Postulated**)*	*Not known*	*Not known*
CLN10	Congenital NCL (CNCL)	*CLN10/CTSD*	Lysosomal hydrolase (aspartyl endopeptidase)
CLN11	ANCL	*CLN11/GRN*	Unknown, resides in secretory pathway (roles in inflammation, embryogenesis, cell motility and tumorigenesis postulated)
CLN12	vJNCL (Kufor-Rakeb Syndrome)	*CLN12/ATP13A2*	Lysosomal transmembrane protein
CLN13	Adult NCL (Kufs type B)	*CLN13/CTSF*	Lysosomal Hydrolase (Cysteine protease)
CLN14	vINCL	*CLN14/KCTD7*	Cytosolic protein, partially associated with membranes

Table 1.1 – Classification of the neuronal ceroid lipofuscinoses (NCLs).

Table describing the name, age of onset, gene defect and protein products of the 14 forms of NCL that have so far been identified. Adapted from (Kollmann et al, 2013; Mole & Cotman, 2015; Williams & Mole, 2012)

Despite the heterogeneity of genetic causes, most forms of NCL present with common clinical symptoms of progressive visual loss due to retinopathy, seizures of increasing severity and progressive decline of cognitive and sensorimotor function, which invariably lead to premature death (Dolisca et al, 2013; Williams et al, 2006; Wisniewski et al, 2001).

b) Pathology in the NCLs

The hallmark of NCL pathology is the pathognomic accumulation of autofluorescent lipopigment storage material inside cells (Zeman & Dyken, 1969), which was shown to contain subunit-C of mitochondrial ATP synthase, Saposins A and D, as well as β4 amyloid and Amyloid Precursor Protein (APP) in varying degrees depending on the type of NCL (Palmer et al, 2002; Wisniewski et al, 1993; Wisniewski et al, 1990; Zeman & Donahue, 1963). However, there is little evidence to suggest that this autofluorescent storage material is itself pathogenic, as there is no direct correlation between its accumulation and neuron loss (Cooper et al., 2006). This is evidenced by the fact that the acummulation of storage material in the CNS is widespread, while other pathological markers such as glial activation and neuron loss correlate with one another and show far greater regional specificity (Cooper, 2010; Weimer et al, 2002), also significantly reducing storage burden in the CNS does not prevent significant neuronal loss (Griffey et al, 2006) and inducing neuronal cells with storage material did not show any effect on cell survival (Ivy et al, 1984).

Apart from the accumulation of autofluorescent storage material in cell, the NCLs are also characterized by synaptic pathology (Cooper, 2010; Cooper et al, 2015; Kielar et al, 2009; Partanen et al, 2008), and widespread neurodegeneration, with GABAergic interneurons, thalamic relay neurons and cerebellar Purkinje cells being shown to be more vulnerable (Cooper, 2010; Cooper et al, 2006; Kielar et al, 2007; Oswald et al, 2005; Pontikis et al, 2004; Pontikis et al, 2005; Sleat et al, 2004; von Schantz et al, 2009). Even the loss of interneurons is graded, with calretinin positive interneurons more resistant to pathological change than other interneuron populations (Bible et al, 2004; Mitchison et al, 2004).

This neuron loss also shows pronounced regional specificity. Severe cerebral and cerebellar atrophy was observed in most human *post-mortem* tissue (Anderson et al, 2013), along with the loss of hippocampal neurons (Tyynelä et al, 2004). Various MRI studies have also consistently shown decreased signal intensity from the thalamus of patients (Autti et al, 2007; Vanhanen et al, 2004). These findings were also seen in various animal models of NCL, with thalamic

relay neurons being lost before any neurodegeneration in the corresponding cortical region (Cooper et al, 2006).

This selectivity of neuron loss is similar to that seen in other LSDs (Vitner et al, 2010), but is unlikely to be caused by the accumulated storage material (Cooper, 2010). Instead, the cause of neuronal death in NCLs has been attributed to various possible mechanisms. One possibility is that NCL protein defects cause defects in intracellular trafficking, which are more damaging in highly polarized cells like neurons (Jarvela et al, 1999; Luiro et al, 2004; Lyly et al, 2009; Lyly et al, 2007). Cells with higher metabolic rates like GABAergic interneurons may also be more vulnerable to these disease changes (Walkley & March, 1993). In CLN3 disease, antibodies against glutamic acid decarboxylase (GAD65) were detected (Chattopadhyay et al., 2002a; Chattopadhyay et al., 2002b). GAD65 helps to convert glutamate to GABA and this may help to further explain GABAergic interneuron vulnerability in this disease (Chattopadhyay et al, 2002a; Chattopadhyay et al, 2002b). There were also many antibodies against other brain proteins detected in CLN3 disease (Lim et al, 2007; Lim et al, 2006), which may potentially also contribute to neuron loss. Furthermore, while apoptosis has been proposed as a mechanism by which cells die in most forms of NCL (Cotman et al, 2002; Koike et al, 2003; Lane et al, 1996; Seigel et al, 2002), this remains unproven, while autophagy has also been implicated (Bronson et al, 1998; Larsen & Sulzer, 2002), Excitotoxicity has also been implicated to play a role in cell death, given the synaptic pathology described in various animal models (Finn et al, 2011; Finn et al, 2012; Kovacs & Pearce, 2008; Kovacs et al, 2006).

Glial activation, represented by astrocytosis and microglial activation, has been observed in all forms of human NCL at autopsy (Anderson et al, 2013; Tyynelä et al, 2004) as well as in various NCL animal models, where a pattern of glial activation, particularly astrocytosis, preceding neuron loss is evident in multiple forms of NCL (Bible et al, 2004; Kielar et al, 2007; Oswald et al, 2005; Partanen et al, 2008; Pontikis et al, 2004; Pontikis et al, 2005). Interactions between neurons and glia (Belin & Hardin, 1991; Burda & Sofroniew, 2014; Fields & Stevens-Graham, 2002; Salmina, 2009), as well as inter-glial interactions are essential for

neuronal homeostasis (Markiewicz & Lukomska, 2006; Polazzi & Contestabile, 2002). Glia are activated in response to brain injury or immunological stimuli and undergo pronounced changes in morphology with astrocytes becoming more hypertrophied with fewer thickened processes, while microglia go from a ramified, 'resting' morphology to a hypertrophied brain macrophage-like morphology (Nedergaard et al, 2003; Nimmerjahn et al, 2005; Ridet et al, 1997). While this glial activation is meant to be protective, over-activation can have a negative impact on neurons and lead to cell death (O'Callaghan & Sriram, 2005; Polazzi & Contestabile, 2002; Shyng & Sands, 2014). Furthermore, given the role that such glial activation plays in other neurodegenerative diseases such as Alzheimer disease, Parkinson disease and Huntington disease (Drew et al, 2006; Hirsch et al, 2003; Salmina, 2009; Unger, 1998), further research into the possible effects of glial activation on neuronal function in the NCLs is warranted and is currently ongoing (Cooper, personal communication).

From the broadly similar clinical symptoms in NCLs, most of the pathology in these diseases has been ascribed to the forebrain and cerebellum (Cooper, 2003; Cooper et al, 2006; Jalanko & Braulke, 2009). However, clinical studies have consistently noted severe sensorimotor deficits in patients that do not always correlate with brain pathology (Dolisca et al, 2013; Schulz et al, 2013; Williams et al, 2006). Recent studies have also shown the accumulation of storage material in various tissues outside the CNS (Anderson et al, 2013; Galvin et al, 2008; Staropoli et al, 2012), which may help to better understand systemic abnormalities in these diseases. Furthermore, there is evidence from human post-mortem tissue (Anderson et al, 2013; Santavuori et al, 1974) for similar autofluorescent storage material in the spinal cord. These data serve to emphasize that NCL pathology is not confined solely to the brain and characterizing these additional sites of pathology may be crucial for targeting future experimental therapies.

1.4 Infantile NCL or Classic CLN1 disease

a) Clinical presentation

The clinical presentation of CLN1 disease shows a general genotype-phenotype correlation and may vary from a devastating disease with infantile onset to an adult onset form (Kousi et al, 2012; Mole et al, 2005). Classically, CLN1 disease represents a very severe form of NCL and presents at 6-24 months of age with a rapid loss of motor and cognitive abilities and the presence of hyperkinesias. Often, there is decelerated head growth and muscular hypotonia preceding the onset of these symptoms. Loss of vision, hyperexcitability and restlessness are common from 16-19 months of age. Loss of vision progresses to blindness by 18-20 months while the onset of epilepsy is usually around 30 months, with myoclonic, tonic, clonic or hypomotor seizures common. As the child's age progresses, there is increased irritability due to generalized spasticity and pain. The child loses almost all cognitive and active motor skills by 3 years of age and the usual life expectancy is between 9 and 13 years (Dolisca et al, 2013; Santavuori et al, 1973; Williams et al, 2006). MRI scans of patients show decreased signal from the thalamus at an early age, followed by progressive cerebral atrophy from around 12 months of age, which becomes very severe around 4 years (Vanhanen et al, 2004).

b) Genetics

Classic CLN1 disease, which is often known as Infantile NCL (INCL) (previously known as Santavuori-Haltia disease) (Mole et al, 2011; Santavuori et al, 1974) is caused by mutations in the *CLN1/PPT1* gene, located on chromosome 1p32. *CLN1/PPT1* encodes the soluble lysosomal enzyme palmitoyl protein thioesterase 1 (PPT1) (Mole & Cotman, 2015; Vesa et al, 1995). Mouse *Ppt1 RNA* can be detected as early as embryonic day 8 (E8) throughout the neuroepithelium, with increasingly regionalized expression from E11 onwards. Furthermore, at post-natal day 15 (P15) the expression of *Ppt1* was*Ppt1*was generally low in the brain, but which increased by P30, especially in the cerebral cortex, hippocampus and hypothalamus (Isosomppi et al, 1999; Salonen et al, 1998). In rats, the cerebellum exhibits a progessive continuous change in *Ppt1* RNA expression until P30. In contrast, there seems to be little change in *Ppt1* RNA

expression in the spleen or liver during development (Suopanki et al, 1999a; Suopanki et al, 1999b). Despite extensive work to study the expression of *Ppt1* in both brain and non-neuronal tissues in rodents and in humans, there is currently no data on its expression in the spinal cord. Indeed, the absence of data for *Ppt1* expression in the spinal cord in the Allen brain atlas (http://www.brain-map.org) is very conspicuous, especially given that similar information is already available for other NCL genes including Cln2, Cln3, Cln5, Cln6 and Cln8.

Up to 64 mutations have been described for the *CLN1* gene with the most common mutation, a premature stop codon at arginine 151 (p. Arg151x), accounting for 40% of alleles (Das et al, 1998; Kousi et al, 2012; Mink et al, 2013). It has been shown that mutations in *CLN1/PPT1* that leave a higher residual level of PPT1 activity result in a later onset and slower progression of the disease. This suggests that the loss of PPT1 activity directly affects pathogenesis (Bonsignore et al, 2006; Kalviainen et al, 2007; Mueller & Coovadia, 2010; Perez-Poyato et al, 2011; Simonati et al, 2009; Van Diggelen et al, 2001). Structural analysis of the effects of mutations on PPT1 also showed that larger mutations and those that were closer to the core of the enzyme, reduced enzymatic activity to a greater degree than smaller mutations, or those near the surface of the enzyme (Ohno et al, 2010), and that the closer the mutation is to the active site of the enzyme, the more severe the disease (Hofmann et al, 2001). Furthermore, Zhang and colleagues also demonstrated that mutations in *CLN1/PPT1* lead to a mis-folding of the protein PPT1 (Zhang et al, 2006).

c) PPT1 function

PPT1 is widely expressed in the CNS of mammals (Isosomppi et al, 1999; Suopanki et al, 2002) and murine *Ppt1* mRNA is expressed in various tissues throughout the body (Camp & Hofmann, 1993; Camp et al, 1994; Salonen et al, 1998). PPT1 is a soluble lysosomal enzyme that removes palmitate groups from S-acylated proteins (Camp & Hofmann, 1993). Many molecules undergo palmitoylation and de-palmitoylation in the cell, and these changes influence many cellular functions including subcellular trafficking and vesicular transport (Aicart-Ramos et al, 2011). PPT1 is targeted to the lysosome via the mannose 6-

phosphate receptor-mediated pathway, and this may be affected in disease (Hellsten et al, 1996; Lyly et al, 2007).

While PPT1 is a lysosomal enzyme, there is growing evidence to suggest that the localization and function of PPT1 is not confined to the lysosome. PPT1 has a substrate-dependent neutral pH (7.0) for optimal enzyme activity, which is unusual for lysosomal enzymes that prefer an acidic pH (4.5-5.0) (Cho et al, 2000) suggesting that it is able to function outside the milieu of the lysosome. PPT1 has been shown to associate with lipid raft domains (Goswami et al, 2005) and has been found in vesicular structures in axons, soma and dendrites (Ahtiainen et al, 2003; Isosomppi et al, 1999; Lehtovirta et al, 2001). The expression of PPT1 in neurons parallels that of abundant presynaptic marker proteins and cultured PPT1 knock-out neurons show altered sensitivity to glutamate (Finn et al, 2012) and there is evidence of PPT1 expression in pre-synaptic vesicles (Virmani et al, 2005). Furthermore, PPT1 seems to play a greater role than previously thought in neurons than in other cell types, as evidenced by the difference in its processing and trafficking in neurons (Lyly et al, 2007). PPT1 is also expressed in several regions of human and rodent brains during development, and has been shown to be required for proper neuronal development, including axon guidance, synaptic pruning and determining cell fates (Chu-LaGraff et al, 2010; Fabritius et al, 2014; Isosomppi et al, 1999; Minye et al, 2016). Other possible functions of PPT1 include roles in lysosomal protein sorting and pH regulation (Cho & Hofmann, 2004), involvement in caspase-mediated apoptotic pathways (Cho & Dawson, 2000), the negative mediation of tumor necrosis factor α (TNF-α) (Tardy et al, 2009), involvement in the mitochondrial respiratory chain (Meyer et al, 2016) and lipid metabolism, calcium homeostasis and thermoregulation (Ahtiainen et al, 2007; Khaibullina et al, 2012; Lyly et al, 2008). PPT1 may potentially interact with other NCL proteins such as CLN5 (Lyly et al, 2009) and Cathepsin D (CLN10/CTSD) (Scifo et al, 2015b), although these data largely depend on antibodies whose specificity is unclear. Proteomic or interactome studies of PPT1 have implicated its role in lipid metabolism, axonal guidance, the myelin proteome, neuronal migration and dopamine receptor mediated signaling (Scifo et al, 2015a; Tikka et al, 2016).

1.5 The *Ppt1*$^{-/-}$ mouse.

Various small eukaryotic *in vivo* model systems have been used to study CLN1 disease (Phillips et al, 2006) including yeast (Pearce, 2001), *C. elegans* (Porter et al, 2005) and *Drosophila* (Chu-LaGraff et al, 2010; Hickey et al, 2006; Korey & MacDonald, 2003). However, the most powerful tools for understanding disease pathology as well as for testing experimental therapies have been mouse models (Cooper et al, 2006). Currently there are four mouse models for CLN1 disease, each produced by a different targeting strategy to produce - a) a null mutant by replacing exon 9 of *Cln1* with a premature stop codon (Gupta et al, 2001), b) a mouse with a targeted deletion of exon 4 of *Cln1* (Jalanko et al, 2005) and c) mice that recreate commonly occurring mutations such as the c.451 C>T nonsense mutation (Bouchelion et al, 2014), or the pR151X mutation (Miller et al, 2015) (*Cln1*^{R151X}). All these models share broadly similar phenotypes of deteriorating motor performance with age, autofluorescent storage material buildup, neuroinflammation, significant cortical atrophy and premature death.

By far, the most commonly used mouse model for the study of CLN1 disease pathology are the null-mutant mice (*Ppt1*$^{-/-}$) (Bible et al, 2004; Kielar et al, 2009; Kim et al, 2008; Lyly et al, 2007; Macauley et al, 2009). These mice were created by homologous recombination to disrupt the *Ppt1* gene, whereby a portion of exon 9 of the *Cln1* gene was replaced by a premature stop codon, resulting in a truncated mRNA and a complete loss of Ppt1 enzyme activity (Gupta et al, 2001).

These *Ppt1*$^{-/-}$ mice exhibit abnormal clasping behavior in the tail-suspension test, myoclonus, seizures and visual, motor and cognitive deficits. They also exhibit abnormal gait with splayed hindlimbs and lowering of the pelvis and they have an average lifespan of 8-8.5 months (Gupta et al, 2001). These mice also show severe motor deficits such as a significantly decreased latency to fall starting at 5 months in the constant speed rotarod-testing paradigm (Macauley et al, 2009), as well as significantly worse performance at in accelerating rotarod, pole-climbing and ambulation tests (Griffey et al, 2006). A recent study of *Ppt1*$^{-/-}$ mouse behavior revealed further subtle motor deficits at earlier time points (1-3 months) in walking initiation and walking up a 60° inclined plane, with more

dramatic visual, cognitive and motor deficits observed at 5-7 months of age including differences in visual acuity tests, the Morris water maze, conditioned fear test, running wheel tests, inclined plane walking tests, and Actometer readings (Dearborn et al, 2015). *Ppt1*$^{-/-}$ mice also showed decreased learning ability in a light-cued T-maze (Wendt et al, 2005). Furthermore, despite a trend towards lower body weights, *Ppt1*$^{-/-}$ mice did not show any statistically significant difference in body weight when compared to their wildtype counterparts at any time point (Galvin et al, 2008). Taken together these data suggest that *Ppt1*$^{-/-}$ mice accurately recapitulate the severe visual, cognitive and motor deficits seen in human CLN1 disease and therefore represent a good model of the disease.

Pathological analysis of *Ppt1*$^{-/-}$ mice has shown that there is a deposition of characteristic autofluorescent granular osmiophillic storage material in the CNS and visceral organs (Bible et al, 2004; Galvin et al, 2008), similar to human CLN1 disease (Anderson et al, 2013). *Ppt1*$^{-/-}$ mice demonstrate significant brain atrophy with age starting at 5 months (Kühl et al, 2013) along with region-specific glial activation and neurodegeneration, with astrocytosis preceding microglial activation and neuron loss in the brain and cerebellum (Kielar et al, 2007; Macauley et al, 2009). Significant astrocytosis is observed in the thalamus as early as 3 months of age, while neuron loss begins at 5 months (Bible et al, 2004; Kielar et al, 2007). Furthermore, the cerebellum and thalamus are affected early in disease progression, with GABAergic interneurons and cerebellar Purkinje cells particularly vulnerable (Bible et al, 2004; Kielar et al, 2007; Macauley et al, 2009). Towards the end of disease progression, there is widespread gliosis and neuron loss in the brain and cerebellum, although it remains most pronounced in the areas initially affected (Kielar et al, 2007; Macauley et al, 2009)

Ppt1$^{-/-}$ mice display significant cerebral synaptic pathology early in disease progression, with reduced levels of presynaptic proteins such as SNAP-25, synaptophysin and the aggregation of synaptobrevin (VAMP2) seen as early as 3 months in the thalamus (Kielar et al., 2009). These changes may contribute to

excitotoxicity and cell death (Kielar et al, 2009; Kim et al, 2008). There was also a significant low-level infiltration of the brain parenchyma by peripheral lymphocytes indicating an adaptive immune response in addition to the innate glial response (Groh et al, 2013), as well as a study that detailed a possible change in the integrity of the blood-brain barrier (BBB) in these mice (Saha et al, 2012). *Ppt1*$^{-/-}$ mice also show abnormalities in the ER, altered energy metabolism and show activation of the unfolded protein response (UPR), possibly to reduce oxidative stress (Wei et al, 2008; Wei et al, 2011; Zhang et al, 2006).

The comprehensive characterization of pathology in the forebrain of *Ppt1*$^{-/-}$ mice has helped us understand CLN1 disease pathology in some detail, but still cannot explain some of the early sensorimotor deficits seen in these mice. The evidence of spinal cord pathology from human CLN1 *post-mortem* tissue (Anderson et al, 2013; Santavuori et al, 1974) as well as the presence of pathology in the viscera of these animals (Galvin et al, 2008), further emphasizes the need for a more comprehensive study of sensorimotor deficits as well as for a pathological survey of the CNS outside the brain.

1.6 Therapeutic approaches for CLN1 Disease

The availability of authentic mouse models of CLN1 disease has facilitated the testing of a range of experimental therapies for this disease. However, despite numerous efforts, few of these therapies have provided both a significant alleviation of symptoms and extension of lifespan. Therefore either combined therapeutic approaches or targeting regions of pathology outside the brain must now also be considered (Hawkins-Salsbury et al, 2013).

a) Enzyme replacement therapy (ERT)

As CLN1 disease is a lysosomal enzyme deficiency, ERT utilizes "cross-correction" between cells, whereby lysosomal enzymes secreted into the extracellular space can be take up by neighboring cells by means of the mannose-6-phosphate receptor system. Thus, recombinant post-translationally modified enzyme can be endocytosed by cells following delivery into the tissue (Kornfeld, 1992; Sands & Davidson, 2006). This approach has been shown to be successful in a variety of enzyme-deficient LSDs including Mucopolysaccharidosis type I and

type IIIA, Niemann Pick-A disease and neuronopathic Gaucher disease (Dierenfeld et al, 2010; Dodge et al, 2009; Hemsley et al, 2009; Lonser et al, 2005). Furthermore, it has previously been shown that restoring 4-5% of PPT1 enzyme activity is sufficient to significantly reduce the neurodegenerative phenotype in *Ppt1*$^{-/-}$ mice (Griffey et al, 2006). This is similar to data from a hypomorph mouse model of CLN2 disease, where residual enzyme (TPP1) activity of just 6% of the normal value was sufficient to significantly ameliorate disease (Sleat et al, 2008).

Initial high-dose intravenous delivery of recombinant PPT1 enzyme was shown to distribute well and reduce storage material burden in the visceral tissue of *Ppt1*$^{-/-}$ mice, as well as not showing any overt toxicity (Hu et al, 2012; Lu et al, 2010). However, very little of the enzyme was shown to cross the blood–brain barrier (BBB) even at high doses, and therefore this approach had very little effect on brain pathology (Hu et al, 2012; Lu et al, 2010). Nonetheless, systemic delivery of recombinant PPT1 enzyme did result in a modest improvement of motor function as well as an increase in lifespan of these mice (Hu et al, 2012). This improvement despite the lack of any appreciable effect in the CNS suggests the presence of clinically significant pathology outside the CNS, and it may therefore be possible to use systemic ERT in combination with other CNS directed therapies.

The lack of effect of ERT for CLN1 disease is in contrast to CLN2 disease, which is also caused by a lysosomal enzyme deficiency (Mole & Cotman, 2015). Intrathecal delivery of recombinant TPP1, the enzyme deficient in CLN2 disease, resulted in significant improvements in the pathology and lifespan in these mice (Xu et al, 2011), while intra-ventricular delivery of the enzyme in a canine model of the disease was also particularly effective in alleviating disease pathology (Katz et al, 2014) and this is now currently being tested in a clinical trial (*https://clinicaltrials.gov/show/NCT02678689*). Thus, adopting similar approaches for ERT in CLN1 disease may also lead to better outcomes.

b) Anti-oxidant drugs

Oxidative and ER stress, as well as disrupted adaptive energy metabolism, have been suggested to have a role in CLN1 disease, and appear to trigger caspase-mediated apoptosis (Kim et al, 2006; Wei et al, 2008; Wei et al, 2011; Zhang et al, 2006). Resveratrol, an anti-oxidant molecule from red grape skins, was shown to reduce apoptotic markers and improve the energy metabolism in CLN3 lymphoblast cells (Yoon et al, 2011) and the administration of resveratrol in the diet of *Ppt1*$^{-/-}$ mice resulted a modest increase in lifespan, as well as a reduction of apoptotic markers (Wei et al, 2011). The increase in lifespan was perhaps surprising, as this drug does not target the primary enzyme deficit (Wei et al, 2011). Further, the anti-inflammatory effect of resveratrol may also help to reduce the BBB defects seen in these mice (Saha et al, 2012). Therefore, this drug that can be easily orally administered with minimal side effects might also be considered as a candidate for combination therapies with other CNS-targeted approaches.

c) PPT1 mimetic drugs

Since PPT1 cleaves thioester linkages in the lysosome (Camp & Hofmann, 1993), it has been reasoned that other molecules that have a similar activity and a lysosomal localization may be useful in treating CLN1 disease (Zhang et al, 2001). Phosphocysteamine and N- acetylcysteine (NAC) were shown to be able to cross the BBB, localize to the lysosome and have thioesterase-like function (Bavarsad Shahripour et al, 2014; Zhang et al, 2001). While *in vitro* data suggested that phosphocysteamine did not produce the same level of activity as PPT1 (Lu & Hofmann, 2006), this nevertheless made for an attractive therapeutic approach. Phosphocysteamine therapy was shown to be effective in clearing storage material from human CLN1 disease lymphoblasts (Zhang et al, 2001), but showed very little change in pathology or lifespan when administered alone to *Ppt1*$^{-/-}$ mice (Roberts et al, 2012). This was mirrored in clinical trials where phosphocysteamine showed little clinical benefit either given alone (Gavin et al, 2013), or in combination with N- acetylcysteine (Levin et al, 2014).

d) Stop codon read- through drugs

Many of the common mutations in CLN1 disease result in the formation of premature termination codons (PTC) as a result of base substitutions, insertions or deletions in introns and exons of the *CLN1* gene which cause aberrant splicing and frame-shifts (Kousi et al, 2012). The resulting mRNA from these mutated genes are prone to nonsense-mediated decay (NMD) (Miller et al, 2013), which is crucial for post-translational control of gene expression in mammalian cells (Chang et al, 2007; Silva & Romao, 2009). Therefore, drugs that can force a read-through of these PTCs or suppress the levels of NMD provide an attractive therapeutic option in LSDs (Brooks et al, 2006; Lee & Dougherty, 2012).

The administration of the stop codon read-through drug ataluran (PTC124) was shown to decrease storage material, increase PPT1 enzyme activity and reduce apoptosis in human CLN1 disease lymphoblasts (Sarkar et al, 2011). The recent creation of two "knock-in" mouse models that recreate commonly occurring point mutations in the *Cln1* gene has facilitated the testing of such drugs (Bouchelion et al, 2014; Miller et al, 2015). Administration of ataluran (PTC124) was shown to increase PPT1 enzyme activity in the brain and liver of $Cln1^{R151X}$ mice in a pilot study (Miller et al, 2015), but a more detailed study revealed greater variation in *Cln1* gene expression and PPT1 activity (Thada et al, 2016). Despite these moderate effects, these drugs still show promise in providing clinical therapies, and more work will be required to make this possible.

e) Bone marrow transplantation (BMT)

Bone marrow transplantation or hematopoietic stem cell transplantation (HSCT) has been found to have varying success in different LSDs depending on the type of LSD, the extent of brain pathology and the age that treatment is initiated (Neufeld & Fratantoni, 1970). This therapy relies on "cross-correction" of the enzyme (Kornfeld, 1992; Sands & Davidson, 2006) with a small number of donor cells believed to migrate to the host brain to supply the missing enzyme (Armitage, 1994; Neufeld & Fratantoni, 1970). Despite a number of trials of both BMT and HSCT in the enzyme deficient forms of NCL, this therapeutic approach has proven to be ineffective (Deeg et al, 1990; Lake et al, 1997; Lonnqvist et al,

2001). Indeed, a recent trial in *Ppt1*$^{-/-}$ mice showed almost no beneficial effect at all upon of BMT by itself (Macauley et al, 2012).

f) Neuronal stem cells

The culture, banking and engraftment of Human-CNS (Hu-CNS) stem cells upon intra-cerebral delivery was shown to be partially successful in immunodeficient mice (Tamaki et al, 2002; Uchida et al, 2000). A trial of similar delivery of Hu-CNS stem cells in Ppt1 deficient mice on a similar immunodeficient background showed wide distribution of these cells upon delivery and an increase in PPT1 levels that significantly reduced the accumulation of storage material, delayed the loss of neurons and improved motor function on these mice (Tamaki et al, 2009). This relatively promising pre-clinical data led to a phase one clinical trial of Hu-CNS stem cell therapy in CLN1 and CLN2 disease (*https://clinicaltrials.gov/ct2/show/NCT00337636*). This was the first such clinical trial for neural stem cell transplantation for any disease. This trial provided no evidence of any deleterious effects of these NSC transplants, but equally showed no positive data for any degree of efficacy. While not as effective in clinical trials, stem cell therapy still remains another potential option for delivering PPT1 to the brain.

g) Gene therapy

Of all the therapeutic approaches for CLN1 disease, the most promising pre-clinical data has come from various experimental studies involving gene therapy. Intracranial (IC) injections of an adeno-associated virus (AAV) vector, AAV2 targeting the forebrain in *Ppt1*$^{-/-}$ mice showed significant improvements in reducing the accumulation of autofluorescent storage material, as well as increased brain mass and cortical thickness (Griffey et al, 2004). Additionally targeting the cerebellum showed more pronounced improvements with better motor function, and reduced seizure activity, along with a greater effect on the accumulation of autofluorescent storage material and neuron loss in these mice (Griffey et al, 2006). Retinal gene therapy in *Ppt1*$^{-/-}$ mice not only reduced the retinal neurodegenerative phenotype, but also showed anterograde axonal transport of PPT1 enzyme to the connected brain regions (Griffey et al, 2005), demonstrating that this approach may be useful in combination with brain-

directed therapies. Recently, the use of a newer AAV vector (AAV2/5) has been shown to have greater distribution and efficacy in delivering the gene product, as evidenced by further improvements in brain pathology and an increased lifespan of about 12 months in *Ppt1*$^{-/-}$ mice (Macauley et al, 2012; Roberts et al, 2012). However, despite significant amelioration of brain pathology in these mice, they still died prematurely, implying that it is crucial to additionally target sites of pathology outside the brain in CLN1 disease (Macauley et al, 2012). Therefore, gene therapy has considerable potential for treating brain pathology in pre-clinical models of CLN1 disease. It is likely that the efficacy of this approach may be enhanced by using newer AAV vectors that have better distribution and neuronal transduction (Aschauer et al, 2013; Cearley & Wolfe, 2006; Gray et al, 2013; Swain et al, 2014), as well as possibly combining this method with other therapeutic approaches.

h) Combination therapies

The efficacy of AAV-mediated brain-directed gene therapy in ameliorating brain pathology, improving the behavioral phenotype as well as improving the lifespan of *Ppt1*$^{-/-}$ mice (Macauley et al, 2012), has led to this approach being tested in combination with other systemic approaches to determine if this combined approach would improve efficacy.

Combination of CNS-directed gene therapy along with the administration of the PPT1 mimetic drug phosphocysteamine (Zhang et al, 2001) showed some improvements in motor function, as compared to the gene therapy alone, with little other effect (Roberts et al, 2012). Surprisingly, bone marrow transplants (BMT), which were shown to have little effect when delivered alone, showed a great synergy with CNS-directed gene therapy with a significantly increased lifespan, improved motor function and a reduction in almost all brain pathological phenotypes, as compared to gene therapy alone (Macauley et al, 2012).

Given the significant neuroinflammatory phenotype seen in the brains of *Ppt1*$^{-/-}$ mice (Bible et al, 2004; Kielar et al, 2007), a BBB-penetrant anti-inflammatory

drug MW151 was tested in combination with CNS-directed gene therapy. Combination therapy treated mice showed improved the lifespan, motor function and reduced seizure activity, as well as reduced neuroinflammation, cytokine upregulation and brain atrophy (Macauley et al, 2014).

The improved efficacy of combining brain directed and systemic therapies, compared to only brain-directed therapies not only hints at the presence of clinically significant pathology outside the brain, but also that therapeutically targeting such pathology can provide significant therapeutic benefits in CLN1 disease.

1.7 The spinal cord in health and disease

The spinal cord is part of the CNS, extending caudally from the brainstem. It is protected by the structures forming the vertebral column. It serves as a bridge between the CNS and the periphery, allowing for the transmission and modulation of information between them. The spinal cord is linked to sensory, autonomic and motor control and is therefore crucial to CNS function (Nógrádi & Vrbová, 2006). It is affected in injury and a variety of diseases including infection, neoplasms and neurodegenerative diseases (Cho, 2015).

a) Structure

In mammals, the spinal cord extends only for the upper two-thirds of the vertebral canal. This is due to the differential growth of bony structures compared to the cord during development. As with the rest of the CNS, it is ensheathed by three layers of meninges – the dura, arachnoid and pia mater. The dura mater in the vertebral canal has two layers that are separated by the epidural space while cerebrospinal fluid is located between the arachnoid and pia mater. The spinal cord can be divided in to cervical, thoracic, lumbar and sacral segments depending on the position within the canal and the entry or exit levels of nerve roots, and the cervical and lumbar segments can be distinguished macroscopically as enlargements. The spinal cord gives rise to spinal nerves throughout its length, and these are formed from the dorsal and ventral roots that emerge from the lateral aspect of the cord on either side. The cord is also bilaterally symmetrical and is divided by the anterior and posterior median

fissures into two symmetrical halves along the median sagittal axis. There are thirty one spinal cord segments – eight cervical, twelve thoracic, five lumbar, five sacral, and one coccygeal (Cho, 2015; Nógrádi & Vrbová, 2006).

In contrast to the brain, the gray matter of the spinal cord is completely surrounded by white matter. The gray matter is divided into the dorsal horn, intermediate gray, the ventral horn and the central gray matter, while the white matter is conventionally divided into various tracts or funiculi – dorsal, dorsolateral, lateral, ventrolateral and ventral. The white matter gradually ceases in the caudal region of the cord, when the gray matter forms the *conus terminalis,* which then divides into spinal roots forming the *cauda equina.* The dorsal horn of the spinal cord gives rise to dorsal roots, which join together and enter the dorsal root ganglion (DRG) in the intervertebral foramen, where the primary sensory neurons are located (Nógrádi & Vrbová, 2006; Rexed, 1954).

The gray matter of the spinal cord has been divided into various laminae based on the topology and density of cells (Brown, 1981; Rexed, 1954) (Fig 1.1). The characteristics and cell types that are present in each lamina are detailed in table 1.2.

b) Cells of the spinal cord

The spinal cord is comprised of two main neuronal types – motor neurons and interneurons. Motor neurons are crucial to the functioning of motor pathways. They are commonly present in lamina IX of the ventral horn and are divided into four columns: ventromedial, ventrolateral, dorsolateral and central. In these columns, motor neurons projecting to proximal muscles are found in ventral and medial positions, while those projecting to distal muscles are located in the dorsal and lateral aspect of each column. The dendrites of motor neurons in the dorsolateral column show a radial distribution, with little overlap. This may contribute to more precise motor control in the distal afferents. The dendrites of motor neurons in the other columns show great overlap and longitudinal polarization of the dendrites suggesting greater synergy and synchronization of the proximal and axial muscle groups (Romanes, 1964; Schoenen, 1982).

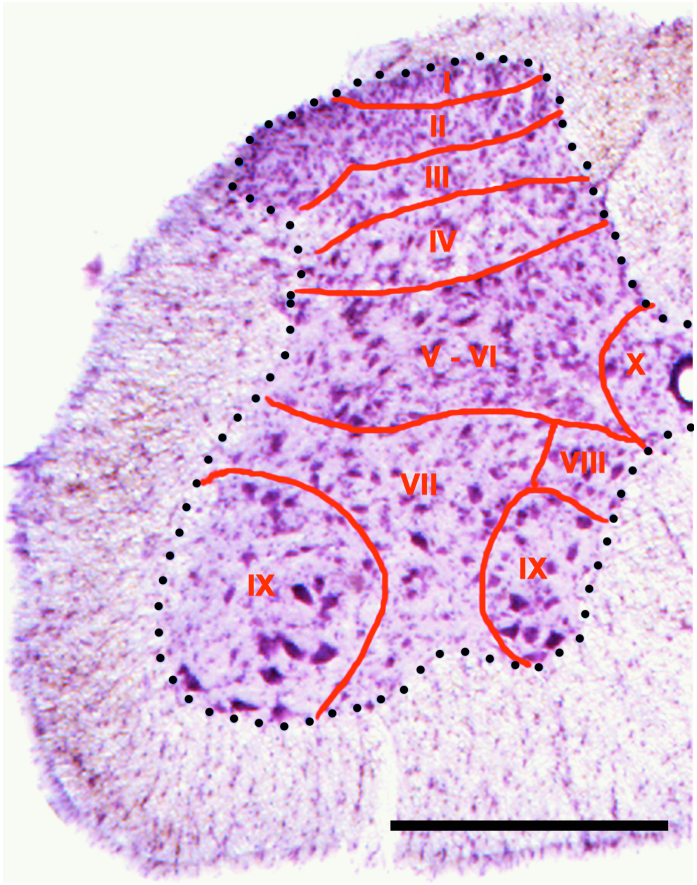

Figure 1.1 – Laminar cytoarchitechture of the spinal cord.

Schematic representation of the laminar organization of the gray matter of the spinal hemi-cord at the level of L4, superimposed over a cresyl fast violet stained section to visualize neuronal cytoarchitechture. Adapted from (Nógrádi & Vrbová, 2006; Sengul, 2013). Red lines separate laminae I-X, while the gray matter is separated from the white matter by a black dotted line. Scale bar = 200μm.

Interneurons are the most abundant and the most important modulating cell type in the spinal cord. In the dorsal horn, they play a crucial role in the transmission of impulses from the primary sensory neurons in the DRG to the ascending pathways that reach the centers in the brain and brainstem. They perform a similar role in the flow of information from these supra-spinal centers to the motor neurons in the ventral horn. Not only do they help in the transmission of impulses, but also help to modulate them by means of functional reorganization of the complex spinal neural networks (Edgley, 2001; Jankowska, 2001).

Apart from the various types of neurons, the spinal cord also contains many glial cells, which have important functions including astrocytes, oligodendrocytes and microglial cells. Astrocytes are stellate cells that have recently been shown to have a variety of functions, in addition to the metabolic and trophic support of neurons including CNS energy metabolism, synaptogenesis and involvement in synaptic transmission by participating in the tripartite synapse (Araque et al, 1999; Kettenmann & Verkhratsky, 2011; Kimelberg & Norenberg, 1989; Sofroniew & Vinters, 2010).

There are two forms of astrocytes in the spinal cord – protoplasmic and fibrous astrocytes. Protoplasmic astrocytes are more common in the gray matter and have dense, thin processes and express lower levels of glial fibrillary acidic protein than fibrous astrocytes that are predominantly seen in the white matter and have long, thick, fibrous processes with high levels of GFAP expression. The former are more commonly associated with synapses, while the later are present at the nodes of Ranvier along axons, which are essential for proper impulse propagation (Kimelberg & Norenberg, 1989; Molofsky et al, 2012).

Oligodendrocytes are glial cells that produce myelin within the CNS, and each oligodendrocyte is able to myelinate several adjacent axons of neurons. Wrapping spiral layers of oligodendrocyte cell membrane around the axon forms myelin, with the inner surfaces of the cell membranes eventually fusing. The myelin contains various special lipids and proteins, for example the glycolipid galactocerebroside and myelin basic protein (MBP). Oligodendrocytes also play a role in supporting the integrity of myelinated axons (Simons & Nave, 2015). The spinal cord, like the rest of the CNS has a unique set of immune cells, microglia. Even in the normal brain, these cells have highly motile processes by which they can “scan” the environment for any noxious substances. They also communicate with both neurons and immune cells through a variety of signaling pathways. When activated, they proliferate, hypertrophy and can release a range of substances that can either be beneficial or detrimental to surrounding cells (Kettenmann et al, 2011; Kettenmann & Verkhratsky, 2011; Marin-Teva et al, 2011).

Lamina	Characteristics
Lamina I	Dorsal-most lamina with typical Waldeyer cells (GABAergic inhibitory) and pyramidal cells with low neuronal density.
Lamina II	Densely packed neurons with two main types of cells - stalked cells and islet cells (inhibitory cells).
Lamina III	Lower neuron density than lamina II. Most cells are inhibitory, expressing GABA or glycine and have an antenna-like or radial appearance.
Lamina IV	Contain a variety of antenna-like cells as well as the so-called transverse cells. Axons of these cells mainly project to the spino-thalamic tract.
Lamina V-VI	Both these laminae have similar composition. The medial part has many triangular and fusiform cells while the lateral part is characterized as having many multipolar cells that correspond to the reticular formation.
Lamina VII	Occupies the intermediate zone of the gray matter. Between T1-L1, it contains the interomediolateral nucleus, which has autonomous and motor function. It also contains the dorsal nucleus of Clarke from T1-L2, the ascending projections of which form the spino-cerebellar tract.
Lamina VIII	Contains a variety of neurons with easily distinguishable dorso-ventral polarity. These neurons have finer Nissl bodies than motor neurons.
Lamina IX	This lamina contains motor neurons that are recognized by the abundance of Nissl bodies in their cytoplasm, their multipolar shape and their size. The α- motor neurons are larger than the γ-motor neurons. This lamina is divided into ventromedial, ventrolateral, dorsolateral and central columns, and the motor neurons in each column innervate a different group of muscles.
Lamina X	This lamina is also termed the *substansia grisea centralis*, and corresponds to the gray matter surrounding the central canal. It is a zone of actively dividing cells and the neurons here have a bipolar shape.

Table 1.2 – Cellular characteristics of the spinal cord laminae.

Adapted from (Brown, 1981; Nógrádi & Vrbová, 2006; Rexed, 1954; Romanes, 1964).

c) Connections of the spinal cord and functions

The spinal cord has three main types of connections or pathways – ascending, descending and intrinsic pathways. The ascending pathways facilitate the movement of information from the periphery to the CNS. In humans, the pseudounipolar axons of the primary sensory neurons in the DRGs send fibers to the dorsal horn of the spinal cord, where they synapse and second order neurons then cross over to the opposite side (anterior to the central canal) to ascend via white matter tracts in the lateral and ventrolateral funiculi to reach the ventral posterior lateral (VPL) nucleus of the thalamus. This forms the spinothalamic tract (Figure 1.2) and helps convey the localization of thermal and pain stimuli.

Alternatively, DRG fibers that may enter the ipsilateral dorsal column situated in the dorsal funiculi ascend the entire length of the spinal cord. This forms the dorsal tract (Figure 1.3), which consists of the medial fasciculus gracilis and the lateral fasciculus cuneatus and becomes thicker rostrally as more fibers are

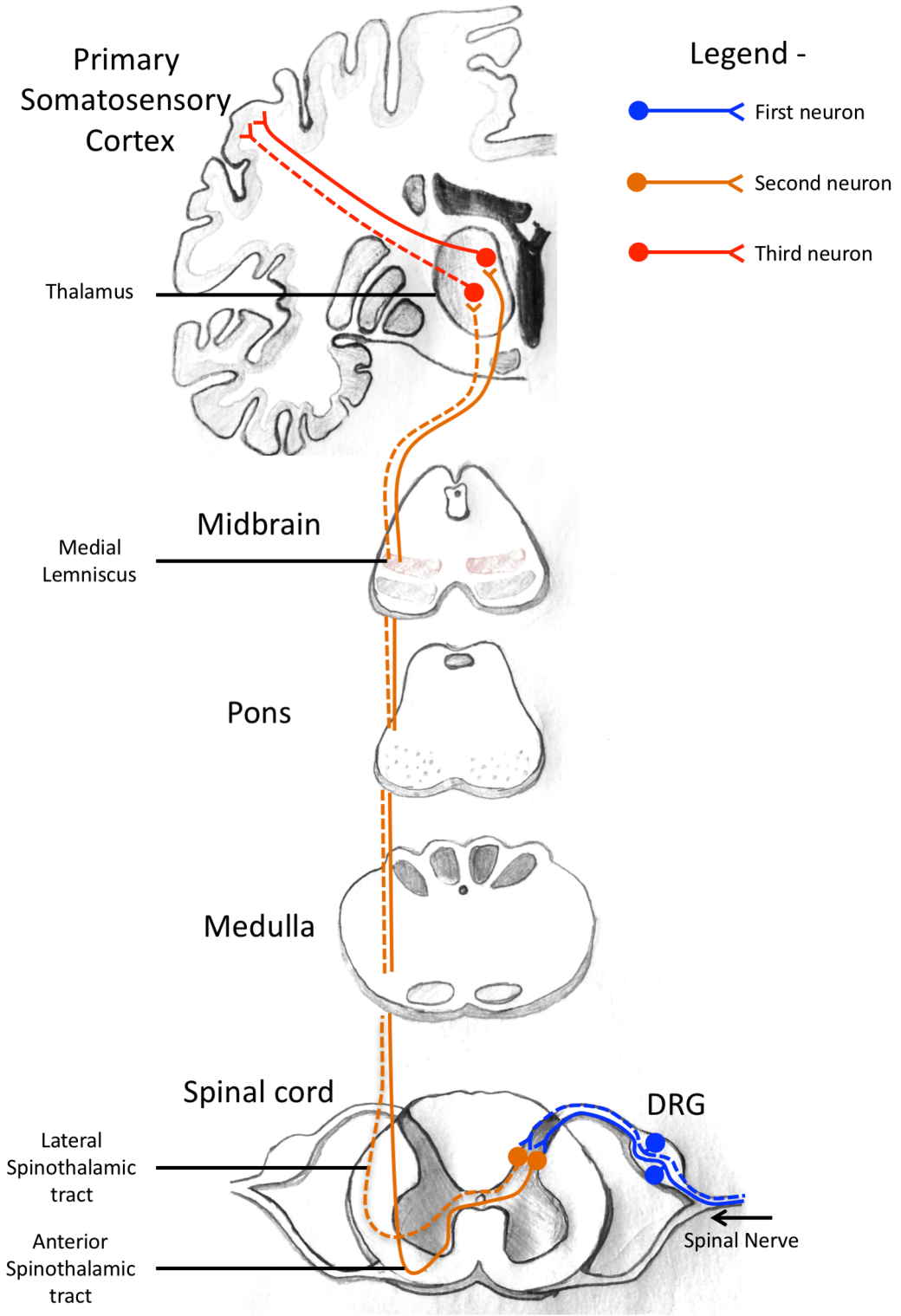

Figure 1.2 – The spinothalamic tract.

Schematic representation of the paths of first, second and third orders of neurons involved in the human spinothalamic tract that helps convey information for localization of thermal and pain stimuli from the periphery. Ascending fibers either form the anterior or lateral spinothalamic tract. Adapted from (Nógrádi & Vrbová, 2006).

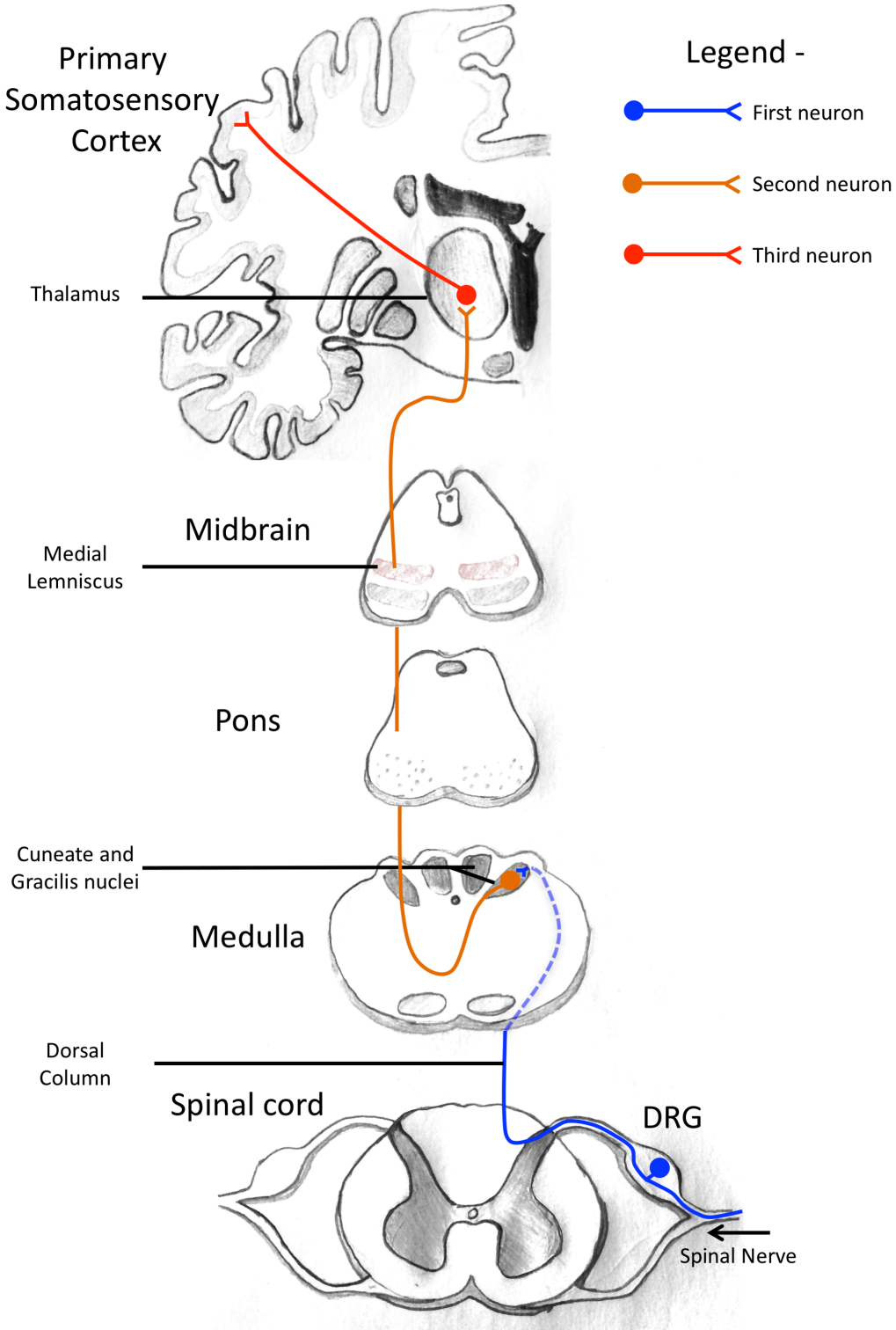

Figure 1.3 – Dorsal column tract.

Schematic representation of the paths of first, second and third orders of neurons involved in the human dorsal tract that helps convey information for discriminatory sensation, proprioception and skin pressure. First order neurons from the lower limbs synapse at the nucleus gracilis (not shown) while those from the upper limbs synapse at the nucleus cuneatus. Adapted from (Nógrádi & Vrbová, 2006).

added to the tract, before synapsing in the nucleus gracilis and nucleus cuneatus in the medulla respectively. The second order neurons from these nuclei then cross the midline before reaching the contralateral medial lemniscus and then to the VPL nucleus of the thalamus. This tract carries information for discriminatory sensation, proprioception and skin pressure. Apart from these major spino-cortical pathways, there are also spino-reticular, spino-hypothalamic tract, spino-mesencephalic tract and spino-cerebellar tracts that control a variety of sensory information (Cho, 2015; Nógrádi & Vrbová, 2006).

In humans, descending tracts carry information from the CNS to the periphery. The cortico-spinal (pyramidal) tract (Figure 1.4) forms the major pathway for motor control and is formed by fibers originating in the precentral gyrus of the motor cortex. These fibers either cross over to the opposite side at the level of the medulla to form the lateral cortico-spinal tract, or some remain on the same side to form the anterior cortico-spinal tract, which crosses at the level of the synapse to the anterior horn cells on the contralateral side. The arrangement of fibers in the lateral cortico-spinal tract is such that the medial fibers synapse more rostrally while the lateral fibers synapse caudally. Apart from the cortico-spinal tract, other descending pathways include the rubro-spinal, reticulo-spinal, vestibule-spinal and tecto-spinal tracts that all help with balance, posture, gait and the co-ordination of movement. Additionally, descending autonomic tracts from the hypothalamus, limbic system and brainstem centers help to exert autonomic control on various organs and tissues in the periphery (Cho, 2015; Nógrádi & Vrbová, 2006).

Apart from the ascending and descending pathways, there exist several intrinsic pathways within the spinal cord that help modulate the impulses of the ascending and descending tracts, as well as to mediate reflexes. These include the Lissauer tract between the dorsal roots and lamina I, the comma tract between fasciculus gracilis and fasciculus cuneatus in the dorsal column, the septomarginal tract in the dorsal white mater, the cornucommissural tract along the dorsal commissure and the lateral and anterior ground bundles (Nógrádi & Vrbová, 2006).

While the anatomy of the human spinal cord described here is largely similar to that seen in the mouse, there are some crucial differences. As a general rule, larger animals have a greater proportion of white matter when viewing the spinal cord in cross section. Accordingly, the human spinal cord has a greater proportion of white matter, relative to gray matter. This is especially the case in the dorsal funiculus which is much larger in human spinal cords than it is in mice. Furthermore, in mice, the corticospinal tract occupies a smaller proportion of the white matter and lies in the dorsal column, while it is larger and lies in the lateral column in humans. The rubrospinal tract, which is involved in locomotion and maintaining posture is larger in mice than it is in humans. Finally, mice are more reliant on the autonomic motor pattern generators for quadrupedal locomotion. These pattern generators can even function in the absence of sensory input. Comparatively, human bipedal locomotion is less reliant on this reflexive automaticity and more on the integration of sensory signals withinwith higher control centers (Sengul, 2013; Treuting et al, 2012).

d) Neurodegeneration of the spinal cord

The spinal cord is affected in various neurodegenerative disorders, the most common of which are the hereditary axonopathies, which include amyotrophic lateral sclerosis (ALS), hereditary motor neuropathy, spinal muscular atrophy, familial spinal paraplegia and Charcot-Marie-Tooth disease. Despite the heterogeneity of genetic causes, these diseases are all characterized by the vulnerability of motor neuron populations leading to spinal neurodegeneration and the presence of neuroinflammation, with common pathogenic mechanisms (Komine & Yamanaka, 2015; Zuchner & Vance, 2005). Another major disease that affects the spinal cord is multiple sclerosis, which is an inherited autoimmune disease with neuroinflammation that affects myelinated neurons and adversely affects spinal cord and CNS function (Mallucci et al, 2015). Furthermore, there is growing evidence for significant spinal cord pathology in neurodegenerative

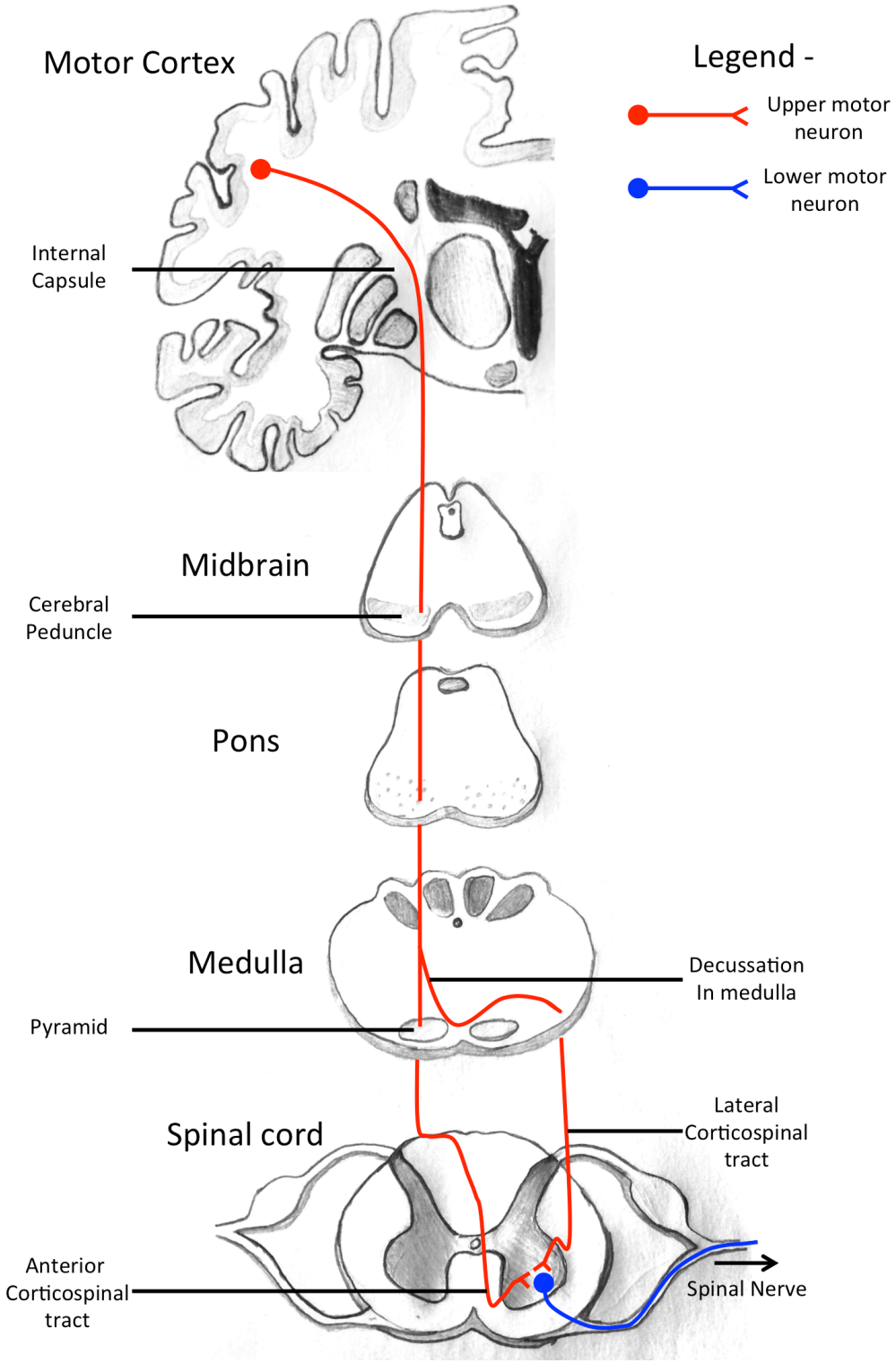

Figure 1.4 – Corticospinal (pyramidal) tract.

Schematic representation of the paths of upper and lower motor neurons in the human corticospinal tract, showing the decussation of fibers at the level of the medulla that divides the fibers into the lateral (crossed over) corticospinal tract or the anterior corticospinal tract, whose fibers cross over at the level of the spinal cord. Adapted from (Nógrádi & Vrbová, 2006).

diseases such as Alzheimer disease (AD) (Wirths et al, 2010), Parkinson disease (PD) (Vivacqua et al, 2011) and Huntington Disease (HD) (Muhlau et al, 2014).

With the extent of neurodegeneration observed in most LSDs, it is easy to conceive that this pathology may extend in to the spinal cord. Indeed, various reports indicate the presence of storage material deposition as well as pathology in the spinal cord in human and experimental models of LSDs especially in GM1 gangliosidosis (Hahn et al, 1997), GM2 gangliosidosis (Tay-Sachs and Sandhoff diseases) (Jellinger et al, 1982; Jeyakumar et al, 2003; Yokoyama et al, 2014), Niemann Pick type A (Marmiroli et al, 2009) and Niemann-Pick type C (Yan et al, 2011). Therefore, there seems to be a potentially considerable overlap of clinical and pathological features between GM2 gangliosidosis, Niemann-Pick type C disease and the motor neuron diseases (Dardis et al, 2016; Shapiro et al, 2008).

In the NCLs, the evidence for spinal cord pathology comes from the study of human post-mortem tissue, where studies of Infantile, Juvenile and Adult NCL *post-mortem* tissue have revealed the deposition of autofluorescent storage material as well as atrophy of the spinal cord in this region (Anderson et al, 2013; Bruun et al, 1991; Santavuori et al, 1974). The *mnd* mouse model that was later shown to be a model of Cln8 (*Cln8*^{mnd}) (Ranta et al, 1999) was shown to have marked neuroinflammation and neuron loss in the spinal cord (Fujita et al, 1998; Plummer et al, 1995), indicating that this may be the case in other forms of NCLs as well.

In CLN1 disease, the presence of profound sensorimotor deficits that are not entirely explained by brain pathology and the limited success of brain-directed therapies, makes the spinal cord a possible site of pathology that may be clinically significant and hence, must be investigated.

1.8 Hypothesis and aims

CLN1 disease is a rapidly progressing and devastating childhood neurodegenerative disease. Despite detailed characterization of the progression of brain and cerebellum pathology in mouse models, the sensorimotor deficits seen in human and murine disease cannot be fully reconciled. Further, there has been very little success with various systemic and brain-directed therapies for CLN1 disease. We therefore hypothesized the presence of pathology in other regions of the CNS that are not affected by these therapeutic approaches, focusing on the spinal cord due to its significant involvement in the sensorimotor pathways.

The aims of this thesis are threefold –

a) To characterize the nature, extent and progression of pathology in the spinal cords of Ppt1 deficient (*Ppt1*$^{-/-}$) mice, studying the known pathological features from the brains of these mice, as well as exploring any novel phenotypes. We then wished to determine if this region of the CNS is affected in the human disease, as well as to analyze the spinal cords of mouse models of CLN2 and CLN3 disease to investigate whether there is any spinal cord pathology in these other major forms of NCL.

b) To detail the occurrence and progression of any gait abnormalities in *Ppt1*$^{-/-}$ mice utilizing the *CatWalk* XT automated gait analysis system (*Noldus Information Technology, Wagenigen, Netherlands*), and how these may relate to the sensorimotor deficits seen in *Ppt1*$^{-/-}$ mice.

c) To test whether therapeutically targeting the spinal cord of *Ppt1*$^{-/-}$ mice with intrathecal (IT) injections of either ERT or AAV-mediated gene therapy will have a beneficial effect on disease pathology and progression in these mice, and to also study the effects of combining intracerebral (IC) and IT gene therapy as an approach for treating CLN1 disease.

Chapter 2. Materials and Methods

2.1 Mice

a) Ppt1$^{-/-}$ mice

A Ppt1 deficient mouse (*Ppt1*$^{-/-}$) model of Cln1 disease was created by gene disruption, whereby a portion of exon 9 of the *Cln1* gene was replaced by a premature stop codon, resulting in a truncated mRNA and a complete loss of Ppt1 enzyme activity (Gupta et al, 2001).

Ppt1$^{-/-}$ mice were backcrossed for at least 10 generations onto a C57BL/6 mouse background (https://www.jax.org/strain/000664) and maintained as homozygous breeding stocks at the Washington University School of Medicine (St. Louis, MO), the University of Texas Southwestern Medical Centre (Dallas, TX) and the Institute of Psychiatry, Psychology and Neuroscience, King's College London (London, UK). All procedures were carried out under NIH guidelines, Institutional Animal Care and Use Committee (IACUC) guidelines at the respective institutions (U.S.A) and the Animals (Scientific) Procedures Act, 1986 (UK).

b) Thy1-YFP/Ppt1$^{-/-}$ mice

The *Thy1-YFP/Ppt1*$^{-/-}$ mouse model was created by crossing *Thy1-YFP* reporter mice (Tg (*Thy1-YFP*) 16Jrs, The Jackson Lab, Bar Harbor, ME, USA) (Feng et al, 2000) with *Ppt1*$^{-/-}$ mice. The reporter mice were maintained as a homozygous breeding stock of *Thy1-YFP*$^{+/-}$*/Ppt1*$^{-/-}$ mice and *Thy1-YFP* reporter mice were used as controls. All procedures were performed in accordance with NIH guidelines, approved by the IACUC at Washington University School of Medicine.

c) C57BL/6 mice

All Wildtype (WT) mice used in this study were C57BL/6 mice (https://www.jax.org/strain/000664). Their average age of survival is 27-28 months (Storer, 1966). These mice were housed and bred as separate stocks in the same facilities as the *Ppt1*$^{-/-}$ mice (above). Appropriately age-matched mice were chosen as controls for the various studies.

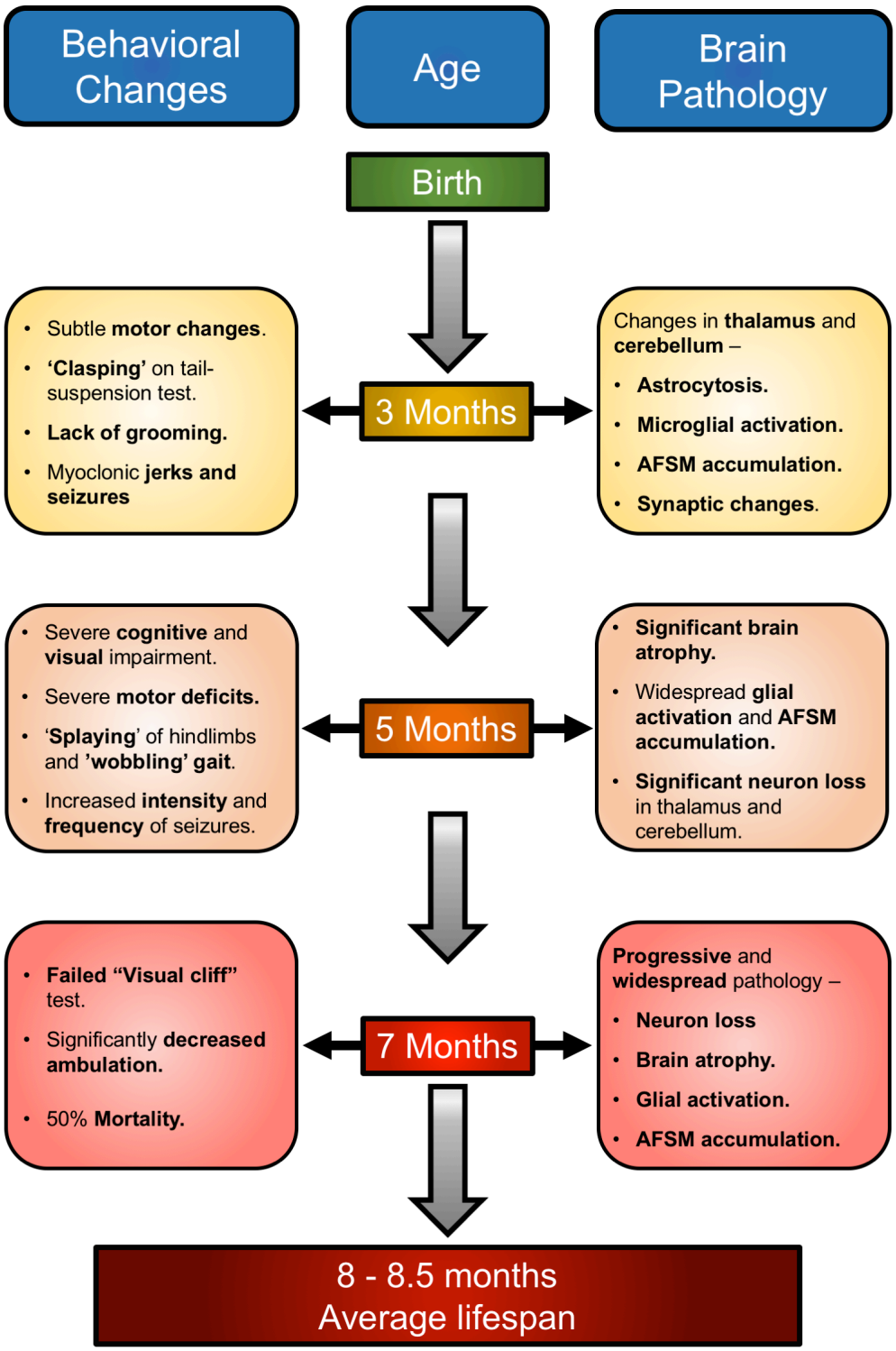

Figure 2.1 – Disease progression in Ppt1$^{-/-}$ mice.

Schematic representation summarizing the progression of major behavioral changes and brain pathology observed in Ppt1$^{-/-}$ mice with increasing age. AFSM denotes Autofluorescent Storage Materia. Incorporates data from (Bible et al, 2004; Dearborn et al, 2015; Gupta et al, 2001; Kielar et al, 2007).

2.2 Human tissue

Paraffin wax-embedded spinal cord tissue of a single INCL patient was obtained from the archives of the Department of Pathology, University of Helsinki. Similarly, a single spinal cord tissue sample from a neurologically normal control was obtained from the Department of Pathology, University of Washington, School of Medicine, St. Louis, MO. These samples were collected at routine autopsies of the individuals with informed, written consent of their families. The work was done under the approval of the Ethical Research Committee at the Institute of Psychiatry, Psychology and Neuroscience, King's College London, UK (Approval numbers: 223/00 and 181/02).

2.3 Quantitative Gait Analysis

Various motor deficits have been described in *Ppt1*$^{-/-}$ mice including an abnormal clasping behavior and a progressive gait abnormality with splaying of hindlimbs and lowering of the pelvis, eventually resulting in hind limb paralysis (Gupta et al, 2001). A more comprehensive study showed that *Ppt1*$^{-/-}$ mice as young as 2-3 months showed subtle deficits on walking initiation tests and a 60° inclined screen test (Dearborn et al, 2015). Collectively these data imply that some of the earliest functional deficits in this mouse model affect the sensorimotor system.

To further detail these gait abnormalities, we used the *CatWalk XT* gait analysis system (Noldus Information Technology bv, Wagenigen, Netherlands.). The *CatWalk XT* system consists of a narrow walkway, a roof with a red backlight, a glass floor which has a green fluorescent light passing through it (using the principle of total internal reflection, TIR) and a digital video camera placed under the walkway (**Figure 2.1**). Therefore, when a mouse's paw comes into contact with the walkway floor, the light is reflected due to the change in the refractive index of the medium and the paw is visualized as a green fluorescent mark. This principle can be further used to measure the intensity of the paw print (Hamers et al, 2006; Hamers et al, 2001; Vrinten & Hamers, 2003). The captured video was then analyzed using *CatWalk XT* 10.5 software (Noldus, Netherlands) to label each paw print as Right Front (RF), Left Front (LF), Right Hind (RH) or Left Hind

(LH) as well as remove any unwanted traces due to other parts of the body (e.g. mouse's belly, scrotum or tail) (**Figure 2.1**).

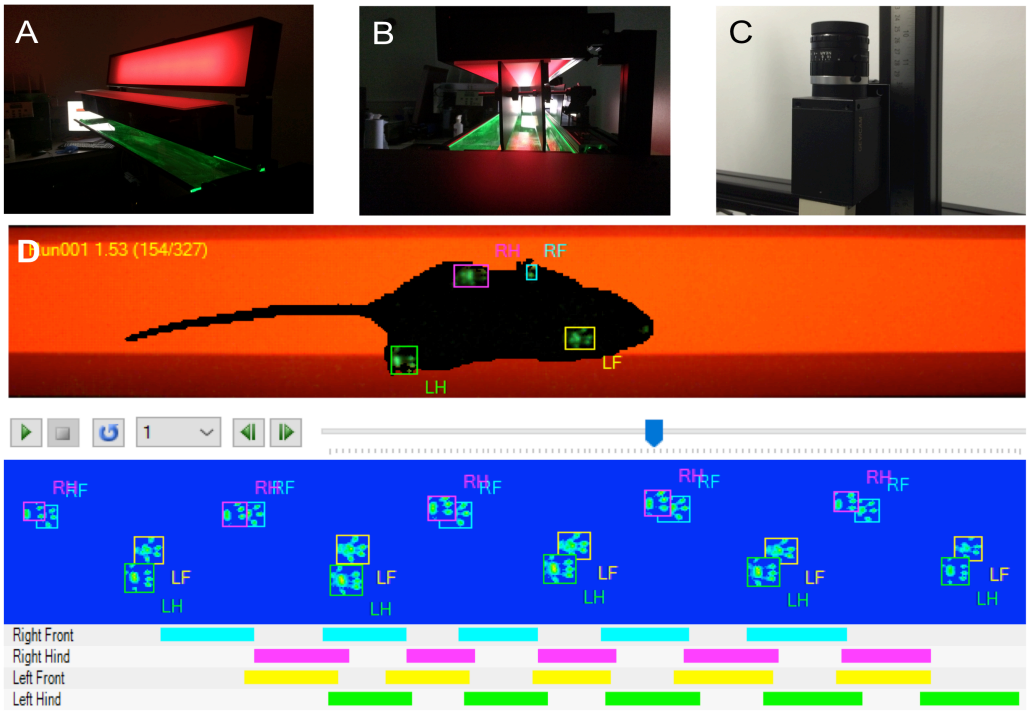

Figure 2.2 – CatWalk XT data acquisition.

*(**A to C**) Images of the CatWalk XT system showing the components of the walkway including the roof (Red), walkway floor (green) and bounding walls (**A, B**) as well as the digital camera used to capture videos (**C**). (**D**) Images showing a frame of the captured video from a single run. Each paw print appears as a fluorescent green mark. These are then classified as Right Front (RF), Left Front (LF), Right Hind (RH) or Left Hind (LH). The Schematics below show placement of these classified paw prints over the duration of the run, with coloured bars indicating the periods when each foot was in contact with the glass floor of the apparatus.*

For this gait analysis study we used 12 age-matched mice per group (n=12) for *Ppt1*$^{-/-}$ mice and WT mice. Mice were initially trained starting at 3 wks of age to walk the Catwalk XT system. Monthly recordings were collected between 1-7 months of age. Each recording day was preceded by a training session to condition the mice. Experimental settings were chosen to allow for accurate detection of walks - Camera gain 20 dB, green intensity threshold 0.10, red

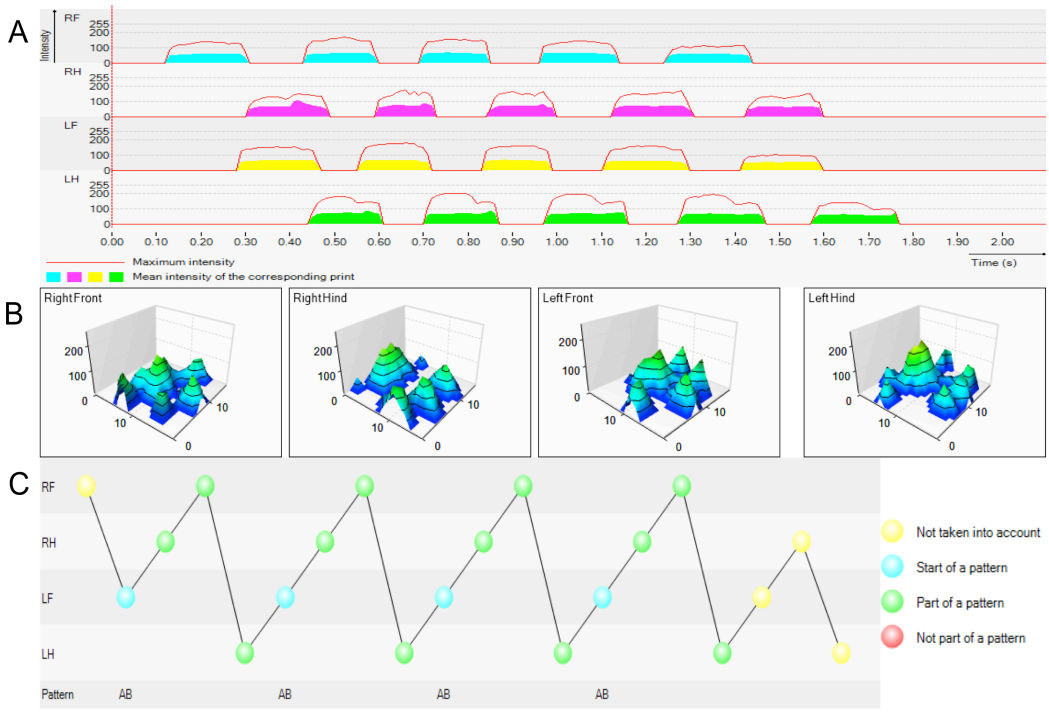

Figure 2.3 – CatWalk XT run visualizations.

*(**A, B**) Representative images showing 2D (**A**) and 3D (**B**) visualizations of paw contact intensities. Maximum intensities (**A**) are represented by the red line, while the coloured blocks represent mean intensities. (**C**) Representative image sowing the footfall patterns for a single run.*

ceiling light 17.7 volts and green walkway light 16.5 volts. Each mouse had a minimum of 3 'compliant' runs measured with the run duration ranging from a minimum of 1 second to a maximum of 5 seconds to be considered compliant.

The *Catwalk XT* software was then used to analyze over 28 different parameters associated with gait including paw print areas, print intensities, stride length, base of support, swing duration and measures of interlimb co-ordination (Summarized in Table 1) (**Figure 2.2, 2.3**). These data were then exported into an *MS Excel* spreadsheet (Microsoft, Seattle) for further statistical analysis as detailed in section 10.

From an initial study of 7-month-old *Ppt1*$^{-/-}$ and wildtype mice (n=5), a maximum speed variation of 80% was selected to allow for compliance of runs at the end-stage of disease.

2.4 Tissue processing

Mice were anesthetized with Euthatal (200mg sodium pentobarbital/ml, Merial Animal Health Ltd., UK), and injected intra-ventricularly with 0.1ml of anti-coagulant heparin sodium (1000 IU/ml) (Wockhardt, Wrexham, UK) and transcardially perfused with Phosphate Buffered Saline (PBS: 50mM Phosphate Buffered Saline with $MgCl_2$ and $CaCl_2$, pH 7.4, Sigma, Gillingham, Dorset, UK.) and 4% paraformaldehyde in 0.1 M Sodium Phosphate buffer, pH 7.4 (PFA).

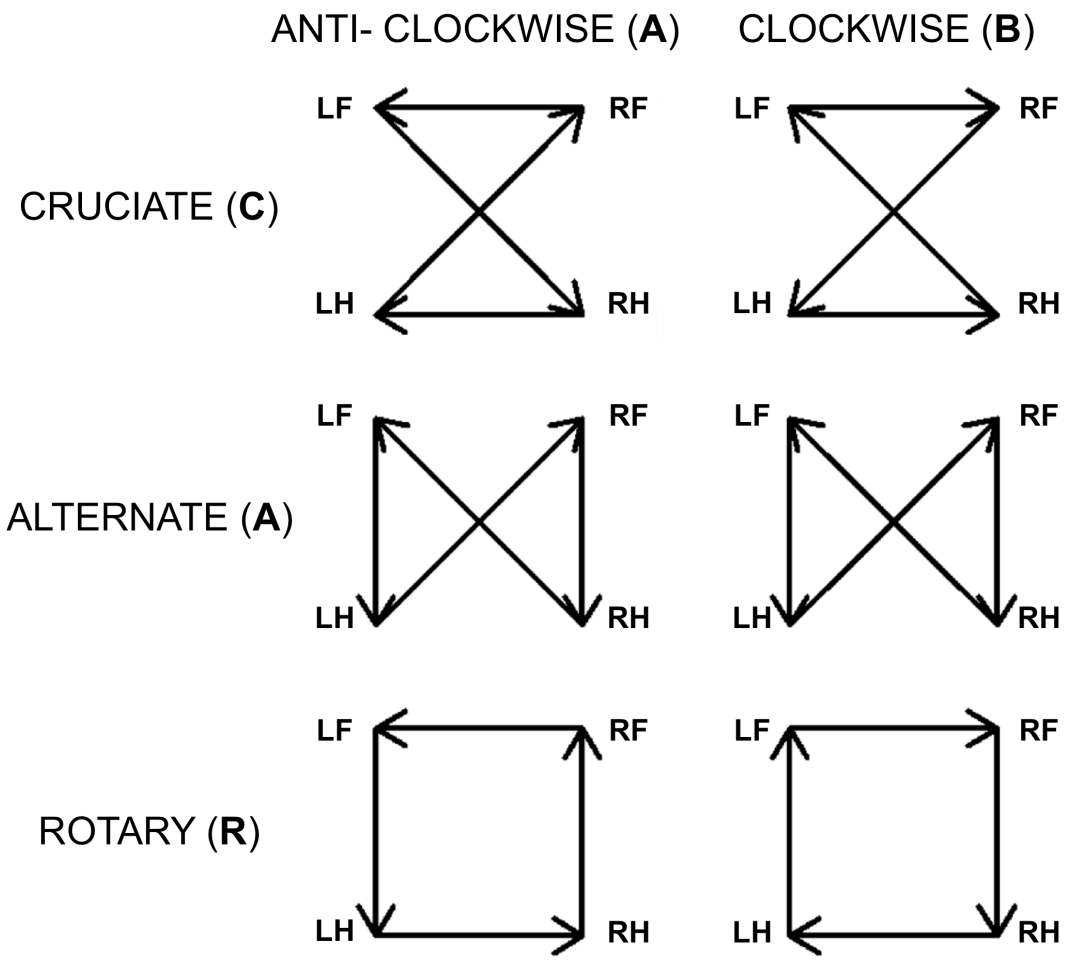

Figure 2.4 – CatWalk XT step-fall patterns.

*Schematic representations of the different types of step fall patterns classified by the CatWalk XT system – which can be cruciate anti-clockwise (**CA**), cruciate clockwise (**CB**), alternate anti-clockwise (**AA**), alternate clockwise (**AB**), rotary anti-clockwise (RA) or rotary clockwise (**RB**). Adapted from (Hamers et al, 2006).*

I. Measures of run speed	
a. Body speed	Average speed (cm/s) of the distance covered to time in a step cycle.
b. Cadence	The number of steps per second (frequency of steps).
c. Run speed variation	Average and maximum variation (%) of speed during a given run.
II. Step cycle measures	
a. Step cycle	Duration (s) between two consecutive initial contacts of the same paw.
b. Stand	Duration in seconds (s) of contact of paw with glass plate.
c. Swing	Duration (s) of no contact of a given paw with glass plate.
d. Duty cycle	Stand expressed as a percentage (%) of step cycle
e. Swing speed	Ratio of stride length/swing (cm/s).
f. Stand Index	Measure of the speed at which the paw loses contact with the glass plate.
III. Paw Measures	Duration (s) between two consecutive initial contacts of the same paw.
a. Print Width Length and area	Sum of all contact lengths (cm), widths (cm) and areas (cm^2) of a given paw in a run (in the direction of walking).
b. Max Contact Area	Maximum area of the paw that comes in contact with glass plate (cm^2).
c. Stride length	Length (cm) between successive placements of each paw.
d. Min., Max. and mean intensities	The minimum, maximum and mean intensities of a paw coming into contact with the glass plate (Ranges from 0-255).
e. Max intensity to stand	Maximum intensity relative to stand duration (%)
IV. Stance and Support	
a. Stance	Duration (s) of contact of single, dual paws.
b. Base of Support (BOS)	Average width between the front paws or hind paws.
c. Support	The fraction of the run (%) spent on one, two, three or four limbs
V. Measures of coordination	
a. Print positions	Relative placement of hind paws to the ipsilateral forepaws (-2 to +2)
b. Normal step sequences	Step sequences that fall within normal footfall patterns **(Figure 2.3**).
c. Regularity Index	Ratio of the number of normal step sequences to the total number of paw placements (%).
d. Phase dispersions	Describes the temporal relationship between the placements of any two paws within a step cycle.

Table 2.1 – CatWalk Parameters.

Table detailing the various parameters measured on CatWalk XT system in the current study. Adapted from (Coulthard et al, 2002; Coulthard et al, 2003; Kloos et al, 2005).

Whole intact mice were then immersion fixed in 4% PFA for at least 48 hours before being transferred to a 50mM Tris Buffered Saline (TBS: 50 mM Tris (VWR, Leicestershire, UK), pH 7.6, 150mM NaCl (VWR)).

To harvest the brain and spinal cord, an initial incision was made from the snout to tail on the dorsal aspect of the mouse and skin was opened. The muscle and fatty tissue in the cervical region of the spinal cord were cleared with Rongeur forceps (Fine Science Tools, Heidelberg, Germany). The head of the mouse was then flexed with one hand to expose the C1 segment of the spinal cord between the foramen magnum at the base of the skull and the C1 vertebra (atlas). From the dorsal aspect, a clean incision was made to the spinal cord, using a size-11 scalpel (Swann-Morton, Sheffield, UK) to separate it from the brainstem. The head was then separated from the body with scissors and the brain carefully dissected out of the skull. The spinal column was dissected out intact by from the rest of the body and all extraneous muscle and connective tissue was removed using a Rongeur forceps to expose the vertebrae. The spinal cord was then dissected out from the column by initial dorsal laminectomies, followed by separation and removal of individual vertebrae (**Figure 2.4**). The brain and spinal cords were then placed in a cryoprotectant solution for 24 hours (30% sucrose solution in TBS with 0.05% Sodium Azide (VWR, UK)). Dorsal Root Ganglia (DRGs) were dissected out from the spinal nerve roots at the lumbar level for separate analysis (see below). Brain hemispheres for sectioning were obtained by separating the cerebellum and brainstem from the forebrain using a single edged razorblade (VWR) to make a coronal cut. An additional sagittal cut was made along the midline to separate the two hemispheres of the brain. Spinal cords were separated into cervical, thoracic and lumbo-sacral regions via coronal cuts with a razorblade (**Figure 2.4**).

Each hemisphere of the brain, and each spinal cord region were mounted on their long axis to the stage of a freezing microtome (Microm HM 430, Wallendorf, Germany), coated with Shandon M-1 embedding matrix (ThermoFisher Scientific, Waltham, MA, USA) and 40µm coronal sections were cut and stored sequentially in 96 well plates containing an anti-freeze cryoprotectant solution

(TBSAF: TBS, 30% Ethylene Glycol (VWR), 15% Sucrose and 0.05% Sodium azide (VWR)).

The DRGs of 7-month-old mice, and spinal cords from *Thy1-YFP and Thy1-YFP/Ppt1*$^{-/-}$ mice (n=3) were embedded in OCT (VWR), frozen on dry ice and sectioned using a Leica CM1850 cryostat (Leica microsystems, Wetzlar, Germany) to obtain 8µm and 32µm sections, respectively, that were collected directly onto Superfrost Plus slides (ThermoFisher Scientific). Paraffin wax-embedded tissue was sectioned into 5µm coronal sections by initially trimming the paraffin blocks with a single edged razor blade and sectioned using a Leica SM2400 base sledge microtome (Leica microsystems, Wetzlar, Germany). The sections were then floated out in a warm water bath and mounted on to Superfrost Plus slides (ThermoFisher Scientific) and dried on a warming plate.

For toluidine blue staining, cervical and lumbo-sacral regions of 7-month-old spinal cords were embedded in epoxy resin and 1 µm semi-thin sections were cut using an ultramicrotome at the laboratory of Dr. Peter Gann, University of Illinois, College of Medicine, IL.

2.5 Tinctorial staining

a) Cresyl Fast Violet (Nissl) staining

To visualize neuronal cytoarchitecture, and to facilitate stereological analyses, 40µm brain and spinal cord sections were mounted as a 1 in 6 series (brains) and 1 in 48 series (spinal cords) on to chrome-gelatin coated slides and left to air-dry overnight at room temperature. The slides were then incubated for 40 minutes in 0.05% cresyl fast violet solution (VWR) (brain sections), or overnight in 0.1% cresyl fast violet solution (VWR) (spinal cord sections), with 0.05% acetic acid (VWR) at 56°C. Similarly, 5µm human spinal cord sections and 8µm DRG sections on Superfrost Plus (ThermoFisher Scientific) slides were incubated for 30 minutes in a 0.05% cresyl fast violet solution (VWR) with 0.05% acetic acid (VWR) at 56°C.

Stained sections were then differentiated through a series of graded Industrial Methylated Spirit (IMS) solutions (70%, 80%, 90%, 95% and 2x100%) before

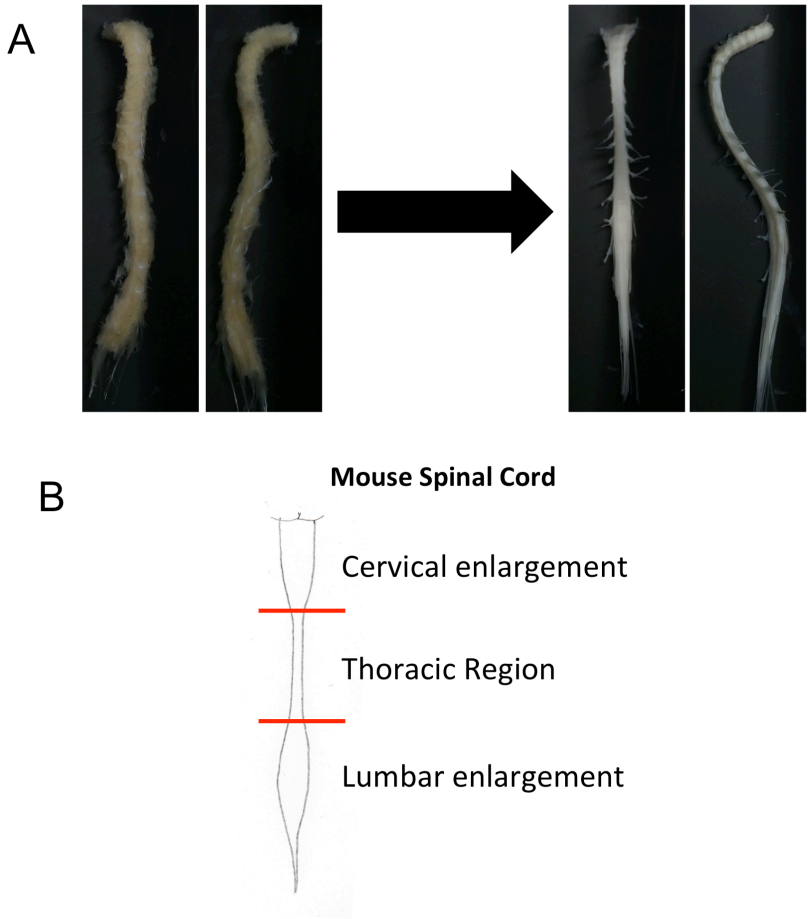

Figure 2.5 – Dissection of the spinal cord.

*(**A**) Representative dorsal and lateral views of spinal columns dissected out of perfused mice (left) and spinal cords after dorsal laminectomies followed by removal of vertebrae. (**B**) Schematic representation of the levels at which the spinal cords were separated into the cervical, thoracic and lumbosacral segments.*

being cleared in Xylene (VWR) and coverslipped with DPX (VWR), a xylene-based mountant (**Figure 2.5**).

b) Luxol Fast Blue

Luxol fast blue was used to visualize the myelin in the white matter of spinal cord sections (Kluver & Barrera, 1953). Selected 40µm sections from the cervical, thoracic and lumbo-sacral spinal cord were mounted on to chrome-

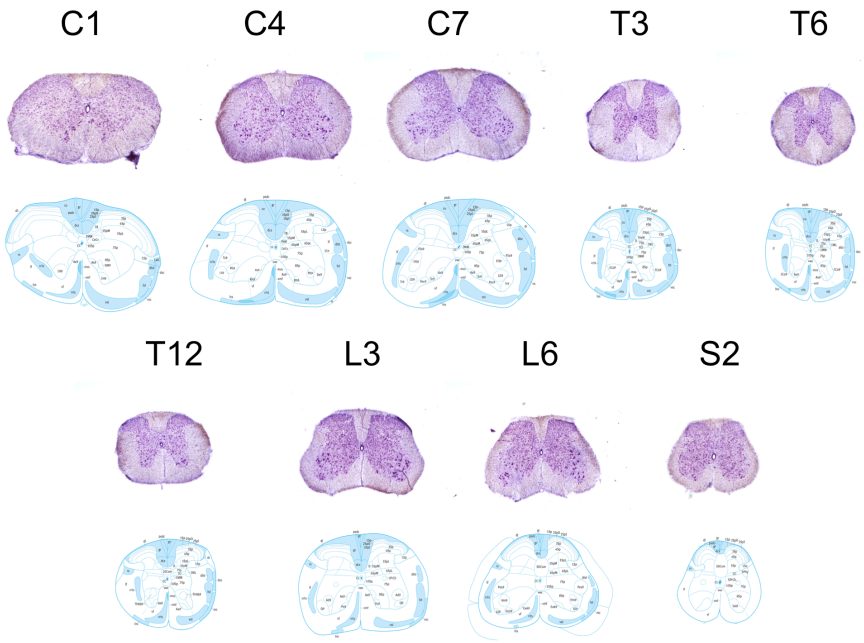

Figure 2.6 – Cresyl fast violet staining.

Representative images of Nissl stained sections of spinal cord aligned with level matched schematic images to allow for visualization of neuronal architecture. Schematic images adapted from (Sengul, 2013).

gelatin coated glass slides and left to air-dry overnight. The slides were then incubated in a 0.1% luxol fast blue solution (VWR) with 0.05% acetic acid (VWR) at 56°C overnight before being differentiated by passing the slides through a 0.05% aqueous solution lithium carbonate and a 70% IMS solution before clearing the sections in xylene (VWR) and coverslipping with DPX (VWR).

c) Toluidine Blue.

1µm thick, semi-thin sections were mounted on to Superfrost Plus (ThermoFisher Scientific) and air-dried. These slides were then shipped to the Pediatric Storage Disorders Laboratory (PSDL) at the Institute of Psychiatry, Psychology and Neuroscience, King's College London, UK for analysis. Toluidine blue staining has previously been shown to allow for the visualization of axon bundles in the white matter of the spinal cord (Jeong et al, 2011). The slides were stained with a 1% solution of toluidine blue-O (Sigma, Poole, UK) and sodium borate (Sigma) for 2 hours on a slide-warming rack. Slides were briefly rinsed under running tap water and again dried on the slide-warming rack for 5

minutes. The slides were then transferred to xylene (VWR) for 30 minutes before being coverslipped with DPX (VWR).

2.6 Immunostaining

a) Immunohistochemistry

Each immunohistochemical staining experiment was performed with an appropriate secondary-only control, keeping all other parameters the same in order to check the specificity of staining.

Free-floating sections were stained as previously described (Bible et al, 2004). Either a 1 in 48 series, or selected 40µm mouse spinal cord sections and a 1 in 6 series of brain sections were immunostained free-floating for markers of interneurons, microglia, astrocytes, peripheral lymphocytes, white matter proteins and pre- or post-synaptic proteins (**Table 2.2**). Endogenous peroxidase activity was quenched with 1% H_2O_2 in TBS with 0.3% Triton-X100 (TBS-T) for spinal cord sections, and with 1% H_2O_2 in TBS for brain tissue, washed and then blocked in 15% normal serum (Vector Laboratories, Peterborough, UK) diluted in TBS-T. The species of normal serum was directed against the host species of the secondary antibody. After blocking, sections were incubated overnight at 4°C in primary antibody in 10% normal serum in TBS-T. Sections were then washed and incubated at room temperature in biotinylated secondary antibody at 1:1000 dilution for 2 hours (**Table 2.2**) followed by washing and incubation in Vectastain Elite ABC kit (1+1:1000, Vector Laboratories) for 2 hours before visualization by incubation with 0.05% 3,3'-diaminobenzidine tetrahydrochloride (DAB) (Sigma) containing 0.001% H_2O_2. Sections were then mounted on to chrome-gelatin coated slides, air-dried overnight, cleared in xylene (VWR) and coverslipped in DPX (VWR).

Paraffin wax-embedded human spinal cord tissue sections were also stained as previously described (Tyynelä et al, 2004). Sections that were collected on Superfrost Plus (ThermoFisher Scientific) slides were de-waxed in xylene, and endogenous peroxidase activity quenched by incubating the sections in methanol containing 1% H_2O_2 for 30 minutes. Sections were rinsed in de-ionized water and antigen retrieval performed by boiling for 20 minutes in 0.01M sodium citrate buffer, pH=6.00. All sections were subsequently rinsed in TBS and blocked in

Primary Antibody	Dilution	Secondary Antibody
I. Interneuron Markers		
a. Rabbit anti-Calbindin (Swant, CB38a)	1:10,000 (SC)	Swine anti- Rabbit 1:1000, Dako
b. Rabbit anti-Calretinin (Swant, 769914)	1:5000 (SC)	Swine anti- Rabbit 1:1000, Dako
II. Motor neurons		
a. Rat anti- CD71 (AbD Serotec, MCA2474EL)	1:200 (SC)	Rabbit anti-Rat 1:1000, Vector
b. Goat anti-ChAT (Chemicon, AB144P)	1:100 (SC)	Rabbit anti-goat 1:1000, Vector
III. Astrocytes		
a. Rabbit anti- GFAP (Dako, Z0334)	1:8000 (SC, Br) 1: 3000 (Hu, DRG)	Swine anti- Rabbit 1:1000 (SC, Br), 1:200 (Hu, DRG) Dako
IV. Microglia		
a. Rat anti- mouse CD68 (AbD Serotec, MCA1957)		
- Immunoperoxidase	1:2000 (SC, Br)	Rabbit anti-Rat 1:1000, Vector
- Immunofluorescence	1:200 (SC)	Goat anti-Rat 1:1000, AlexaFluor 633 ThermoFisher Scientific
b. Mouse anti-CD68 (Dako, clone PG-M1)	1:800 (Hu, DRG)	Goat anti- mouse, 1:200, Vector
V. Peripheral Lymphocytes		
a. Rat anti-CD4 (AbD Serotec, MCA1767)	1:50 (SC, DRG)	Rabbit anti-Rat 1:1000, Vector
b. Rat anti-CD8 (AbD Serotec, MCA609G)	1:100 (SC, DRG)	Rabbit anti-Rat 1:1000, Vector
VI. Synaptic Markers		
a. Mouse anti- Synaptophysin (Upstate, ADI-VAM-SV011)	1:100 (SC)	Goat anti- mouse, 1:1000, Vector
b. Rabbit anti-SNAP25 (Abcam AB5666)	1: 1000 (SC)	Goat anti-Rabbit, 1:1000, Vector
c. Chicken anti-mouse VAMP2 (Chemicon, AB5625)	1:400 (SC)	Goat anti- chicken, 1:1000, vector
d. Mouse anti-PSD95 (Neuromab)	1:1000 (SC)	Goat anti- mouse, 1:1000, Vector
VII. White matter		
a. Chicken anti-Neurofilament H (Acris, AP31813PU-N)	1:16,000 (SC)	Goat anti- chicken, 1:1000, vector
b. Rat anti-Myelin Basic Protein (MBP) (Merck Millipore, MAB386)	1:16,000 (SC)	Rabbit anti-Rat 1:1000, Vector

Table 2.2 – Primary and secondary antibodies used for immunohistochemistry (IHC) and immunofluorescence (IF).

SC= Spinal cord sections, Br= Brain sections, Hu= Human sections and DRG= Dorsal root ganglia sections.

15% normal serum, as before, in TBS-T for 30 minutes, before overnight incubation at 4°C with primary antiserum diluted in TBS-T containing 10% normal serum (**Table 2.2**). Sections were rinsed and incubated in secondary antibody (**Table 2.2**), and followed as above by treatment with *Vectastain Elite ABC* kit (1:200; Vector Laboratories), and visualization with DAB (Sigma).

b) Immunofluorescence

40µm mouse spinal cord sections from the cervical, thoracic and lumbosacral cord were stained to visualize staining of CD68-positive microglia in relation to the accumulation of autofluorescent storage material. Sections from the cervical, thoracic and lumbo-sacral spinal cord were blocked in a 15% normal goat serum (Vector) solution in TBS-T for 2 hours and incubated overnight at 4°C in primary antibody (**Table 2.2**) diluted in 10% normal serum in TBS-T. Sections were then washed and incubated at room temperature in biotinylated secondary antibody at a 1:1000 dilution for 2 hours (**Table 2.2**). Sections were washed with TBS and mounted on to slides and coverslipped with Fluoromount-G mounting medium (Southern Biotech, Birmingham, AL).

2.7 Stereology

Stereology allows for the rapid, efficient and unbiased quantitative measurement of 3D parameters of an object using 2D sections. Design-based stereology enables the accurate measurement of regional volumes and cell counts, as well as measurements of thickness, area and density (reviewed in (Schmitz & Hof, 2005). Design-based stereology is done by first designing a random and systematic sampling scheme such that the objects measured are sampled independent of size, shape, spatial orientation and distribution (West, 2002). This is important, as the measurements of objects will therefore be unbiased to any differences in the morphology and size of any brain or spinal cord regions being compared. Furthermore, this assumption of three-dimensional spatial independence allows for the reduction of systemic errors in counting, as compared to other counting methods (Gundersen & Jensen, 1987; West, 1993).

To perform design-based stereological measurements for brains and spinal cords, sections of known thickness are collected at a consistent periodicity. In

this study, we have used 40µm brain sections at a 1 in 6 interval and 40µm spinal cord sections at a 1 in 48 interval. These sections were stained for specific markers of interest, such as cresyl fast violet to view neuronal cytoarchitechture or for markers for interneurons. These sections are then compared to a reference atlas (Paxinos, 2001; Sengul, 2013), so as to accurately draw anatomical boundaries of the regions of interest in which parameters will be assessed. Such repeated comparisons of anatomical boundaries allows for an accurate representation of the region. All stereological measures in this study were carried out using *Stereoinvestigator* software (MBF Bioscience) connected to a Zeiss Axioskop 2 MOT (Zeiss) with a DAGE-MTI CCD-100 camera (DAGE-MTI).

a) Measurements of cell area

An increase in cell size of both Nissl-stained neurons and interneurons has previously been documented in the brains of *Ppt1*$^{-/-}$ mice, presumably as a result of storage material accumulation (Bible et al, 2004; Haltia et al, 1973a). Cell areas in µm^2 were measured for Nissl-stained motor neurons based on their location and morphology (Rexed, 1954; Sengul, 2013), as well as of calbindin and calretinin positive interneurons by drawing contours around their cell bodies for a 100 cells per region of spinal cord, per mouse.

b) Regional volume Measurements

Regional volumes were measured using a Cavalieri estimator, whereby the volume of a region is calculated by multiplying the area of the region of interest measured on each section by the distance or interval between each section (Lucocq, 2007). Further, as two-dimensional areas measured for each section do not take into account the areas at the top and bottom of a given section, these measures are prone to over-estimation and final measures are therefore corrected, and the accuracy of the measures assessed by means of Gundersen Co-efficient of Error (COE) (Gundersen et al, 1999).

In this study we measured total spinal cord volumes and gray matter volumes by drawing the appropriate contours on each section (**Figure 2.6A**). White matter volumes were then calculated as a subtractive value of the total regional volume and regional gray matter volume. A 125x125µm grid with a suitable density of

points is placed over a marked contour of the region of interest (**Figure 2.6B**) and all grid points within the contour are marked (**Figure 2.6C**). This process is then repeated for every section in the region and a final volume is obtained in μm^3.

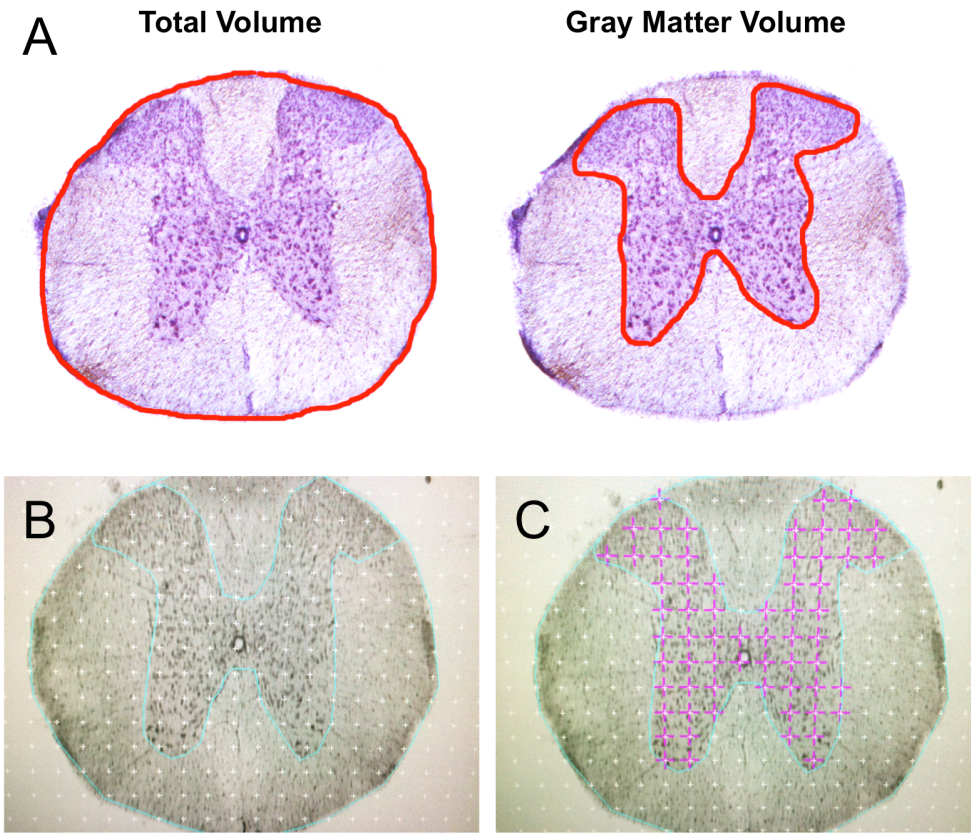

Figure 2.7 – Measuring regional spinal cord volumes.

(A) *Representative images of a thoracic spinal cord sections stained for Nissl with contours (red) showing the contours drawn to measure total and gray matter volumes respectively.* ***(B-C)*** *Representative images of thoracic spinal cord with contours for total volume and gray matter superimposed with a 125x125µm grid (**B**) and the gray matter contour filled with markers for the Cavalieri estimator (**C**).*

c) Neuron counts of Nissl sections.

Cell counts were performed using an optical fractionator technique (West, 2002). This combines an optical dissector, which is a method used to count nuclei in a three dimensional context with a fractionator, which is a method for systematic and uniform sampling of a two-dimensional area (West, 2002). The optical

dissector includes the optical section planes by moving the focal plane along the z-axis, and estimates cell numbers without any bias towards their size or shape. The fractionator (Gundersen & Jensen, 1987), applies systematic sampling sites, thus reducing the total number of cells counted, as well as removing any sampling bias.

To count cells using the optical fractionator, first, data regarding the thickness of the sections and periodicity is recorded. The region of interest is identified in each section, as with regional volume measurements (see above), and a contour is drawn around it at a low magnification. An appropriately sized grid is then superimposed onto the drawn contour to provide a succession of systematic sampling sites.

The grid sizes used for different brain regions are given in **table 2.3**. A counting frame is then defined at a high magnification such that there is a uniform distribution of counting frames for every sampling site defined by the grid. We used 70x40μm for the frame size. Cells are then counted at each sampling site, to include those within the defined counting frame and those that lie in contact with the upper and right borders of the frame (coloured green), while excluding those outside the counting frame or in contact with the left and upper borders of the counting frame (coloured red) (**Figure 2.7**).
Counts obtained by the optical fractionator were within the limits of the Gundersen mean co-efficient of error (COE) of 0.05-0.1.

d) Interneuron and motor Neuron counts

Because of the relatively low numbers of interneurons, stereological methods prove inefficient for counting them (Cooper et al, 1999). Therefore, counts of interneurons in Laminae IV-IX, stained for calbindin and calretinin were carried out manually in hemi-cords within a 1 in 48 series of sections at a 10x magnification for each section. Total estimates were obtained as the product of the counted cells, periodicity and the number of intervals.

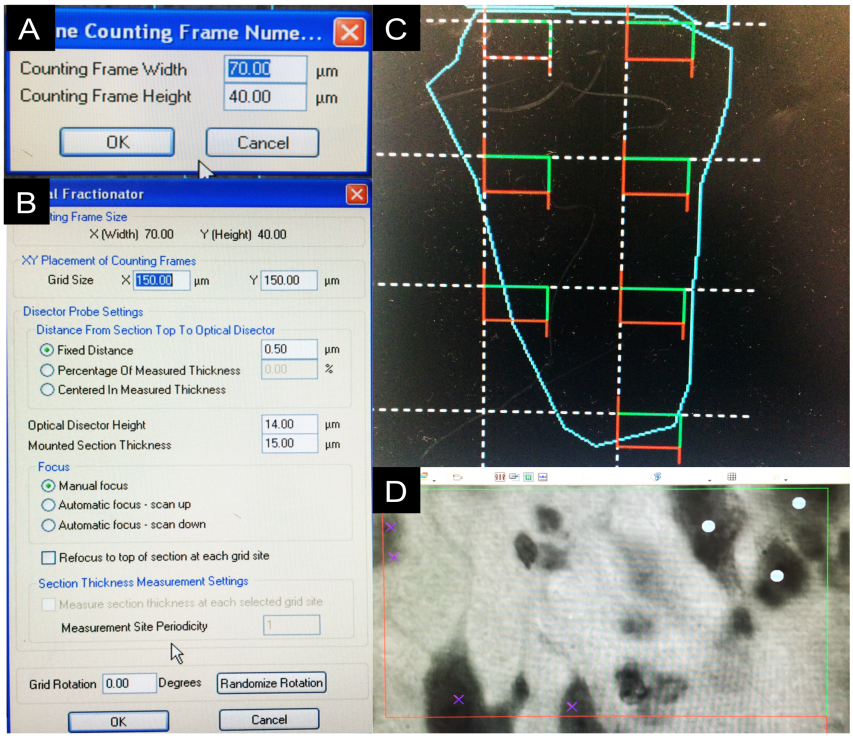

Figure 2.8 – Optical fractionator cell counts.

(A-C) *Example of defining the counting frame (**A**) and grid size (**B**) for the optical fractionator probes, showing the distribution of sampling sites over a given contour (**C**). (**D**) Sample image demonstrating the counting of cells within the borders. Cells within the frame and in contact with the green borders (upper, right) are counted (represented by blue dots) while cells either outside the frame or in contact with red borders (lower, left) are not counted (pink cross)*

e) Measurement of axon density

For semi-thin sections stained for toluidine blue, axon density measures were obtained in the dorsal and ventral funiculi by means of line sampling using *Stereoinvestigator* software (MBF Bioscience) connected to a Zeiss Axioskop 2 MOT (Zeiss) with a DAGE-MTI CCD-100 camera (DAGE-MTI), whereby a vector is drawn across a region to be measured and regularly distributed sampling sites are obtained. The counting frame was 25x25 µm in size. The numbers of axons were then counted in each sampling site, using the same counting rules for counting frames when making the optical fractionator estimates. Measures were obtained for a minimum of 4 sections per region of each spinal cord, and expressed as the number of axons per 100 µm sampled.

Region	Grid Size (*μm* x *μm*)
I. Brain	
a. Primary motor (M1) Cortex	225x225
b. Primary somatosensory Barrel-field (S1BF) Cortex	225x225
c. Medial and Lateral Ventral Posterior Thalamic Nuclei (VPM/VPL)	175x175
d. Dorsal Lateral Geniculate Body of Thalamus (LGnD)	125x125
II. Spinal Cord (Dorsal and Ventral Horns)	150x150

Table 2.3 – Grid sizes for optical fractionator counts in different regions.

2.8 Thresholding Image Analysis.

If a protein or marker is densely distributed in a region, the intensity of immunostaining can make it difficult to accurately discriminate individual cells. For example, GFAP staining for fibrous astrocytes within any given region. Therefore, attempts to quantify such staining by the use of counting methods proved difficult. In such cases, semi-automated thresholding image analysis was employed to obtain a measure of the amount of staining per microscope field, which can be compared across samples (Bible et al, 2004; Kielar et al, 2007; Pontikis et al, 2004).

This technique was employed in the current study to analyze the levels of glial activation for astrocytes (GFAP) and microglia (CD68), lamiae I-III of sections stained for interneuron markers (calbindin and calretinin) and for the accumulation of autofluorescent storage material (AFSM). To visualize the AFSM, unstained sections were de-waxed in xylene (VWR) where required, and mounted on slides. These were then coverslipped with Fluoromount-G (Southern Biotech) mounting medium.

Whether for quantifying AFSM or an immunoperoxidase stained marker a similar sampling method was used. In this a set number of images were obtained for each region measured – 30 non-overlapping images over 3 sections per region using

a 40x objective (for GFAP, CD68 and AFSM), or 50 non-overlapping images from 5 sections per region using a 63x objective.

Images for the CD68, GFAP, calbindin and calretinin stained sections were obtained using a Leica DRMB microscope (Leica Microscopy & GmBH, Wetzlar, Germany) with a Zeiss AxioCam HRc Rev 2 digital camera (Zeiss). Images of autofluorescent storage material were obtained using a Leica SP5 confocal microscope (Leica Microsystems, Welwyn Garden City, UK). Images were sampled in a chosen uniform pattern, so as to sample the entire region of interest, while not sampling adjacent areas. All images were obtained while maintaining consistent parameters of light intensity, camera setup and calibrations. In the case of confocal microscopy, a consistent relative relationship between amplitude offset and detector gain was maintained between animals.

The obtained images were analyzed using *Image Pro Plus* software (Media Cybernetics, Chicago, IL), to select appropriate thresholds for every region (**Figure2.8**). Thresholds were chosen to best distinguish between specific immunoreactivity for each antigen and the background. Results obtained for each region and each antigen was expressed as % immunoreactivity per image. The mean percentage immunoreactivity per region per animal was then obtained for further analysis.

For the analysis of *Thy1-YFP* and *Thy1-YFP/Ppt1*$^{-/-}$ mouse spinal cords, images were captured using a 10x objective in the lumbar regions of the cords using a confocal microscope similar to the analysis of AFSM (see above). Images were analysed using ImageJ (Schindelin et al, 2015; Schneider et al, 2012) to calculate relative fluorescence units by first converting images to black and white and expressing the number of white (fluorescent) pixels over the total number of pixels. Three images were taken for each section and their values averaged. Therefore, the average relative fluorescence for each spinal cord was obtained.

2.9 Qualitative Analysis

Some staining was able to provide qualitative information about the distribution, morphology or density of an antigen, without the need for quantification. Images were taken at required magnifications using x5, x10, x20, x40, x63 and x100 objectives on either using a Leica DRMB microscope (Leica Microsystems) with a Zeiss AxioCam HRc Rev 2 digital camera (Zeiss) for bright field microscopy or a Leica SP5 confocal microscope (Leica Microsystems) for confocal images. Images were then carefully examined to comment on the nature of the staining in these sections.

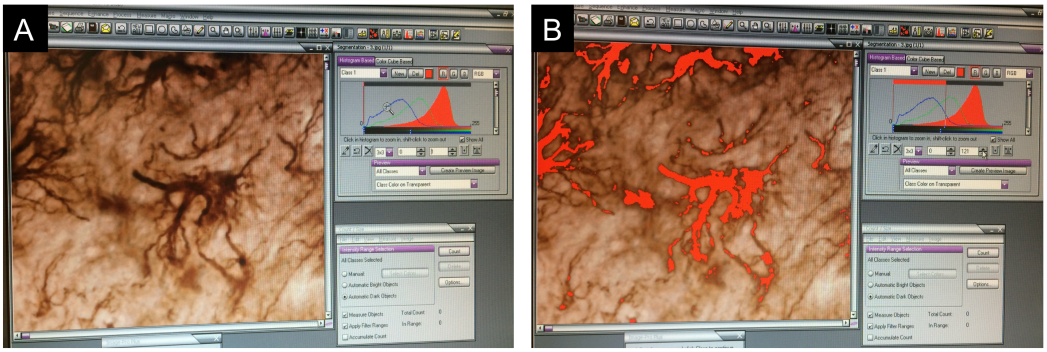

Figure 2.9 – Selecting thresholds for thresholding image analysis.

Representative images showing positive GFAP (astrocyte) staining (left) and the selection of a threshold for red, green and blue channels so as to accurately discriminate positively immunostained cells from the background (right) using the Image Pro Plus software (Media Cybernetics).

2.10 Statistical Analysis

All measurements were performed blind to genotype. All statistical analysis was performed using *GraphPad Prism* software (GraphPad Software Inc., La Jolla, CA). The mean co-efficient of error for individual measures of neuron counts in Nissl-stained sections was calculated by the Gundersen method (Gundersen & Jensen, 1987), and was between the recommended range of 0.05 - 0.10. Statistical analyses for measurements of regional volumes, neuron counts, cell areas and thresholding image analysis between two groups at a given time-point was calculated by a two-tailed, unpaired, parametric t-test where $p \leq 0.05$ was considered significant. For comparison between time-points, for each genotype in each data set, a two-way ANOVA, with a post-hoc Bonferroni correction was

employed, where $p \leq 0.05$ was considered significant. Lastly, for the analysis of three or more groups for therapeutic efficacy, a one-way ANOVA with a post-hoc Bonferroni correction was used where $p \leq 0.05$ was considered significant.

Chapter 3. Early and widespread spinal cord neuropathology in CLN1 disease

3.1 Introduction

In CLN1 disease, as with other forms of NCL, the brain has been considered the main locus of pathology (Cooper, 2003; Haltia et al, 1973a; Santavuori et al, 1973), mainly due to the clinical presentation of symptoms (Dolisca et al, 2013). The extent and progression of pathological changes occurring in the brains of *Ppt1*$^{-/-}$ mice has been described in detail, revealing extensive degenerative changes particularly affecting the thalamocortical system and cerebellum (Bible et al, 2004; Kielar et al, 2007; Macauley et al, 2009).

While there have been a few reports that have briefly mentioned spinal cord pathology in the NCLs (Bruun et al, 1991; Haltia et al, 1973a; Haltia et al, 1973b), there has been no detailed analysis of pathology in this region of the CNS in any form of these diseases. Furthermore, the characterization of brain pathology in *Ppt1*$^{-/-}$ mice so far has not fully been able to explain the sensorimotor deficits seen in these mice (Dearborn et al, 2015; Gupta et al, 2001), and previous experimental therapies targeting the brain have only had limited success for CLN1 disease (Lu et al, 2010; Macauley et al, 2012; Tamaki et al, 2009).

This study is the first to detail the nature, extent and progression of pathological changes occurring in the spinal cord in CLN1 disease, utilizing histochemical techniques to compare spinal cord and DRG tissue of wildtype control (C57BL/6) and *Ppt1*$^{-/-}$ mice, as well as *post-mortem* spinal cord samples of a human INCL case with a neurologically normal control.

3.2 Altered spinal cord volumes in *Ppt1*$^{-/-}$ mice.

Progressive regional atrophy of the brain has previously been documented in *Ppt1*$^{-/-}$ mice, and has been observed as early as 5 months of age (Kühl et al, 2013). Therefore, to determine whether the volume of *Ppt1*$^{-/-}$ mouse spinal cords is similarly altered, we employed a Cavalieri estimator (Kühl et al, 2013; Lucocq, 2007) to measure total volumes and gray matter volumes as previously described (Figure 2.5), the white matter volumes were calculated as a subtractive value of these volumes. As already mentioned stated in chapter 1.5, there are no statistically significant difference between the overall body weights of *Ppt1*$^{-/-}$ and

wildtype control mice at any age (Galvin et al, 2008). As such, these volume measurements were not normalized to the animals' respective body weights.

The volume of the mouse spinal cord has been shown to increase during development between 1-3 months of age, affecting both the white and gray matter (Sakla, 1959; Sakla, 1962; Sakla, 1969). A similar initial, significant increase was observed during these time-points in the total, gray matter and white matter volumes of the wildtype mouse spinal cords. However, the regional volumes of *Ppt1*$^{-/-}$ mouse spinal cords did not increase to the same extent during this time. This may suggest a possible postnatal developmental delay in the spinal cords of these mice (Figure 3.1).

There was a consistent, significant difference in all the measured spinal cord volumes between *Ppt1*$^{-/-}$ and control mice from 2 months of age. This difference appeared earlier than any regional volume difference seen in the brain (Kühl et al, 2013). Furthermore, the difference observed in spinal cord white matter volumes was a novel finding, as previous studies of brain pathology in *Ppt1*$^{-/-}$ mice had not revealed any significant changes in brain white matter volumes (Bible et al, 2004; Kielar et al, 2007; Kühl et al, 2013).

The patterns of altered spinal cord volumes observed in the cervical, thoracic and lumbo-sacral spinal cord segments of *Ppt1*$^{-/-}$ mice were similar to those for whole cord volumes (Figure 3.2), suggesting that these volumetric changes do not have any regional specificity, as they do in the brain, and that the spinal cord as a whole seems to be affected at all levels at the same time in these mice.

3.3 Profound neuron loss in *Ppt1*$^{-/-}$ mouse spinal cords.

Being a severely neurodegenerative disease, a prominent feature of CLN1 pathology is the profound loss of neurons with disease progression (Cooper, 2003; Kohlschutter & Schulz, 2009). Significant neuron loss is observed in the brains of *Ppt1*$^{-/-}$ mice from 5 months of age, with the thalamus and cerebellum being affected first (Kielar et al, 2007; Macauley et al, 2009). To determine whether there was a similar pathology present in the spinal cords of these mice,

40µm spinal cord sections were Nissl stained to visualize neuronal cytoarchitechture, in addition to markers for specific neuronal populations. Unbiased stereological estimates as well as thresholding image analysis of neuronal numbers were then obtained from these stained sections. As before, in the absence of significant differences in body weight between *Ppt1*$^{-/-}$ and wildtype control mice (Galvin et al, 2008), these stereological counts were not normalized to the animals' respective body weights.

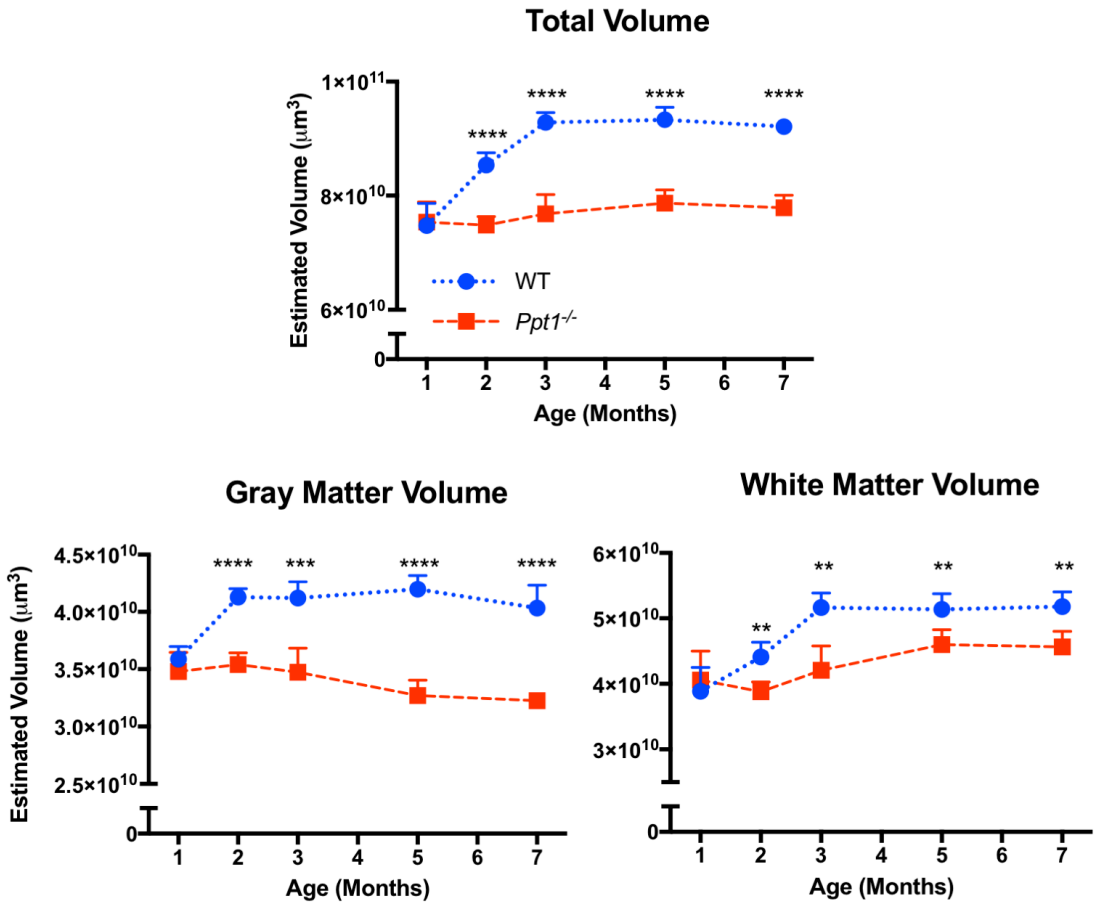

Figure 3.1 – Altered spinal cord volumes in Ppt1$^{-/-}$ mice.

*Decreased volumes of the whole spinal cord by Cavalieri estimates, were evident in Ppt1 deficient (Ppt1$^{-/-}$) mice, as compared to age-matched wildtype controls (WT) as early as 2 months of age in total, gray matter and white matter volumes. **p<0.01, ***p<0.001, ****p<0.0001, two-tailed unpaired parametric t-test. Values shown are non-continuous observations from each cohort at each time point as mean ± Standard Error of the Mean (SEM) . (n= 5 mice/group)*

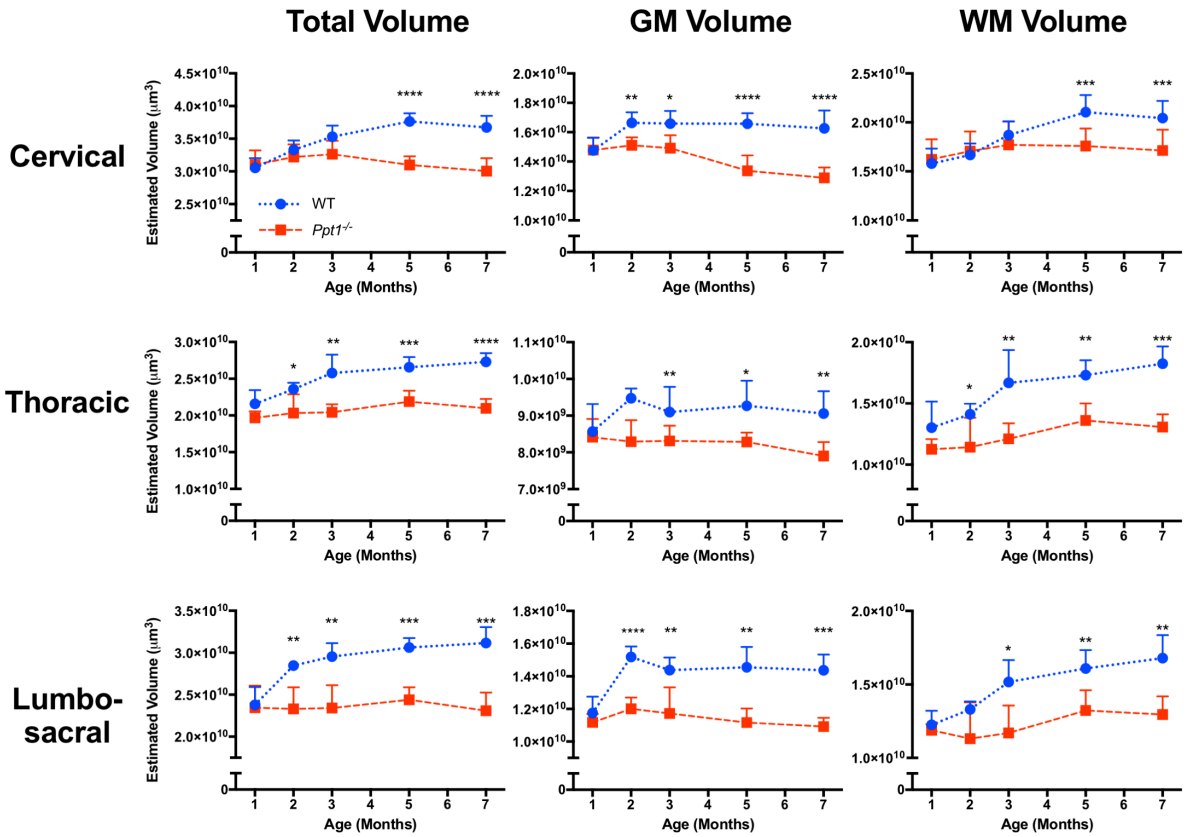

Figure 3.2 – Altered spinal cord volumes at all levels of Ppt1$^{-/-}$ mouse spinal cord.

*Cavalieri estimates of total, gray matter and white matter volumes of cervical, thoracic and lumbosacral regions of the spinal cord show a significant difference between Ppt1 deficient (Ppt1$^{-/-}$) and wild type control (WT) spinal cords as early as 2 months of age, at all levels. *p<0.05, **p<0.01, ***p<0.001,****p<0.0001, two-tailed, unpaired parametric t-test. Values shown are non-continuous observations from each cohort at each time point as mean ± SEM. (n= 5 mice/group).*

a) Early loss of neurons at all levels of *Ppt1*$^{-/-}$ mouse spinal cords.

To determine if there was any loss of neurons in *Ppt1*$^{-/-}$ mouse spinal cords, a 1 in 48 series of spinal cord sections from 1, 2, 3, 5 and 7 month old *Ppt1*$^{-/-}$ and wildtype mice were Nissl stained with cresyl fast violet. The dorsal and ventral horns were counted separately to represent the sensory and motor regions of the spinal gray matter. Neurons in both of these regions were counted in the cervical, thoracic and lumbo-sacral spinal cord segments using an design-based optical fractionator (West, 2002), with the regions delineated according to landmarks in a spinal cord atlas (Sengul, 2013).

These data revealed that there was an early and profound loss of neurons at all levels of the *Ppt1*$^{-/-}$ mouse spinal cord (Figure 3.3). Significant neuron loss was observed in both the dorsal and ventral horns, with some regions affected as early as 3 months, namely the dorsal horns of the cervical and lumbosacral region and the ventral horn of the thoracic region. All regions of the spinal cord showed significant neuron loss from 5 months onwards, which worsened with time. This loss of neurons is further illustrated in Table 3.1, which shows that there is an average loss of 14.89% of neurons in the dorsal horn and 9.31% in the ventral horn of *Ppt1*$^{-/-}$ mice, compared to their wildtype counterparts as early as 3 months of age. These values then significantly progress to 34.4% and 28.61% at 7 months respectively. These data further emphasize the progressive and profound nature of neuron loss in the spinal cord of these mice. Indeed, the severity of this neuron loss is comparable to that seen in Cln8 (*Cln8*^{mnd}) (Fujita et al, 1998; Plummer et al, 1995) as well as to other models of neurodegenerative diseases affecting the spinal cord such as ALS (Dal Canto & Gurney, 1997; Ravits et al, 2007)and SMA(Simone et al, 2016; Sleigh et al, 2011), Parkinson's disease (Martin et al, 2006; Vivacqua et al, 2011), Alzheimer's disease (Seo et al, 2010) and HD (Valadao et al, 2016).

This neuron loss occurs earlier than that seen in the brain, which begins at 5 months of age (Kielar et al, 2007). Furthermore, as with the volume changes, all levels of the cord seem to be affected at the same time, with little rostro-caudal variation. This is in marked contrast to the region-specific pattern of neuron loss

seen in the brain (Kielar et al, 2007). The early onset of such profound neuron loss in the spinal cords of *Ppt1*$^{-/-}$ mice is indicative that this region is severely affected by CLN1 disease and raises the possibility that it may contribute to disease progression.

b) Loss of GABAergic interneurons in *Ppt1*$^{-/-}$ mouse spinal cords.

Interneuron populations are severely affected early in disease progression in the brains of *Ppt1*$^{-/-}$ mice (Bible et al, 2004; Kielar et al, 2007). Interneurons form a large subset of the neurons in the spinal cord and are critical to the normal functioning of spinal neural networks (Edgley, 2001; Jankowska, 2001).

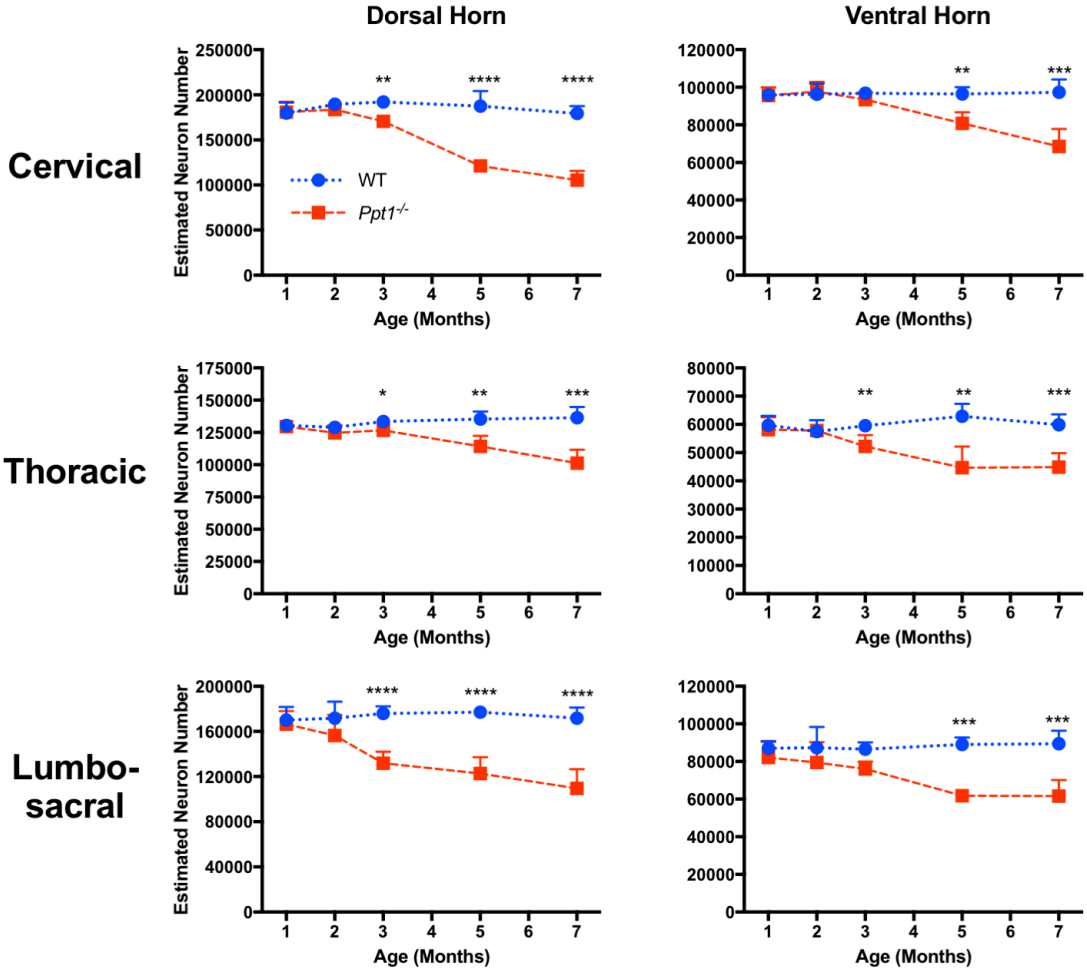

Figure 3.3 – Early neuron loss in spinal cords of Ppt1$^{-/-}$ mice.

*Unbiased optical fractionator counts reveal the significant loss of Nissl (cresyl fast violet) stained neurons in the dorsal and ventral horn of the cervical, thoracic and lumbosacral cord of Ppt1 deficient (Ppt1$^{-/-}$) mice beginning as early as 3 months of age, compared to age-matched wildtype controls (WT). *p<0.05, **p<0.01, ***p<0.001, ****p<0.0001, two-tailed, unpaired parametric t-test. Values shown are non-continuous observations from each cohort at each time point as mean ± SEM. (n= 5 mice/group).*

A 1 in 48 series of spinal cord sections from *Ppt1*$^{-/-}$ and wildtype mice were stained for calbindin (CB) and calretinin (CR), which are established markers of GABAergic interneuron populations (Andressen et al, 1993; Defelipe et al, 1999). Additionally, these markers had been used in characterizing interneuron populations in *Ppt1*$^{-/-}$ mouse brains (Kielar et al, 2007).

Age	% Loss of neurons (*Ppt1*$^{-/-}$: WT)							
	Dorsal Horn				Ventral Horn			
	Cervical	Thoracic	Lumbo-Sacral	Average	Cervical	Thoracic	Lumbo-Sacral	Average
1 MO	-0.55	0.63	2.22	0.76	0.38	2.66	5.59	2.88
2 MO	3.16	3.19	4.31	3.55	-1.52	-0.50	9.06	2.34
3 MO	11.17	5.08	28.42	14.89	3.47	12.33	12.15	9.31
5 MO	35.36	15.64	30.65	27.22	16.25	28.95	30.62	25.27
7 MO	41.20	25.82	36.19	34.40	29.65	25.09	31.10	28.61

Table 3.1 – Percentage loss of neurons in Nissl stained sections

Table showing the percentage loss of neurons in Nissl stained sections of Ppt1deficient (Ppt1$^{-/-}$*) mice to wildtype (WT) mice from the averaged neuron counts (n=5 mice/group) at each time point in the dorsal and ventral horns. Negative (-) values indicte lower WT neuron counts than in Ppt1*$^{-/-}$ *mice. Average is the combined average of cervical, thoracic and lumbo-sacral values at each time point.*

Staining for CB and CR revealed a dense band of interneurons and their terminals in laminae I-III of the gray matter with sparsely scattered interneurons, with intensely stained cell bodies in the remaining gray matter of spinal cord sections (Rexed, 1954) (Figure 3.4A, 3.5A). Our analysis therefore employed semi-automated thresholding image analysis for the neuron dense laminae I-III and stereological counts of neurons in laminae IV-IX of each section. Results were obtained for the cervical, thoracic and lumbo-sacral spinal cord segments at all ages.

These analyses of sections stained for calbindin (CB) revealed a significant decrease in the number of these neurons as early as 3 months of age in laminae IV-IX at all levels of the cord of *Ppt1*$^{-/-}$ mice (Figure 3.4B). There was also a similar significant decrease in laminae I-III of the cervical cord starting at 3 months, and

in the thoracic and lumbo-sacral segments at 5 months. These data suggest that this loss of CB positive interneurons is at least partly responsible for the loss of neurons observed in Nissl-stained sections in *Ppt1*$^{-/-}$ mice. The early loss of calbindin positive interneurons in the spinal cord is similar to events in the brain, where calbindin positive interneurons have been shown to be one of the first neuron populations to be lost in the forebrain of *Ppt1*$^{-/-}$ mice (Kielar et al, 2007).

Similar analysis of sections stained for calretinin (CR) revealed that there was also a significant loss of these neuron populations in *Ppt1*$^{-/-}$ mice (Figure 3.5B). There was significant loss of CR positive neurons at all levels at 5 months, with laminae IV-IX of the cervical and lumbo-sacral segments showing significant loss as early as 3 months of age. Again, this was similar to events in the brain, where the loss of calretinin positive interneurons seems to follow the loss of calbindin positive neurons in *Ppt1*$^{-/-}$ mice (Kielar et al, 2007).

These data show that similar interneuron populations are affected in the *Ppt1*$^{-/-}$ mouse spinal cord as they are in the brain, but at an earlier time point. Furthermore, unlike the brain, there was no regional specificity of this neuron loss, with all levels of the cord equally affected. These data, along with the counts of Nissl stained sections, provide further evidence for severe neurodegenerative pathology in the spinal cord of *Ppt1*$^{-/-}$ mice. It will therefore be interesting to study whether there is aberrant Ca^{2+} homeostasis in the spinal cords of *Ppt1*$^{-/-}$, as is seen in JNCL (Fossale et al, 2004; Luiro et al, 2006) as well as in other lysosomal storage disorders (Kiselyov et al, 2010).

c) Loss of motor neurons in *Ppt1*$^{-/-}$ mouse spinal cords.

Motor neurons play a critical role in relaying signals along motor pathways (Romanes, 1964). To determine whether these neuron populations are lost in the *Ppt1*$^{-/-}$ mouse spinal cord, we initially immunostained sections for two markers of motor neurons, choline acetyl transferase (ChAT) and the anti-transferrin receptor maker, CD-71.

Sections stained for both ChAT and CD-71 showed a consistency in marking pools of large motor neurons with varying staining intensities. Counts of cells marked with either marker were compared between wildtype and *Ppt1*$^{-/-}$ mouse spinal cord sections in the lumbosacral region at 7 months of age. This analysis demonstrated a consistency in detecting motor neuron populations in this region of the spinal cord, with a significant loss of motor neurons stained for either marker observed in the *Ppt1*$^{-/-}$ deficient cords (Figure 3.6 A). Additional counts of CD-71 stained neurons in the cervical, thoracic and lumbosacral segments of wildtype and *Ppt1*$^{-/-}$ spinal cords showed that there was indeed significant loss of motor neurons at 5 months of age at all levels (Figure 3.6 C), which seemed to worsen similarly at all levels of the cord until 7 months.

This loss of motor neurons in *Ppt1*$^{-/-}$ mouse spinal cords is a previously undocumented phenotype, and may help to better explain the motor deficits seen in these mice (Chapter 4). As altered homeostasis of iron is a common feature in neurodegenerative states in motor neurons (Carri et al, 2003; Yu et al, 2009) as well as in the NCLs (Grubman et al, 2014), it will also be interesting to study whether the expression of CD-71 is altered in the surviving motor neurons.

3.4 Accumulation of autofluorescent storage material in *Ppt1*$^{-/-}$ mouse spinal cords.

The progressive accumulation of autofluorescent storage material within cell bodies is pathognomic of the NCLs (Cooper, 2003; Mole et al, 2005). In CLN1 disease, the intralysosomal accumulations of granular autofluorescent osmiophillic deposits have been shown to be present in the CNS (Tyynela et al, 1993), as well as visceral tissue (Galvin et al, 2008). While there is little evidence to suggest that this storage material is directly causative of neuron loss, the progressive accumulation is easily visualized via fluorescence or confocal microscopy and therefore makes a useful readout of disease burden.

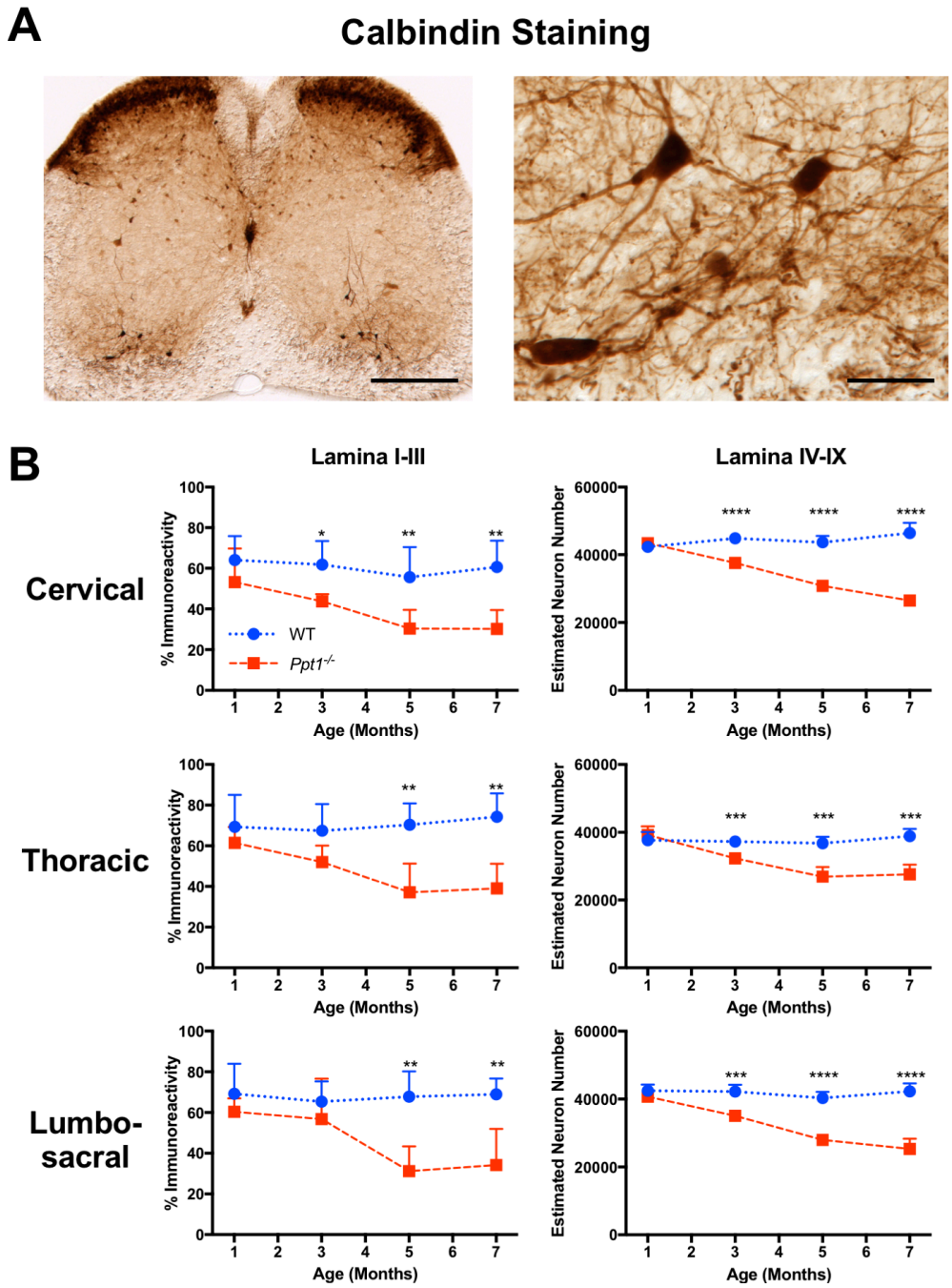

Figure 3.4 – Loss of Calbindin positive interneurons in Ppt1$^{-/-}$ mouse spinal cords.

*(**A**) Representative images of a lumbo-sacral spinal cord section stained for calbindin at low magnification (left) showing Laminae I-III as a dense band of interneurons in the dorsal horn of the gray matter with sparsely scattered interneurons in the remaining laminae, and at higher magnification (right) showing neurons stained for calbindin. Scale bars = 200μm (left panel) and 25μm (right panel). (**B**) Thresholding image analysis (Laminae I-III) and stereological counts (Laminae IV-IX) show significant loss of calbindin positive neurons as early as 3 months at all levels of the cord. *p<0.05, **p<0.01, ***p<0.001, ****p<0.0001, two-tailed, unpaired parametric t-test. Values shown are non-continuous observations from each cohort at each time point as mean ± SEM. (n= 5 mice/group).*

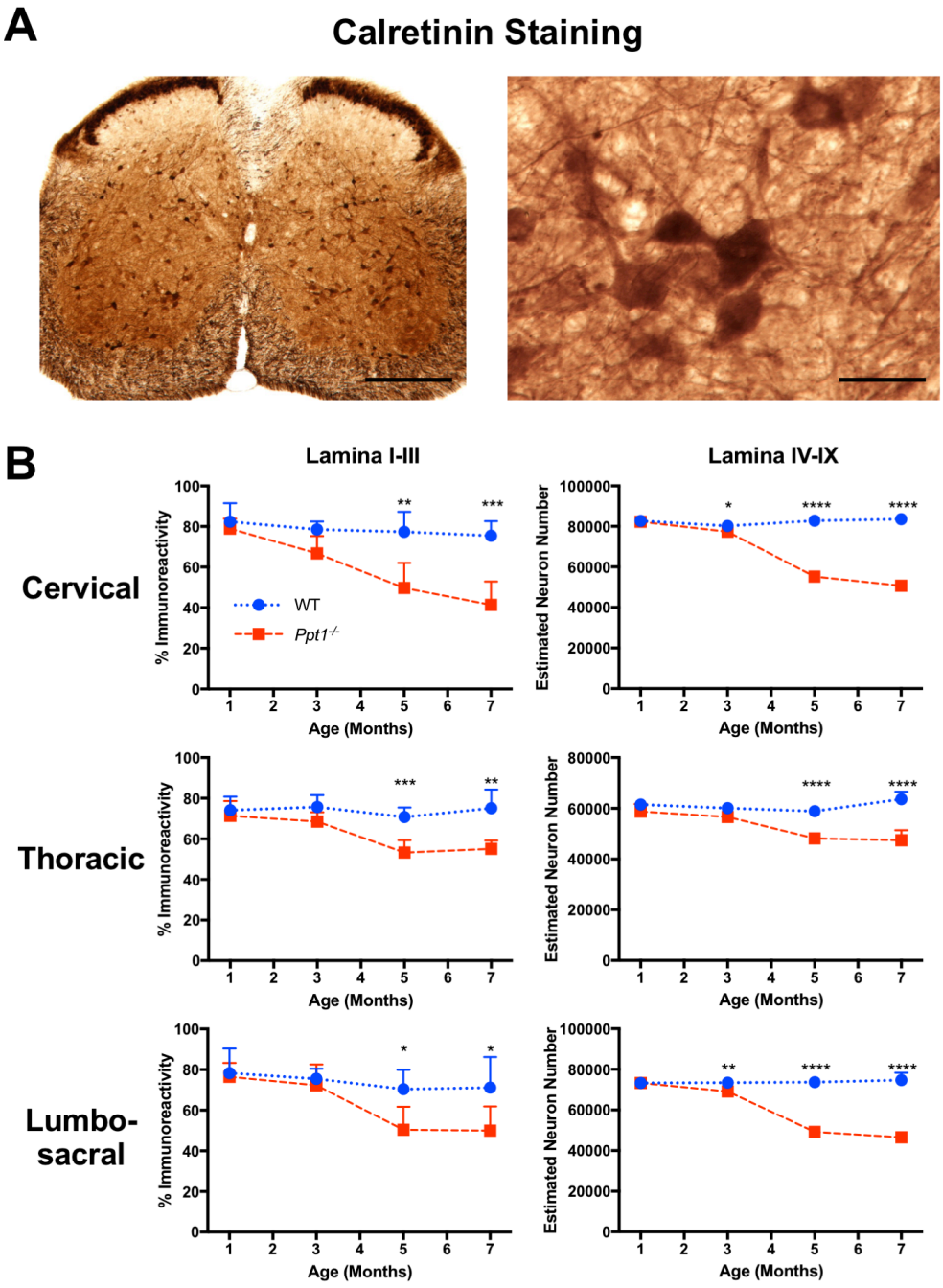

Figure 3.5 – Loss of Calretinin positive interneurons in Ppt1$^{-/-}$ mouse spinal cords.

*(**A**) Representative images of a lumbo-sacral spinal cord section stained for calretinin (left) at low magnification showing Laminae I-III as a dense band of interneurons in the dorsal horn of the gray matter with sparse interneurons in the remaining laminae, and at higher magnification (right) showing neuronal cells stained for calretinin. Scale bars = 200µm (left panel) and 25µm (right panel). (**B**) Thresholding image analysis (Laminae I-III) and stereological counts (Laminae IV-IX) show significant loss of calretinin positive neurons as early as 3 months in the cervical and lumbosacral laminae IV-IX. *p<0.05, **p<0.01, ***p<0.001, ****p<0.0001, two-tailed, unpaired parametric t-test. Values shown are non-continuous observations from each cohort at each time point as mean ± SEM. (n= 5 mice/group).*

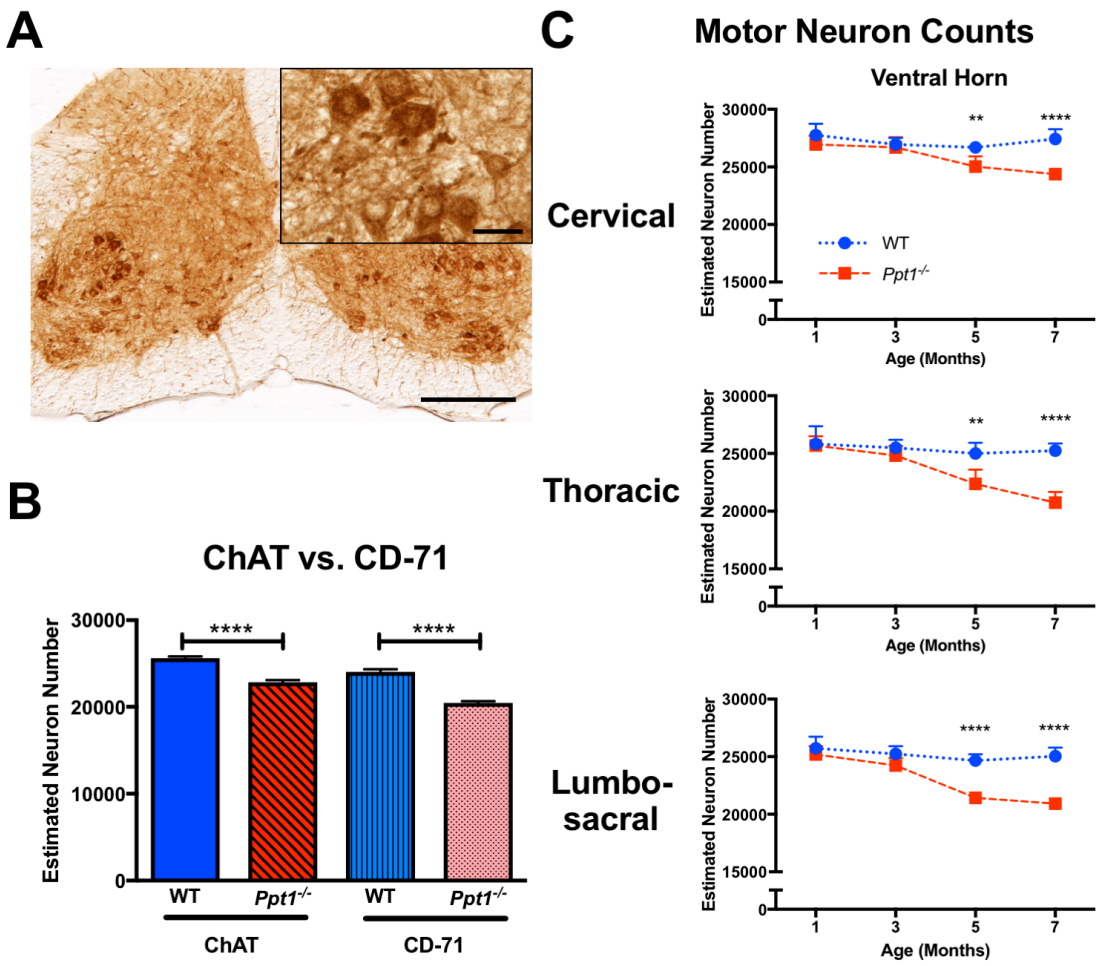

Figure 3.6 - Loss of motor neurons in Ppt1$^{-/-}$ mouse spinal cords.

*(**A**) Representative images of a lumbo-sacral spinal cord section stained for the anti-transferrin receptor marker, CD-71 showing pools of motor neurons in the ventral horn. CD-71 positive motor neurons show a varying degree of staining intensities (Insert). Scale bars = 200μm and 25μm (insert). (**B**) Stereological counts of ChAT and CD-71 positive cells in the lumbosacral region at 7 months revealed consistent counts with either marker, demonstrating a significant loss of motor neurons in Ppt1 deficient (Ppt1$^{-/-}$) spinal cords. (**C**) Stereological counts of CD-71 positive cells in the ventral horns of the cervical, thoracic and lumbosacral spinal cord showed a significant loss of motor neuron populations at all levels starting at 5 months in Ppt1 deficient (Ppt1$^{-/-}$) mice compared to wildtype (WT) controls. **p<0.01, ****p<0.0001, two-tailed, unpaired parametric t-test. Values shown are non-continuous observations from each cohort at each time point as mean ± SEM. (n= 5 mice/group).*

A confocal microscopy survey of *Ppt1*$^{-/-}$ spinal cord sections revealed that there was a similar accumulation of autofluorescent storage material within the gray matter of the spinal cord at all levels, starting at 3 months of age (Figure 3.7). This provides further evidence of a disease process occurring in the spinal cord at this early time point. This storage material initially seemed localized to cells with neuronal morphology, but increasingly also appeared as dense clusters within smaller cells starting at 5 months of age.

In light of previous evidence of re-distribution of the autofluorescent storage material to microglial cells in a sheep model of NCL (Oswald et al, 2005), we hypothesized that a similar process may occur in *Ppt1*$^{-/-}$ mouse spinal cords. Selected sections from cervical and lumbosacral spinal cords at each time point were stained with CD68, a marker for microglia. Confocal microscopy was then used to simultaneously visualize these stained microglia and the storage material.

The staining revealed that some of the autofluorescent storage material was indeed localized within CD68 positive activated microglia starting at 5 months of age (Figure 3.8). This re-distribution may be effected by the activated microglia phagocytizing degenerating neurons, providing further evidence of a pathological process in the spinal cord before that which appears in the brain.

3.5 Hypertrophy of neuronal populations in *Ppt1*$^{-/-}$ mouse spinal cords.

An increase in the soma size of different neuron populations has previously been documented in severely affected *Ppt1*$^{-/-}$ mouse brains, presumably due to the accumulation of storage material within lysosomes (Bible et al, 2004). Furthermore, a qualitative study of human CLN1 spinal cord samples described the anterior horn cells to be “distended”(Santavuori et al, 1974).

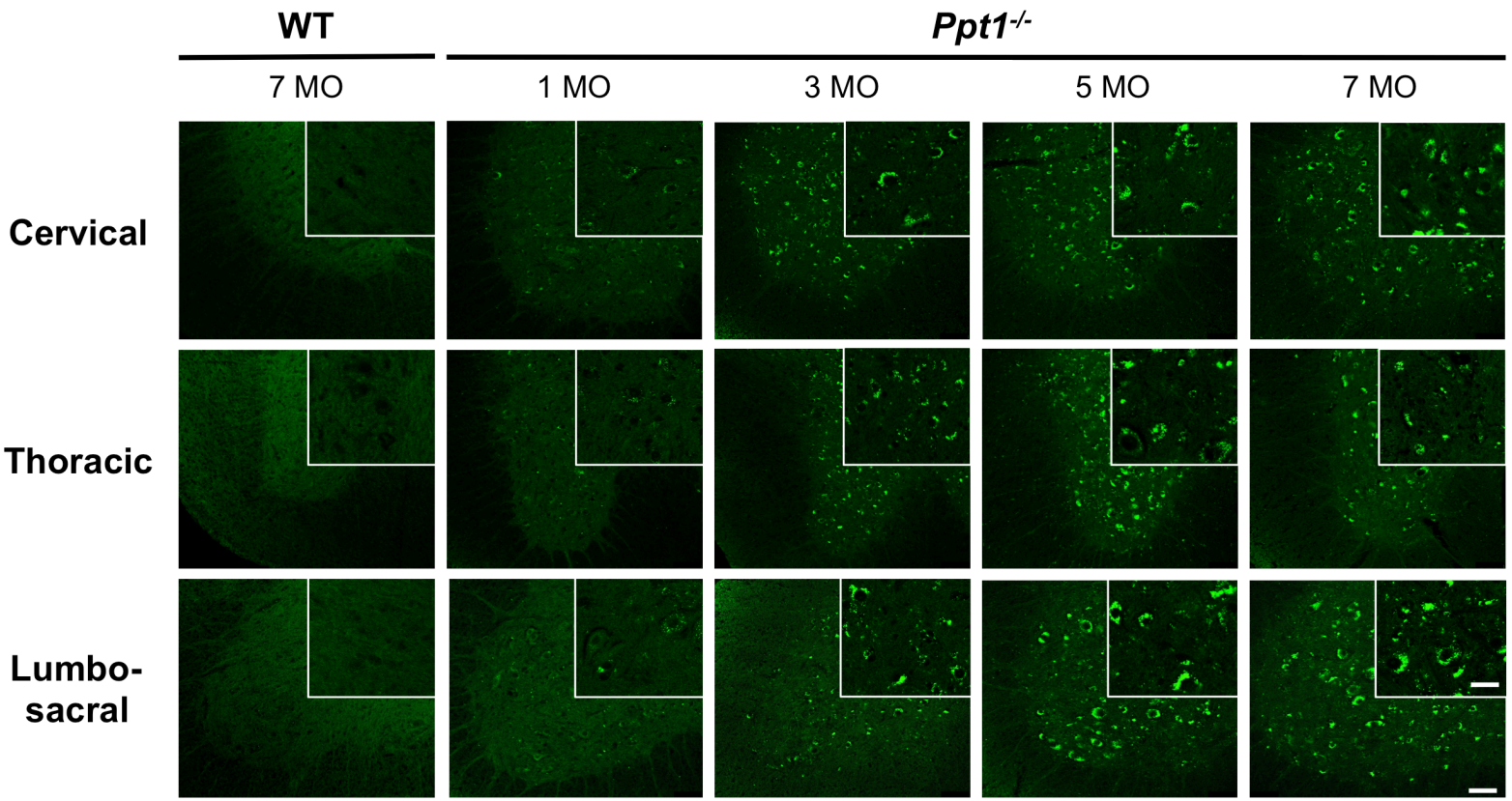

Figure 3.7 – Accumulation of autofluorescent storage material in the spinal cord of Ppt1$^{-/-}$ mice.

Representative confocal microscope images of unstained sections of cervical, thoracic and lumbosacral spinal cord showing the progressive accumulation of autofluorescent storage material (green) within morphologically identified neuronal cell bodies in the ventral horns of Ppt1 deficient (Ppt1$^{-/-}$) mice as early as 3 months, compared to age-matched wildtype controls (WT). Scale bars = 100μm and 25μm (inserts).

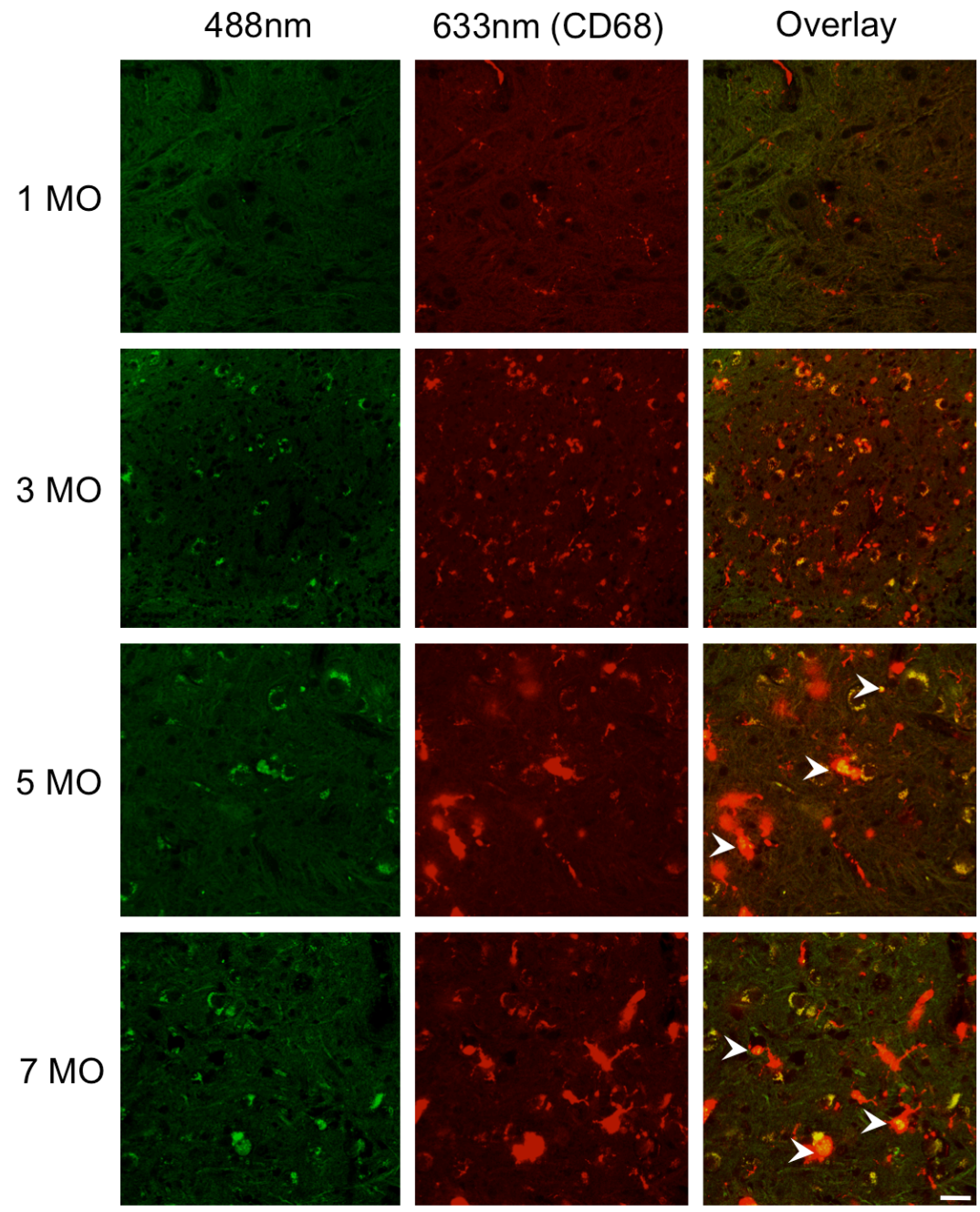

Figure 3.8 - Re-distribution of autofluorescent storage material in Ppt1$^{-/-}$ mouse spinal cords.

Representative confocal microscope images of the ventral horn of the lumbosacral spinal cord of Ppt1$^{-/-}$ mice stained for the microglial marker CD68 (red). From 5 months onwards progressively more of this storage material (488nm (green) and 633nm (red) channels) was also present within CD68 positive microglia (633nm, red), appearing yellow in the merged overlay (white arrows). Scale bar = 25μm.

To determine if such a phenotype was present in the spinal cords of 7 month old *Ppt1*$^{-/-}$ mice, we measured the cross-sectional cell body area of calbindin and calretinin positive interneurons, as well as Nissl stained motor neurons. The latter were identified by their location and morphology within the ventral horn of the spinal cord (Romanes, 1964; Sengul, 2013).

Analysis of average cell areas revealed a significant increase in the size of both calbindin and calretinin positive interneurons, as well as that of motor neurons, at all levels of the cord in 7 month old *Ppt1*$^{-/-}$ mice (Figure 3.9). This provides further evidence for similar pathological changes in spinal cord neurons as there are in the brain (Bible et al, 2004; Kielar et al, 2007).

3.6 Synaptic pathology in *Ppt1*$^{-/-}$ mouse spinal cords

Ppt1 has been suggested to have an extra-lysosomal localization at synapses, and its deficiency has been shown to affect synaptic vesicle recycling (Kim et al, 2008). Early synaptic pathology has previously been reported in *Ppt1*$^{-/-}$ mouse brains (Kielar et al, 2009), and an altered expression of pre-synaptic markers involved in the synaptic vesicle formation such as synaptophysin, synaptobrevin (VAMP2) and SNAP25.

To determine whether there was any appreciable synaptic pathology in the synapse-rich spinal cord (Rexed, 1954), we stained sections of *Ppt1*$^{-/-}$ and wildtype spinal cords at 7 months of age for the pre-synaptic markers synaptophysin, VAMP2 and SNAP25, as well as the post-synaptic marker PSD-95, which is known to undergo palmitoylation (El-Husseini et al, 2000), and may therefore be a substrate for Ppt1.

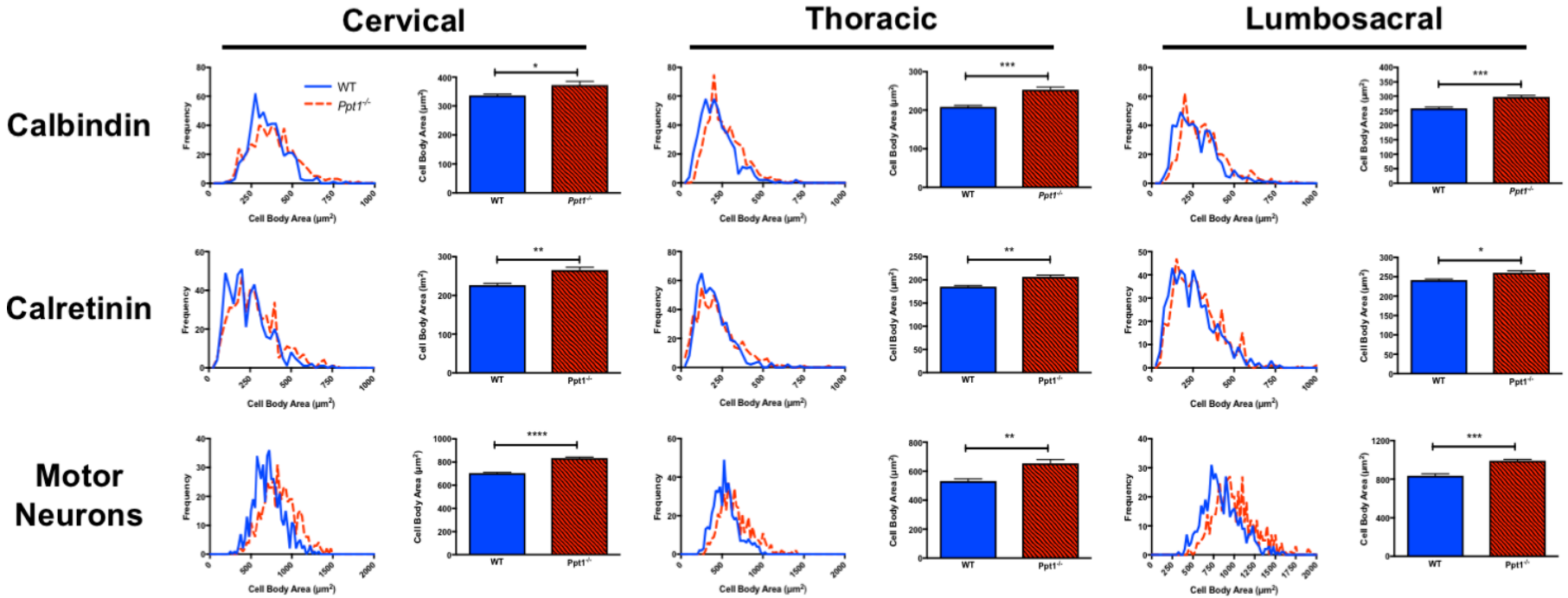

Figure 3.9 - Spinal neuron hypertrophy in Ppt1$^{-/-}$ mice.

*Frequency distribution graphs and histograms of mean cell body areas for Calbindin and Calretinin positive interneurons, as well as Nissl-stained motor neurons reveal significant hypertrophy of all these neuronal types at 7 months at all levels of the cord of Ppt1 deficient (Ppt1$^{-/-}$) mice at 7 months, compared to age-matched wildtype controls (WT). *p<0.05, ***p<0.001, two-tailed, unpaired parametric t-test. Values shown are mean ± SEM. (n= 5 mice/group).*

Our analysis revealed very little difference between the genotypes (Figure 3.10) for any of the markers stained. Staining for synaptophysin and SNAP25 showed almost no alteration in the distribution of these markers in the gray matter of *Ppt1*$^{-/-}$ mouse spinal cord compared to the WT cords (Figure 3.10). However, VAMP2 staining showed a similar pattern of dense aggregates within cells of neuronal morphology in the *Ppt1*$^{-/-}$ mouse spinal cord sections, as seen in the brain (Kielar et al, 2009) (Figure 3.10). Staining for PSD-95 showed only a slight increase in intensity in the *Ppt1*$^{-/-}$ mouse spinal cord, as compared to the controls. However, these sections also showed staining of blood vessels in the gray matter of the spinal cord in both *Ppt1*$^{-/-}$ and WT mice, thus preventing any meaningful quantification to be performed made (Figure 3.10)..

While it may be reasoned that there may be similar synaptic pathology in the synapse-rich spinal gray matter, as occurs in the brains of *Ppt1*$^{-/-}$ mice (Kielar et al, 2009), our findings show little evidence of such pathology, with the exception of VAMP2. Therefore, future work using more sensitive techniques such as western blotting of synaptosomal preparations, which has been previously employed (Kielar et al, 2009) would be very informative.

3.7 Dorsal Root Ganglion (DRG) pathology in *Ppt1*$^{-/-}$ mice.

The dorsal root ganglia contain the cell bodies of the primary sensory afferent neurons, and therefore are vital to the sensory pathways (Rexed, 1954). Having shown there to be profound pathology in the dorsal horns of *Ppt1*$^{-/-}$ mouse spinal cords, we conducted a qualitative survey of 7 month old DRGs from the lumbar level of *Ppt1*$^{-/-}$ and wildtype mice in sections stained with cresyl fast violet, and by using confocal microscopy of unstained sections to determine the presence of autofluorescent storage material.

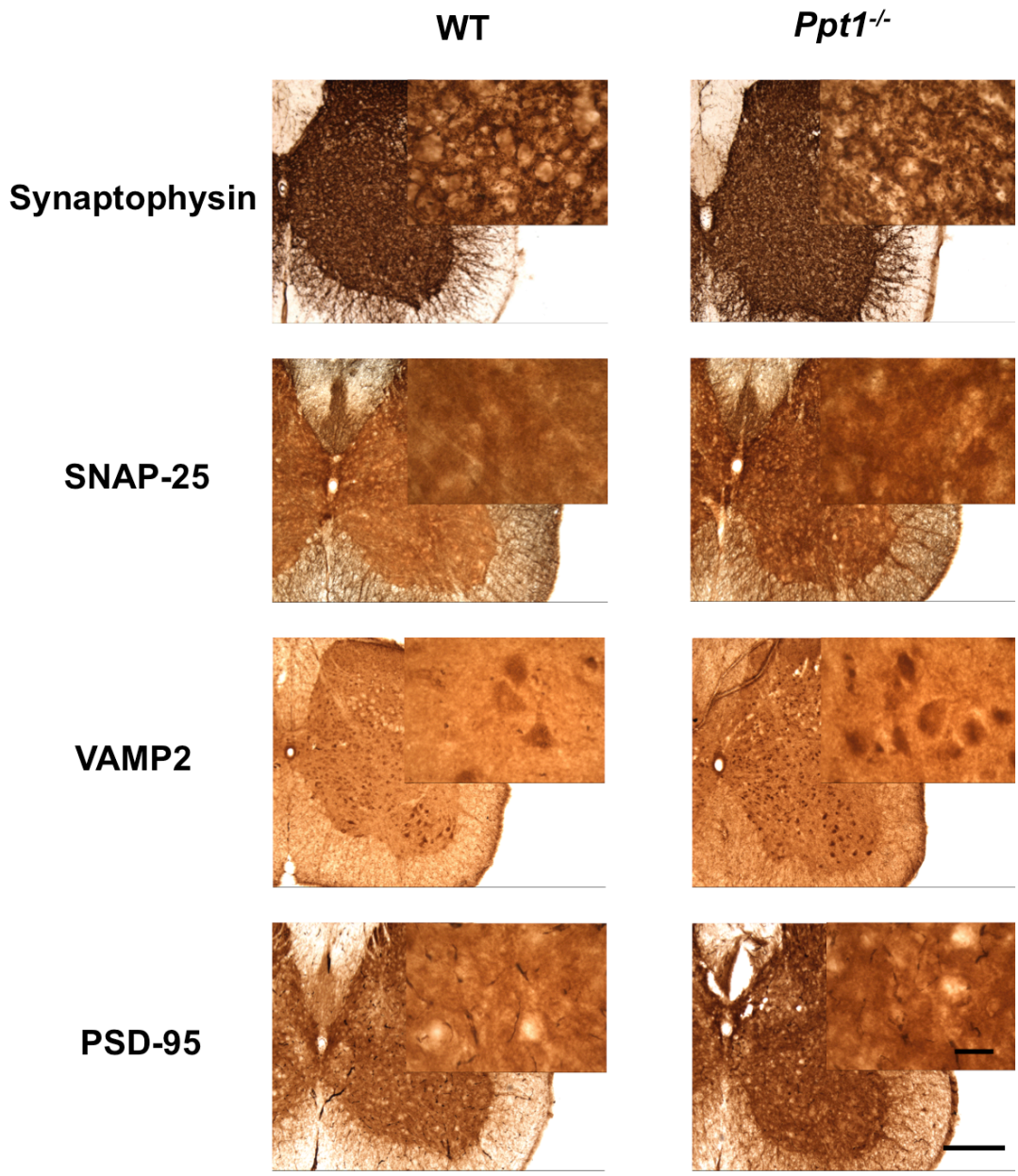

Figure 3.10 – Synaptic marker distribution in the spinal cord of Ppt1$^{-/-}$ mice.
Representative images of the ventral horn of the cervical spinal cord of 7 month old Ppt1$^{-/-}$ mice stained for various synaptic markers showing slightly altered distribution of Synaptophysin and SNAP25, dense aggregates of VAMP2 within cell bodies and increased intensity of PSD-95 staining in Ppt1 deficient (Ppt1$^{-/-}$) mouse spinal cord sections as compared to wildtype (WT) sections. Scale bar = 200μm and 25μm (insert).

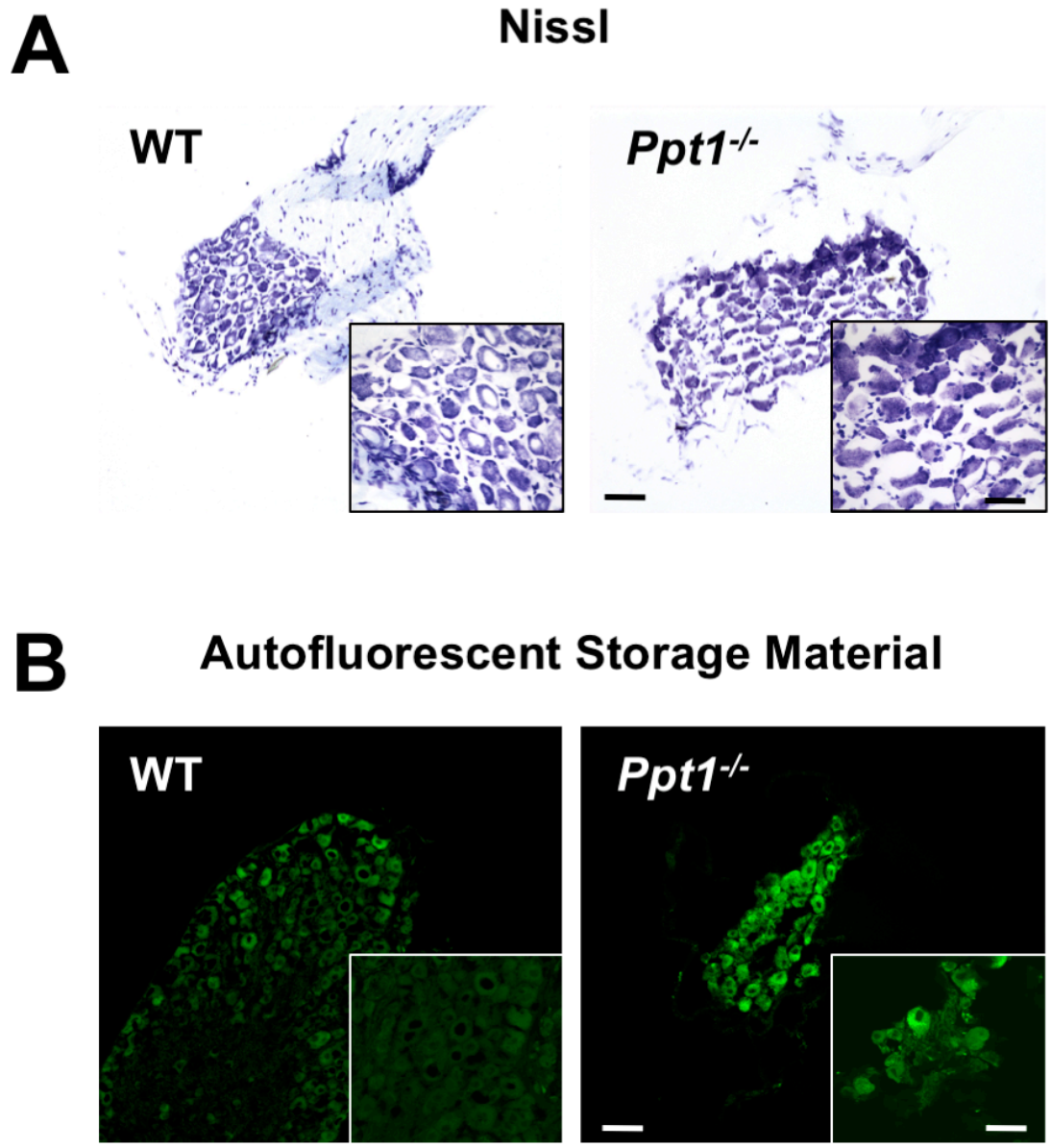

Figure 3.11 – Dorsal Root Ganglion (DRG) pathology in Ppt1$^{-/-}$ mice.

(A) Nissl stained neurons in the DRGs of 7 month old Ppt1$^{-/-}$ mice appear shrunken and more darkly stained with some pale neurons as compared to wildtype (WT) controls. (B) Representative confocal images of unstained DRG sections show the characteristic accumulation of autofluorescent storage material in Ppt1$^{-/-}$ mouse DRGs at 7 months compared to age-matched WT controls. Scale bars = 100μm and 25μm (inserts).

Nissl staining showed *Ppt1$^{-/-}$* mouse DRGs to have neurons with generally denser cytoplasmic staining than the wildtype DRGs, along with some palely stained cells, presumably due to the accumulation of storage material (Figure 3.11). This was confirmed by confocal microscopy, where cells in the *Ppt1$^{-/-}$* mouse DRGs were shown to contain punctate autofluorescent storage material.

These data show there to be similar pathology in the DRG, as there is in the spinal cord of *Ppt1*$^{-/-}$ mice. However, staining these tissues for GFAP to label satellite cells, as well as a combination of CD4 and CD8 to stain peripheral lymphocytes (Hanani, 2005; Scholz & Woolf, 2007), did not show any positive staining for any of these antigens (data not shown). Therefore, having demonstrated the presence of pathology at 7 months in the lumbar DRGs of *Ppt1*$^{-/-}$ mice, further work will now be required to detail the progression and extent of this pathology. This anysis should include investigating the potential presence of any inflammatory phenotype, within DRGs at various levels of the cord in order to provide a comprehensive understanding of when and how these primary sensory neurons are affected in these mice.

3.8 Early onset innate and adaptive immune response in the *Ppt1*$^{-/-}$ mouse spinal cord.

Profound astrocytosis and microglial activation are a prominent feature of the pathology seen in *Ppt1*$^{-/-}$ mouse brains, and have been shown to occur in the same regions of the brains of *Ppt1*$^{-/-}$ mice as where neuron loss occurs, typically preceding neurodegeneration (Bible et al, 2004; Kielar et al, 2007). To determine whether a similar glial response occurs in the spinal cords of these mice, sections from the cervical, thoracic and lumbosacral segments of the spinal cord of 1, 2, 3, 5 and 7 month old *Ppt1*$^{-/-}$ and wildtype mice were immunostained for Glial Fibrillary Associated Protein (GFAP) to mark astrocytes and CD68 to mark microglia. The forebrain of *Ppt1*$^{-/-}$ mice is also progressively infiltrated by peripheral lymphocytes, both by cytotoxic and helper T cells (Groh et al, 2013). Therefore, sections from 1, 3, 5 and 7 month old *Ppt1*$^{-/-}$ and wildtype mouse spinal cords were immunostained for CD4 and CD8 to mark peripheral lymphocytes.

a) Astrocytosis in the *Ppt1*$^{-/-}$ mouse spinal cord.

In the brain, there are fibrous astrocytes in the white matter and protoplasmic astrocytes in the gray matter. Fibrous astrocytes show intense GFAP staining in white matter in the brains of both the wildtype and *Ppt1*$^{-/-}$ mice (Bible et al, 2004; Kielar et al, 2007). Similarly, in the spinal cord, GFAP staining revealed intense staining of fibrous astrocytes in the white matter. However, as compared to

wildtype controls, in the spinal gray matter of *Ppt1*$^{-/-}$ mice there was early and profound astrocytosis. Many more positively stained astrocytes was observed in the dorsal and ventral horns at all levels of the cord of *Ppt1*$^{-/-}$ mice as early as 3 months. These astrocytes were present throughout the gray matter with no obvious laminar specificity. At 5 and 7 months, these astrocytes almost covered the entirety of the gray matter of *Ppt1*$^{-/-}$ mouse spinal cord sections (Figure 3.12 A).

Upon viewing these sections at higher magnification, wildtype spinal cords showed only scarce GFAP positive protoplasmic astrocytes in the gray matter, which were faintly stained with small cell bodies and numerous thin processes. A similar distribution and staining of astrocytes was present at all ages in these mice. In contrast, from 3 months of age, *Ppt1*$^{-/-}$ mouse spinal cords showed an increased abundance of darkly stained reactive astrocytes with relatively fewer thickened processes. There was an increased abundance of astrocytes with this typically activated morphology at 5 and 7 months of age (Figure 3.12 B).

Thresholding image analysis was performed to quantify these observations and this analysis showed that there was a significant astrocytosis at all levels of the *Ppt1*$^{-/-}$ mouse spinal cord, as early as 2 months, which was seen in both the dorsal and ventral horns, and further increased with age (Figure 3.12 C). This is similar to events in the forebrain of these mice, where astrocytosis precedes neuron loss. However, compared to the brain, there was significant astrocytosis in the cord at a very early time point and there was no regional specificity, with all levels of the *Ppt1*$^{-/-}$ mouse spinal cord affected uniformly. This pattern of astrocytosis, however, is very similar to the neuron loss described above (Chapter 3.3), and further emphasizes the close relationship between astrocytosis and neuron loss.

b) Microglial activation in *Ppt1*$^{-/-}$ mouse spinal cords.

As with astrocytosis, sections of *Ppt1*$^{-/-}$ mouse spinal cords showed increased intensity of CD68 staining in the gray matter as early as 3 months of age. This increased immunoreactivity was observed in both the dorsal and ventral horns, with no laminar specificity, and was present at all levels of the cord. The

abundance of these positively stained microglia continued to increase at 5 and 7 months of age (Figure 3.13 A).
In the wildtype spinal cords, CD68 staining revealed several faintly stained cells, with small cell bodies and a sometimes "dotted" or punctate appearance typical of resting or quiescent microglia. This appearance of microglia did not seem to change with age in these wildtype mice. At 3 months of age, *Ppt1*$^{-/-}$ mouse spinal cords showed microglia that stained more intensely with larger cell bodies and shortened processes, typical of activated brain macrophages. The abundance and intensity of staining of these cells continued to increase with age in these mutant mice (Figure 3.13 B).

Quantification of these observations by thresholding image analysis showed there to be a significant increase in microglial activation, as early as 2 months of age in *Ppt1*$^{-/-}$ mouse spinal cords, which further increased with age. This was observed in the dorsal and ventral horns at all levels of the cord (Figure 3.13 C). Therefore, as with astrocytosis, microglial activation seems to precede neuron loss in *Ppt1*$^{-/-}$ mouse spinal cords, occurring earlier than in the brain and showing no regional specificity for any one level of the cord.

Furthermore, examining microglia in the white matter of 7 month old *Ppt1*$^{-/-}$ mice revealed a similar brain macrophage-like morphology to those in the gray matter. Thresholding image analysis was therefore additionally performed for the dorsal and ventral funiculi of the white matter in cervical and lumbosacral cords of wildtype and *Ppt1*$^{-/-}$ mice. This analysis revealed significant microglial activation within these white matter fiber tracts at very early time points in all regions in *Ppt1*$^{-/-}$ mice. Furthermore, there was a dramatic increase in microglial activation within the white matter at 7 months at all levels, suggesting an increased microglial response in fiber tracts following that seen in the gray matter (Fig. 3. 14). These data give the first evidence of a

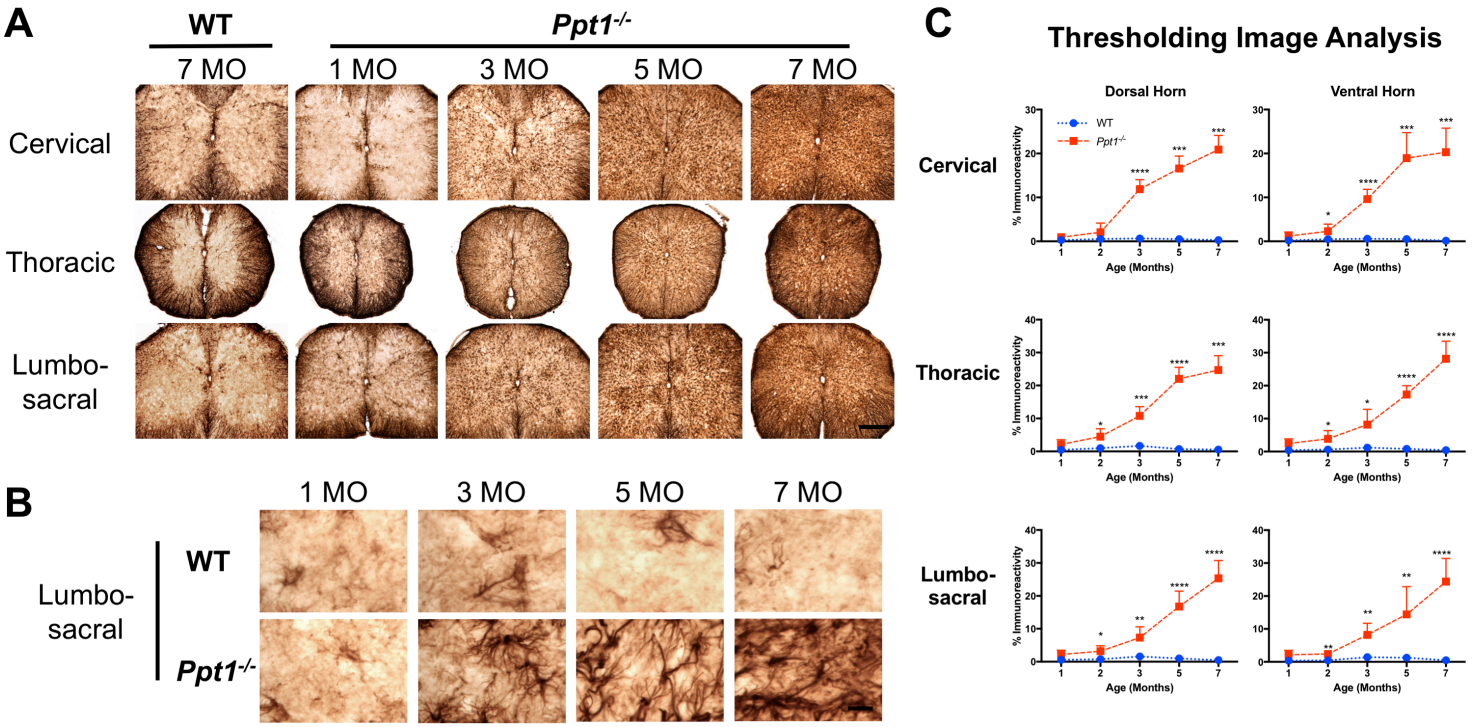

Figure 3.12 - Progressive astrocytosis in the spinal cord of Ppt1$^{-/-}$ mice.

*(**A**) Representative images of the cervical, thoracic and lumbosacral spinal cords from Ppt1 deficient (Ppt1$^{-/-}$) and wild type control mice (WT) stained for GFAP reveal an increase in abundance and staining intensity of astrocytes over time at all levels of Ppt1$^{-/-}$ spinal cords. Scale bar = 200μm. (**B**) Representative high power images showing increased staining intensity, altered morphology and increased abundance of GFAP positive astrocytes in the gray matter of Ppt1$^{-/-}$ spinal cords, compared to wildtype cords. Scale bar = 25μm. (**C**) Thresholding image analysis of GFAP stained sections reveals a significant increase in staining intensity as early as 2 months of age in the dorsal and ventral horns of Ppt1$^{-/-}$ mice, compared to WT controls, which increases with time. *p<0.05, ***p<0.001,****p<0.0001, two-tailed, unpaired parametric t-test. Values shown are non-continuous observations from each cohort at each time point as mean ± SEM. (n= 5 mice/group).*

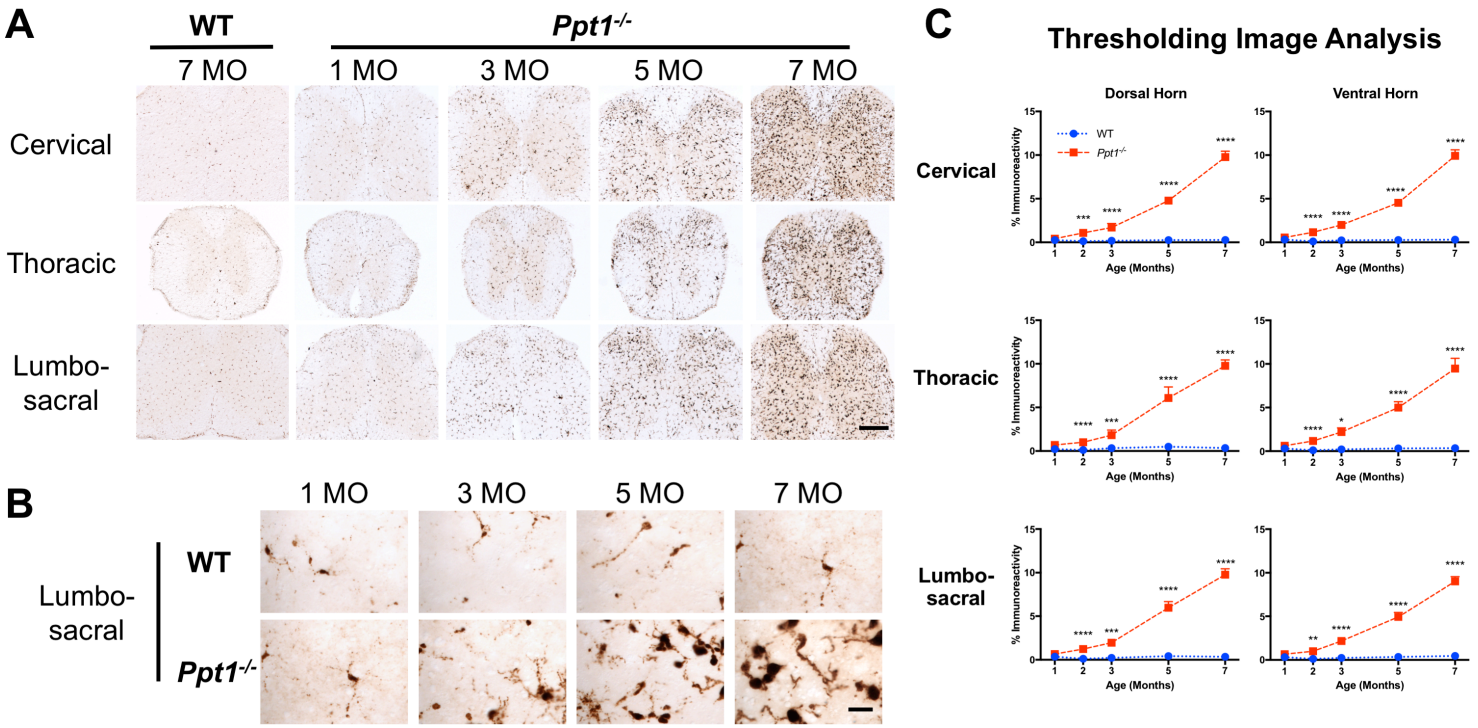

Figure 3.13 - Progressive microglial activation in the spinal cord of Ppt1$^{-/-}$ mice.

*(**A**) Representative images of the cervical, thoracic and lumbosacral spinal cords from Ppt1 deficient (Ppt1$^{-/-}$) and wild type control mice (WT) stained for CD68 reveal an increase in abundance and staining intensity of microglia over time at all levels of Ppt1$^{-/-}$ spinal cords. Scale bar = 200μm. (**B**) Representative high power images showing increased staining intensity, altered morphology and increased abundance of microglia in the gray matter of Ppt1$^{-/-}$ lumbosacral spinal cords, compared to wildtype cords. Scale bar = 25μm. (**C**) Thresholding image analysis of CD68 stained sections reveals a significant increase in staining intensity as early as 2 months of age in the dorsal and ventral horns of Ppt1$^{-/-}$ mice, compared to WT controls, which increases with time. *p<0.05, ***p<0.001,****p<0.0001, two-tailed, unpaired parametric t-test. Values shown are non-continuous observations from each cohort at each time point as mean ± SEM. (n= 5 mice/group).*

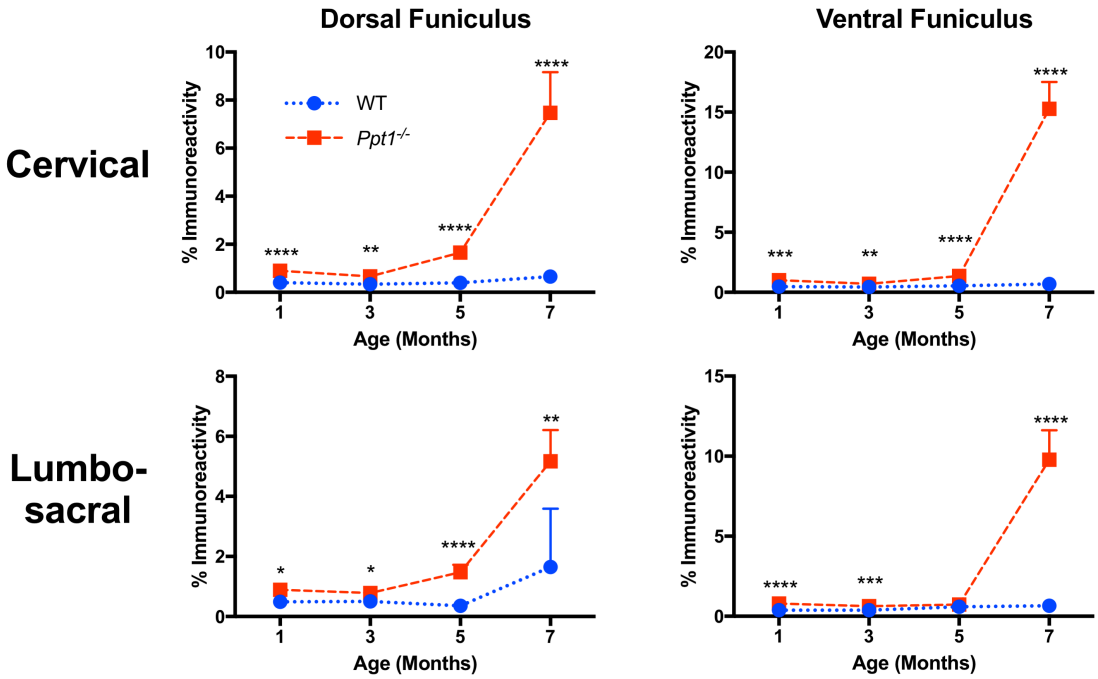

Figure 3.14 - Progressive microglial activation in the white matter of Ppt1$^{-/-}$ mouse spinal cords.

*Thresholding image analysis of CD68 stained sections reveals a significant increase in staining intensity as early as 1 month of age in the dorsal and ventral funiculi of Ppt1$^{-/-}$ mice, compared to WT controls, which increases with time, showing a drastic increase at 7 months. *p<0.05, ***p<0.001,****p<0.0001, two-tailed, unpaired parametric t-test. Values shown are non-continuous observations from each cohort at each time point as mean ± SEM. (n= 5 mice/group).*

pronounced pathological process in the white matter of the *Ppt1*$^{-/-}$ mouse spinal cord, something that is not observed in the brain.

c) Peripheral lymphocyte infiltration of *Ppt1*$^{-/-}$ mouse spinal cords.

Selected sections from the cervical, thoracic and lumbosacral spinal cords of wildtype and *Ppt1*$^{-/-}$ mice were immunostained with a combination of CD4 and CD8 to detect the presence of peripheral lymphocytes.

Positively stained cells were not seen in any of the wildtype spinal cord sections. However, as early as three months, single cells and small clusters of CD4 and CD8 positively stained cells were detected in the gray matter of *Ppt1*$^{-/-}$ mouse spinal cords. This is consistent with infiltration from the vasculature of the central canal. However, there was no evidence of any overt perivascular cuffing. At 5 and 7 months, there was an increased abundance of CD4 and CD8 positive cells in the

gray matter, with only the occasional lymphocyte seen in the white matter (Figure 3.15). Taken together, these observations suggest that there is an early, low-level infiltration of peripheral lymphocytes in the spinal cord, similar to that seen in the brain.

3.9 White matter pathology in *Ppt1*$^{-/-}$ mouse spinal cords

While there was no appreciable pathology observed in the white matter of *Ppt1*$^{-/-}$ mice brains (Bible et al, 2004), the differences in white matter volumes (Figures 3.1, 3.2), as well as progressive microglial activation within the white matter (Figure 3.14) of *Ppt1*$^{-/-}$ spinal cords suggested that there was previously undocumented pathology in the spinal white matter of these mice.

To study myelin changes, we stained selected cervical and lumbo-sacral sections at 1, 3, 5 and 7 month time points for luxol fast blue, a marker of myelin (Figure 3.16 A), but there was little observable difference between the genotypes, even at end-stage time points. Staining for myelin basic protein (MBP) revealed clusters of intense MBP immunoreactivity starting at 5 months in *Ppt1*$^{-/-}$ mouse cords at the cervical and lumbosacral levels, with a general disorganization of the distribution of MBP staining (Figure 3.16 B).

In order to study axonal changes, we stained spinal cord sections with an antibody against Neurofilament-H 200kD, and this revealed a decrease in staining intensity in *Ppt1*$^{-/-}$ mice at 7 months, with patches of markedly decreased staining in the dorsal and ventral funiculi, compared to wildtype controls (Figure3.16 C). This decrease in neurofilament-H staining intensity is consistent with axonal loss (Wujek et al, 2002). To further investigate this apparent axonal loss, semi-thin sections of & month old mice were stained with toluidine blue-O. This revealed similar findings to that seen in MBP staining, with *Ppt1*$^{-/-}$ mouse cords showing a general vacuolar disorganization of axon bundles. There were also many myelin dense bodies (MDB) scattered throughout the dorsal and ventral funiculi, similar to the axonal spheroids

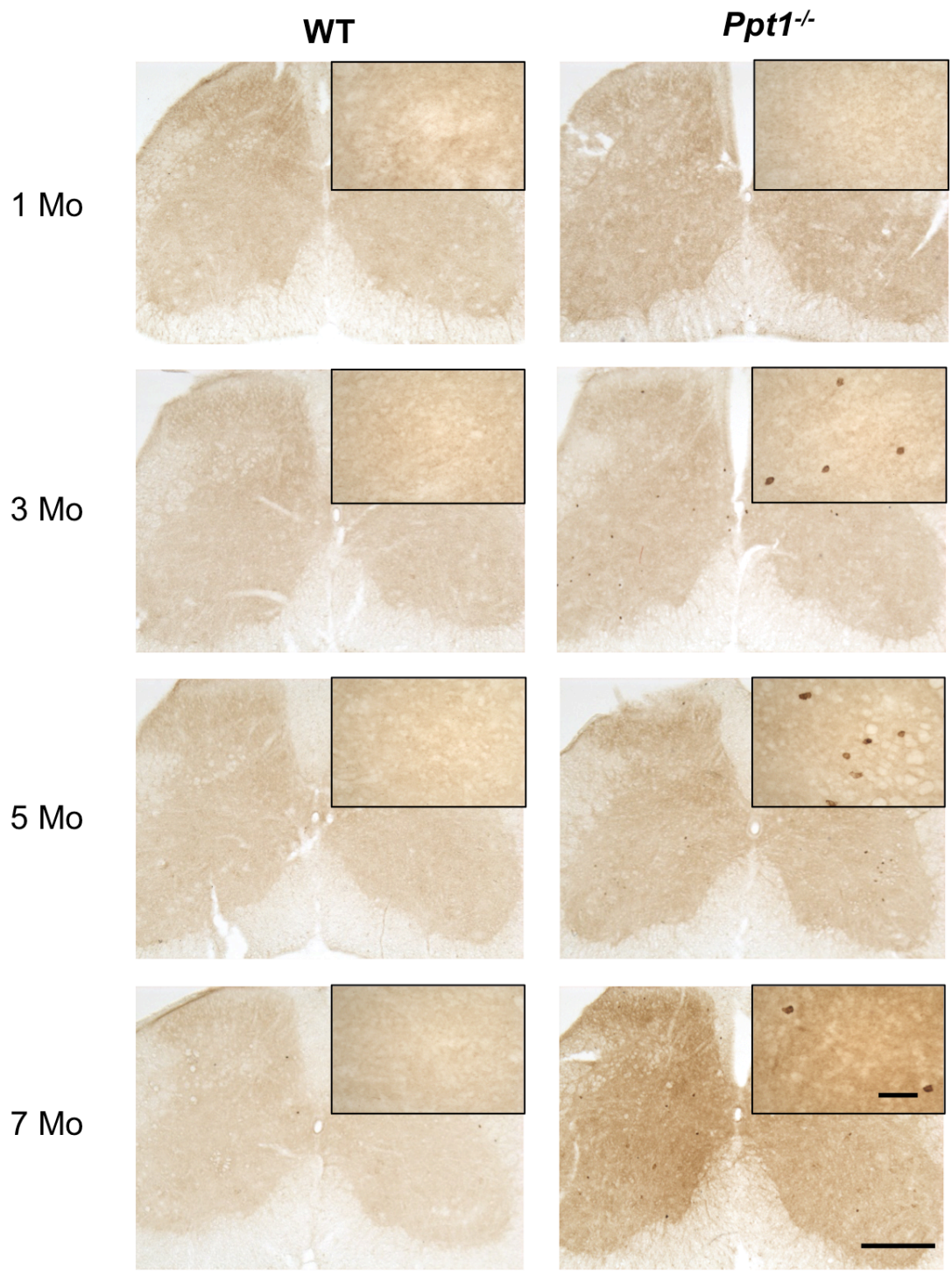

Figure 3.15 - Progressive lymphocyte infiltration activation of Ppt1$^{-/-}$ mouse spinal cords.

Representative images of lumbosacral spinal cord sections showing an increased abundance of CD4/CD8 positive cells in the gray matter of Ppt1 deficient (Ppt1$^{-/-}$) mice compared to wildtype (WT) cords, starting at 3 months. Scale bar = 200μm and 25μm (insert).

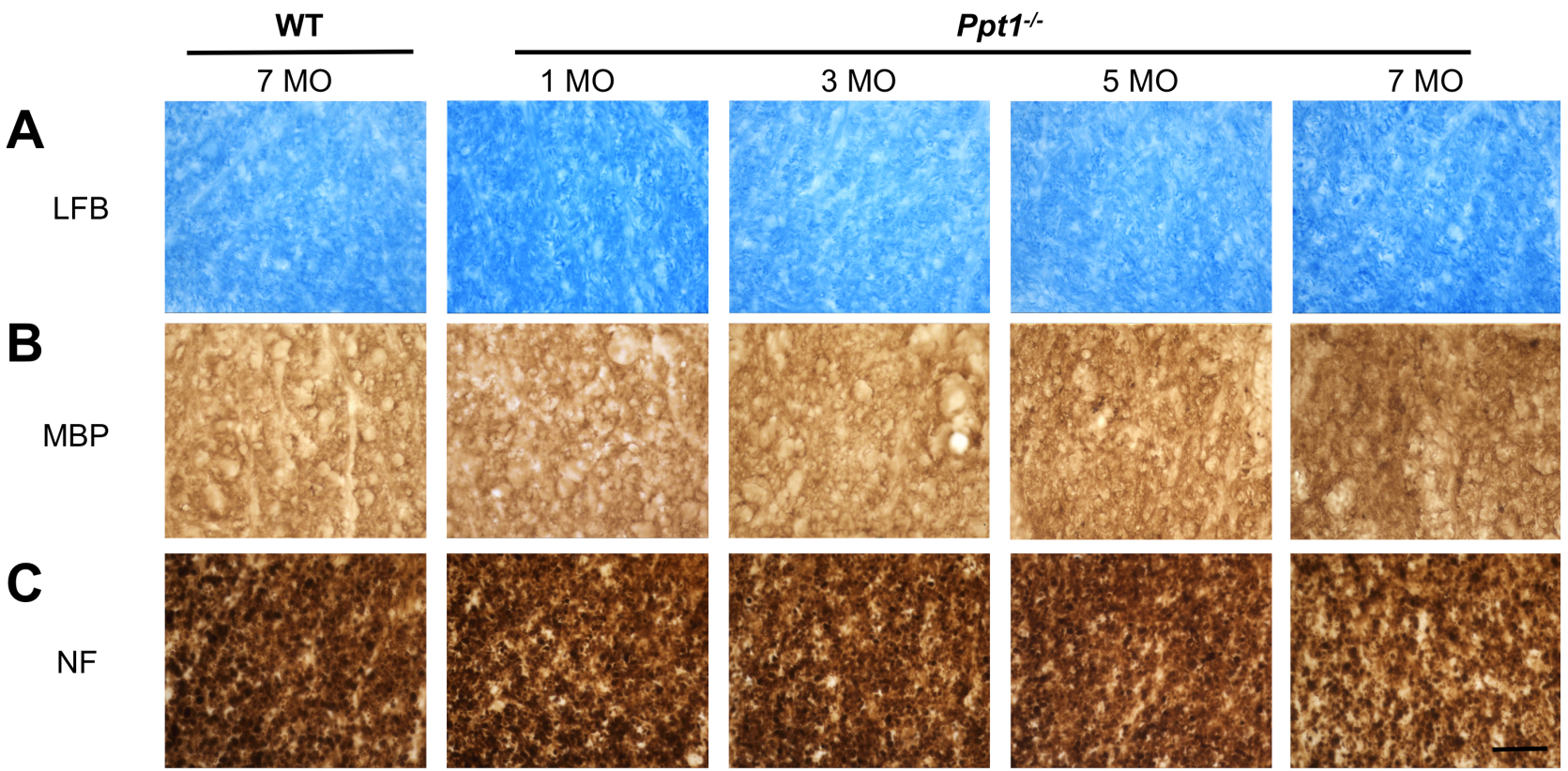

Figure 3.16 - White matter pathology in the Ppt1$^{-/-}$ mouse spinal cord.

*Representative images of sections of ventral funiculi of lumbosacral spinal cords stained for (**A**) Luxol Fast Blue (LFB) showing little difference between Ppt1 deficient (Ppt1$^{-/-}$) and wild type control (WT) mice at all ages; (**B**) Myelin Basic Protein (MBP) showing clusters of increased immunoreactivity in Ppt1$^{-/-}$ mice as early as 5 months of age and (**C**) Neurofilament-H 200kD (NF) displaying patches of markedly decreased immunoreactivity in Ppt1$^{-/-}$ mice at 7 months. Scale bar = 25µm.*

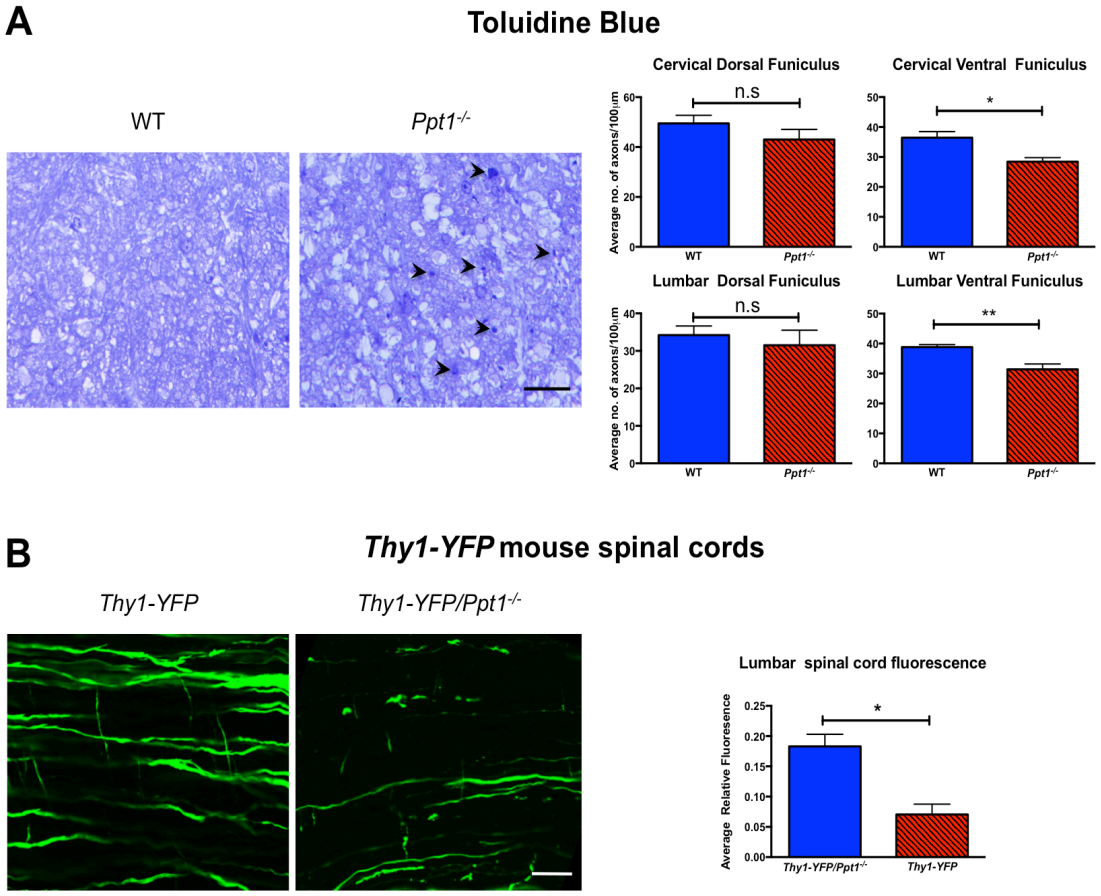

Figure 3.17 – Axon loss in the white matter of Ppt1$^{-/-}$ mouse spinal cords.

*(**A**) Representative images of the ventral funiculi of lumbosacral semi-thin spinal cord sections stained for Toluidine Blue showing general disorganization of axons (including apparent vacuolar degeneration, white spaces) along with Myelin Dense Bodies (Black arrows), scale bars = 20μm (Left). Line sampling of toluidine blue stained semi-thin sections showed a trend towards decreased axon density in the cervical and lumbosacral dorsal funiculi of Ppt1$^{-/-}$ mice, and a significant decrease in axon density in the corresponding ventral funiculi. *p<0.05, **p<0.01, two-tailed, unpaired parametric t-test (right). (**B**) Confocal images from the lumbosacral spinal cord of Thy1-YFP/Ppt1$^{-/-}$ mice reveal the marked loss of axons loss from the white matter of these mice compared to Thy1-YFP mice, in which many YFP-expressing axons were still present, scale bar = 100μm (left). Quantifying the amount of YFP signal present confirmed this loss to be significant. *p<0.053, two-tailed, unpaired parametric t-test. Scale bar = 100μm.*

observed in the optic nerve of these mice (Groh et al, 2013),which are a hallmark of axonal degeneration (Jeong et al, 2011)(Figure 3.17 A). Quantitative line sampling of these toluidine blue sections revealed a non-significant trend towards decreased axon density in the dorsal funiculi of both the cervical and lumbosacral cords of *Ppt1*$^{-/-}$ mice, but showed a significant decrease in axon density in the ventral funiculi of these regions (Figure 3.17 A). Analysis of longitudinal sections of *Thy1-YFP/Ppt1*$^{-/-}$ mouse spinal cords (Castelvetri et al, 2011; Feng et al, 2000) showed similar axonal blebs and gross axonal degeneration in these mice at 7 months, compared to the *Thy1-YFP* mice (Figure 3.17 B). Moreover, there was a significant ($p<0.05$) decrease in axonal fluorescence in the lumbar spinal cords (Figure 3.17 B)

Taken together these data, indicate the presence of significant pathology in the white matter of *Ppt1*$^{-/-}$ mouse spinal cords, which is a phenotype that has not been reported in the brain, other than the optic nerve (Groh et al., 2013).

3.10 Human CLN1 spinal cord pathology.

In an early study of human CLN1 disease, the spinal cord was described as not being as severely affected as the brain and cerebellum (Santavuori et al, 1974). However, histopathological analysis revealed the anterior horn cells of the spinal cord to be “distended” in appearance, presumably due to the accumulation of storage material (Haltia et al, 1973a; Santavuori et al, 1974). To determine whether the profound histopathological changes seen in the spinal cords of *Ppt1*$^{-/-}$ mice were also seen in human CLN1 disease, we obtained thoracic spinal cord tissue from a single 10-year old diseased case and an age-matched neurologically normal spinal cord. The tissues were sectioned and Nissl stained to examine their cytoarchitectural organization, and immunostained for CD68 to examine microglial activation. Additionally, confocal microscopy images were also obtained to look for the presence of autofluorescent storage material (Figure 3.18).

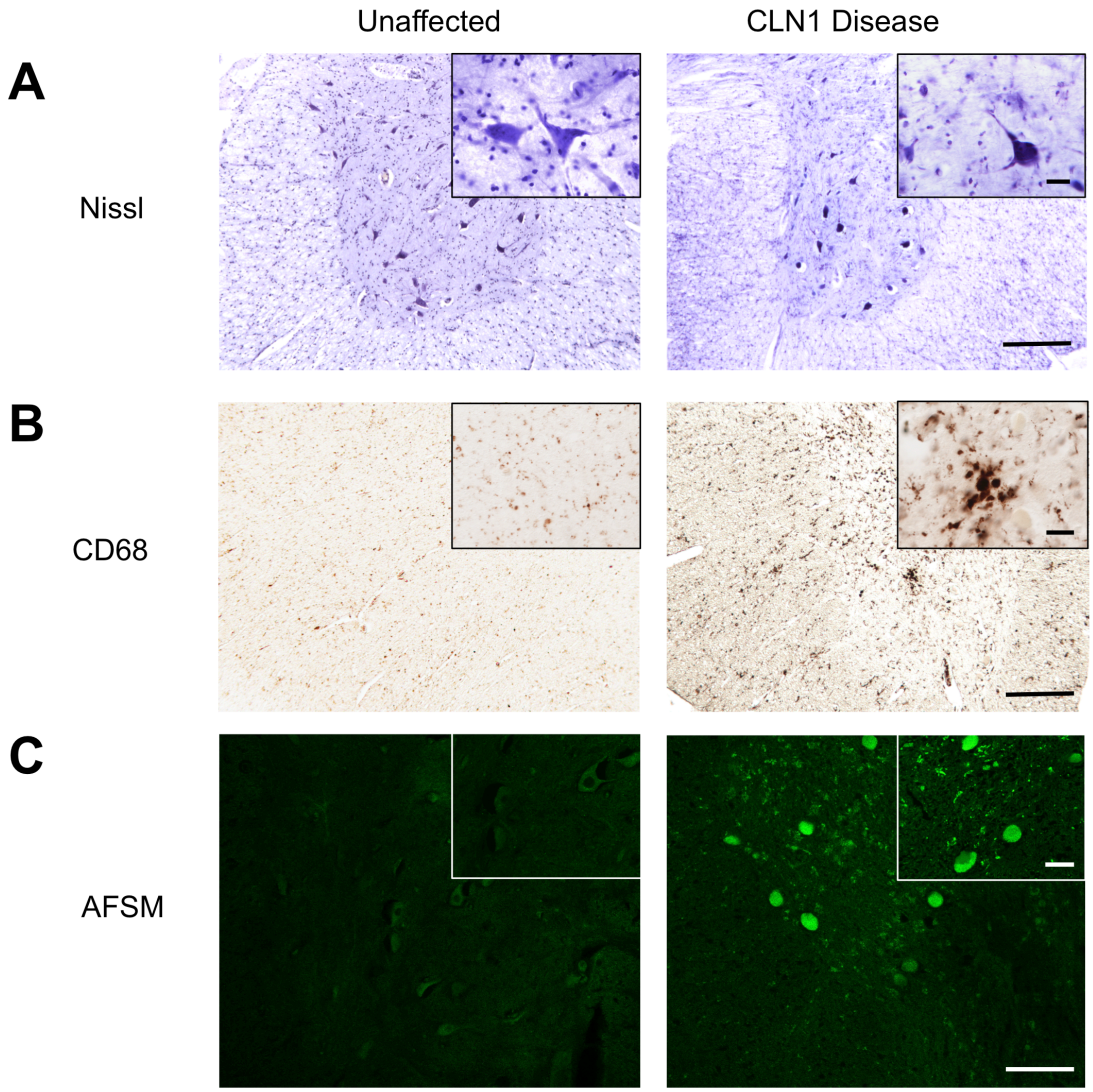

Figure 3.18 – Human CLN1 Disease spinal cord pathology.

*Representative images of ventral horns of human thoracic spinal cord showing fewer, more darkly Nissl stained neurons of CLN1 disease tissue in Nissl stained sections (**A**). CD68 stained sections showed increased abundance and hypertrophy of intensely immunoreactive microglia in CLN1 disease spinal cords (**B**). There was also pronounced accumulation of Autofluorescent Storage Material (AFSM) in persisting neurons in the gray matter of disease spinal cords (**C**). Scale bars = 100μm and 25μm (inserts).*

Examination of the human CLN1 tissue revealed similar end-stage pathology to that seen in *Ppt1*$^{-/-}$ mouse spinal cords. Nissl stained human CLN1 disease spinal cord sections revealed fewer neurons than in the control tissue. The neurons that were present displayed a range of morphologies with some that were intensely stained and shrunken, while others appeared distended and palely stained, presumably due to the accumulation of storage material (Figure 3.18 A). CD68 staining revealed an abundance of intensely stained, hypertrophied microglia that were often found in clumps. These activated microglia were largely present in the gray matter with a lesser number in the white matter (Figure 3.18 B). Lastly, confocal images of the human CLN1 disease spinal cords revealed intense accumulation of autofluorescent storage material in cells within the gray matter of the spinal cord. This storage material, as expected, was largely present in cells with a neuronal morphology, but some was also distributed in clusters within smaller cells, as seen before in *Ppt1*$^{-/-}$ mouse spinal cords (Chapter 3.11 b). Presumably, this is also due to the re-distribution of storage material to phagocytizing microglial cells (Figure 3.18 C).

These data indicate that there is indeed a pathological process occurring in human CLN1 disease spinal cords, similar to that seen in *Ppt1*$^{-/-}$ mouse spinal cords. This is significant as it shows that the spinal cord will need to be targeted by future therapies for this disease, in addition to the brain.

3.11 Spinal cord pathology in other NCL mouse models.

The NCLs are a group of lysosomal storage disorders with similar clinical presentations, but dissimilar etiology (Cooper, 2003; Jalanko & Braulke, 2009). Therefore, having observed early and profound pathology in the spinal cords of *Ppt1*$^{-/-}$ mice, we conducted a qualitative survey of other available mouse models of major forms of NCL.

Thoracic spinal cord tissue was available from *Tpp1*$^{-/-}$ mice, a model for CLN2 disease (Sleat et al, 2004) at 13.5 weeks and *Cln3*$^{-/-}$ mice amodel for CLN3 disease (Mitchison et al, 1999) at 12 months. Timepoints were chosen where

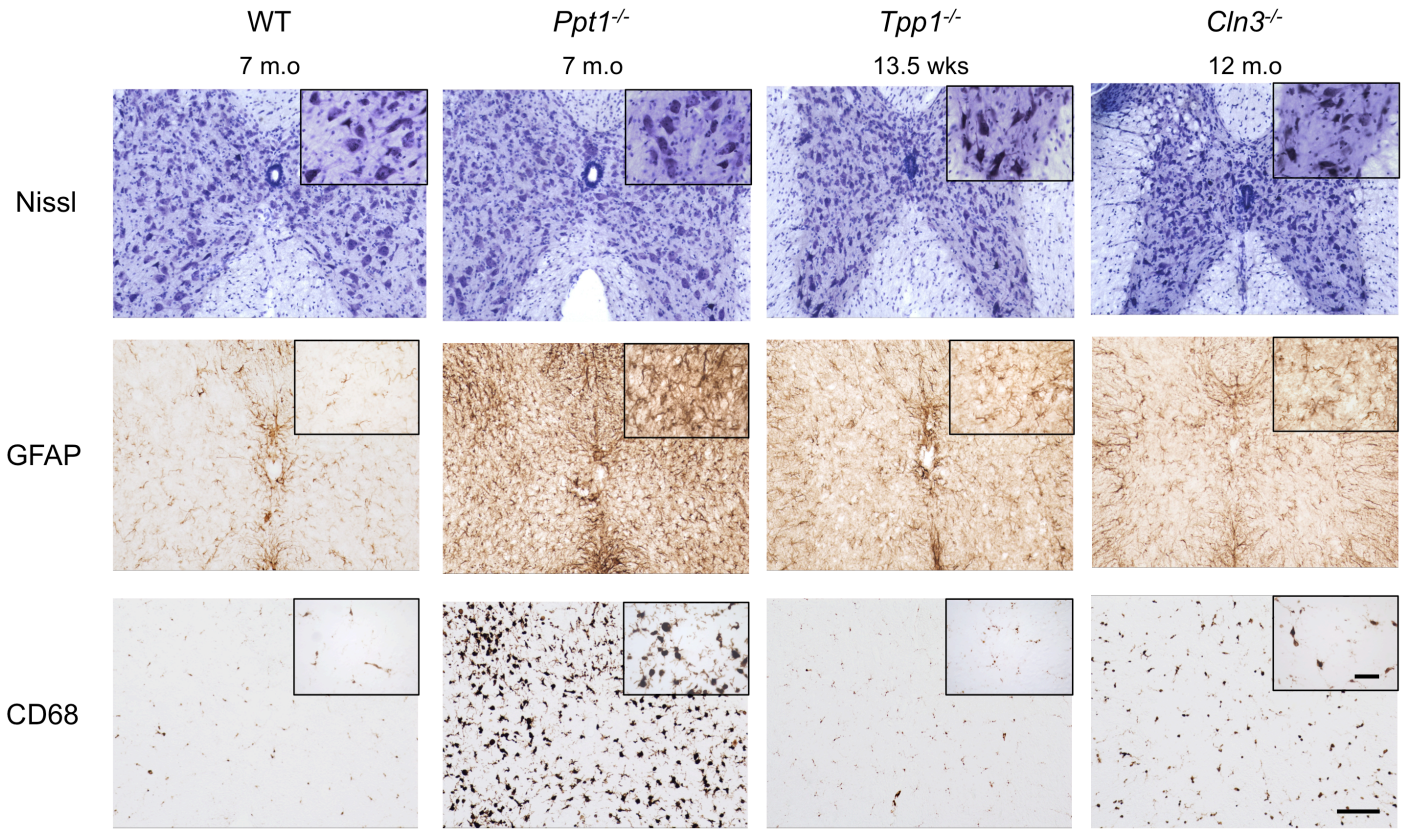

Figure 3.19 - Presence of spinal cord pathology in other mouse models of NCL.

Representative images of thoracic spinal cord sections from wild type control (WT), Ppt1 deficient ($Ppt1^{-/-}$, Cln1), Tpp1 deficient ($Tpp1^{-/-}$, Cln2) and Cln3 deficient ($Cln3^{-/-}$) mice. Nissl staining shows altered morphology of neurons in $Tpp1^{-/-}$ and $Cln3^{-/-}$ mice with intensely stained, shrunken neurons, a morphology dissimilar to that seen in both WT and $Ppt1^{-/-}$ mice. There was also a moderate level of astrocytosis in $Tpp1^{-/-}$ and $Cln3^{-/-}$ mouse spinal cords, which was more than was present in WT mice, but markedly less than in $Ppt1^{-/-}$ mice. $Cln3^{-/-}$ mouse spinal cords showed a low level of microglial activation

forebrain pathology was known to be present (Pontikis et al, 2004; Sleat et al, 2004). These samples were sectioned, Nissl stained and immunostained for CD68 and GFAP and compare to sections from *Ppt1*$^{-/-}$ and wildtype mice.

In the Nissl stained tissue, *Tpp1*$^{-/-}$ and *Cln3*$^{-/-}$ cord sections showed neurons that were deeply stained and pyknotic, a morphology that had not been seen in either the *Ppt1*$^{-/-}$ or the wildtype mice (Figure 3.19), indicating that there was indeed a pathology present in these tissue, but this may be dissimilar to that seen in *Ppt1*$^{-/-}$ mice.

Tpp1$^{-/-}$ and *Cln3*$^{-/-}$ mouse spinal cords also showed lower levels of astrocytosis in both the dorsal and ventral horns, compared to that seen in *Ppt1*$^{-/-}$ mice, but still higher than the wildtype control tissue. *Tpp1*$^{-/-}$ mouse spinal cords did not show any microglial activation, similar to the wildtype control, but the *Cln3*$^{-/-}$ mouse spinal cords displayed an increased level of microglial activation compared to the wildtype, but still lower than that seen in *Ppt1*$^{-/-}$ mice (Figure 3.19).

These observations provide the first evidence of the presence of spinal cord pathology in mouse models of NCL other than that for CLN1 disease. Although the nature, extent and timing of pathology may differ in these models, these data show that the spinal cord is a hitherto unexplored region of pathology, not just in CLN1 disease, but also in other forms of NCL and may be critically involved in disease progression.

3.12 Summary

Our analysis of *Ppt1*$^{-/-}$ mouse spinal cords has demonstrated a profound pathological process in this region of the central nervous system (CNS). The nature of this pathology is largely similar to that seen in the brains of these mice (Bible et al, 2004; Kielar et al, 2007; Macauley et al, 2009), showing overall atrophy (Figures 3.1, 3.2), severe neuronal loss (Figure 3.3-3.6), progressive accumulation of autofluorescent storage material (Figure 3.7), synaptic changes (Figure 3.10) and progressive glial activation (Figure 3.12-3.15). However, the spinal cord pathology observed crucially differs from that seen in the brain in

that these pathological features appear at an earlier timepoint in disease progression than in the forebrain and that they do not show any regional specificity in the spinal cord by occuring to similar extents at all levels of the cord (Kielar et al, 2007; Macauley et al, 2009). Furthermore, novel phenotypes of a possible postnatal developmental delay in the spinal cord (Figure 3.1, 3.2) and significant white matter pathology (Figures 3.16, 3.17) highlight that the nature of spinal cord pathology may differ to that in the forebrain. These data also raise the possibility that this newly-described spinal pathology may contribute to disease outcome in these mice.

Profound pathological changes were also shown in CLN1 human *post-mortem* spinal cord tissue, demonstrating that this spinal pathology is not just limited to the murine disease but is also present in human disease, making this region of the CNS a possible therapeutic target for future therapies. Lastly, the presence of pathological changes in the spinal cords of *Tpp1*$^{-/-}$ and *Cln3*$^{-/-}$ mice shows that this region may be affected in other forms of NCL, indicating the need to further investigate the role that spinal cord pathology plays in multiple NCLs.

CHAPTER 4. Altered gait in *Ppt1*$^{-/-}$ mice.

4.1 Introduction

Cases of human CLN1 disease initially present with muscle hypotonia, clumsiness and ataxia along with decelerated head growth in the first year, this is then followed by the irritability, visual loss and the development of epileptic seizures, together with the abnormal fine motor movements or hyperkinesias that are also characteristic of the disease (Dolisca et al, 2013; Williams et al, 2006; Wisniewski et al, 2001). Collectively, these findings suggest that the sensorimotor system is affected early in CLN1 disease progression.

Similarly, *Ppt1*$^{-/-}$ mice display a range of sensorimotor defects, with the initial study describing these mice demonstrating an abnormal clasping behavior in the tail-suspension test as well as reporting the lowering of the pelvis, splayed hindlimbs and an abnormal wobbling gait towards the later stages of disease progression (Gupta et al, 2001). In view of demonstrable cerebellar pathology in these mice, constant speed rotarod testing in these mice revealed a significant decrease in the latency of fall from 5 months onwards (Macauley et al, 2009). Recently, a broader behavioral characterization of both younger (1-3 month old) and older (5-7 month old) *Ppt1*$^{-/-}$ mice showed subtle changes in walking initiation and walking up a 60° inclined plane in younger mice, while older mice showed a wide array of motor deficits that affected their speed of movement and stride length as well demonstrating other cognitive deficits (Dearborn et al, 2015).

Having characterised early, progressive and profound spinal cord pathology in *Ppt1*$^{-/-}$ mice (Chapter I), we wished to detail gait deficits in these mice so as to gain a more comprehensive understanding of how Cln1 pathology affects the sensorimotor system in these mice. For this, we employed the *CatWalk XT* gait analysis system and software (Noldus, Wageningen, Netherlands). As previously described, this system allows for a detailed and relatively non-invasive study of gait in rodents (Hamers et al, 2006; Hamers et al, 2001; Kloos et al, 2005) (Chapter 2.3).

For this initial study of gait, we chose to study a group of *Ppt1*$^{-/-}$ and wildtype (C57BL/6) control mice (n=12) at monthly intervals between 1 and 7 months of age. Runs of mice were then analyzed using the *CatWalk XT 10.5* software (Noldus) to classify each footfall and produce results describing their gait. As previously stated (Chapter 1.5), there was no statistically significant difference in the overall body weights of *Ppt1*$^{-/-}$ and wildtype control mice at any age(Galvin et al, 2008). Therefore, all gait analysis parameters are reported without being normalized to the animals' respective body weights. showed that *Ppt1*$^{-/-}$ mice have a progressive motor deficit demonstrated by various measures of their gait that is similar to previous studies of motor function in these mice, but adds considerably more detail(Dearborn et al, 2015; Macauley et al, 2009). Furthermore, we also demonstrate an initial period when these mice move more quickly than wildtype controls, demonstrate a progressive lack of co-ordination of movement, as well as an increased reliance on fore-paws for locomotion in *Ppt1*$^{-/-}$ mice that have not previously been documented.

4.2 Decreased run speed in *Ppt1*$^{-/-}$ mice.

Various measures describing the speed of mice moving along the *CatWalk* (Noldus) runway demonstrated differences between *Ppt1*$^{-/-}$ and wildtype mice. Measurements of cadence, defined as the number of steps taken by a mouse per second (Hamers et al, 2001; Neumann et al, 2009) (Table 2.1), as well as the average speed were surprisingly higher in *Ppt1*$^{-/-}$ mice than wildtype mice at 2 months, but this was followed by lower measures for *Ppt1*$^{-/-}$ mice from three months onwards, reaching significance at 5 months (Figure 3.20). Conversely, the measures of the maximum speed variation in each run showed the opposite pattern to body speed, with *Ppt1*$^{-/-}$ mice showing lower variation at 2 months and higher variation at 4 months onwards, compared to their wildtype counterparts, which showed a trend towards decreased in variation with age (Figure 4.1).

Similar measures to the average speed were observed in the body speed measured for individual paws (Figure 4.2 A), while the speed variation for individual paws showed less difference between *Ppt1*$^{-/-}$ and wildtype mice paws

at 1, 2 and 6 months, as compared to the other time points, as that seen for maximum variation (Figure 4.2 B).

Taken together, these data suggest that at 2 months, *Ppt1*$^{-/-}$ mice move at a significantly faster pace with much less variation in speed than wildtype mice, but show a drastic reduction of speed and an increase in run variation from 3 moths onwards, with a significant difference seen as early as 4 months in the latter measure (Figure 4.2). This demonstrates that these mice have appreciable difficulty in movement as early as 3-4 months, which is the same time that initial neuron loss is observed in the spinal cord (Chapter 3.3).

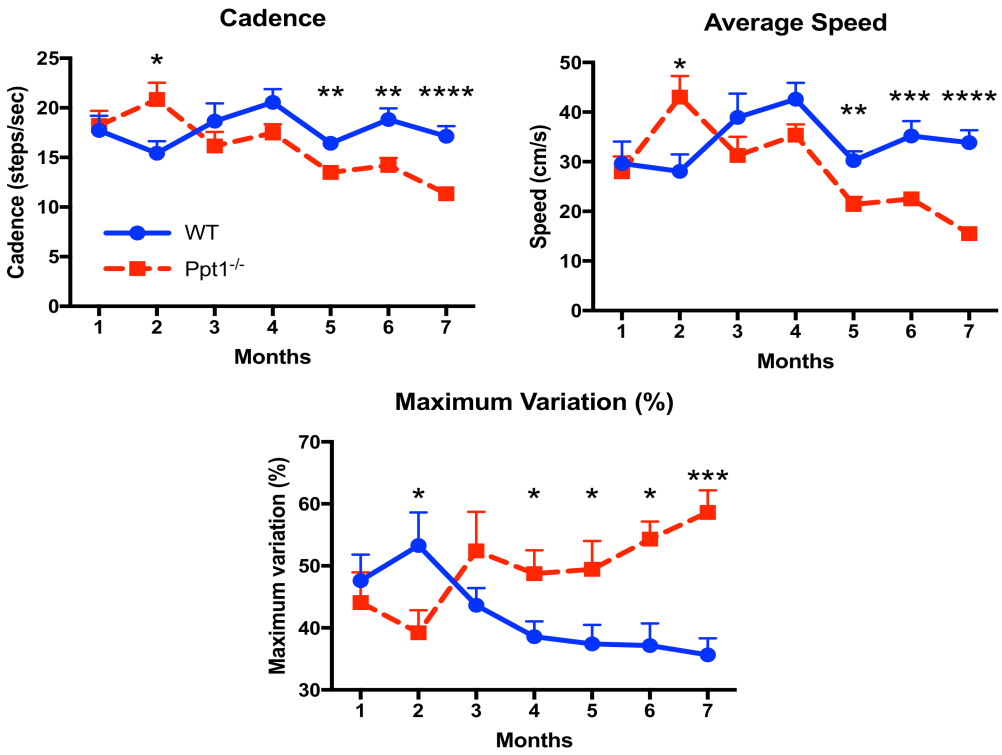

Figure 4.1 - Decreased speed and increased variation with advancing age in Ppt1$^{-/-}$ mice. *CatWalk XT (Noldus) measures of cadence and average run speed showing Ppt1 deficient (Ppt1$^{-/-}$) mice to have a higher rate of movement at 2 months, followed by decreased speeds from 3 months onwards, becoming significant at 5 months compared to age-matched wildtype (WT) mice. Maximum variation showed an opposite pattern with decreased values at 2 moths followed by significantly higher values starting at 4 months in Ppt1 deficient (Ppt1$^{-/-}$) mice, compared to wildtype mice, *p<0.05, **p<0.01, ***p<0.001, ****p<0.0001, two-tailed, unpaired parametric t-test. Values shown are continuous observations from each cohort at each time point as mean ± SEM. (n= 12 mice/group).*

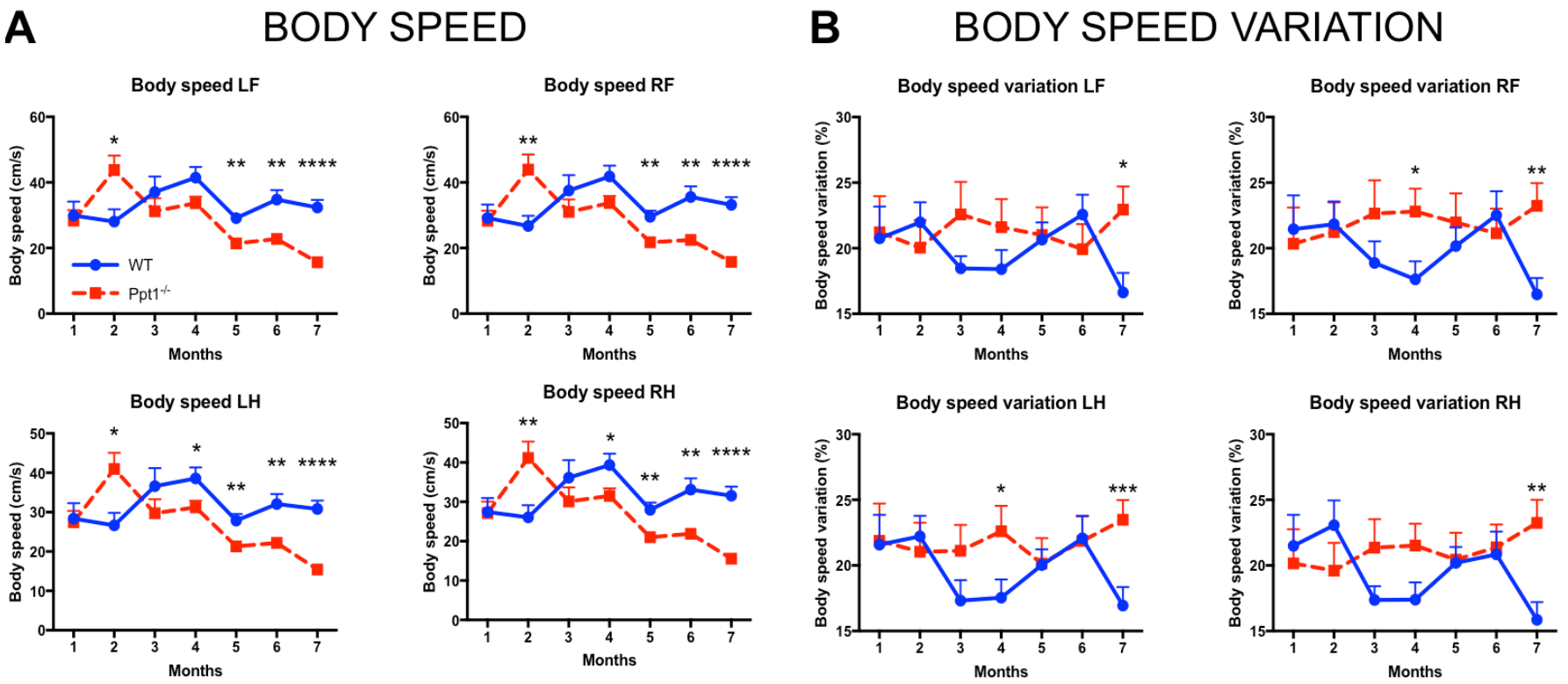

Figure 4.2 - Decreased body speed and increased average variation with advancing age in Ppt1$^{-/-}$ mice.

*CatWalk XT (Noldus) measures of body speed showing similar patterns as that of average speed values for individual paws. Increased speed of Ppt1 deficient (Ppt1$^{-/-}$) mice at 2 months and lower speed of these mice from 3 months onwards was seen in all paws compared to wildtype (WT) mice. Variation of body speed in each paw showed Ppt1 deficient (Ppt1$^{-/-}$) mice to have higher speed variation at 3,4 and 7 months in each paw, with most of these measures being significant compared to WT mice. *p<0.05, **p<0.01, ***p<0.001, ****p<0.0001, two-tailed, unpaired parametric t-test. Values shown are continuous observations from each cohort at each time point as mean ± SEM. (n= 12 mice/group).*

4.3 Measures of the step cycle.

Having observed significant differences in the body speed in *Ppt1*$^{-/-}$ mice, we then analyzed measures of the step cycle. The step cycle was defined as the time between two successive initial contacts of a given paw. This consisted of two phases – a) the stand, where the paw remains in contact with the plate, and b) the swing, where the paw is lifted off or is not in contact with the plate (Hamers et al, 2006; Hamers et al, 2001) (Table 2.1).

Measures comparing the step cycle and duty cycle (Figure 4.3) values for each paw showed that while *Ppt1*$^{-/-}$ mice had shorter step cycles and duty cycles consistent with their increased speed at 2 months, both their step and duty cycles showed higher values than wildtype mice from 3 months onwards, with forelimbs and hindlimbs showing significantly higher values from 5 months onwards (Figure 4.3A). These data show that, in accordance with changes in their speed, *Ppt1*$^{-/-}$ mice were successively spending less time at 2 months, and more time from 3 months onwards completing each step cycle. The duty cycle, which is the fraction of time standing in each step cycle (Table 2.1), also showed that this change in step cycle duration was in greater part due to the amount of time *Ppt1*$^{-/-}$ mice spent in contact with the plate, rather than in the swing phase (Figure 4.3B).

To confirm this, we individually analyzed the stand and swing time for each paw. This showed that the paws of *Ppt1*$^{-/-}$ mice uniformly spent significantly less time on the plate during a step cycle at 2 months, but more time on the plate per step cycle from 3 months onwards, with stand times being significantly higher from 5-7 months in all paws, as compared to wildtype mice (Figure 4.4A). Stand index, a measure of the paw transitioning between stand and swing phases, showed a similar pattern with *Ppt1*$^{-/-}$ mice displaying significantly lower values at 2 months in all paws, followed by significantly higher values from 3 months onwards in the right hind paw, and in all limbs from 5 months onwards compared to age-matched wildtype control mice (Figure 4.4B).

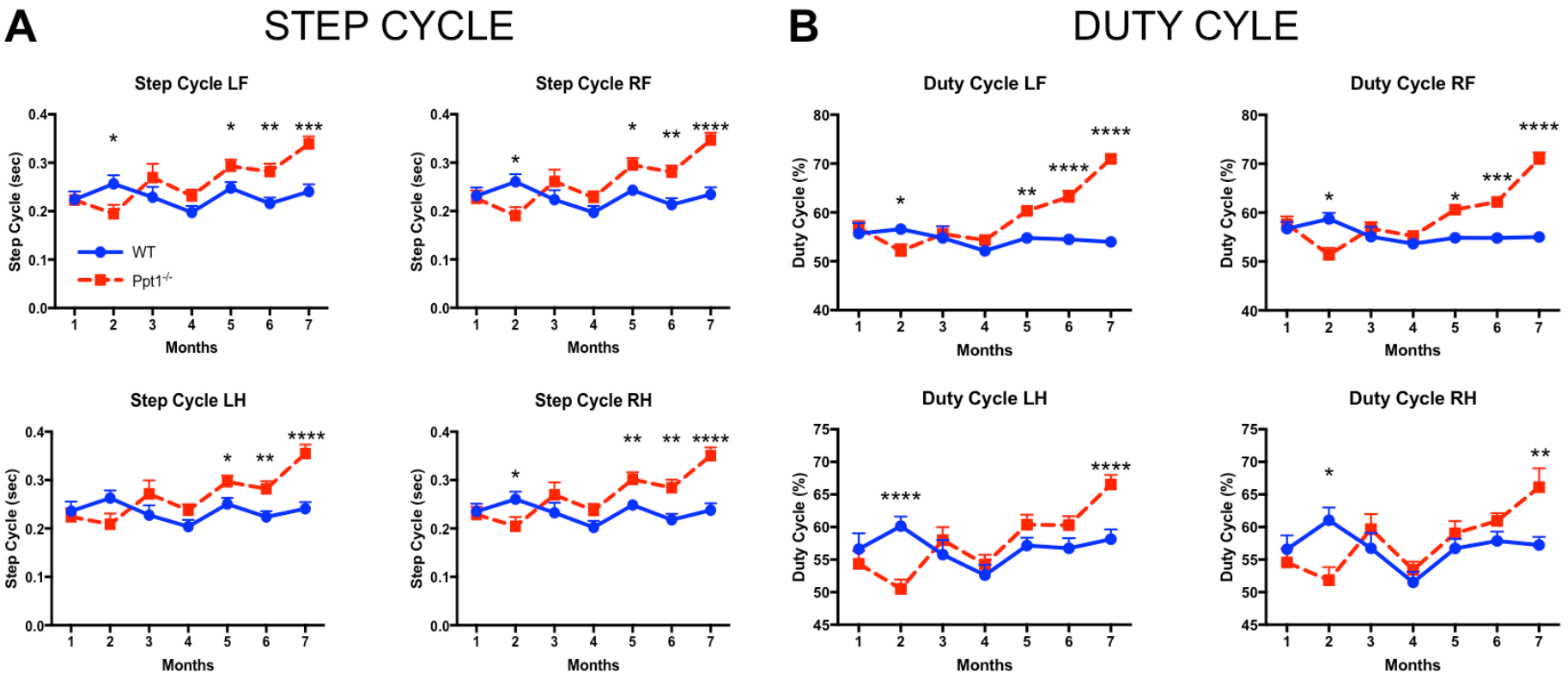

Figure 4.3 - Varying duration of walking cycles in Ppt1$^{-/-}$ mice.

*CatWalk XT (Noldus) measures of step cycle (**A**) show 2-month Ppt1 deficient (Ppt1$^{-/-}$) mice take shorter time to complete a cycle, but a longer time from 5 months onwards, compared to wildtype (WT) mice. The duty cycle (**B**) measures show that these increased times are mainly due to a variation in the time these mice spend in contact with the plate. *p<0.05, **p<0.01, ***p<0.001, ****p<0.0001, two-tailed, unpaired parametric t-test. Values shown are continuous observations from each cohort at each time point as mean ± SEM. (n= 12 mice/group).*

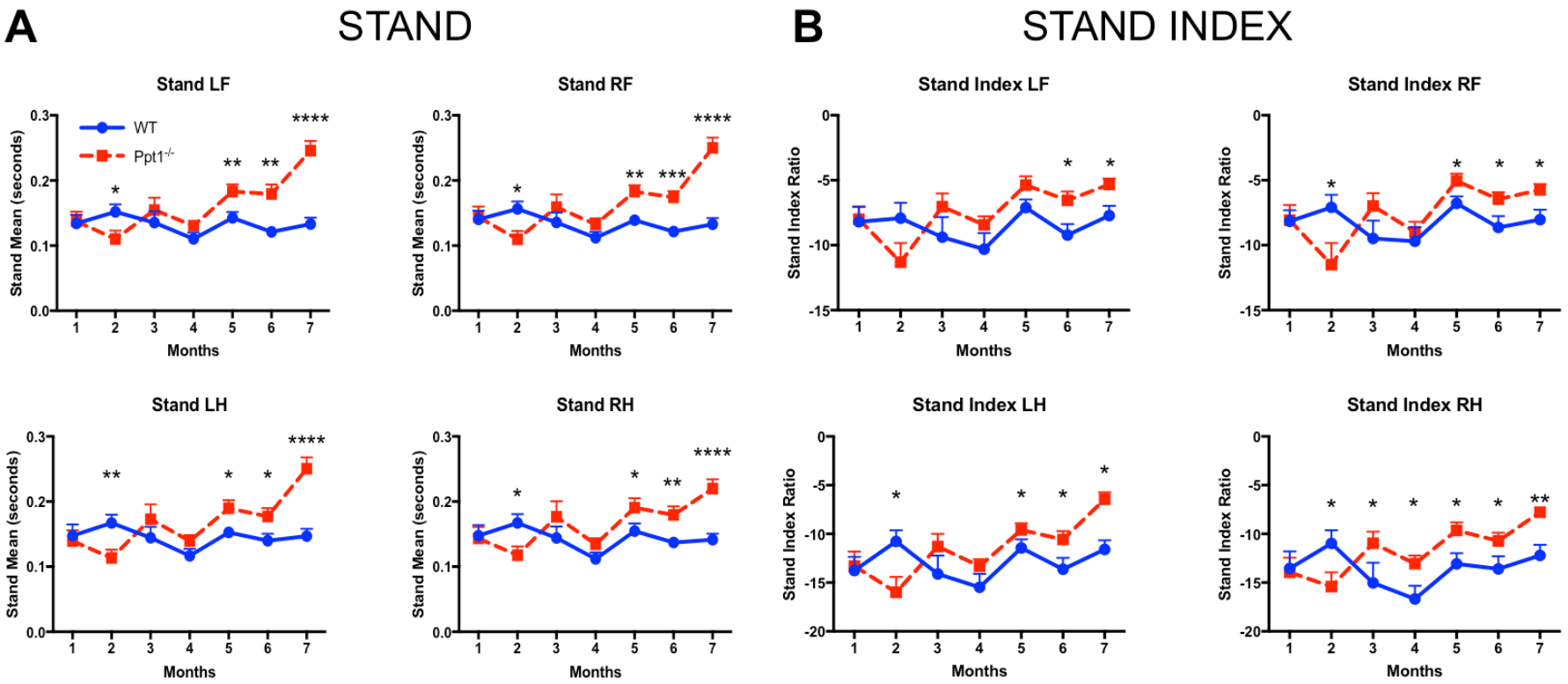

Figure 4.4 - Measures of stand in Ppt1$^{-/-}$ mice.

*CatWalk XT (Noldus) measures of the stand phase (**A**) showing that 2-month Ppt1 deficient (Ppt1$^{-/-}$) mice spend less time, but more time from 5 months onwards in contact with the plate compared to wildtype (WT) mice. Stand index (**B**) shows a similar pattern to stand for the transition between stand and swing. *p<0.05, **p<0.01, ***p<0.001, ****p<0.0001, two-tailed, unpaired parametric t-test. Values shown are continuous observations from each cohort at each time point as mean ± SEM. (n= 12 mice/group).*

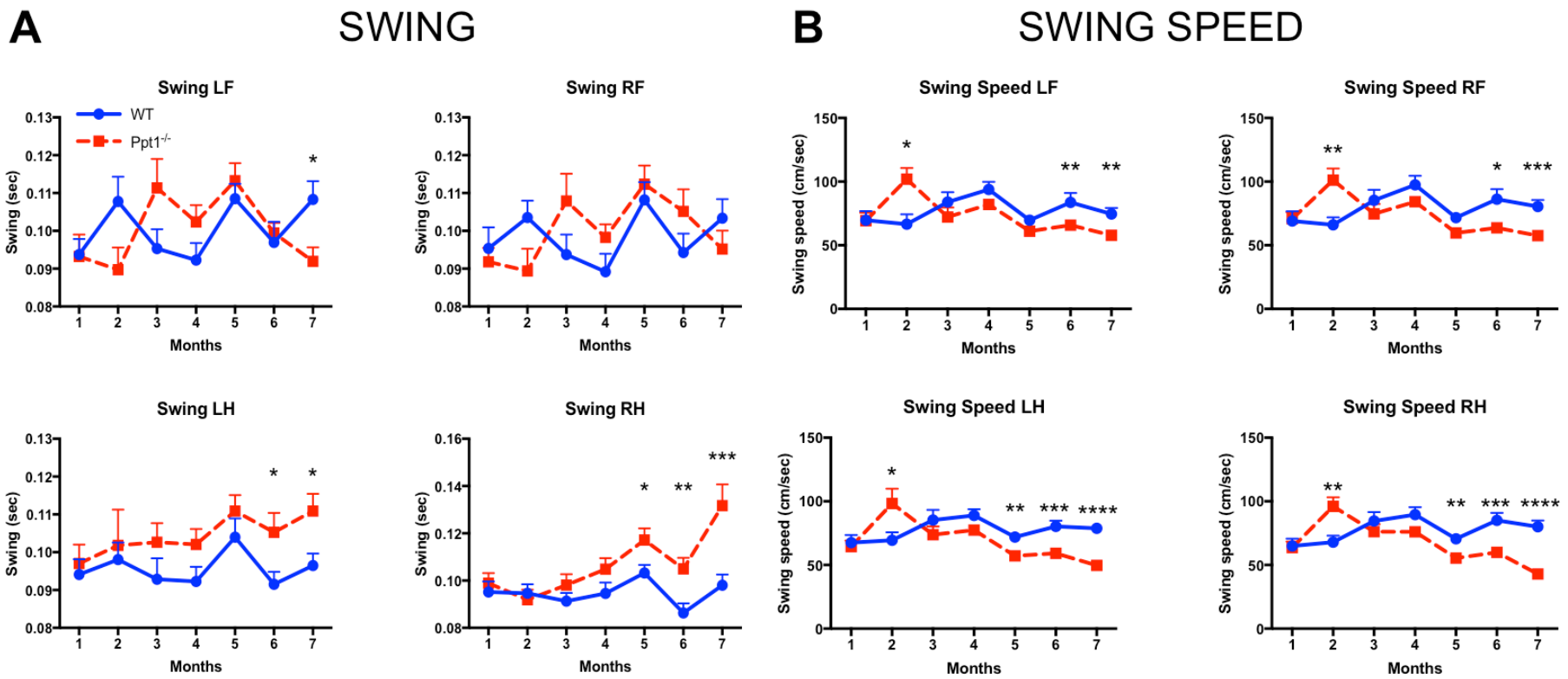

Figure 4.5 - Measures swing and swing speed in Ppt1$^{-/-}$ mice.

*CatWalk XT (Noldus) measures of the swing (**A**) is more affected in the hindlimbs than in forelimbs in Ppt1$^{-/-}$ as compared to WT mice; while swing speed (**B**) is increased at 2 months, and decreased from 5 months onwards in Ppt1$^{-/-}$ compared to WT mice. *p<0.05, **p<0.01, ***p<0.001, ****p<0.0001, two-tailed, unpaired parametric t-test. Values shown are continuous observations from each cohort at each time point as mean ± SEM. (n= 12 mice/group).*

These data confirmed observations in the duty cycle, in that *Ppt1*$^{-/-}$ mice spend a greater amount of time during a step cycle with their paw in contact with the ground (or plate) after 3 months of age, a common feature in spinal cord injury and disease (Hamers et al, 2006; Hamers et al, 2001).

Measures of the swing phase showed no significant difference between genotypes in the fore paws until 7 months, where *Ppt1*$^{-/-}$ mice had lower swing times, especially in the left front (LF) paws. However, the hind limbs, showed a consistent trend of longer swing times from 3 months onwards, with significantly higher values from 5 months, as compared to wildtype mice (Figure 4.5 A). Furthermore, *Ppt1*$^{-/-}$ mice had a significantly higher swing speed at 2 months followed by consistently lower speeds from 3 months onwards, as compared to wildtype mice. These values were significantly lower from 5 months onwards in the hind limbs and 6 months onwards in the fore limbs (Figure 4.5 B). These data suggest that, while the overall movement of limbs at 2 months is faster in *Ppt1*$^{-/-}$ mice, they subsequently take more time to move their hindlimbs than their forelimbs from 3 months onwards. These data, along with the stand phase data show that *Ppt1*$^{-/-}$ mice may support themselves more with their forelimbs than their hindlimbs during a step cycle from 3 months onwards.

4.4 Individual paw measurements

We next analyzed how the mice of both genotypes were placing their paws on the glass plate, by measuring the length, width and area of each footfall. Measurements of print length showed an increase in *Ppt1*$^{-/-}$ mice at 2 and 4 months compared to the wildtype mice in the fore paws, while the hind paws did not show much variation between genotypes until 6-7 months, when *Ppt1*$^{-/-}$ mice showed a decreased print length, compared to wildtype mice (Figure 4.6 A). Measurements of print width, however, showed an increase in the width of fore paw prints at 2, 6 and 7 months in *Ppt1*$^{-/-}$ mice, but an opposite decrease in width at 6 and 7 months in their hind paws, with the exception of the 3 month time point in the right hind paw, which showed a higher print width (Figure 4.6 B). Overall, these data imply that *Ppt1*$^{-/-}$ mice have wider and longer forepaw prints at two months, when they also appear to move faster, while they continue to

make wider fore paw prints with narrower hind paw prints with disease progression, presumably because they rely more on their fore paws for support. This supports the data obtained from the measures of swing and swing speed (Figure 4.5).

Following from the higher print length and width of *Ppt1*$^{-/-}$ mouse fore paws at 2 months (Figure 4.6 A, B), their print areas were also predictably higher than wildtype mice at this time point, with little variation in hind paw values (Figure 4.7 A). From 3 months onwards, there were varying values of print areas between genotypes for all paws, with the hind paws consistently showing significantly reduced areas at 6 and 7 months, as was seen for the measures of print length and width. Similar data were also obtained when analyzing the maximum contact area (Figure 4.7 B), as were found for the average paw print areas (Figure 4.7 A).

From the individual paw measures, the stride lengths for each limb were measured as the distance between two contacts of the same paw (Table 2.1). This analysis revealed a significant increase in stride length in *Ppt1*$^{-/-}$ mice at 2 months for all limbs, consistent with their increased speed, decreased step cycle and stand phase (Figures 4.1, 4.3, 4.4). A significant decrease in stride length was subsequently observed in all limbs of *Ppt1*$^{-/-}$ mice, starting as early as 5 months (Figure 4.8). This is consistent with the findings of decreased stride length in older *Ppt1*$^{-/-}$ mice (Dearborn et al, 2015).

Measurements of paw intensities as described above (Chapter 2.3)(Figure 2.2) (Table 2.1), showed little variation of the basal minimum intensities over time between genotypes. The only exceptions were the increased minimum intensities at the oldest 7 month time point in the hind paws of *Ppt1*$^{-/-}$ mice, presumably due to the significantly reduced area of contact in these paws (Figure 4.9A). Similarly, the left front paws higher minimum intensities,

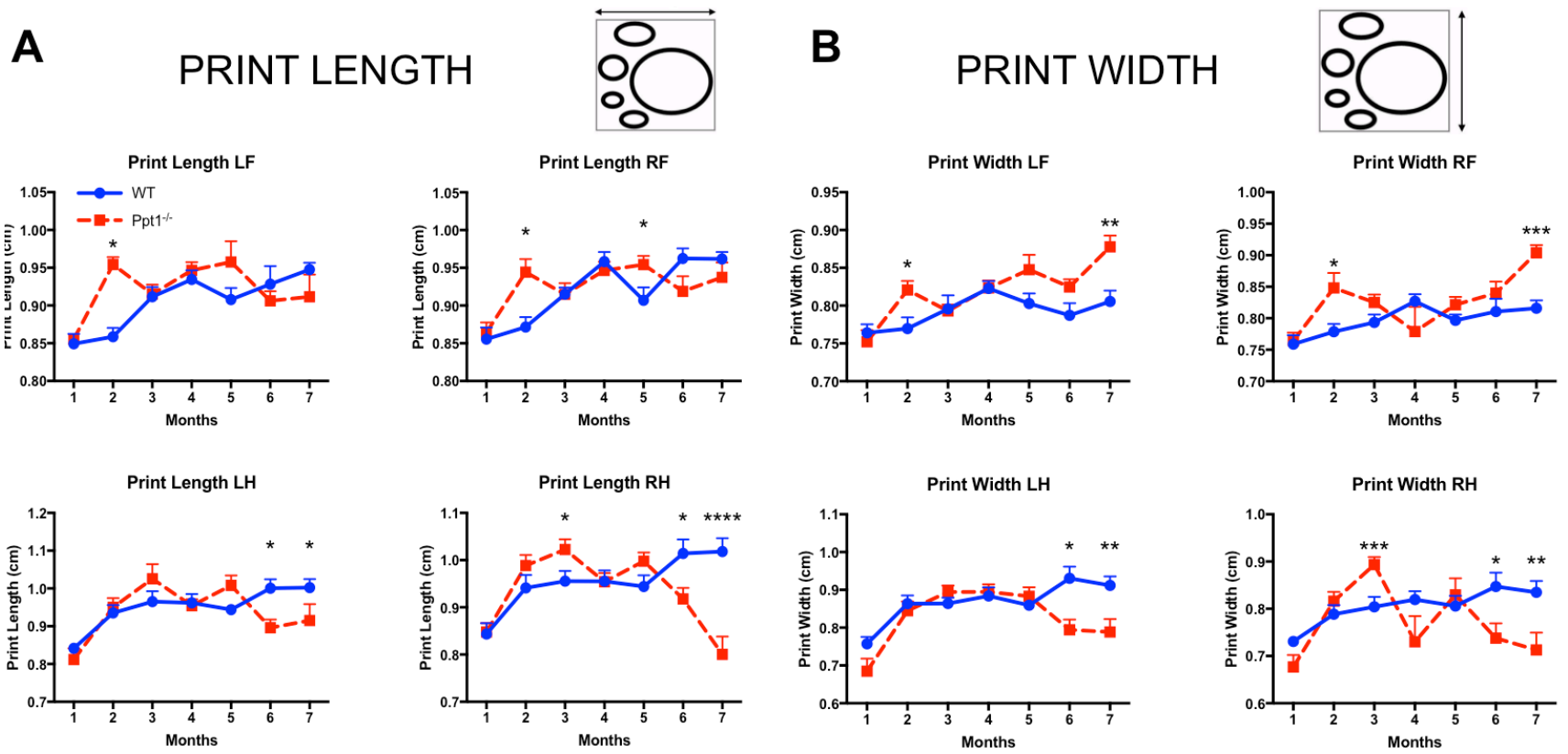

Figure 4.6 - Varying paw measures in Ppt1$^{-/-}$ mice.

*CatWalk XT (Noldus) measures of print length (**A**) and print width **(B)** showing that overall, Ppt1 deficient (Ppt1$^{-/-}$) mice relied more on their forelimbs as compared to wildtype (WT) mice. Evidenced by increased print length and width in the fore paws compared to decreases of these measures in the hind paws. *p<0.05, **p<0.01, ***p<0.001, ****p<0.0001, two-tailed, unpaired parametric t-test. Values shown are continuous observations from each cohort at each time point as mean ± SEM. (n= 12 mice/group).*

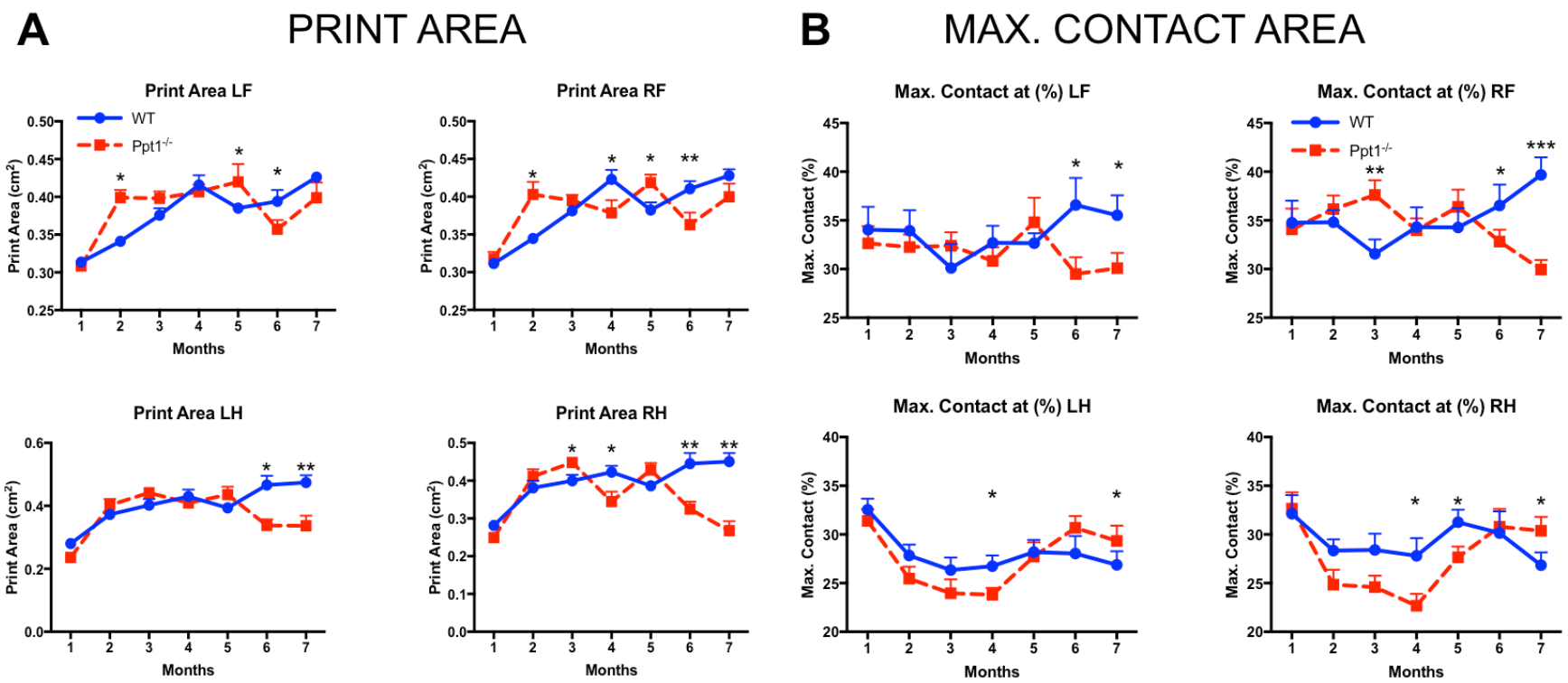

Figure 4.7 - Varying paw area measurements in Ppt1$^{-/-}$ mice.

*CatWalk XT (Noldus) measures of mean print area (**A**) and maximum print area (**B**) showed a similar pattern to print length and width measures of increased Ppt1$^{-/-}$ mice fore paw areas at 2 months and decreased hind paw areas at 6 and 7 months. Maximum contact area was also reduced in the forepaws at 6 and 7 months. *p<0.05, **p<0.01, ***p<0.001, ****p<0.0001, two-tailed, unpaired parametric t-test. Values shown are continuous observations from each cohort at each time point as mean ± SEM. (n= 12 mice/group).*

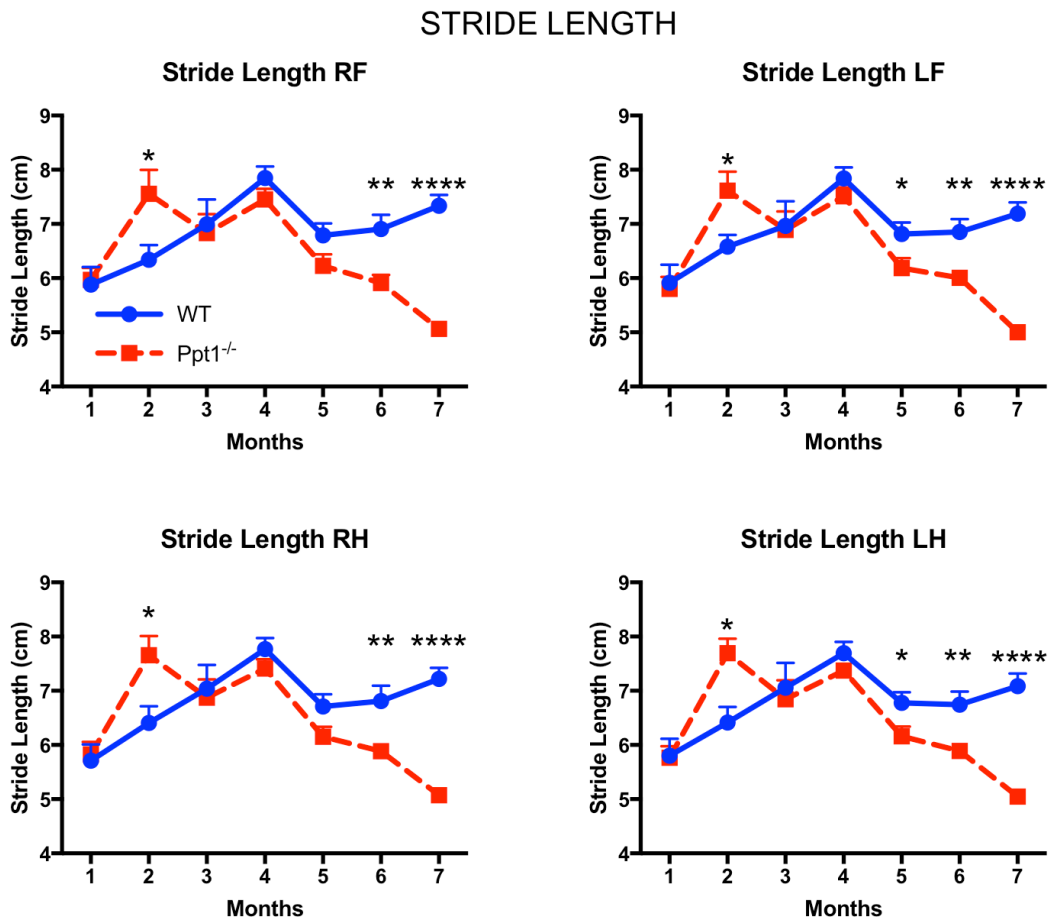

Figure 4.8 - Altered stride length in Ppt1$^{-/-}$ mice.

*CatWalk XT (Noldus) measures of stride length showed that 2 month old Ppt1 deficient (Ppt1$^{-/-}$) mice had a longer stride length for all limbs, as compared to wildtype mice (WT), while having significantly shorter strides in all limbs as early as 5 months onwards. *p<0.05, **p<0.01, ****p<0.0001, two-tailed, unpaired parametric t-test. Values shown are continuous observations from each cohort at each time point as mean ± SEM. (n= 12 mice/group).*

possibly due to these mice's apparent increased reliance on these limbs (Figure 4.9A). *Ppt1$^{-/-}$* mice also showed an increase in maximum intensity of the right front paw at 2 months compared to wildtype mice, again possibly due to increased reliance on their fore limbs. However, these mice subsequently showed a decrease in maximum intensities for all limbs at 6 and 7 months, consistent with neurological disease or spinal cord injury (Hamers et al, 2006; Starkey et al, 2005) (Figure 4.9 B). A similar decrease of mean intensities was observed at 6 and 7 months in all limbs of *Ppt1$^{-/-}$* mice, compared to wildtype mice (Figure 4.10 A).

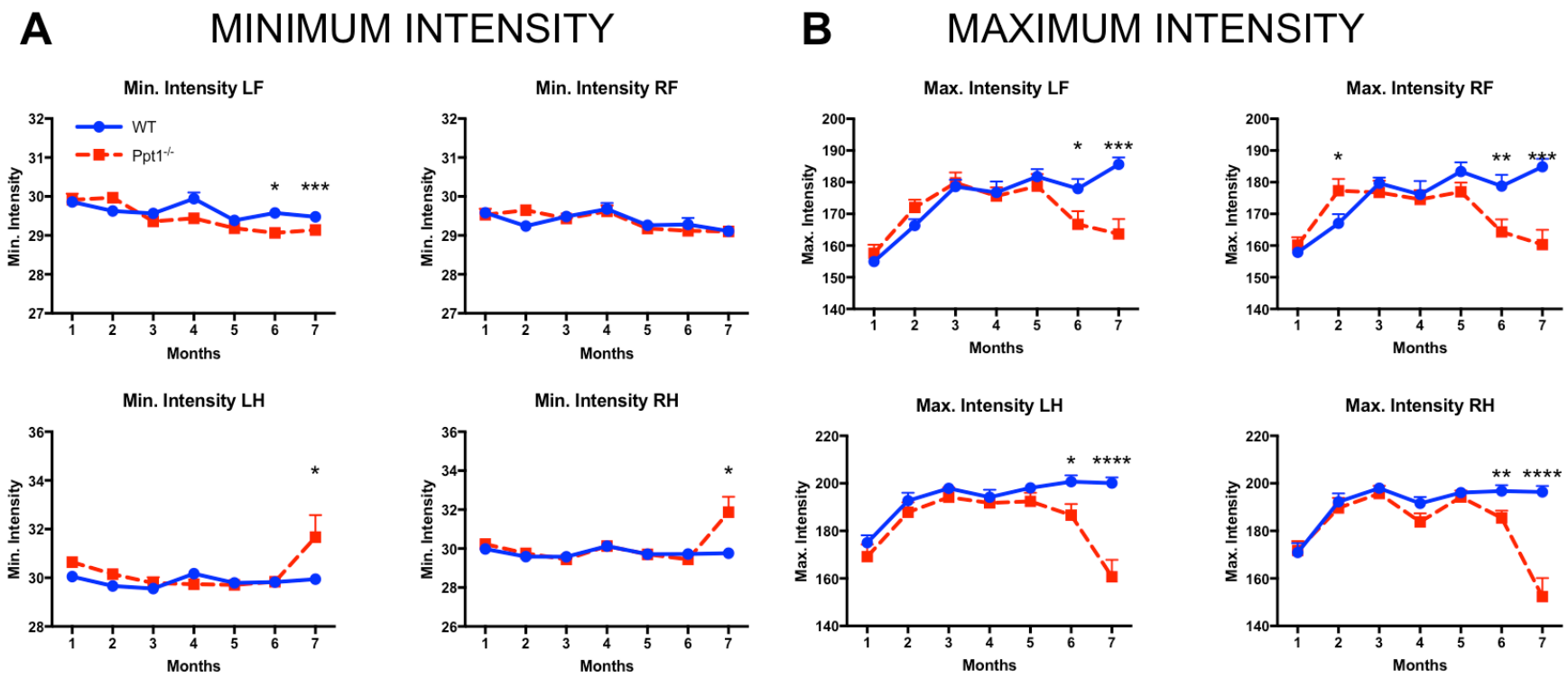

Figure 4.9 - Altered minimum and maximum paw intensities in Ppt1$^{-/-}$ mice.

*CatWalk XT (Noldus) measures of minimum intensity (**A**) show little variation until 6 months after which Ppt1 deficient (Ppt1$^{-/-}$) mice having significantly higher values than wildtype (WT) mice. Ppt1$^{-/-}$ mice have decreased maximum (**B**) paw intensities in all limbs at 6 and 7 months compared to WT mice. *p<0.05, **p<0.01, ***p<0.001, ****p<0.0001, two-tailed, unpaired parametric t-test. Values shown are continuous observations from each cohort at each time point as mean ± SEM. (n= 12 mice/group).*

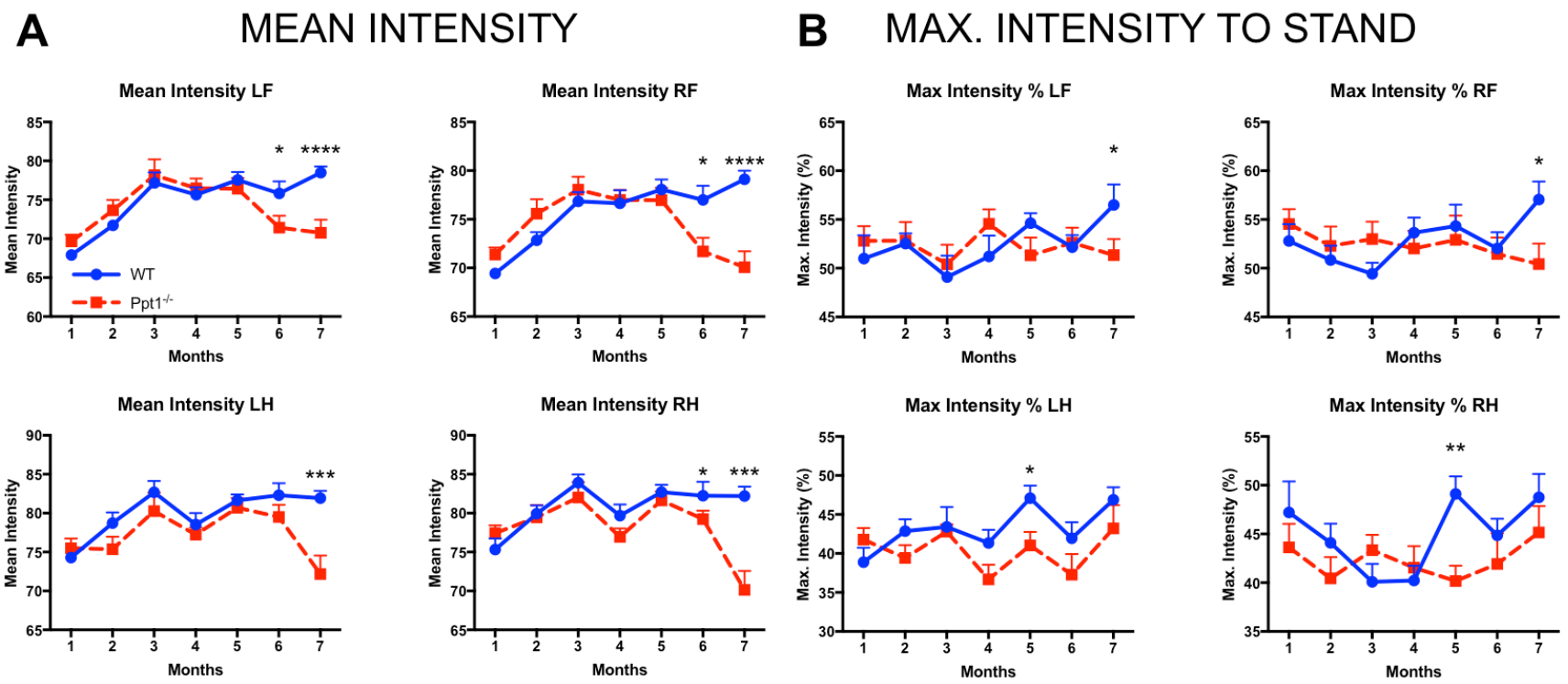

Figure 4.10 - Altered mean paw intensity and intensity relative to stand in Ppt1$^{-/-}$ mice.

*CatWalk XT (Noldus) measures of mean (**A**) paw intensities in all limbs at 6 and 7 months compared to WT mice, while they show lower ratios of maximum intensity relative to stand (**B**) in the fore paws and hind paws at 7 and 5 respectively. *p<0.05, **p<0.01, ***p<0.001, ****p<0.0001, two-tailed, unpaired parametric t-test. Values shown are continuous observations from each cohort at each time point as mean ± SEM. (n= 12 mice/group).*

However, the measure of maximum intensity relative to the stand phase (Table 2.1), only became significantly different at 7 months in the fore paws, and at 5 months in the hind paws, for which the wildtype mice fared significantly better than the *Ppt1*$^{-/-}$ mice (Figure 4.10 B). This data shows that the variations in paw intensities are consistent with the changes observed in the stand phase.

4.5 Measures of stance and support

Having shown initial evidence that *Ppt1*$^{-/-}$ mice seem to have altered values for placing their feet in contact with the plate in a step cycle (as revealed by their duty cycle, stand and stand index measures, Figures 4.3, 4.4), we then looked at measures of stance and support. Stance, describes the duration of contact of two paws in a step cycle (Table 2.1), and this data is then classified as either – a) single stance - where a single paw is in contact with the plate, b) initial dual stance – where both fore or hind paws are in contact with the plate at the start of a step cycle, or c) terminal dual stance – where both fore or hind paws are in contact with the plate at the end of a step cycle (Coulthard et al, 2002; Coulthard et al, 2003).

This analysis revealed that *Ppt1*$^{-/-}$ mice had significantly less single and initial dual stance durations at 2 months compared to wildtype mice, however, their initial and terminal dual stance times significantly increased from 5 months onwards, compared to wildtype mice (Figure 4.11). These data suggest that *Ppt1*$^{-/-}$ mice have greater difficulty moving without additional support from the contralateral limb with advancing age, which has been previously reported qualitatively (Gupta et al, 2001). Further analysis of the base of support (BOS) as the average distance between contralateral fore and hind paws showed a consistent trend towards higher BOS values in *Ppt1*$^{-/-}$ mouse fore limbs as early as 3 months, as compared to wildtype mice, with significantly higher values at 4 and 7 months. However, their hindlimbs only showed a significant increase in BOS at 6 and 7 months, compared to wildtype mice (Figure 4.12). This supports the notion that *Ppt1*$^{-/-}$ mice are more reliant on their fore paws to stabilize themselves while moving from an early age, as also shown by similarly altered measures of swing and print width (Figures 4.5, 4.6).

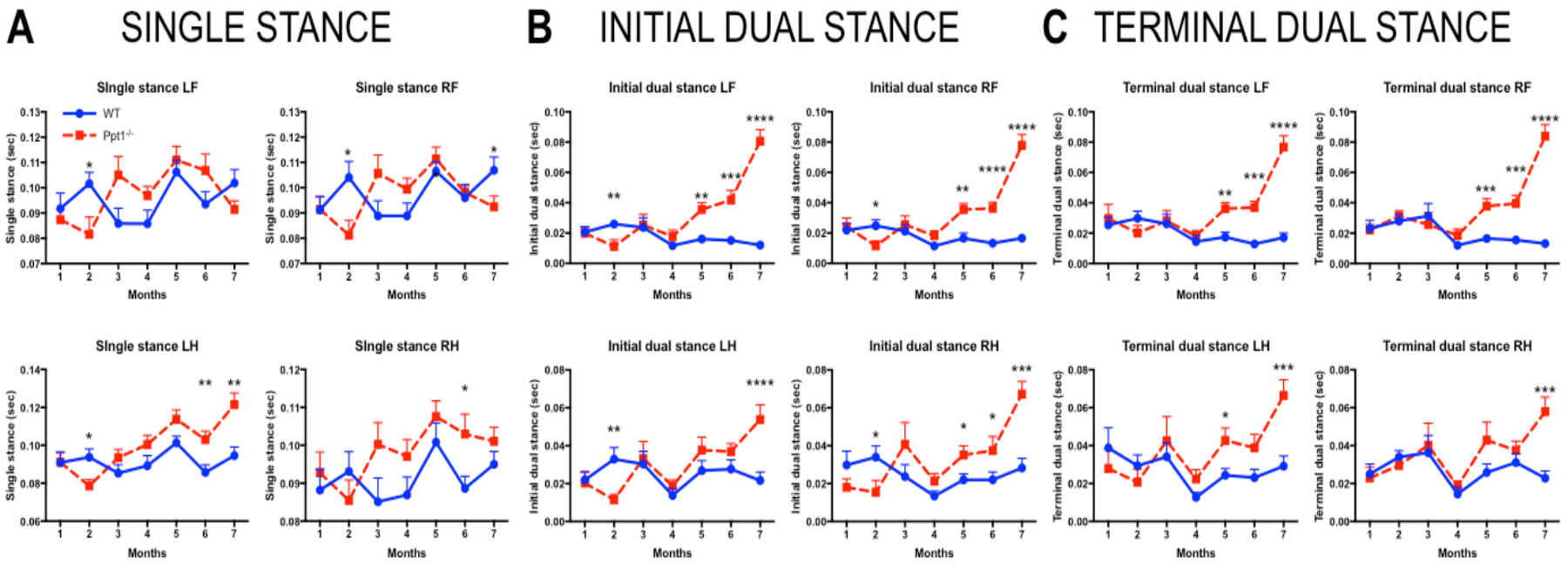

Figure 4.11 - Altered hind paw stance in Ppt1$^{-/-}$ mice.

*CatWalk XT (Noldus) measures of stance that Ppt1 deficient (Ppt1$^{-/-}$) mice had a shorter single stance (**A**) at 2 and 7 months compared to wildtype (WT) mice in forelimbs, and longer single stance at 6 and 7 months in the hind limbs. Ppt1$^{-/-}$ mice had reduced initial dual stance (**B**) at two months, and increased initial and terminal dual stance (**C**) from 5 months onwards. *p<0.05, **p<0.01, ***p<0.001, ****p<0.0001, two-tailed, unpaired parametric t-test. Values shown are continuous observations from each cohort at each time point as mean ± o SEM. (n= 12 mice/group).*

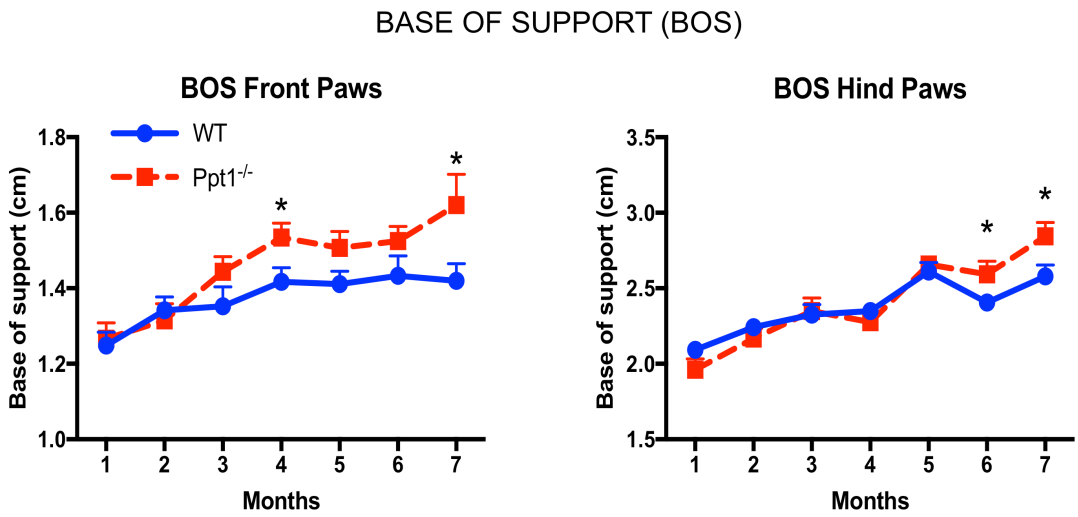

Figure 4.12 - Increased base of support in Ppt1$^{-/-}$ mice.

*CatWalk XT (Noldus) measures of base of support (BOS) in fore and hind limbs shows an earlier, significant increase in forelimb BOS at 4 months, than hind limb BOS at 6 months in Ppt1 deficient (Ppt1$^{-/-}$) mice as compared to wildtype (WT) mice. *p<0.05, two-tailed, unpaired parametric t-test. Values shown are continuous observations from each cohort at each time point as mean ± SEM. (n= 12 mice/group).*

Our analysis of stance and the base of support led us to analyze the overall support, which is the relative duration of simultaneous contact of a given paw (or combination of paws) for a given run. These parameters were classified as shown in table 4.1. A majority of support is generally seen in as diagonal support (Hamers et al, 2006), and this was seen in wildtype mice at all time points (Figure 4.13). At 2 months, *Ppt1*$^{-/-}$ mice also showed a significantly higher percentage of diagonal support compared to wildtype mice, however, in addition, they also showed an increased percentage of single and girdle support compared to wildtype mice at this time point (Figure 4.13), presumably due to their higher speed of movement (Figure 4.1). From 5 months onwards, there was a significant, and drastic decrease in the percentage of diagonal support in *Ppt1*$^{-/-}$ mice, with a concurrent increase of lateral, three-limb and four-limb support in these mice, as compared to wildtype mice (Figure 4.13). This data reveals that with advancing age, *Ppt1*$^{-/-}$ mice show less stability and therefore require greater support from other limbs to move. The increase of lateral support at 6 and 7 months is similar to the "lateral wobbling" gait previously observed in *Ppt1*$^{-/-}$ mice (Gupta et al, 2001). This increased utilization of three and four-limb support in *Ppt1*$^{-/-}$ mice

would also, in part explain the increased stand durations observed in these mice (Figure 4.4).

Support Parameter	Simultaneous paw contact (s) measured
Zero	No paw.
Single	Any one paw.
Diagonal	Contralateral fore-and hind paw.
Girdle	Contralateral set of either forepaws or hind paws.
Lateral	Ipsilateral fore- and hind paw.
Three	Any three paws.
Four	All four paws.

Table 4.1 – Support parameters for CatWalk XT analysis.

Table detailing the parameters for support formulas for a given run (Hamers et al, 2006).

4.6 Measures of inter-limb co-ordination

Ppt1$^{-/-}$ mice seem to rely more heavily on their forelimbs during movement, as shown by the swing of the hind paws (Figure 4.5), as well as their print width (Figure 4.6). Therefore we next analyzed the relative print positions of ipsilateral fore- and hind paws. This measure described the positional relationship of the placements of fore and hind paws of the same side during a step cycle, with a greater positive value indicating that the hind paw is placed further behind the forepaw (Table 2.1).

Our analysis revealed a consistent trend to more negative values at nearly all time points in *Ppt1*$^{-/-}$ mice, as compared to wildtype mice. This analysis shows that these mice generally place their hind paws closer to the fore paws than wildtype mice, presumably because they rely their fore paws more for stability while walking (Figure 4.14).

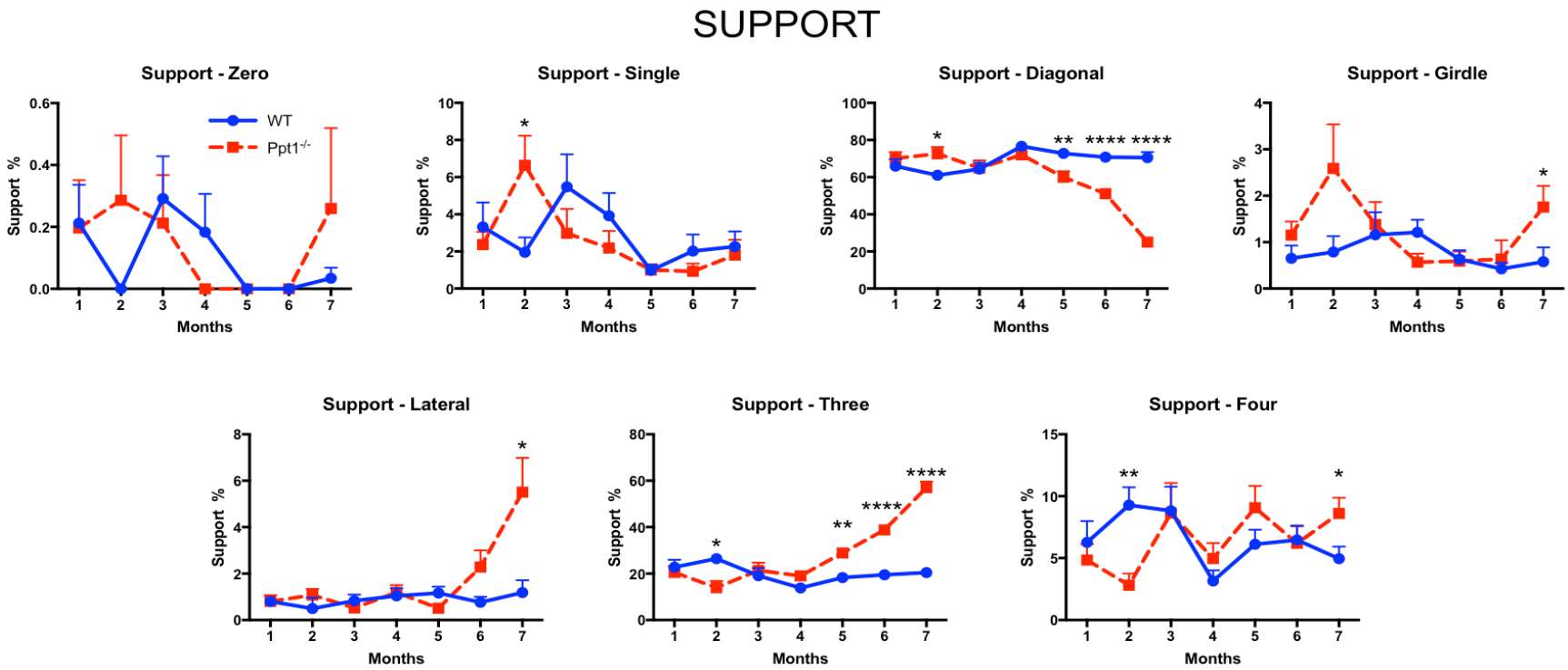

Figure 4.13 - Altered support in Ppt1$^{-/-}$ mice.

*CatWalk XT (Noldus) measures of support for a given run, showing a significant increase in single and diagonal support in Ppt1 deficient (Ppt1$^{-/-}$) mice as compared to wildtype (WT) mice at 2 months, along with a decrease in four-limb support at this time point for Ppt1$^{-/-}$ mice. Between 5-7 months, Ppt1$^{-/-}$ mice show a significant decrease in diagonal support and an increase in lateral and three-limb support, along with four-limb support at 7 months, compared to wildtype mice. *p<0.05, **p<0.01, ***p<0.001, ****p<0.0001, two-tailed, unpaired parametric t-test. Values shown are continuous observations from each cohort at each time point as mean ± SEM. (n= 12 mice/group).*

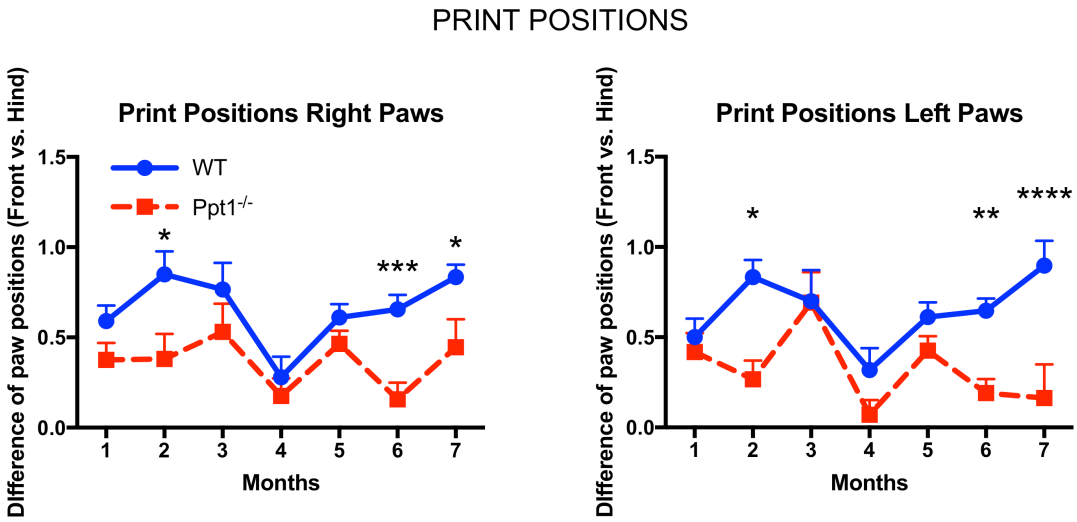

Figure 4.14 - Ppt1$^{-/-}$ mice place hind paws closer to fore paws.

*CatWalk XT (Noldus) measures of print positions showing consistently lower values on both sides for Ppt1 deficient (Ppt1$^{-/-}$) mice as compared to wildtype (WT) mice at nearly all time points, implying that these mice place their hind paws closer to fore paws during step cycles. *p<0.05, **p<0.01, ***p<0.001, ****p<0.0001, two-tailed, unpaired parametric t-test. Values shown are continuous observations from each cohort at each time point as mean ± SEM. (n= 12 mice/group).*

We then analyzed step patterns, as described above (Chapter 2.3) (Figure 2.3) to determine whether *Ppt1*$^{-/-}$ mice were walking in an altered fashion. Until 3 months of age, both wildtype and *Ppt1*$^{-/-}$ mice showed variability in step sequences, a majority of which were either AA or AB patterns. However, with age, wildtype mice showed an increasing percentage of the AB pattern. This was similar to previous observations in injured rats (Hamers et al, 2006), despite the fact that the absolute percentage of AB pattern in wildtype mice but this was still lower than described previously. *Ppt1*$^{-/-}$ mice, however, showed an increasing preference for the AA pattern with age, which has been previously shown to be associated with anterolateral spinal cord lesions in cats (Bem et al, 1995) (Figure 4.15 A).

There was also a significant decrease in the percentage of CA and CB patterns in *Ppt1*$^{-/-}$ mice at 6 and 7 months of age. RA and RB patterns, that are only seen during severe spinal cord injury or disease (Hamers et al, 2006), were seen to be significantly increased in *Ppt1*$^{-/-}$ mice at 7 months (Figure 4.15 A).

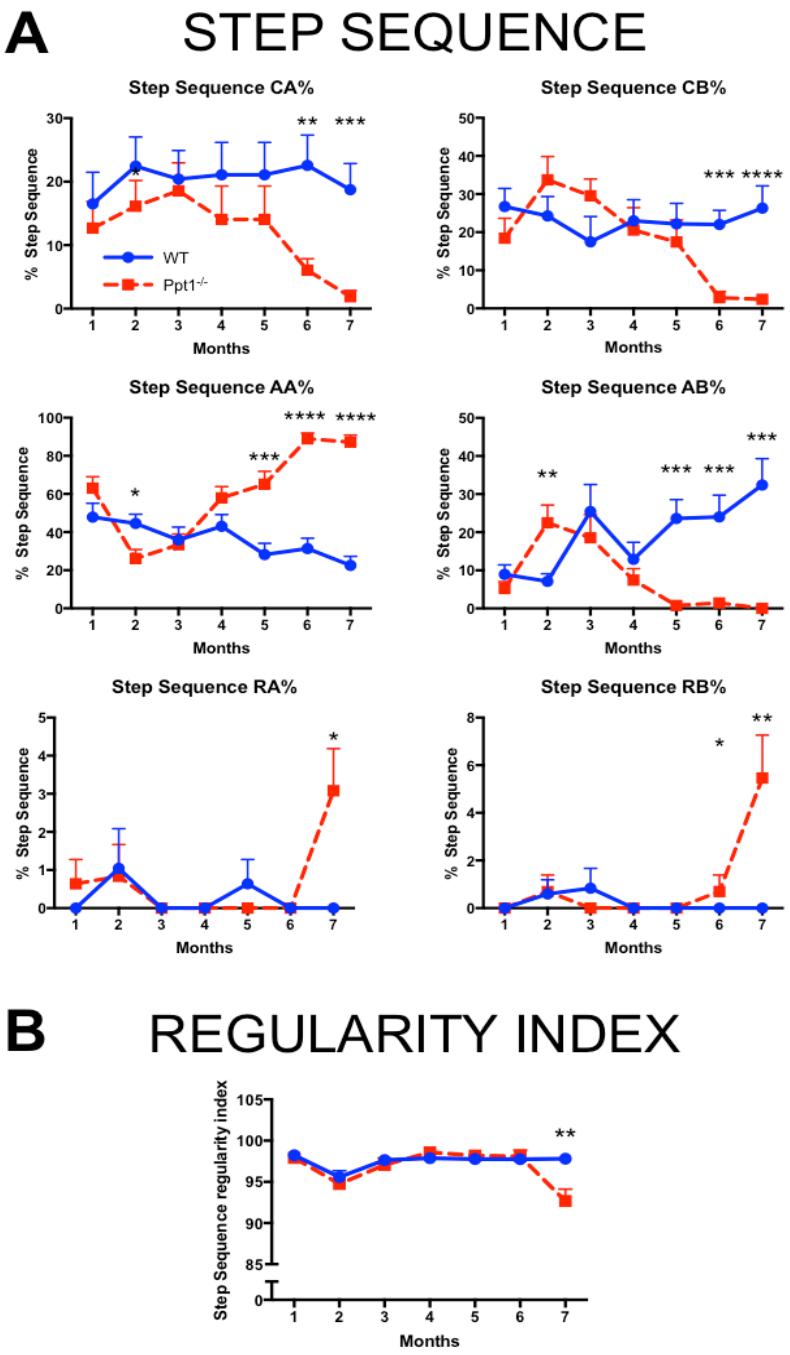

Figure 4.15 - Ppt1$^{-/-}$ mice show altered but regular step-fall patterns

*CatWalk XT (Noldus) measures of step-fall patterns (**A**) show that Ppt1 deficient (Ppt1$^{-/-}$) mice show an increasing shift towards an AA pattern with age, with an increase in RA pattern at 7 months, compared to wildtype (WT) mice that showed a majority of the AB pattern with age. The regularity index for these patterns was almost identical between genotypes until 7 months when Ppt1$^{-/-}$ mice showed significantly lower regularity of step patterns. *p<0.05, **p<0.01, ***p<0.001, ****p<0.0001, two-tailed, unpaired parametric t-test. Values shown are continuous observations from each cohort at each time point as mean ± SEM. (n= 12 mice/group).*

A measure of the regularity of step sequences of step cycles within a run remained consistent until 7 months, when *Ppt1$^{-/-}$* mice showed a significant

decrease in regularity, compared to wildtype mice (Figure 4.15 B). This shows that, while *Ppt1*$^{-/-}$ mice show altered step sequences starting at 3 months, the regularity, which can also be described as a measure of the number of missteps, was the same as that of wildtype mice until 7 months, when this regularity of steps significantly decreased.

Another way of studying co-ordination between limbs is to analyze the temporal relationship between any two limbs in a given step cycle. These phase dispersions describe the duration of contact with the glass of a target paw in relation to the stand of the first or "anchor" paw (Hamers et al, 2006). Positive values indicate that the target paw is placed after the anchor paw. Our analysis of the mean values of phase dispersions showed little difference between genotypes for either diagonal or girdle limbs (Figure 4.16), with the LH-RH dispersion showing significantly lower values at 2 and 7 months for *Ppt1*$^{-/-}$ mice compared to wildtype mice, and the LF-RH dispersion showing significantly higher values for *Ppt1*$^{-/-}$ mice at 7 months, compared to wildtype mice. The biggest difference was seen between the ipsilateral limbs (LF-LH and RF-RH), where there were significantly more positive values for *Ppt1*$^{-/-}$ mice from 5 months, and this seemed to increase with age (Figure 4.16). This may be a result of increased step cycle durations observed at these time points, as well as being indicative of increasing lateral support used by *Ppt1*$^{-/-}$ mice with age.

4.7 Summary

Overall, the analysis of gait using the *CatWalk XT* system (Noldus) has revealed unexpectedly early and significant changes in *Ppt1*$^{-/-}$ mice, while also confirming the extensive deterioration of their ambulatory ability with the further progression of disease.

A quick survey of the spatial and temporal primary run visualizations (previously shown in Figure 2.2) revealed readily observable changes in measures such as stride length (SL) as early as 2 months in *Ppt1*$^{-/-}$ mice (Figure 4.17 and 4.18).

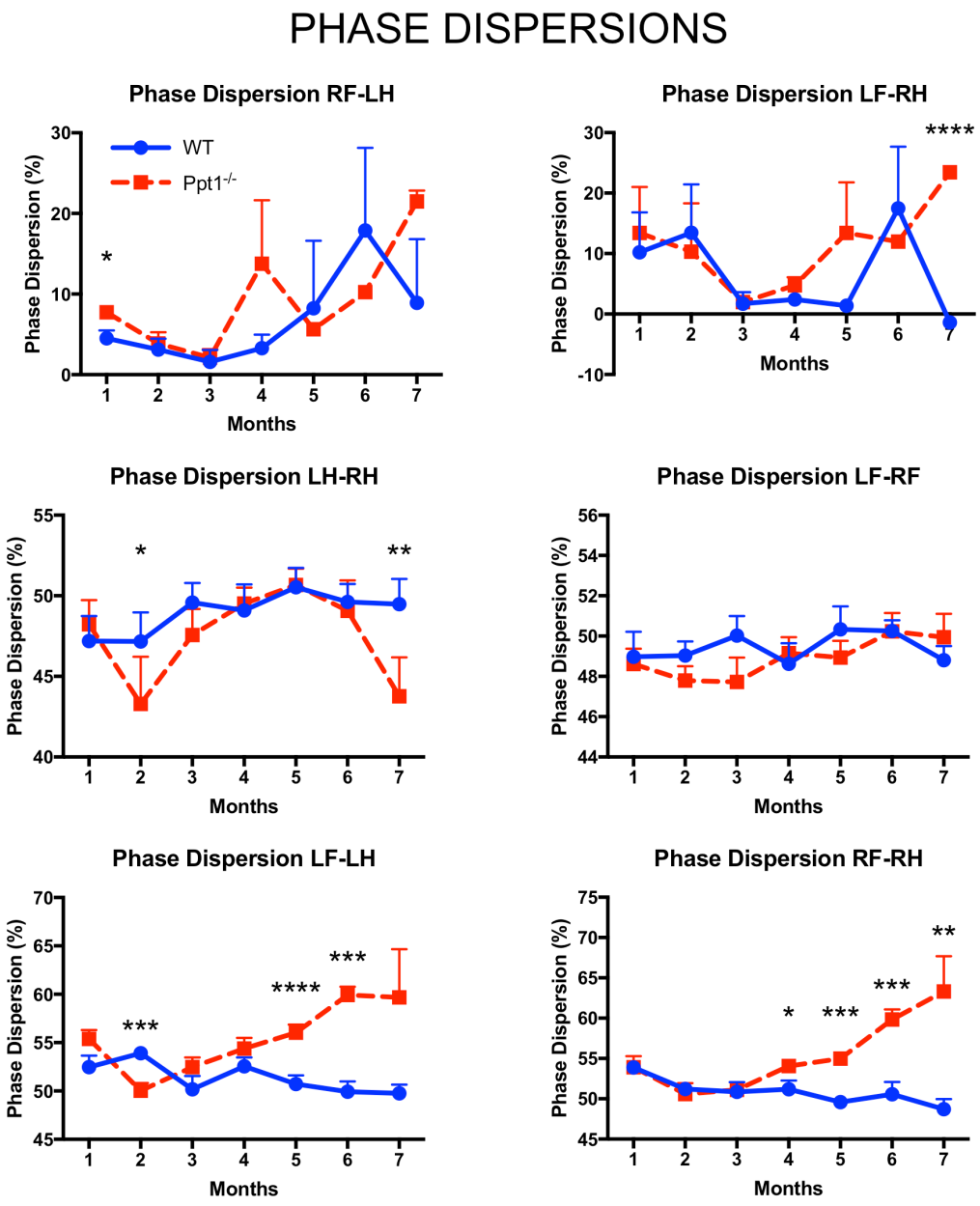

Figure 4.16 - Phase dispersions of Ppt1$^{-/-}$ show changes in ipsilateral limbs.
*CatWalk XT (Noldus) measures of mean phase dispersions showing generally more positive values for Ppt1 deficient (Ppt1$^{-/-}$) mice in LF-RH dispersion at 7 months and ipsilateral limbs from 5-7 months compared to wildtype mice, while the opposite relationship was seen for hind limb dispersions at 2 and 7 months respectively. *p<0.05, **p<0.01, ***p<0.001, ****p<0.0001, two-tailed, unpaired parametric t-test. Values shown are continuous observations from each cohort at each time point as mean ± SEM. (n= 12 mice/group).*

A noticeable decline in both spatial and temporal readings was seen in *Ppt1*$^{-/-}$ mice compared to wildtype mice from 5 months onwards (Figure 4.17 and 4.18). These readily observable differences serve to further demonstrate the extent of the changes seen in the gait of *Ppt1*$^{-/-}$ mice compared to wildtype mice and are reinforced by the statistical analysis of data produced by the *CatWalk XT 10.5* software (Noldus).

This *CatWalk XT* analysis has shown that at an early time point of 2 months, *Ppt1*$^{-/-}$ mice unexpectedly seemed to perform better than wildtype mice, as they moved with greater speed, larger strides and shorter step cycles compared to wildtype mice (Figures 4.1, 4.3, 4.8). This is a surprising finding, as no previous study of these mice has suggested either hyperactivity or improved motor performance at any age. However, this apparent improved function may be a result of various other factors including variations in weight gain, learning ability. This may also be caused by the possible effect of the postnatal developmental delay (Chapter 3.2) or the significant inflammation (Chapter 3.8) that have been documented in the spinal cords of these mice at this age (Beh et al, 2013; Eilam, 1997; Hausmann, 2003).

From 3 months of age, *Ppt1*$^{-/-}$ mice appeared to move more slowly, with smaller strides, increased step cycles, stand and phase dispersions as well as showing a trend to decreased paw intensities (Figures 4.1 – 4.10, 4.16). These data are very similar to previous more qualitative studies of motor function in these mice (Dearborn et al, 2015; Gupta et al, 2001; Macauley et al, 2009). However, these studies only provided evidence of these deficits from 5 months of age onwards. Therefore, this current study provides further evidence for early sensorimotor defects in these mice.

Ppt1$^{-/-}$ mice showed a greater reliance on their fore paws to move, as shown by their increased fore paw width, increased fore paw base of support, increased swing duration of hind paws and lower print position values (Figures 4.5, 4.6, 4.12, 4.14). Furthermore, *Ppt1*$^{-/-}$ mice also showed a general instability while

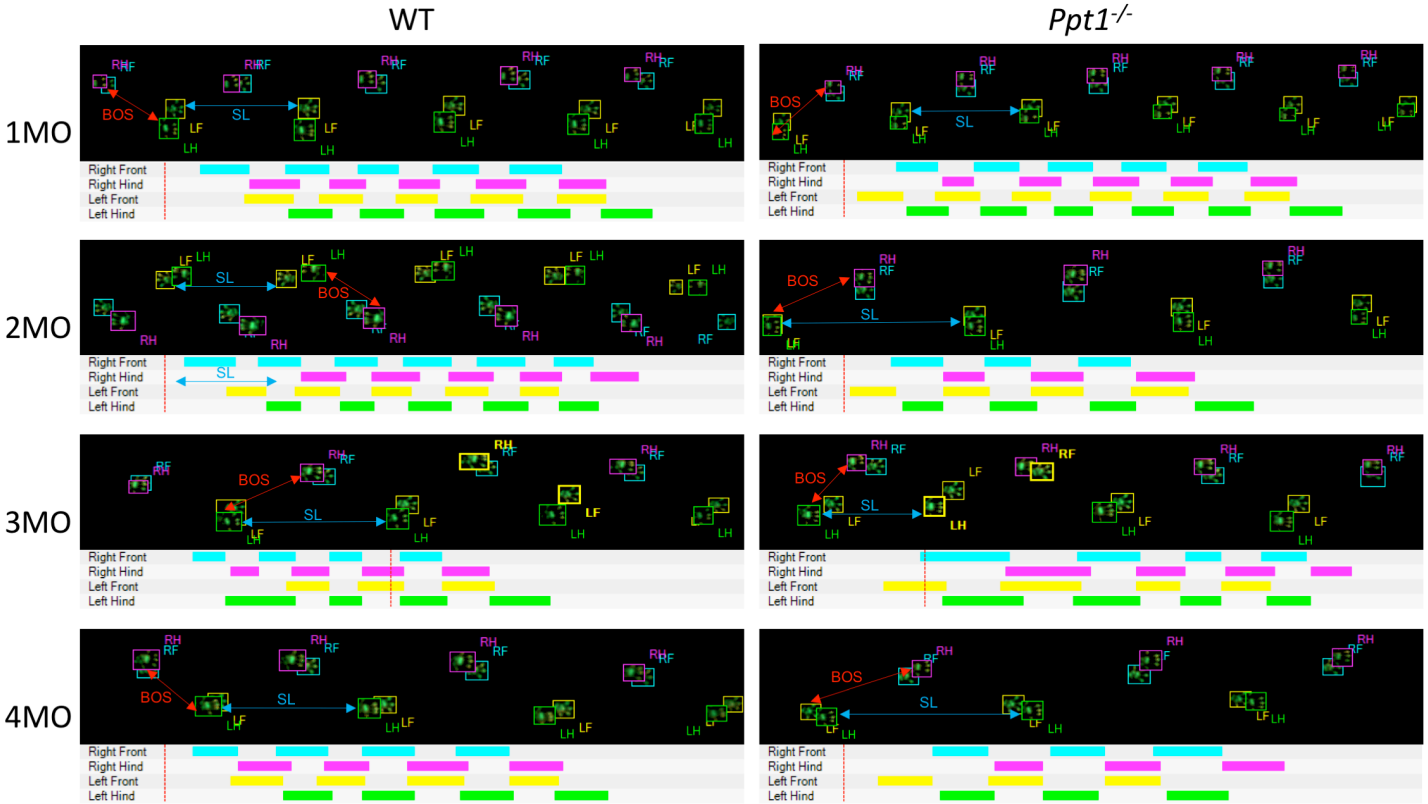

Figure 4.17 – Early changes in spatial and temporal primary run visualizations in Ppt1$^{-/-}$ mice compared to WT mice between 1 and 4 months. *Representative primary run visualizations from CatWalk XT (Noldus) software showing spatial (black) and temporal (gray) measures of paw placements between Ppt1 deficient (Ppt1$^{-/-}$) mice and wildtype (WT) mice. Ppt1$^{-/-}$ mice show a readily visible increase in stride length (SL) at 2 months, but not in the Base of Support (BOS), while the time. Each paw print appears as a separate fluorescent mark. These are then classified as blue for Right Front (RF), yellow for Left Front (LF), pink for Right Hind (RH) and green for Left Hind (LH).*

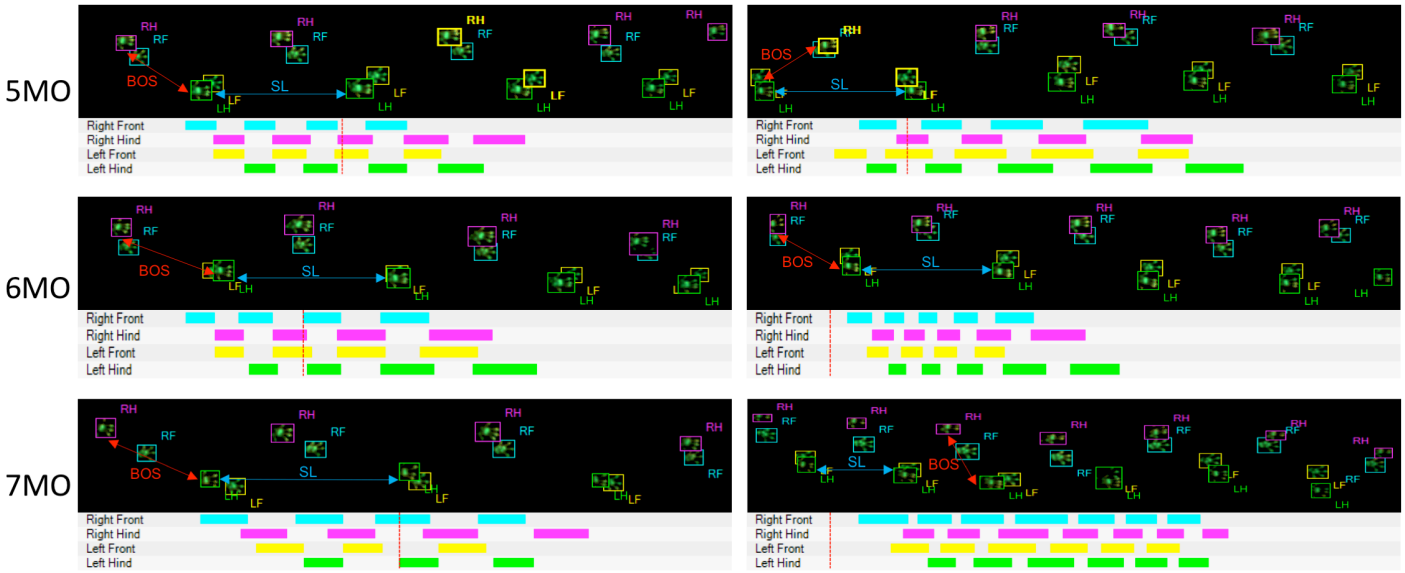

Figure 4.18 – Late changes in spatial and temporal primary run visualizations in Ppt1$^{-/-}$ mice compared to WT mice between 5 and 7 months. *Representative primary run visualizations from CatWalk XT (Noldus) software showing spatial (black) and temporal (gray) measures of paw placements between Ppt1 deficient (Ppt1$^{-/-}$) mice and wildtype (WT) mice. Ppt1$^{-/-}$ mice show a readily visible decrease in stride length (SL) at 5 months, but not in the Base of Support (BOS), as well as a decrease in the duration of each paw's placement. Each paw print appears as a separate fluorescent mark. These are then classified as blue for Right Front (RF), yellow for Left Front (LF), pink for Right Hind (RH) and green for Left Hind (LH).*

walking as evidenced by increases in dual stance, as well as three and four-limb support (Figure 4.11. and 4.13). Lastly, measures of co-ordination showed a switching of step sequence preference that is often seen in spinal injury (Bem et al, 1995), that was seen as early as 4 months (Figure 4.15). Changes seen between 3-5 months in *Ppt1*$^{-/-}$ mice are more readily explainable as being significantly due to spinal pathology, while changes after 5 months are possibly a result of multiple loci of pathology including the thalamocortical region and the cerebellum (Bible et al, 2004; Kielar et al, 2007; Macauley et al, 2009).

The findings of increased early reliance on forepaws for locomotion in *Ppt1*$^{-/-}$ mice are a novel finding, and further elucidate early sensorimotor changes in *Ppt1*$^{-/-}$ mice. They also provide an interesting juxtaposition to the generalized nature of spinal cord neuropathology described in chapter 3, further indicating that regional peripheral pathology may have a greater role to play in causing the sensorimotor deficits in these mice.

CHAPTER 5. The impact of spinal cord targeted therapies in *Ppt1*$^{-/-}$ mice.

5.1 Introduction

CLN 1 disease or Infantile NCL (INCL) is one of the most rapidly progressing forms of NCL (Dolisca et al, 2013; Mole et al, 2005; Santavuori et al, 1974). Despite many advances in our understanding of CLN1 disease pathology, there is currently no effective curative therapy available for this disease (Hawkins-Salsbury et al, 2013).

The *Ppt1*$^{-/-}$ mouse model for CLN1 disease has proved to be a powerful tool, not just as a means of studying disease pathology and progression, but also for testing various experimental therapies (Hawkins-Salsbury et al, 2013). Until now, the brain has been considered the main locus of pathology in CLN1 disease, as had previously been demonstrated in *Ppt1*$^{-/-}$ mice (Bible et al, 2004; Kielar et al, 2007; Macauley et al, 2009). Therefore, almost all experimental therapies for CLN1 disease have been targeted to the brains of these mice. The various experimental therapeutic approaches have so far included the administration of anti-oxidants such as Resveratrol (Wei et al, 2011), Human CNS stem-cell neurosphere (HuCNS-SCns) implants in the brain (Tamaki et al, 2009), brain-directed Enzyme Replacement Therapy (ERT) (Hu et al, 2012; Lu et al, 2010) and brain-directed gene therapy (Griffey et al, 2004; Griffey et al, 2006; Macauley et al, 2012). However, all these therapies have only been partially successful in treating CLN1 disease.

A previous study had shown that intrathecal (IT) administration of a large dose of human recombinant enzyme in a mouse model of CLN2 disease or late-infantile NCL (LINCL) increased survival and positively affected brain pathology (Xu et al, 2011). These intrathecal injections were administered into the sub-arachnoid space, between the L5 and L6 spinal cord vertebrae. Having demonstrated early and profound pathology in the spinal cords of *Ppt1*$^{-/-}$ mice (Chapter 3), we hypothesized that the limited success of forebrain-directed therapies in these mice was in part because they had little or no effect on the pathology in the spinal cords of these mice. Therefore, similar IT delivery of therapeutic agents may have a significant beneficial effect on spinal cord and brain pathology in these mice.

5.2 Intrathecal (IT) administration of human recombinant PPT1 Enzyme in *Ppt1*$^{-/-}$ mice.

Based on the encouraging results seen from delivering intrathecal recombinant human TPP1 enzyme in a mouse model of CLN2 (Xu et al, 2011), as well as the partial efficacy of human recombinant PPT1 enzyme in alleviating brain pathology (Hu et al, 2012), we undertook a pilot study to investigate the effect of IT administration of human recombinant PPT1 (hPPT1) enzyme in *Ppt1*$^{-/-}$ mice.

For this study, 4 groups of 16-20 *Ppt1*$^{-/-}$ mice were administered with increasing titers of the human recombinant enzyme at 6 weeks of age, when there is no detectable brain or spinal cord pathology. Mice were initially anesthetized with isoflurane, and then injected using a 30-gauge needle placed between L5 and L6 lumbar vertebrae on three consecutive days. The groups of treated mice received either 0 (Vehicle), 2.6, 5.3 or 10.6 mg/ml doses of hPPT1. They were then tested for motor performance at 3, 5, 7, 8 and 9 months, and compared to untreated *Ppt1*$^{-/-}$ and wildtype (C57BL/6) mice (Lu et al, 2015) (Figure 5.1 A).

Encouragingly, the treated *Ppt1*$^{-/-}$ mice showed a significant dose-dependent increase in survival, with a mean survival of 284 days for mice that received the highest dose (10.6 mg/ml) of PPT1 enzyme, compared to 234 days for the untreated *Ppt1*$^{-/-}$ mice. The treated mice also showed a significant improvement in motor performance for the constant speed rotarod paradigm, again in a dose-dependent fashion (Lu et al, 2015).

Mice receiving the highest dose (10.6 mg/ml) of recombinant human enzyme were also sacrificed at various time points post-injection to study the time course of PPT1 activity in the brain (Figure 5.1 B). The half-life of the enzyme was found to be about 1 day. However, at 9 days post-injection, PPT1activity of around 20%

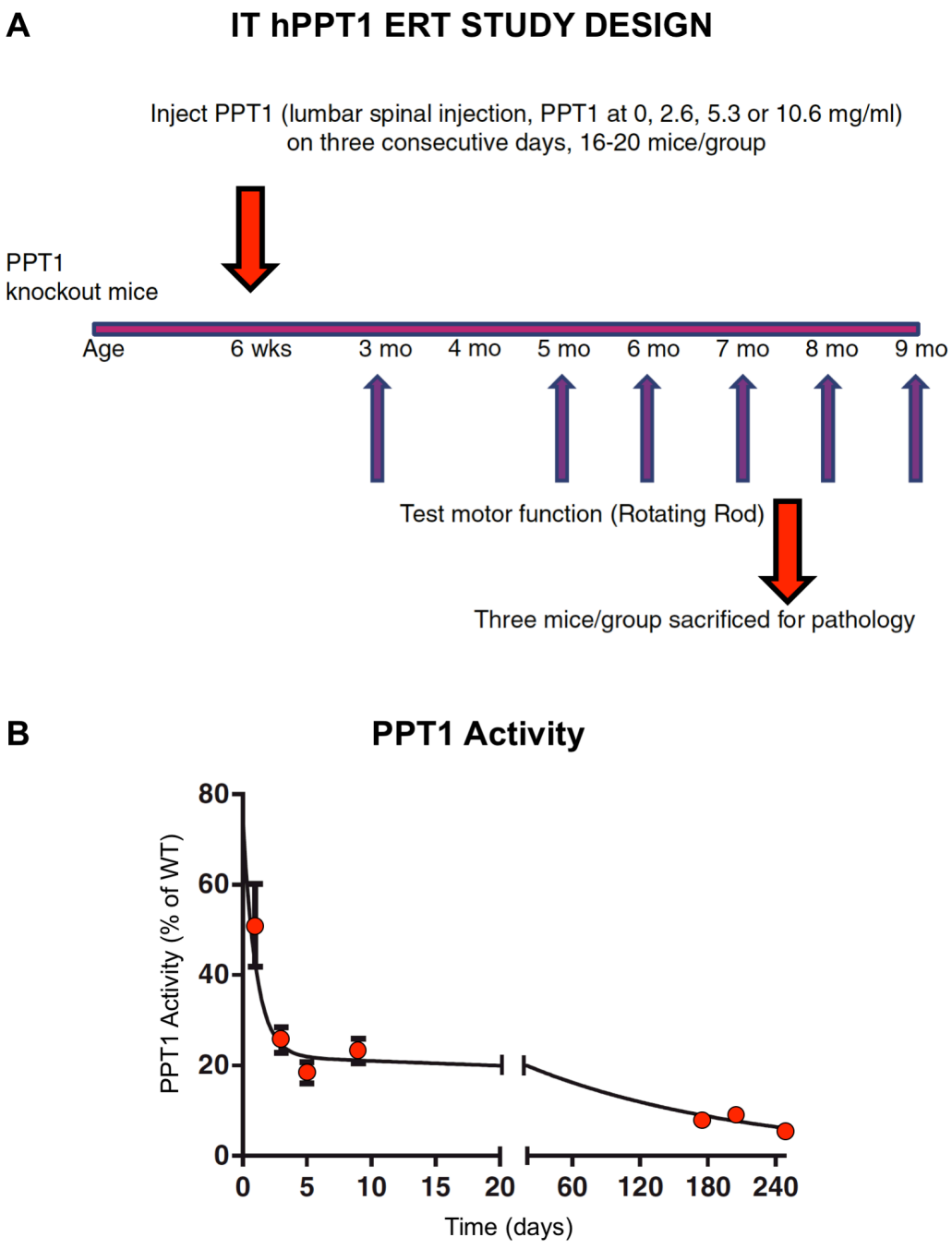

Figure 5.1 - Investigating the effects of intrathecal (IT) administration of human recombinant PPT1 enzyme – study design and biodistribution of PPT1 enzyme.

*(**A**) Four groups of Ppt1 deficient ($Ppt1^{-/-}$) mice were randomized and received three consecutive daily lumbar spinal infusions of 80µl human recombinant PPT1 (hPPT1) at concentrations of 0, 2.6, 5.3 or 10.6 mg/ml at six weeks of age. Rotarod testing was performed at successive monthly time points with age-matched untreated $Ppt1^{-/-}$ and wildtype mice. Mice from each group (n=3) were sacrificed at 7.5 months for pathological examination. (**B**) PPT1 activity in whole brain homogenates following intrathecal injection of 80µl of 10.6 µg/µ hPPT1 at 6 weeks showing persistent enzyme activity (n=4,3,3,3 at 1,3,5,9 days respectively and n=1 at later time points). Adapted from (Lu et al, 2015).*

of wildtype (WT) enzyme levels was observed, and 5-9% of PPT1 activity was present as late as 248 days post-injection (Figure 5.1 B). This demonstrated that IT injections of hPPT1 distributed the enzyme sufficiently to result in brain PPT1 activity that persisted for a long period. The mechanisms underlying this unexpectedly prolonged persistence of PPT1 activity remain unclear. However, it is considered that low levels of enzyme activity are sufficient to correct the disease phenotype in LSDs (Donsante et al, 2007; Neufeld & Fratantoni, 1970). This may help explain the significant improvements in motor performance and increase in lifespan observed in these mice (Lu et al, 2015).

To further explore this, a subset of mice from the same cohort of mice as this study were sacrificed at 7.5 months for histological analysis (Figure 5.1A), so as to include mice from each of the treatment groups, as well as *Ppt1*$^{-/-}$ and wildtype controls (n=3) (Lu et al, 2015). With the administration of recombinant PPT1 enzyme into the sub-arachnoid cerebrospinal fluid (CSF), a greater effect was predicted in the superficial areas of the brain and spinal cord compared to deeper structures (Hu et al, 2012; Xu et al, 2011). Therefore to provide a comprehensive view of the effect of IT ERT on pathology in *Ppt1*$^{-/-}$ mice from our study, we chose to examine established markers of disease progression in both the brain and spinal cords of these mice (Bible et al, 2004; Kielar et al, 2007; Macauley et al, 2009).

We first immunostained for markers of glial activation - GFAP for astrocytes and CD68 for microglia. Both microglia and astrocytes are activated early in disease progression in the brain (Kielar et al, 2007) and the spinal cord (Chapter 3.8), and levels of glial activation were quantified using semi-automated thresholding image analysis (Chapter 2.8). Similar methods were used for assessing the levels of accumulated autofluorescent storage material within cells (Chapter 2.8). Lastly, stereological estimates of neuron number were obtained to determine if the therapy had any neuroprotective effect (Chapter 2.7).

Regions of the brain that have been shown to be significantly affected by disease pathology in *Ppt1*$^{-/-}$ mice were analyzed, including the medial and lateral ventral

posterior thalamic nuclei (VPM/VPL), the dorsal lateral geniculate nucleus (LGnD) and the primary somatosensory barrel-field of the cortex (S1BF) (Bible et al, 2004; Kielar et al, 2007). The cervical and lumbar regions of the spinal cord were similarly analyzed to study the proximal and distal effects of lumbar IT ERT administration.

a) Effect of IT human recombinant ERT on glial activation in *Ppt1*$^{-/-}$ mice.

Both microglia and astrocytes are activated early in disease progression in the brains (Kielar et al, 2007) and spinal cords (Chapter 3) of *Ppt1*$^{-/-}$ mice, typically before the occurrence of neuron loss. There is a growing body of evidence for glial cells playing a significant role in disease progression of CLN1 disease (Shyng & Sands, 2014) (Lange, PhD Thesis). Therefore, we investigated whether IT administration of human recombinant PPT1 had any effect on this glial activation.

A survey of various regions of the brain and spinal cord stained for the microglial marker revealed a clearly visible dose-dependent reduction of microglial activation in the somatosensory cortex and spinal cord of treated compared to untreated *Ppt1*$^{-/-}$ mice, while lesser effects were seen in their thalamic nuclei. This was a result of not only a decreased density of activated microglia, but also due to fewer microglial cells showing the hypertrophic morphology typical of activated microglia. However, these levels of microglial activation in treated *Ppt1*$^{-/-}$ mice were still higher than that seen in the wildtype controls (Figure 5.2). Quantitative thresholding image analysis confirmed a greater effect of the IT human recombinant ERT in more superficial structures of the brain and spinal cord, with a significant reduction of microglial activation seen in the S1BF as well as both the dorsal and ventral horns of the cervical and lumbar cord. While there was a trend towards reduced microglial activation in the LGnD with increased dosage of the recombinant enzyme, this did not reach statistical significance. Similarly, the VPM/VPL showed a reduced level of CD68 immunoreactivity in treated *Ppt1*$^{-/-}$ mice, but again, this was not statistically significant (Figure 5.3).

Analysis of sections from treated *Ppt1*$^{-/-}$ mice stained for GFAP showed a low-level astrocyte response to the human recombinant PPT1, especially in the *Ppt1*$^{-/-}$ mice that received 2.6mg/ml and 5.3mg/ml dose of the recombinant enzyme. Nevertheless, there was a visible decrease in astrocytosis in the S1BF, VPM/VPL and lumbar SC of the *Ppt1*$^{-/-}$ mice that received the highest dose (10.6mg/ml) of recombinant enzyme, compared to their untreated counterparts. Where reduced levels of astrocytosis were seen, GFAP positive astrocytes were less numerous and stained less intensely with thinner processes compared to those observed in untreated *Ppt1*$^{-/-}$ mice. However, the astrocytes in treated *Ppt1*$^{-/-}$ mice were still hypertrophied and more darkly stained than those in wildtype controls (Figure 5.4). Thresholding image analysis showed significant reductions of astrocytosis in the S1BF, VPM/VPL and dorsal horn of the cervical SC, especially in the *Ppt1*$^{-/-}$ mouse group treated with 10.6 mg/ml of ERT, compared to untreated *Ppt1*$^{-/-}$ mice. There were also reduced measures of astrocytosis in the LGnD and other spinal cord regions in treated mice, but these did not reach statistical significance, mainly due to high variability within treatment groups (Figure 5.5).

Overall, the administration of IT human recombinant ERT in *Ppt1*$^{-/-}$ mice was shown to be effective in reducing the glial response in these mice. While there was a clearly dose-dependent increase in efficacy for reducing microglial activation, the mild astrocyte response to the therapy means that the dosage would have to be more carefully titrated in future experiments. Furthermore, as the mice were analyzed nearly 6 months after the administration of ERT, it demonstrates that early therapeutic intervention can apparently have a lasting effect on disease pathology.

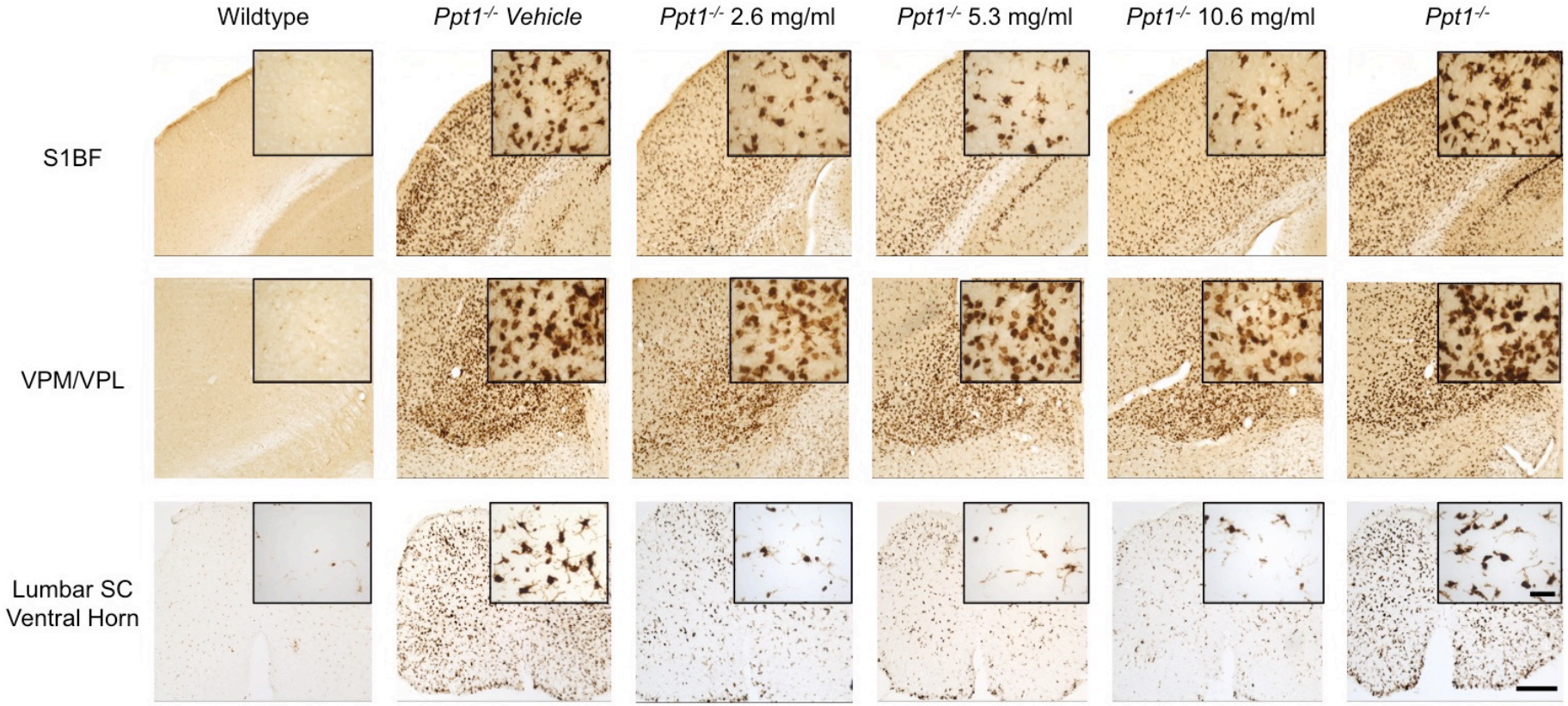

Figure 5.2 – Altered microglial activation in IT human recombinant ERT Ppt1$^{-/-}$ mice.

Representative images of the primary somatosensory cortex (S1BF), ventral posterior medal and lateral thalamic nuclei (VPM/VPL) and lumbar spinal cord (SC) showing a dose-dependent reduction of microglial activation in the S1BF and lumbar SC, but little change in the VPM/VPL in treated vs. untreated Ppt1$^{-/-}$ mice. Scale bars = 200μm and 25μm (inserts).

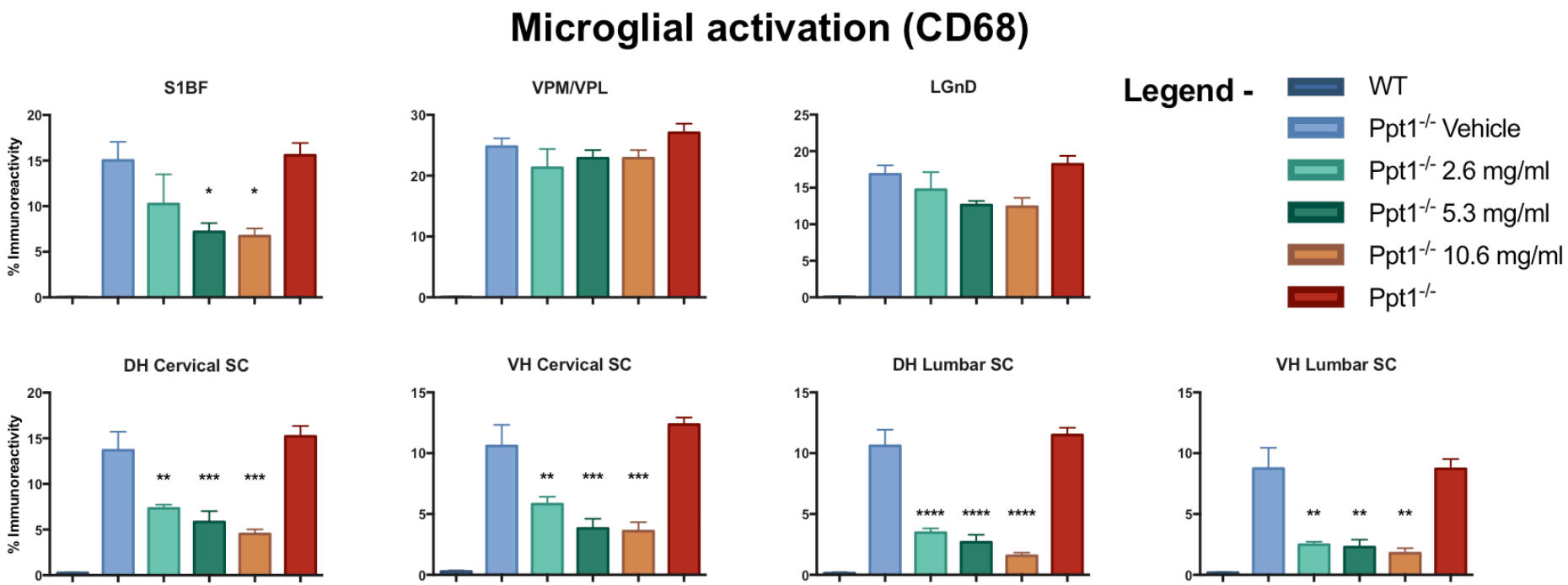

Figure 5.3 – Reduction of microglial activation in IT human recombinant ERT Ppt1$^{-/-}$ mice.

*Thresholding image analysis confirmed the significant reduction of microglial activation in the S1BF as well as dorsal (DH) and ventral (VH) horns of cervical and lumbar SC, with a non-significant reduction seen in the VPM/VPL and the dorsal lateral geniculate nucleus (LGnD). Significance is compared to untreated Ppt1$^{-/-}$ mice. *p<0.05, **p<0.01, ***p<0.001, ****p<0.0001, one-way ANOVA with post-hoc Bonferroni correction. Values shown are mean ± SEM (n=3 mice/group).*

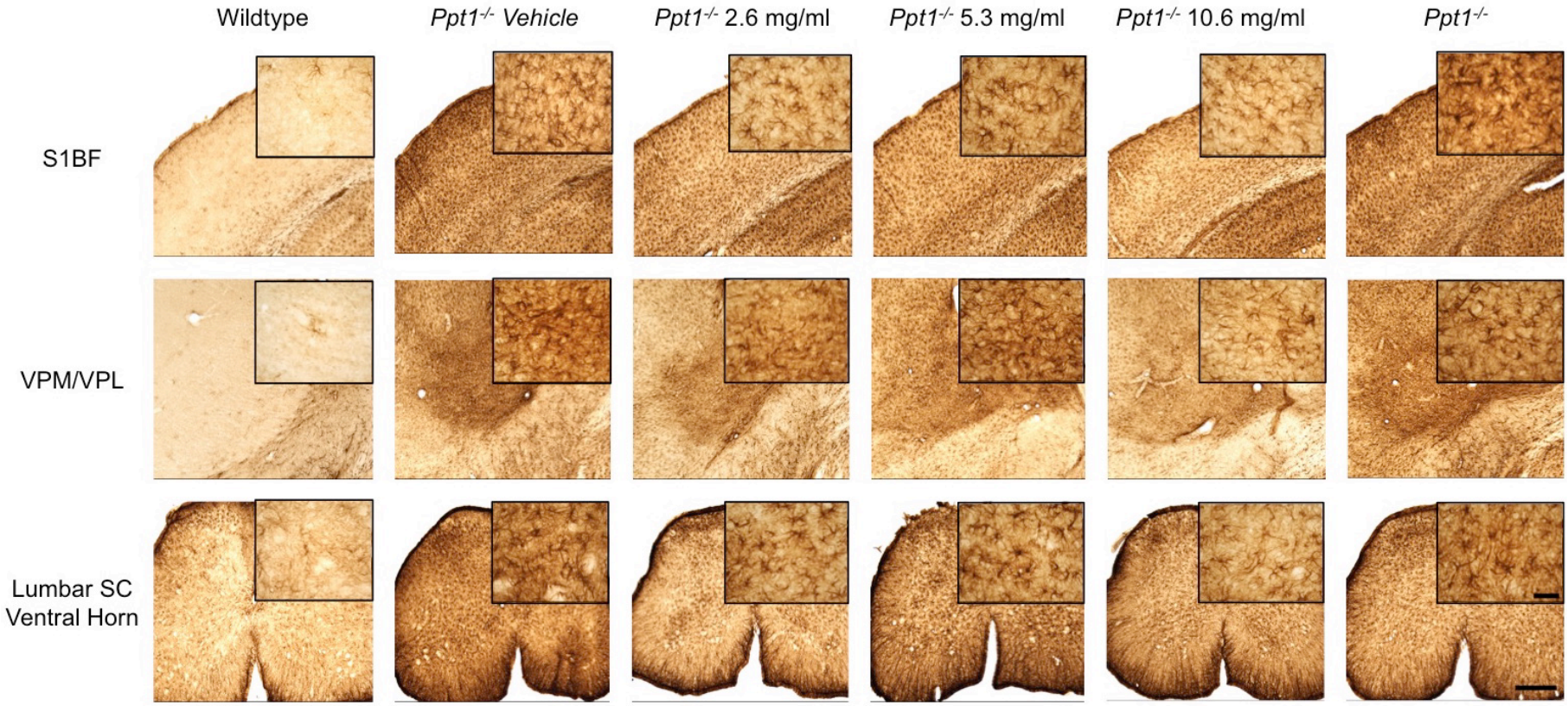

Figure 5.4 – Astrocytosis in IT human recombinant ERT Ppt1$^{-/-}$ mice.

Representative images of the primary somatosensory cortex (S1BF), ventral posterior medal and lateral thalamic nuclei (VPM/VPL) and lumbar spinal cord (SC) showing a low level astrocyte response in animals administered with 2.6mg/ml and 5.3mg/ml, while animals receiving 10.6mg.ml showed visible reduction of astrocytosis in all regions compared to untreated Ppt1$^{-/-}$ mice. Scale bars = 200μm and 25μm (inserts).

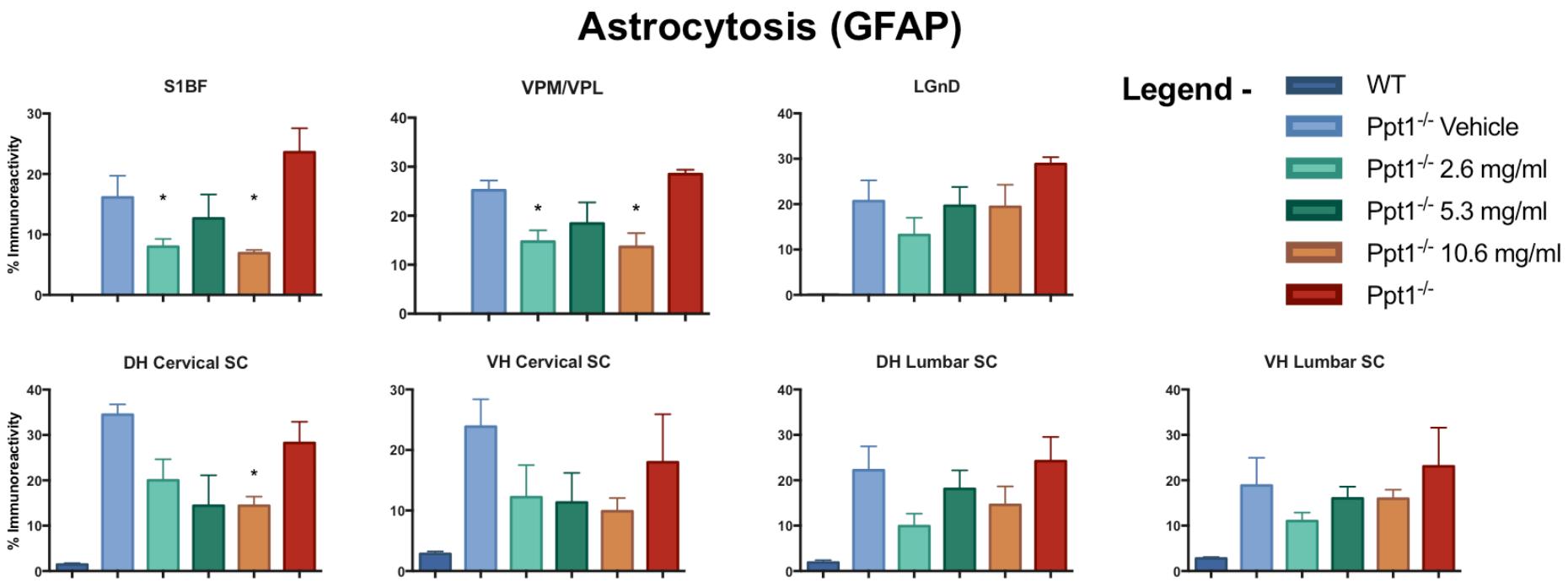

Figure 5.5 – Reduction of astrocytosis in IT human recombinant ERT Ppt1$^{-/-}$ mice.

*Thresholding image analysis confirmed the significant reduction of microglial activation in the S1BF and VPM/VPL, as well as dorsal horn (DH) of cervical SC, but not in the ventral horn (VH) with a non-significant reduction seen in the dorsal lateral geniculate nucleus (LGnD) and lumbar spinal cord. Significance is compared to untreated Ppt1$^{-/-}$ mice. *p<0.05, one-way ANOVA with post-hoc Bonferroni correction. Values shown are mean ± SEM (n=3 mice/group.*

b) Reduction of autofluorescent storage material (AFSM) accumulation in *Ppt1*$^{-/-}$ mice treated with IT human recombinant ERT.

There is a characteristic progressive accumulation of autofluorescent storage material (AFSM) within the cells of the brain (Bible et al, 2004; Kielar et al, 2007) and spinal cord (Chapter 3) in *Ppt1*$^{-/-}$ mice. While there is no evidence for this storage material being directly involved in causing neuron loss, a reduction in storage material burden in these tissues would be indicative of either a reduction or reversal of the disease process. Furthermore, the use of AFSM as a prognostic measure of therapeutic efficacy has been well established (Hu et al, 2012; Macauley et al, 2012; Tamaki et al, 2009), and such analysis would allow us to compare the efficacy of IT human recombinant ERT with previous experimental therapies.

Upon observing sections of *Ppt1*$^{-/-}$ mice treated with IT human recombinant ERT via confocal microscopy, a clear dose-dependent reduction of storage material was observed in the S1BF and lumbar SC, with a lesser effect observed in the VPM/VPL, compared to untreated *Ppt1*$^{-/-}$ mice (Figure 5.6). Thresholding image analysis of confocal microscopy images revealed that there was a significant reduction in AFSM in the cervical spinal cord of *Ppt1*$^{-/-}$ mice that received either a 2.6mg/ml or 10.6mg/ml dose of recombinant enzyme, and in the lumbar spinal cord of *Ppt1*$^{-/-}$ mice that received a 10.6mg/ml dose of recombinant enzyme, as compared to their untreated counterparts. Other regions including the S1BF, VPM/VPL and the LGnD showed a decrease of AFSM accumulation for all treatment groups, compared to untreated *Ppt1*$^{-/-}$ mice, but this did not reach significance (Figure 5.7).

Overall, the reduction of AFSM levels in the cord and the brain indicate the partial efficacy of IT human recombinant ERT. The fact that this was significant in the spinal cord, but not the brain, is presumably due to a reducing effect of ERT with greater distance from the site of administration. The reduction of AFSM anywhere was particularly surprising, given that these tissues were analyzed 6 months after ERT administration, and suggests that there might be either a

lasting therapeutic effect with early therapeutic intervention or a pool of PPT1 enzyme that persists much longer than expected.

c) Effect of IT human recombinant ERT on neuron loss in *Ppt1*$^{-/-}$ mice.

There is a profound and progressive loss of neurons seen in both the brain (Bible et al, 2004; Kielar et al, 2007) and spinal cord (Chapter 3) of *Ppt1*$^{-/-}$ mice. Therefore, for an experimental therapy to be effective, it must be able to either prevent or halt this neurodegeneration.

To determine if there was any neuroprotective effect of IT delivered human recombinant ERT, we obtained stereological counts of neurons in VPM/VPL, LGnD, S1BF, Cervical and lumbar spinal cords from Nissl stained sections prepared as described in Chapter 2.7. Counts in all these regions showed no significant improvement in neuron counts in any of the treatment groups compared to untreated *Ppt1*$^{-/-}$ controls. However, neuron counts from *Ppt1*$^{-/-}$ mice receiving 10.6mg/ml of recombinant enzyme revealed a trend to improved neuron number in the S1BF and the dorsal and ventral horns of the cervical and lumbar spinal, but this did not reach significance (Figure 5.8).

This apparent lack of neuroprotection via IT delivered ERT may be due to the fact that mice were analyzed 6 months after treatment was administered, and any effects of this treatment may have long worn off resulting in significant neurodegeneration. This minimal neuroprotective effect was similar to that observed in other pre-clinical experiments using recombinant human PPT1 (Hu et al, 2012; Lu et al, 2010). However, given the improvements seen in rotarod testing and the significant improvements in lifespan of treated *Ppt1*$^{-/-}$ mice (Lu et al, 2015), as well as taking into account the late time point that the mice were sacrificed after receiving the IT injections, we can see that there is a protracted course of the disease in treated animals, perhaps due to an early neuroprotective effect of the therapy along with its effects on gliosis (Chapter 5.1 a), which may lead to delayed neuron loss, which we observe at this 7 month time point.

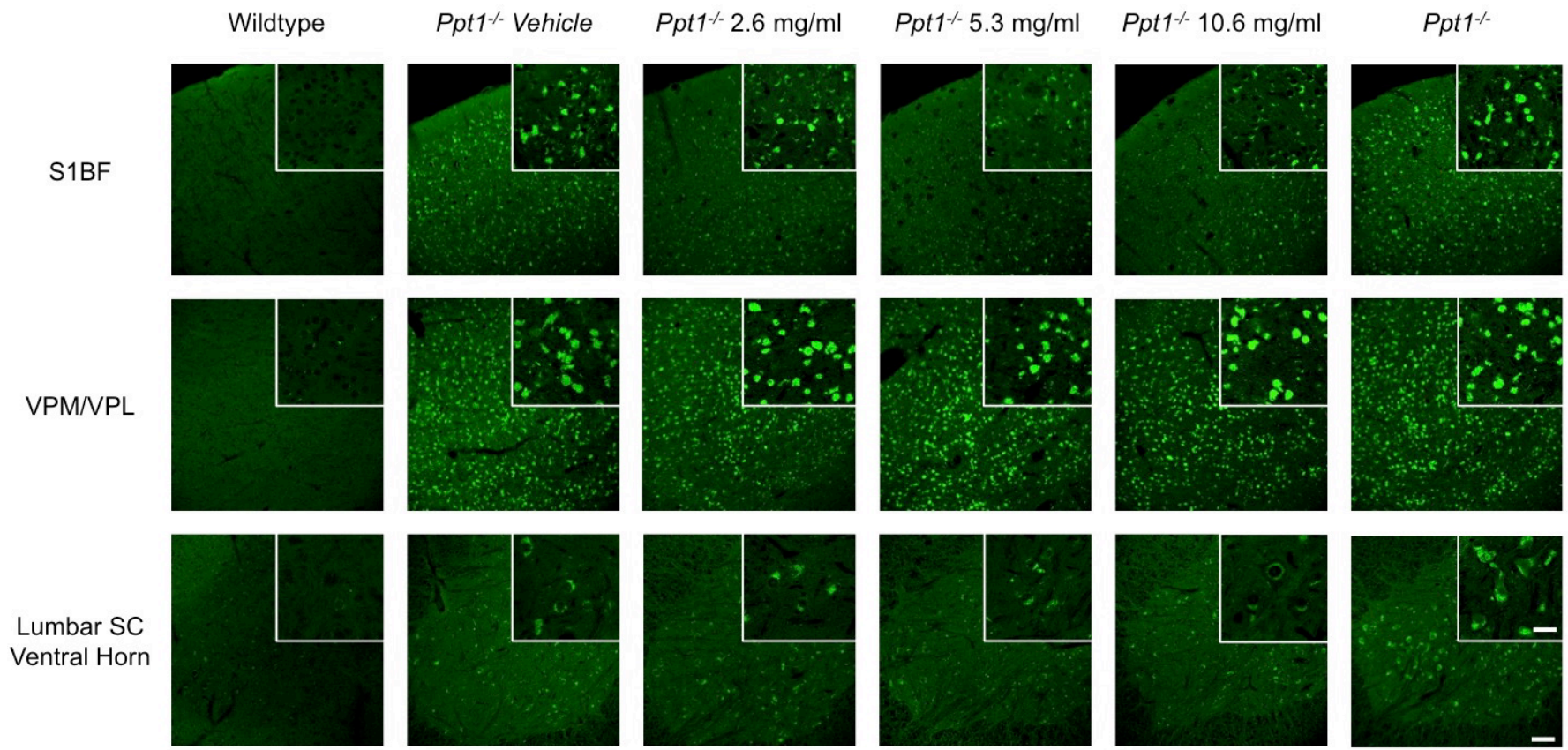

Figure 5.6 – Effect of IT human recombinant ERT on autofluorescent storage material (AFSM) accumulation in Ppt1$^{-/-}$ mice.

Representative images of the primary somatosensory cortex (S1BF), ventral posterior medal and lateral thalamic nuclei (VPM/VPL) and lumbar spinal cord (SC) showing a dose-dependent reduction of autofluorescent storage material (AFSM) in S1BF and lumbar SC of treated vs. untreated Ppt1$^{-/-}$ mice. Scale bars = 100μm and 25μm (inserts).

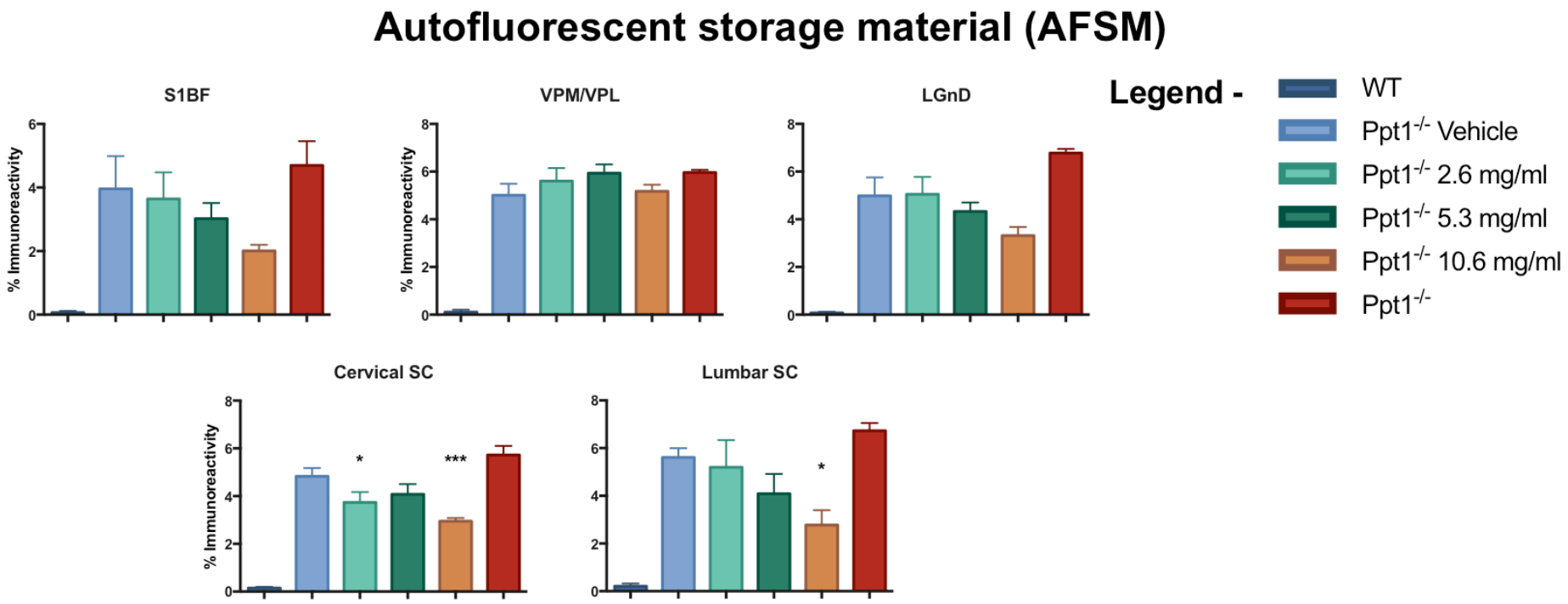

Figure 5.7 – IT human recombinant ERT in Ppt1$^{-/-}$ mice reduces autofluorescent storage material (AFSM) accumulation.

*Thresholding image analysis confirmed the significant reduction in AFSM accumulation in the cervical and lumbar SC of treated Ppt1$^{-/-}$ mice. There were reduced levels of AFSM in the S1BF, VPM/VPL and dorsal lateral geniculate nucleus (LGnD), but these did not reach statistical significance. Significance is compared to untreated Ppt1$^{-/-}$ mice. *p<0.05, one-way ANOVA with post-hoc Bonferroni correction. Values shown are mean ± SEM (n=3 mice/group).*

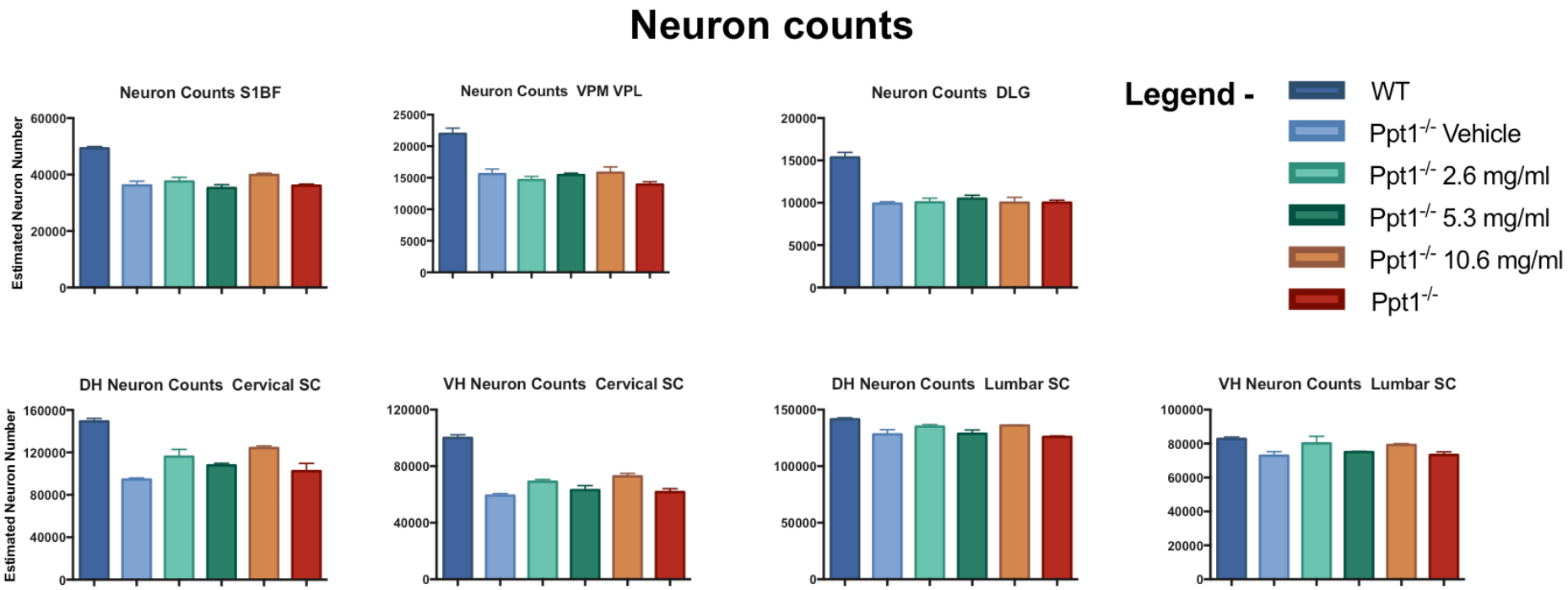

Figure 5.8 – Lack of significant neuroprotection in Ppt1$^{-/-}$ mice treated with IT human recombinant ERT.

Optical fractionator estimates of neuron numbers in brain and spinal cord regions showing a non-significant increase in neuron number in Ppt1$^{-/-}$ mice receiving 10.6mg/ml recombinant enzyme in the S1BF as well as all spinal cord regions. There was no significant increase in neuron numbers in any region of IT treated mice compared to untreated Ppt1$^{-/-}$ mice. All measures are by one-way ANOVA with post-hoc Bonferroni correction. Values shown are mean ± SEM (n=3 mice/group).

5.3 Combination intracranial (IC) and intrathecal (IT) delivery of gene therapy in *Ppt1*$^{-/-}$ mice.

Of the various experimental therapies that have been tested in *Ppt1*$^{-/-}$ mice, the most promising results have been obtained from various trials of forebrain-directed gene therapy, either alone or in combination with other therapeutic agents (Griffey et al, 2004; Griffey et al, 2006; Macauley et al, 2012; Macauley et al, 2014; Roberts et al, 2012). Despite this approach showing improvements in various pathological parameters including glial activation, ASFM accumulation and restoration of PPT1 levels in the brain, together with a moderate increase in median lifespan (Macauley et al, 2012; Macauley et al, 2014; Roberts et al, 2012), the clinical improvements observed in these mice were modest. This may possibly be due to the lack of widespread distribution of the Adeno-associated viral (AAV) vector used (Aschauer et al, 2013; Gray et al, 2013). Therefore, we wished to analyze the spinal cords of mice receiving intracranial gene therapy to test whether this route of administration had any effect upon the spinal cord pathology we have described in *Ppt1*$^{-/-}$ mice (Chapter 3).

With promising results from the pilot study of intrathecal (IT) delivery of human recombinant PPT1 in *Ppt1*$^{-/-}$ mice (Chapter 5.1), we hypothesized that similar IT delivery of AAV-mediated gene therapy would prove more effective in alleviating brain and spinal cord pathology. Furthermore, a third generation AAV vector, AAV 2/9 had been shown to have broader distribution within the CNS upon IT delivery in various animal models (Dayton et al, 2012; Schuster et al, 2014; Swain et al, 2014), and therefore showed greater promise for widespread delivery of gene therapy in *Ppt1*$^{-/-}$ mice. Lastly, we also assessed the efficacy of the combined intracranial (IC) and intrathecal (IT) administration of AAV2/9 mediated gene therapy on brain and spinal cord pathology in *Ppt1*$^{-/-}$ mice.

For this study, mice at postnatal day 1 or 2 were injected intracranially (IC) or intrathecally (IT) as previously described (Elliger et al, 1999; Griffey et al, 2005; Macauley et al, 2012), with 22 mice in each of 5 treatment groups – Untreated *Ppt1*$^{-/-}$ mice (*Ppt1*$^{-/-}$), intracranial injected *Ppt1*$^{-/-}$ mice (IC), intrathecal injected *Ppt1*$^{-/-}$ mice (IT), combination intracranial and intrathecal injected *Ppt1*$^{-/-}$ mice

(IC/IT) and wildtype control mice. Survival was monitored and motor function assessed using a constant speed rotarod paradigm at 2-month intervals, starting at 5 months (Griffey et al, 2006). Randomly selected mice from each group (n=3) were sacrificed at 3, 5, 7 and 9 month time points for histological analysis (Shyng et al., 2016, submitted for publication).

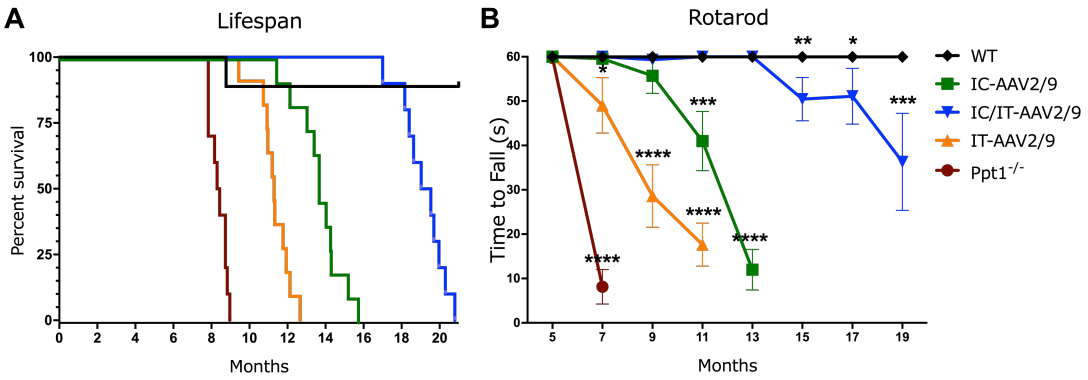

Figure 5.9 – Combined intracranial (IC) and intrathecal (IT) treated mice show greatest improvements in motor function and lifespan.

*(**A**) Constant speed rotarod test for motor function revealed that untreated Ppt1 deficient (Ppt1$^{-/-}$) mice (blue) were unable to stay on the rotarod past 7 months, IT treated mice (red) showed motor deficits at 7 months and could not stay on the rotarod past 11 months, IC treated mice (green) showed deficits at 9 months and could not stay on the rotarod past 13 months, and IC/IT treated mice (purple) showed deficits at 15 months and could not stay on the rotarod past 19 months. Significance is compared to wildtype mice. *p<0.05, **p<0.01, ***p<0.001, ****p<0.0001, two-way repeated measure ANOVA. Values shown are continuous observations from each cohort at each time point as mean ± SEM. (n= 10 mice/group). (**B**) Kaplan-Meier survival curve showing the median lifespan for Ppt1$^{-/-}$ mice (blue) was 8.4 months, IT treated mice (red) had an extension in lifespan of 11.3 months (+3 months), IC treated mice (green) had an extension in lifespan of 13.7 months (+5.3 months) and combination IC/IT treated mice (purple) had an extension in lifespan of 19.3 months (+11.5 months). Analysis by log-rank test for trend was significant for overall survival (p<0.0001). Individual comparisons between curves, using Bonferroni correction were each significant (p<0.002). n= 10 mice/group.*

All treatment groups showed a significant increase in median lifespan, compared to untreated *Ppt1*$^{-/-}$ mice, which had a median lifespan of 8.4 months. IC/IT mice had the longest median lifespan of 19.3 months, with the longest-lived mouse at 22 months, compared to IT mice (11.8 months) or IC mice (13.6 months).

However, these were still short of the median wildtype mouse lifespan, of which all but one mouse remained alive at 24 months. Similarly, rotarod testing revealed that IC/IT mice performed better, and showed a later decline in motor function as compared to either IC or IT mice (Figure 5.9) (Shyng et al. 2016, submitted for publication).

The brains and spinal cords of mice from all treatment groups collected at 3, 5, 7 and 9 months for histological analysis were sectioned and analyzed for the same disease markers as those for the IT human recombinant ERT study, including CD68 for microglial activation, GFAP for astrocytosis, autofluorescent storage material (AFSM) and neuron counts. These measures were collected from the primary (M1) motor cortex, where the IC gene therapy had been targeted, the ventral posterior medial and lateral thalamic nuclei (VPM/VPL) and the lumbar spinal cord.

a) Combination therapy reduces glial activation in brain and spinal cord of *Ppt1*$^{-/-}$ mice.

Microglial activation and astrocytosis have been shown to typically precede neuron loss in the brains and spinal cords of *Ppt1*$^{-/-}$ mice (Kielar et al, 2007) (Chapter 3.8). Therefore, we stained sections for CD68, a marker for microglia. This staining revealed that, at the 7-month time point, there was a clearly observable increase of CD68 staining in all regions of untreated *Ppt1*$^{-/-}$ mice as compared to wildtype controls. There was a decrease in CD68 staining in the M1 cortex of IC and IC/IT mice (Figure 5.10), and a slight decrease in IT mice compared to untreated *Ppt1*$^{-/-}$ mice. There was also significant decrease in CD68 staining in the lumbar spinal cords of IT and IC/IT mice, with no observable difference in the lumbar spinal cords of IC mice compared to untreated *Ppt1*$^{-/-}$ mice (Figure 5.10). Furthermore, IC/IT mice showed a greater reduction of CD68 staining in the VPM/VPL than either IC or IT mice, compared to untreated *Ppt1*$^{-/-}$ mice (Figure 5.10). Less pronounced reductions in CD68 staining were observed as a result of decreased microglial density, as well as fewer microglia having the hypertrophied and intensely stained soma typical of activated macrophages. Indeed, microglia in the lumbar spinal cords of IC/IT and IT mice showed a

similar distribution and morphology as the "quiescent" or resting microglia seen in the wildtype controls (Figure 5.10). Thresholding image analysis showed that there was a significant reduction of microglial activation in the M1 cortex of IC and IC/IT mice at all time points, and of IT mice at 3 and 5 months. At 9 months, when there were no remaining untreated *Ppt1*$^{-/-}$ mice, only IT mice showed significantly higher levels of microglial activation in the M1 cortex, compared to wildtype control mice (Figure 5.11). Similarly, for the ventral horn of the lumbar spinal cord, IC/IT and IT mice showed significantly lower microglial activation than untreated *Ppt1*$^{-/-}$ mice at all time points, but IC mice showed similar levels to untreated *Ppt1*$^{-/-}$ mice from 5 months onwards. At 9 months, only IC mice showed significantly higher levels of microglial activation, as compared to wildtype controls (Figure 5.11). In the VPM/VPL, IC/IT mice were shown to have significantly less microglial activation compared to IC or IT mice at 9 months (Figure 5.11).

Similar to CD68 staining, there was an increase in GFAP staining in all regions of untreated *Ppt1*$^{-/-}$ mice, as compared to wildtype controls. There was a clear decrease in GFAP staining intensity in the M1 cortex of IC and IC/IT mice (Figure 5.12), but this was not as evident in IT mice. Only IC/IT mice showed a clear reduction of astrocytosis in the VPM/VPL as compared to untreated *Ppt1*$^{-/-}$ mice (Figure 5.12), while both IC/IT and IT mice showed a reduction in astrocytosis in the lumbar spinal cord, with IC mice showing almost identical levels of GFAP staining to untreated *Ppt1*$^{-/-}$ mice (Figure 5.12).

Where present, reduced GFAP immunostaining was as a result of a decrease in the density and intensity of staining of astrocytes, which also appeared to have thinner processes (Figure 5.12). Thresholding image analysis of GFAP-stained sections showed that IC and IC/IT mice had more significant reductions in astrocytosis in the M1 cortex and VPM/VPL than IT mice, as compared to untreated *Ppt1*$^{-/-}$ mice at all time points (Figure 5.13). Conversely, IC/IT and IT mice showed the most reduction in GFAP staining intensity in the ventral horn of the lumbar spinal cord.

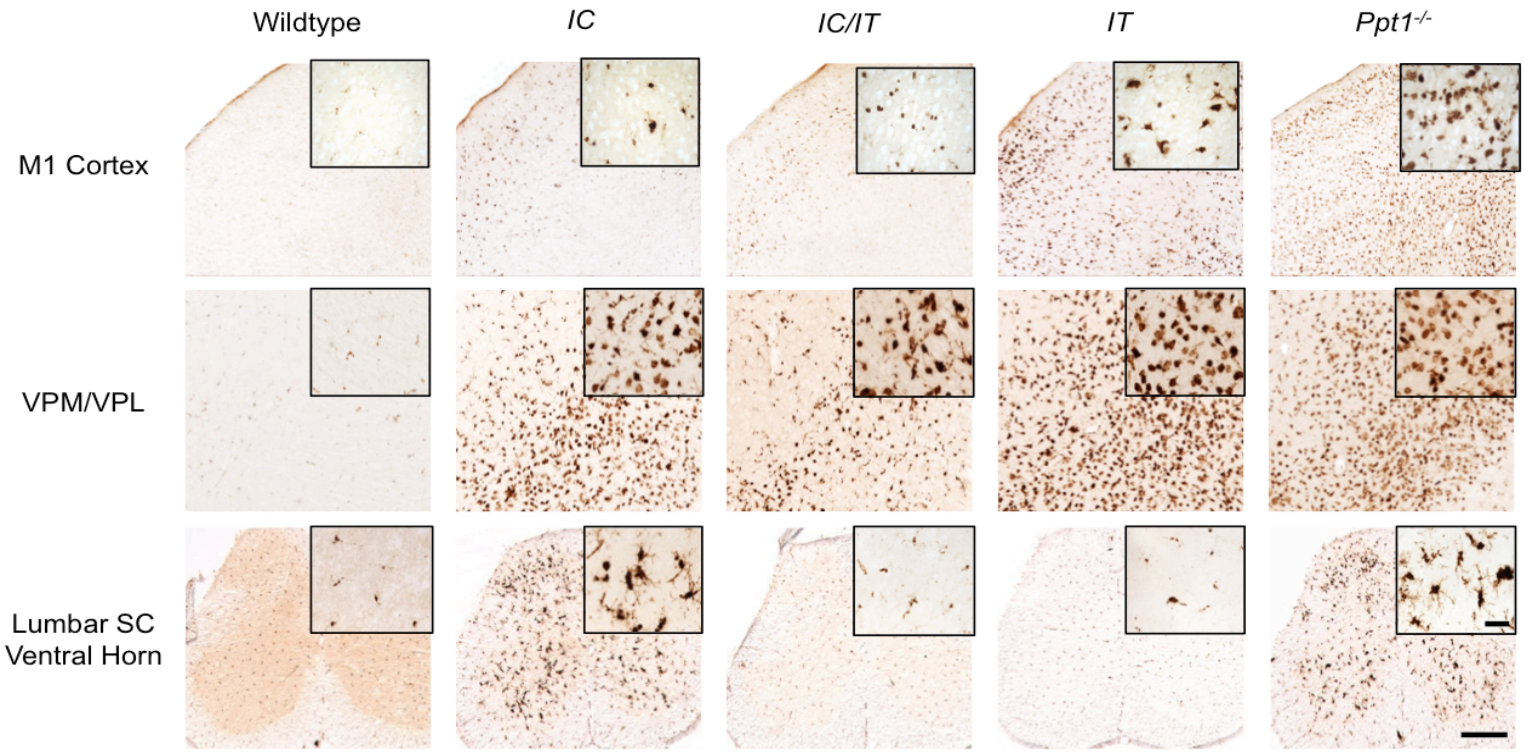

Figure 5.10 – Targeted gene therapy leads to differential microglial activation in Ppt1$^{-/-}$ mice.

Representative images of CD68 staining in treated animals and controls at 7 months. CD68 staining was examined in the primary motor cortex (M1), the VPM/VPL of the thalamus, and the ventral horn (VH) of the lumbar spinal cord showing differential patterns of reduction of microglial activation in intracranial (IC), intrathecal (IT) and combination intracranial and intrathecal (IC/IT) treated Ppt1$^{-/-}$ mice, compared to untreated Ppt1 deficient (Ppt1$^{-/-}$) and wildtype (WT) control mice. IC/IT mice showed an overall greater reduction in microglial activation than either IC or IT therapy alone. Scale bar = 200μm and 25μm (inserts).

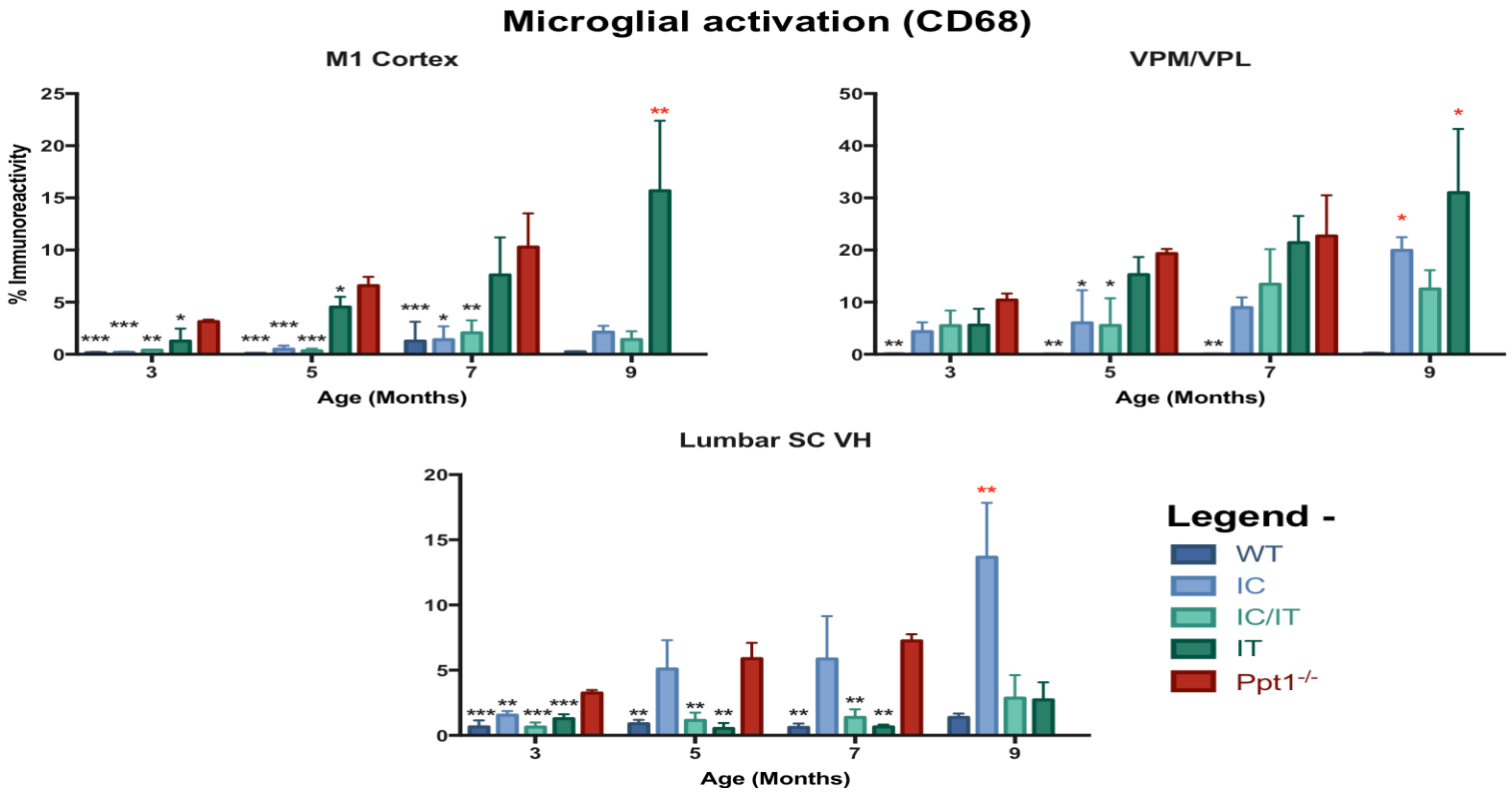

Figure 5.11 – Combination gene therapy reduces microglial activation in Ppt1$^{-/-}$ mice.

*Thresholding image analysis at 3, 5, 7 and 9 month time points in the primary motor cortex (M1), Ventral posterior thalamic nuclei (VPMVPL) and the ventral horn of the lumbar spinal cord (Lumbar SC VH) revealed a significant, but treatment-specific pattern in the impact upon microglial activation based on the site of drug administration, with IC/IT treated mice showing the greatest overall reduction of microglial activation. Significance is compared to untreated Ppt1$^{-/-}$ mice (black stars) or wildtype controls (red stars). *p<0.05, **p<0.01, ***p<0.001 one-way ANOVA with post-hoc Bonferroni correction. Values shown are mean ± SEM (n=3 mice/group).*

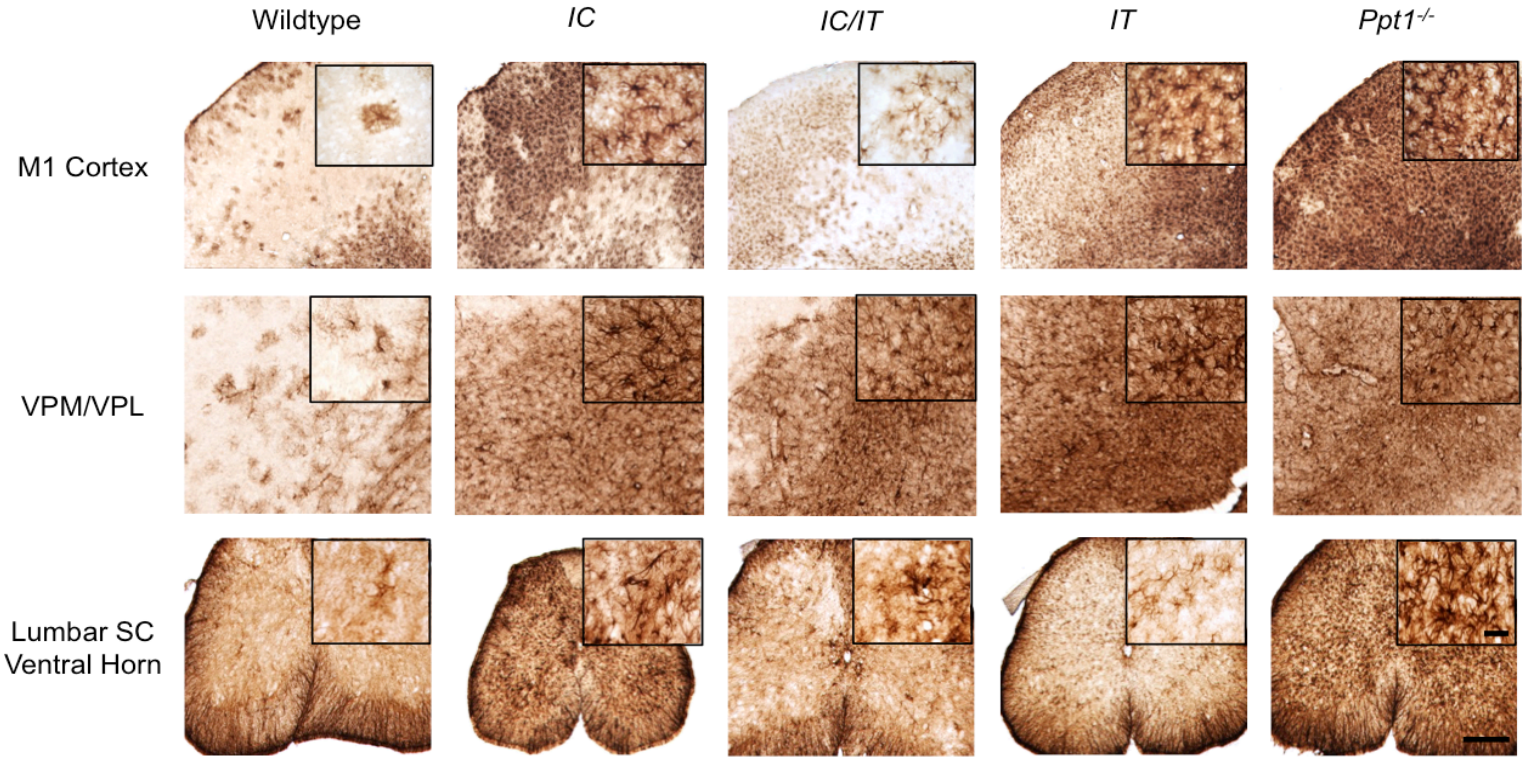

Figure 5.12 – Targeted gene therapy affects astrocyte activation in Ppt1$^{-/-}$ mice.

Representative images of GFAP staining in treated animals and controls at 7 months. GFAP staining was examined in the primary motor cortex (M1), the VPM/VPL of the thalamus, and the ventral horn (VH) of the lumbar spinal cord showing differential patterns of reduction of astrocytosis in intracranial (IC), intrathecal (IT) and combination intracranial and intrathecal (IC/IT) treated Ppt1$^{-/-}$ mice, compared to untreated Ppt1 deficient (Ppt1$^{-/-}$) and wildtype (WT) control mice. IC/IT mice showed an overall greater reduction in astrocytosis than either IC or IT therapy alone. Scale bar = 200μm and 25μm (inserts).

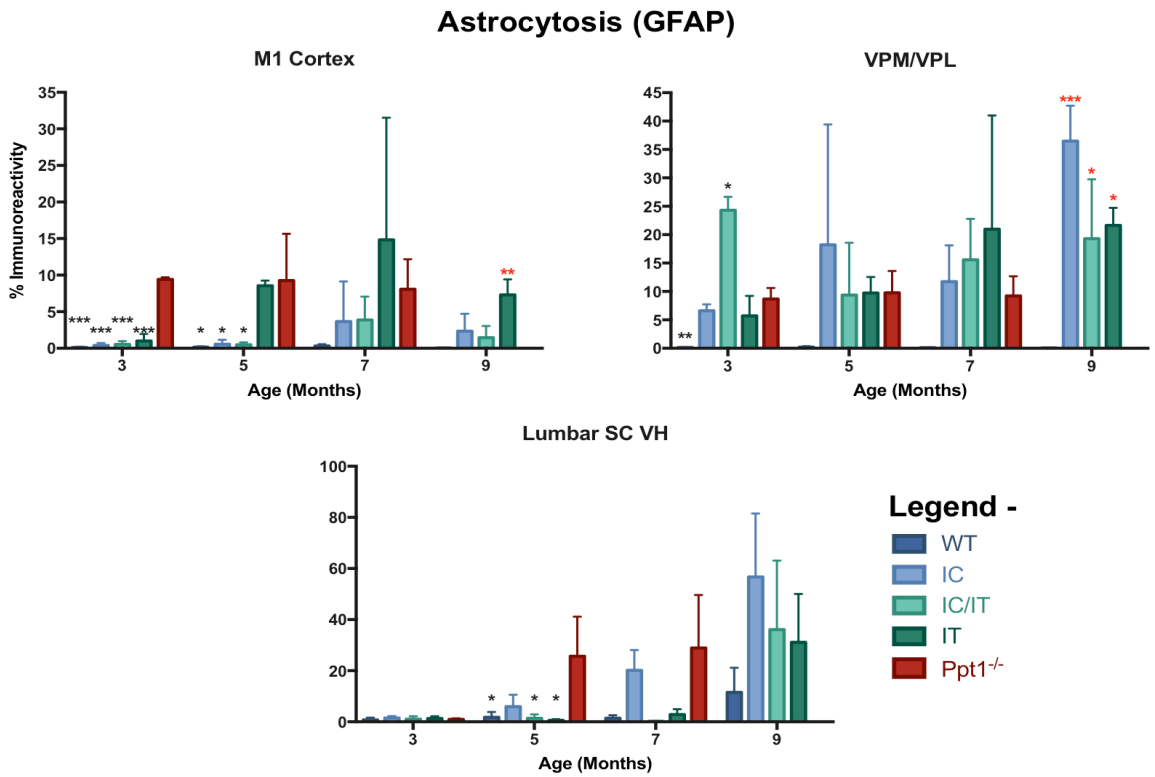

Figure 5.13 – Combined gene therapy reduces astrocytosis in Ppt1$^{-/-}$ mice.

*Thresholding image analysis at 3, 5, 7 and 9 month time points in the primary motor cortex (M1), Ventral posterior thalamic nuclei (VPMVPL) and the ventral horn of the lumbar spinal cord (Lumbar SC VH) showed a significant, but treatment-specific pattern of the reduced astrocytosis based on the site of drug administration, with IC/IT treated mice showing the greatest overall reduction of astrocytosis. Significance is compared to untreated Ppt1$^{-/-}$ mice (black stars) or wildtype controls (red stars). *p<0.05, **p<0.01, ***p<0.001 one-way ANOVA with post-hoc Bonferroni correction. Values shown are mean ± SEM (n=3 mice/group).*

Taken together, these data show that IC therapy alone has very little effect on gliosis in the spinal cord despite significant effects in the brain regions analyzed. Moreover, while IT therapy alone is effective at treating the spinal cord pathology, it does have a mild beneficial effect on the superficial brain structures, but not to the same extent as IC-delivered gene therapy. Combined IC/IT therapy appears to have a greater effect in reducing the glial activation in *Ppt1*$^{-/-}$ mice than either IC or IT therapy alone, with combination therapy treated mice showing a greater effect on the thalamus than the other treatment groups.

b) IC and IT delivery of gene therapy differentially reduce ASFM in the brains and spinal cords of *Ppt1*$^{-/-}$ mice.

As previously discussed, the progressive accumulation of AFSM in the brains and spinal cords of *Ppt1*$^{-/-}$ mice is a good prognostic marker for therapeutic efficacy (Hu et al, 2012; Macauley et al, 2012; Tamaki et al, 2009). Therefore, using confocal microscopy, the levels of AFSM accumulation was compared between treatment groups and controls (Chapter 2.8).

At 7 months, untreated *Ppt1*$^{-/-}$ mice showed significantly higher AFSM levels than wildtype controls in all regions. In the M1 cortex, IC/IT mice showed significantly reduced AFSM levels, as compared to IC or IT mice (Figure 5.14). However, all treatment groups showed levels of AFSM accumulation that were higher than wildtype controls, but lower than untreated *Ppt1*$^{-/-}$ mice.

Similarly, in the VPM/VPL, IC and IT mice showed little reduction of AFSM, while IC/IT mice showed significantly lower AFSM levels than untreated *Ppt1*$^{-/-}$ mice (Figure 5.14). In the lumbar spinal cord, both IC/IT and IT mice showed AFSM levels comparable to wildtype controls while IC mice showed similar amounts of AFSM accumulation to untreated *Ppt1*$^{-/-}$ mice (Figure 5.14). Thresholding image analysis confirmed these observations, in that IC and IC/IT mice showed significantly lower levels of AFSM storage in the M1 cortex and VPM/VPL at almost all time points, while IC/IT and IT mice showed significantly lower levels of AFSM at all time points, compared to untreated

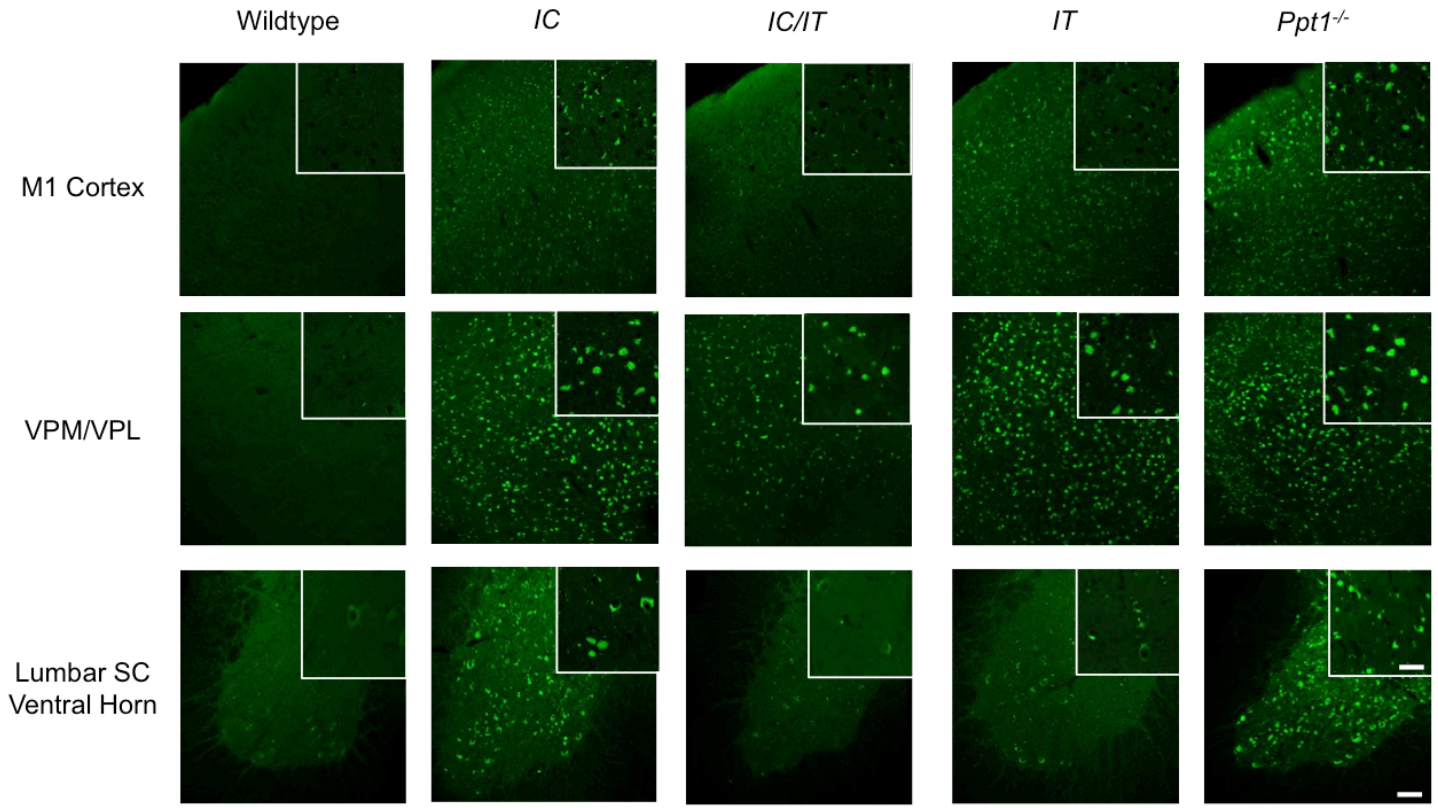

Figure 5.14 – Regional differences in autofluorescent storage material accumulation in Ppt1$^{-/-}$ mice receiving targeted gene therapy.
Representative confocal microscopy images of treated animals and controls at 7 months, showing the primary motor cortex (M1), the VPM/VPL of the thalamus, and the ventral horn (VH) of the lumbar spinal cord showing differential patterns of reduction of AFSM accumulation in intracranial (IC), intrathecal (IT) and combination intracranial and intrathecal (IC/IT) treated Ppt1$^{-/-}$ mice, compared to untreated Ppt1 deficient (Ppt1$^{-/-}$) and wildtype (WT) control mice. IC/IT mice show an overall greater reduction in AFSM than either IC or IT therapy alone. Scale bar = 100μm and 25μm (inserts).

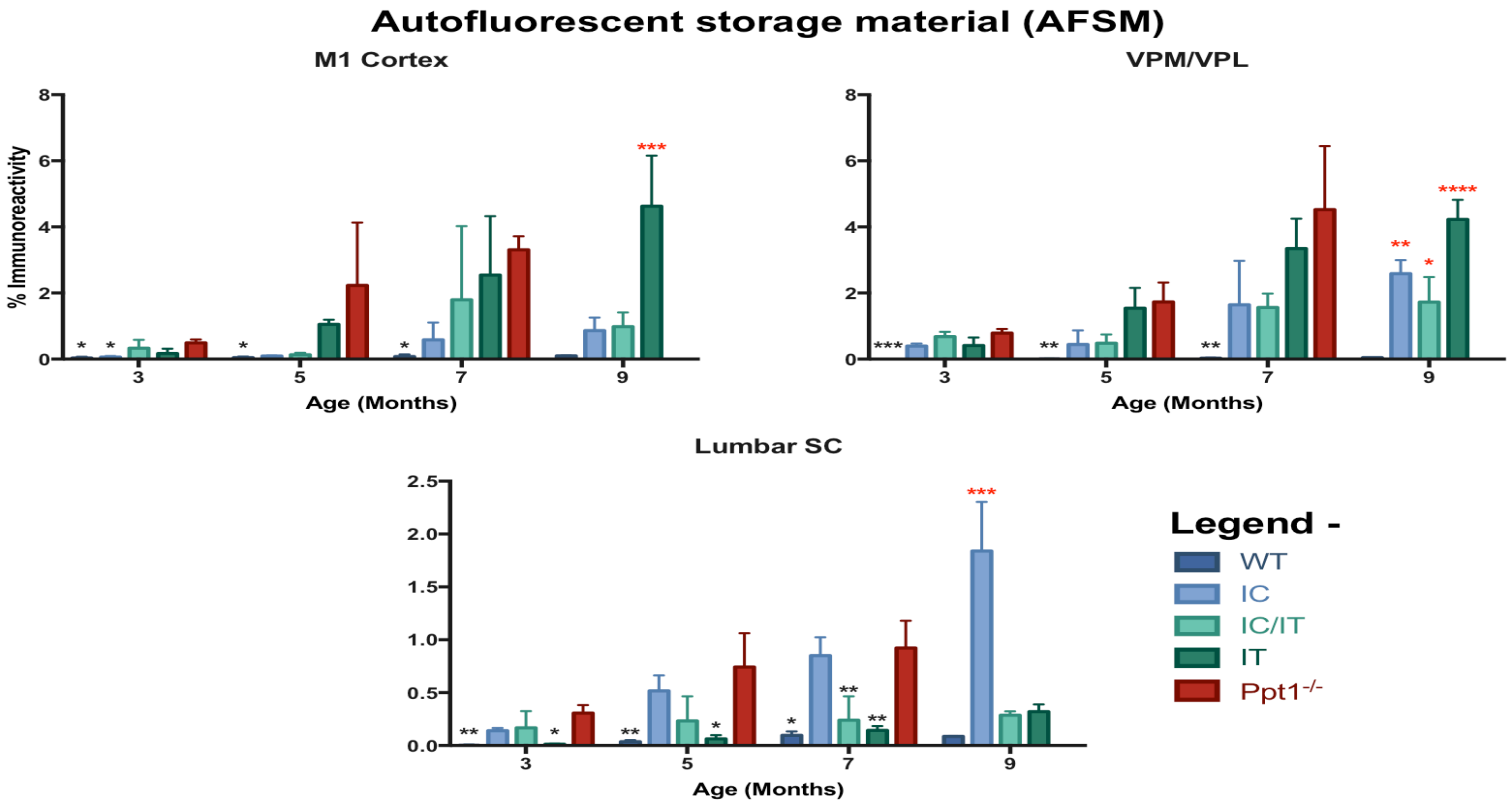

Figure 5.15 – Combined gene therapy significantly reduces autofluorescent storage material accumulation in Ppt1$^{-/-}$ mice.

*Thresholding image analysis at 3, 5, 7 and 9 month time points (**B**) showing a significant, but differential pattern of the reduction of AFSM accumulation based on the site of drug administration, with IC/IT treated mice showing the greatest overall reduction of AFSM. Significance is compared to untreated Ppt1$^{-/-}$ mice (black stars) or wildtype controls (red stars). *p<0.05, **p<0.01, ***p<0.001 one-way ANOVA with post-hoc Bonferroni correction. Values shown are mean ± SEM (n=3 mice/group).*

Ppt1$^{-/-}$ mice. Furthermore, at 9 months, only IT and IC mice showed a significantly higher level of AFSM compared to the wildtype in the M1 cortex and lumbar spinal cord respectively (Figure 5.15).

These data are consistent the analysis of glial markers with IC therapy alone having little to no effect on the accumulation of AFSM in the spinal cord. On the other hand, IT therapy had some early effect in reducing AFSM accumulation in the cortex while effectively treating the spinal cord. However, IC/IT mice show the greatest overall reduction of pathology than either IC or IT therapy alone. Furthermore, this combination IC/IT therapy seems to have an additional effect on reducing pathology in the thalamus, which is not readily observed in either of the single therapies.

c) Delayed neurodegeneration in combination IC/IT treated *Ppt1*$^{-/-}$ mice.

Profound and progressive neuron loss is observed in the brains and spinal cords of *Ppt1*$^{-/-}$ mice (Bible et al, 2004; Kielar et al, 2007; Macauley et al, 2009)(Chapter 3.3). Therefore, to assess any neuroprotective effect afforded by either the single IC or IT therapies or the combination IC/IT therapy; unbiased stereological neuron counts were obtained from a series of Nissl stained sections in the M1 cortex, the VPM/VPL and the ventral horn (VH) of the lumbar spinal cord (Chapter 2.7).

In the M1 cortex, all treatment groups showed a neuroprotective effect from 3 to 7 months, with significant neuron loss only seen in untreated *Ppt1*$^{-/-}$ mice compared to wildtype controls. At 9 months, however, all treatment groups showed a significant reduction in estimated neuron number compared to wildtype controls (Figure 5.16 A). IC/IT and IC mice did not show any significant neuron loss in the VPM/VPL until 7 months, unlike IT mice and untreated *Ppt1*$^{-/-}$ mice, but all groups showed significant neuron loss in the VPM/ VPL after 7 months (Figure 5.16 B). Lastly in the ventral horn of the lumbar spinal cord, only untreated *Ppt1*$^{-/-}$ mice showed significant neuron loss at 3 and 5 months compared to wildtype mice, with all treatment groups showing significant neuron loss at 7 months (Figure 5.16 C).

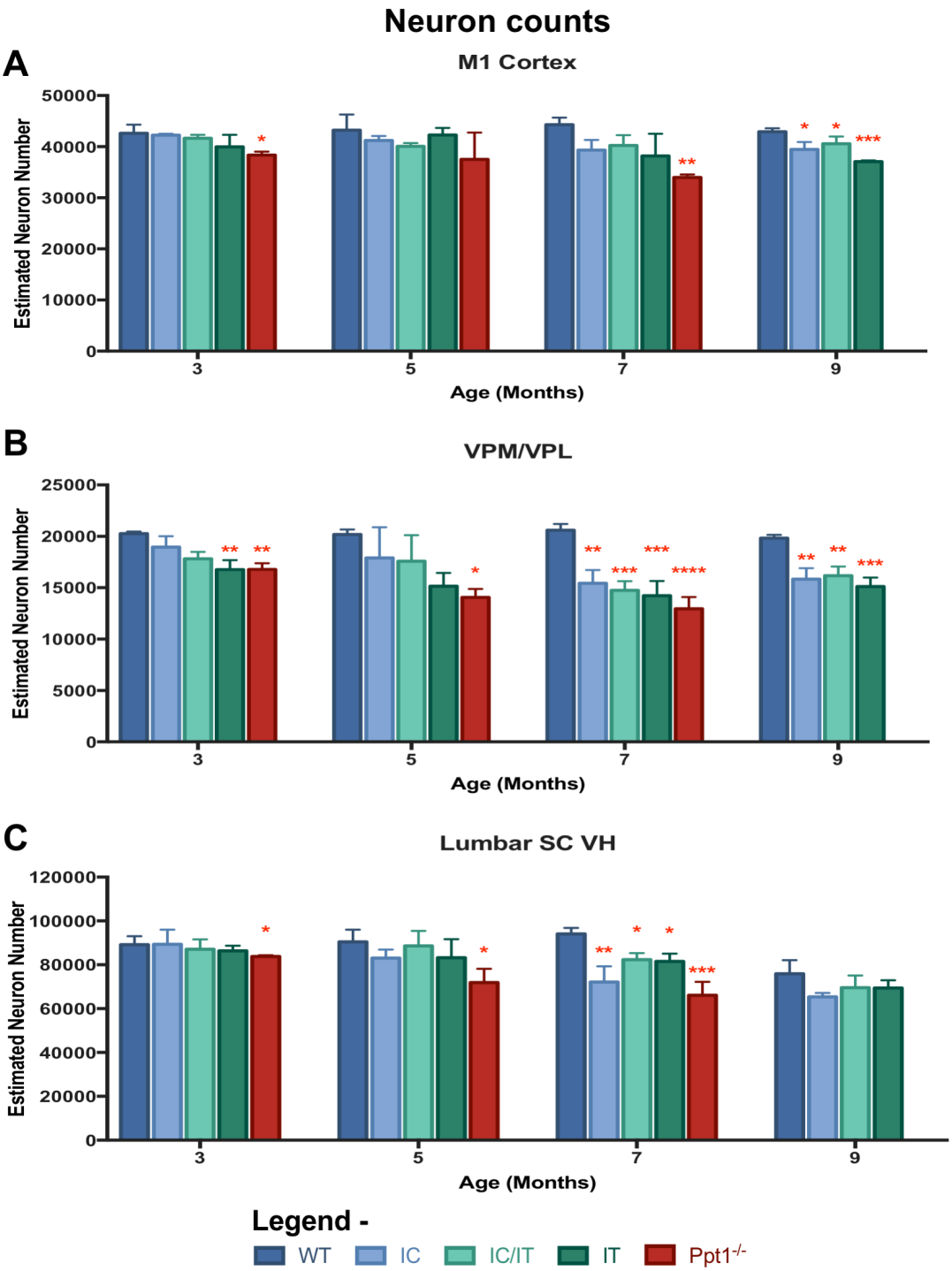

Figure 5.16– Delayed neuron loss in Ppt1$^{-/-}$ mice receiving gene therapy

*Optical fractionator estimates of neuron numbers in brain and spinal cord regions showing a delayed loss of neurons in almost all regions between 3 and 7 month time points across intracranial (IC), intrathecal (IT) and combination intracranial and intrathecal (IC/IT) treated Ppt1$^{-/-}$ mice, as compared to untreated Ppt1$^{-/-}$ mice and wildtype controls. Significance is compared to wildtype controls (red stars).). *p<0.05, **p<0.01, ***p<0.001, one-way ANOVA with post-hoc Bonferroni correction. Values shown are mean ± SEM (n=3 mice/group).*

Collectively these data reveal that combination IC/IT therapy has a greater neuroprotective effect than either IC or IT therapy alone. Both IC and IT therapy show good regional effects, but have significantly reduced impact away from the site of delivery. The rotarod testing and survival data (Figure 5.9), corroborates these data showing that combination therapy affords the best therapeutic efficacy in *Ppt1*$^{-/-}$ mice, and we can infer that this protracted disease course is in part due to the delayed neuron loss observed here (Figure 5.16).

5.4 Summary

Having demonstrated early and profound spinal cord pathology in *Ppt1*$^{-/-}$ mice, it was imperative to test whether this significantly contributes to disease progression and the appearance of sensorimotor deficits. Therefore, we tested whether targeting this region of the CNS with experimental therapies would prove beneficial in treating these mice.

A pilot study to test the feasibility of administering intrathecal human recombinant PPT1 showed a significant reduction in glial activation and autofluorescent storage material accumulation in the spinal cords and the cortex of *Ppt1*$^{-/-}$ mice. Although there was little neuroprotection afforded by this therapeutic approach at such a late time point after receiving IT administered ERT, the improvements in longevity, motor performance and some pathological features such as gliosis and AFSM accumulation (Figures 5.1-5.8) (Lu et al, 2015) showed a significantly protracted disease progression in these mice that was dose dependent. It also demonstrated that the spinal cord contributes to disease progression and that reducing pathology in this region of the CNS is not only feasible, but can also be an effective therapeutic approach in *Ppt1*$^{-/-}$ mice. Furthermore, delivering the therapy to the CSF was shown to have a greater impact on brain structures, especially the cortex, than was initially predicted.

Targeting gene therapy to the brain alone was shown not to have any significant effect on spinal cord pathology, while targeting the same therapy only to the spinal cord only showed minor improvements in brain pathology (Figures 5.10-

5.16). In contrast, adopting a combination approach to targeting both the brain and spinal cord showed the greatest improvements in longevity, motor performance and pathological features, with no overt signs of toxicity even at the early time point. Taken together, these data suggest that it will be necessary to treat both the spinal cord and brain to achieve maximum therapeutic efficacy. Interestingly, these data also show that targeting both the brain and spinal cord results in synergistic improvements, rather than a simple additive effect, as evidenced by the increased efficacy of reducing glial activation and AFSM accumulation in the thalamus (Figures 5.10-5.15). This is the first study to show such significant and long-lasting improvements in *Ppt1*$^{-/-}$ mice, not only confirming the clinical significance of the spinal cord pathology observed in these mice but also demonstrating that early, targeted therapy to sites of pathology is imperative to treating CLN1 disease.

Chapter 6. General Discussion

The research presented in this thesis represents the first study to characterize the spinal cord as a site of significant pathology in CLN1 disease, or indeed in any major form of NCL. We have also demonstrated gait defects in Ppt1 deficient (*Ppt1*$^{-/-}$) mice that may relate to this pathology, and have defined the spinal cord as a novel therapeutic target in this disease that can be treated effectively.

Characterizing the nature and progression of pathology in the spinal cord of *Ppt1*$^{-/-}$ mice has not only revealed widespread and profound changes in this region of the CNS, but also that these changes precede the onset of similar events within the brain. Furthermore, there is evidence of a postnatal developmental delay as well as significant white matter pathology that are not seen in the forebrains of these mice. Similar pathology to that seen in *Ppt1*$^{-/-}$ mice was also described in human CLN1 *post-mortem* spinal cord tissue. Taken together, these data serve to highlight the spinal cord as a novel and unexpected site of pathology that is profoundly affected early in CLN1 disease progression (Chapter 3). The presence of similar spinal cord pathology in mouse models of CLN2 and CLN3 disease suggests that this region of the CNS may also be a potential therapeutic target across various forms of NCL (Chapter 3.11).

We demonstrate a variety of novel gait abnormalities in *Ppt1*$^{-/-}$ mice, including an increased reliance on the forelimbs for support and altered inter-limb co-ordination that begin early in disease progression (Chapter 4). These early changes in gait may not only relate to the spinal cord pathology demonstrated at these ages in *Ppt1*$^{-/-}$ mice (Chapter 3), but also provide evidence for early motor deficits as seen in human CLN1 disease (Dolisca et al, 2013). This gait analysis also corroborated evidence from previous studies for a significant and overall decline in motor function with age in these mice (Dearborn et al, 2015; Gupta et al, 2001; Macauley et al, 2009).

Lastly, we show that therapeutically targeting the *Ppt1*$^{-/-}$ mouse spinal cord via intrathecal administration of either ERT or AAV-mediated gene therapy positively impacts disease progression and that the later approach combined with brain-directed gene therapy results in synergistic and significant

improvements in lifespan, behavior and pathology in these mice (Chapter 5). These data not only demonstrate the spinal cord to be clinically significant to disease progression in these mice, but that targeting it in addition to the brain will be important for the success of future therapies for CLN1 disease.

6.1 Spinal cord pathology in human and murine CLN1 disease.

The initial study of human CLN1 disease pathology briefly described the spinal cord to be atrophied, but to a lesser extent than either the forebrain or the cerebellum and as having "distended" anterior horn cells, presumably due to the accumulation of storage material (Haltia et al, 1973a; Santavuori et al, 1974). However, thus far, the brain has been considered the main locus of pathology (Bible et al, 2004; Kielar et al, 2007; Macauley et al, 2009) in CLN1 disease possibly due to the nature of clinical symptoms (Dolisca et al, 2013).

Despite the comprehensive pathological characterization of brain and cerebellar pathology in CLN1 disease (Bible et al, 2004; Kielar et al, 2007; Macauley et al, 2009), the sensorimotor deficits observed in both human cases and mouse models cannot be completely explained (Dearborn et al, 2015; Dolisca et al, 2013; Schulz et al, 2013). Combined with the limited success of various brain directed therapies (Chapter 1.6), we hypothesized the presence of significant pathology in CNS outside either the forebrain or cerebellum. We initially focused our efforts on the spinal cord due to its involvement in the sensory and motor pathways connecting the brain and peripheral nervous system (PNS) (Chapter 1.7).

a) Early generalized pathology in *Ppt1*$^{-/-}$ mice spinal cord

Given the profound and progressive pathology that has already been described in the forebrain and cerebellum of *Ppt1*$^{-/-}$ mice (Bible et al, 2004; Kielar et al, 2007; Macauley et al, 2009), it is perhaps not entirely surprising to have found some degree of pathology in the spinal cord of these mice. Indeed, the various pathological changes seen in the brain including regional atrophy, neuron loss, accumulation of autofluorescent storage material and glial activation are all also observed in the cord. However, the early onset and severity of spinal cord pathology in these mice was unexpected. Indeed, all the above pathological

phenotypes seen in the brain seem to have an earlier onset in the spinal cord (Summarized in Fig 6.1).

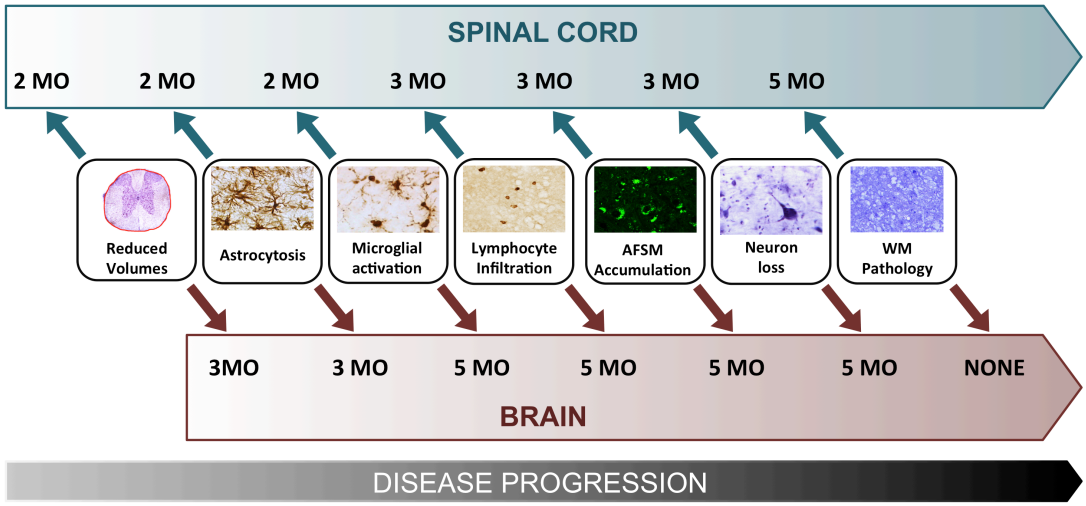

Figure 6.1 – Disease progression in the brain vs. spinal cord in Ppt1$^{-/-}$ mice.

Figure summarizing the timing of key neuropathological features in brains vs. spinal cords in Ppt1$^{-/-}$ mice. The ages shown represent the age of onset of a given pathological phenotype in that region of the CNS. All pathological phenotypes were shown to have an earlier onset in the spinal cord than in the brain with the exception of white matter (WM) pathology, which was present in the spinal cord, but not observed in the brain.

Despite this early onset of pathology, the progression of the disease in *Ppt1*$^{-/-}$ mice followed the same general pattern in the spinal cord as in the brain, with spinal cord neurons in the dorsal and ventral horns of *Ppt1*$^{-/-}$ mice showing a clearly visible increase of AFSM accumulation as early as 3 months, which is earlier than seen in the forebrain (Chapter 3.4). Furthermore, various neuron populations have hypertrophied cell bodies at 7 months (Chapter 3.5). These data indicate that not only was there an early onset in disease progression, but that the changes observed were consistent with those seen in the brain and cerebellum, indicating the presence of a similar disease process in both regions (Bible et al, 2004; Kielar et al, 2007).

Similarly, astrocytosis and microglial activation preceded significant neuron loss in the spinal cord (Chapter 3.8), in a similar fashion to in the forebrain, although CD68 reveals an earlier onset of microglial activation than F4/80 that was used

in previous studies in the forebrain (Bible et al, 2004; Kielar et al, 2007). Despite this early onset of pathology, the progression of the disease in *Ppt1*$^{-/-}$ mice essentially occurs as it does in the brain (Kielar et al, 2007; Macauley et al, 2009). This further emphasizes the role that glial activation may play in the disease progression of CLN1 disease with regions of glial activation "predicting" where neuron loss occurs in the CNS, and studies to determine the exact nature of this neuron-glia interaction are currently ongoing. These have revealed a range of functional deficits in Ppt1 deficient astrocytes and microglia, which appear to be capable of directly harming neurons (Lange, PhD thesis).

The re-distribution of AFSM from within neuron cell bodies to activated microglial cells that we documented in the spinal cord (Figure 3.8), has also been documented in the brains of CLN6 sheep (Oswald et al, 2005), most likely due to activated microglia phagocytizing dead or dying neurons. This suggests that the microglial activation seen in the *Ppt1*$^{-/-}$ spinal cord is also similar in nature to that occurring in other forms of NCL. Indeed, taken together, the glial activation observed in *Ppt1*$^{-/-}$ mouse spinal cords appears similar to that occurring in the brains of these mice, indicating that the same disease process may be at work at an earlier time point in this region of the CNS. Microglial activation and astrocytosis in the spinal cord have been shown to be associated with altered spinal cord function in spinal cord injury and diseases such as transverse myelitis and multiple sclerosis, with symptoms including increased pain, irritability and altered mobility as well as actual damage to spinal cord structures (Beh et al, 2013; Hausmann, 2003). Furthermore, the low-level infiltration of peripheral lymphocytes observed in the spinal cord, may also contribute to these symptoms, similar to the brain (Groh et al, 2013). Therefore, we may hypothesize that the progressive increase in spinal cord inflammation observed in *Ppt1*$^{-/-}$ mice may have a profound effect on the sensorimotor function in these animals, although it would take the generation of cell type-specific knockout mice to determine if this was the case experimentally.

Recently, a mouse model where Ppt1 is tethered to the LAMP1 protein in the lysosomal membrane has been generated (Cooper and Sands, personal

communication). Such a mouse model would reduce any extra-lysosomal functions of Ppt1 (Chapter 1.4 c), but would also prevent cross-correction of the enzyme by the mannose-6-phosphate (Chapter 1.6 a) receptor system both *in vivo* and *in vitro*. Therefore, this model could prove to be a powerful tool to create cell-specific knock outs of Ppt1 to study *in vivo* the contribution of glial cells to disease.

As discussed in Chapter 3.3, our data revealing the average loss of 34.4% of neurons in the dorsal horn and 28.61% in the ventral horn of *Ppt1*$^{-/-}$ mice, compared to their wildtype counterparts by 7 months of age (Table 3.1) reinforce that *Ppt1*$^{-/-}$ mice have a severe neurodegenerative pathology in the spinal cord. These values are comparable to that seen in Cln8 (*Cln8*^{mnd}) (Fujita et al, 1998; Plummer et al, 1995) `(before it was confirmed as an NCL mouse model) as well as to other models of neurodegenerative diseases affecting the spinal cord such as ALS (Dal Canto & Gurney, 1997; Ravits et al, 2007) and SMA(Simone et al, 2016; Sleigh et al, 2011), Parkinson disease (Martin et al, 2006; Vivacqua et al, 2011), Alzheimer disease (Seo et al, 2010) and HD (Valadao et al, 2016). Interestingly however, while nearly all of these diseases show a vulnerability of motor neuron populations over interneuron populations, our observations show that interneuron populations are more vulnerable than motor neurons early in disease progression in the spinal cords of *Ppt1*$^{-/-}$ mice.

The loss of calbindin positive interneurons, before either calretinin positive interneurons or motor neurons, which we saw in the spinal cord of *Ppt1*$^{-/-}$ mice (Chapter 3.3) was also observed in the brain (Kielar et al, 2007), which further suggests the common pathological themes in both regions, but this process starts at an earlier time point in the spinal cord. This initial selective loss of interneurons in the spinal cord may potentially lead to a reduction of inhibitory tone in the spinal cord that is required for the integration of central motor commands and sensory feedback signals in the spinal cord (Rossignol et al, 2006), and it would be informative to investigate whether this is the case. The loss of inhibitory interneurons in the dorsal horn of the spinal cord is associated with the development of pain and increased pruritis or itching (Adams et al,

2010; Bardoni et al, 2013; Meisner et al, 2010; Ross et al, 2010), while the loss of interneurons can also affect motor function with an initial "release" leading to increased activity of motor neurons, causing muscular spasticity and hyper-reflexia (Florman et al, 2013). These findings may in part help explain the early clinical presentation of human CLN1 disease including irritability, motor clumsiness, ataxia, spasticity and hyperkinesias (Dolisca et al, 2013; Williams et al, 2006). To further investigate this, testing *Ppt1*$^{-/-}$ mice for nociceptive assays such as von Frey testing (Bradman et al, 2015), tests for itch (Shimada & LaMotte, 2008) or other tests for pain (Wilson & Mogil, 2001) at early time points may provide further evidence of such sensory deficits. Furthermore, crossing these mice with other knockout mouse models used in pain research such those which have genes for opioid receptors, cytokines or neurotrophins genetically inactivated, may also help to further understand these mechanisms (Dierich & Kieffer, 2004). If such a sensory defect can be established, similar non-invasive tests for nociception can also be used to detect such early changes in the clinical diagnosis of CLN1 disease.

The early selective loss of interneurons before that of motor neurons suggests a similarity between pathological processes in the spinal cords and brains of *Ppt1*$^{-/-}$ mice, where there also is an early loss of GABAergic interneurons in the cortex and hippocampus (Kielar et al, 2007). There may also be a similar process in the spinal cords of *Cln8*^{mnd} mice where GABAergic interneurons are preferentially lost in the forebrain (Cooper et al, 1999), but it remains to be seen if such interneuron loss precedes motor neuron loss in the spinal cords of these mice (Plummer et al, 1995; Ranta et al, 1999). This however, is in contrast to models of other LSDs such as gangliosidoses (Hahn et al, 1997; Jellinger et al, 1982) or Neimann-Pick type A (Marmiroli et al, 2009) or type C (Dardis et al, 2016; Yan et al, 2011), which preferentially seem to affect motor neurons. The mechanism underlying this neuronal selectivity in the spinal cord, similar to that in the brain remains unexplained, and will require further work to better understand disease pathophysiology in *Ppt1*$^{-/-}$ mice.

The subsequent loss of motor neurons at 5 months, as well as the loss of primary sensory neurons in the DRG (Chapter 3.3, 3.7), may both contribute to the overall decline in motor function seen in both *Ppt1*$^{-/-}$ mice and human CLN1 disease, along with the pathology in the brain and cerebellum (Kielar et al, 2007; Macauley et al, 2009). Therefore, from our preliminary description of lumbar DRG pathology in 7 month old *Ppt1*$^{-/-}$ mice (Chapter 3.7) and given the severity of pathology affecting spinal cord neurons, it will be of great interest to study the extent and nature and progression of DRG neuron loss and how this relates to pathology within the spinal cord. It is not clear whether an inflammatory process also occurs within DRGs, as staining for satellite cells of the DRG with GFAP revealed no overt differences between genotypes (data not shown), and it will require the use of other markers such as TNF-α, IL-6, S100 or glutamine synthetase in order to determine if the disease cascade within the DRG also involves such cells (Hanani, 2005). Furthermore, staining DRG tissue for peripheral lymphocytes with CD4+CD8 did not reveal any positive staining, and therefore, further investigation will be required to see if there is any peripheral lymphocyte infiltration in this tissue, which is often associated with the development of pain (Scholz & Woolf, 2007). Understanding DRG pathology may provide us with a better understanding of in how sensory and motor pathways may be affected differentially in this disease, and may help to better explain the sensory symptoms of CLN1 disease.

Interestingly, very little change was observed when staining for synaptic markers in *Ppt1*$^{-/-}$ spinal cords, as compared to the changes that have been reported in their brains (Chapter 3.6) (Kielar et al., 2009). With the exception of changes seen in VAMP2 staining, which closely resemble those seen in the brain, staining 7 month old tissue for pre- and post-synaptic markers revealed very little change in these markers in the spinal gray matter of *Ppt1*$^{-/-}$mice. This discrepancy may also be a result of the relatively thick (40 microns) sections used to examine the synapse-rich grey matter of the spinal cord (Chapter 1.7). Furthermore, many synaptic markers are known to have “down-up” or “up-down” temporal expression profiles during disease progression (Kielar et al, 2009). Thus, analyzing 7 month old tissue may not reflect changes seen earlier in disease

progression. Alternatively, this may indicate that synaptic defects, while present, may be of a different nature to those seen in the brain. Regardless of the cause, further work will be required to determine the exact nature and temporal progression of synaptic pathology, if any, in the *Ppt1*$^{-/-}$ mouse spinal cord. Currently, we plan on employing western blotting from synaptosomal preparations to determine whether the expression of synaptic markers is significantly altered at 7 months in *Ppt1*$^{-/-}$ mouse spinal cords, as was demonstrated in their brains (Kielar et al, 2009).

In addition to the early onset of disease in the spinal cords of *Ppt1*$^{-/-}$ mice, the other unexpected feature was the simultaneous onset of pathology at all levels of the cord, involving both the dorsal and ventral horn (Chapter 3). This is in marked contrast to the regional specificity of brain pathology where there is more pronounced pathology in the sensory versus motor regions (Bible et al, 2004; Kielar et al, 2007; Macauley et al, 2009). Differences in cellular architecture and function may play a major role in the regional specificity of neuron loss in the brain of *Ppt1*$^{-/-}$ mice (Cooper, 2003; Cooper, 2010). Why there should be such fundamental differences in cellular selectivity between the *Ppt1*$^{-/-}$ brain and spinal cord is unclear, but the relatively similar regional architecture at all levels of the spinal gray matter (Chapter 1.7), as well as the high population of spinal interneurons in the dorsal and ventral horns may be determining factors in the generalized nature of spinal cord pathology in these mice. However, the existence of region-specific differences in disease mechanisms in the spinal cord of *Ppt1*$^{-/-}$ mice cannot be excluded.

b) Novel pathological phenotypes in *Ppt1*$^{-/-}$ mice spinal cord.

The difference in the age of onset as well as the generalized nature of spinal cord pathology in *Ppt1*$^{-/-}$ mice makes it important to consider that there may be slightly different disease mechanisms occurring in this region of the CNS than in the brain. This is corroborated by the presence of novel pathological phenotypes in the spinal cord that are not observed in the brain including evidence for a possible postnatal developmental delay, and significant white matter pathology.

The volumes of both the spinal gray and white matter has been shown to increase in the postnatal period in both mice and humans (Lassek AM, 1938; Sakla, 1959; Sakla, 1969). Our analysis revealed that between 1-3 months of age, in wildtype (C57BL/6) mice there is an increase in whole cord, as well as gray and white matter volumes at all levels of the cord. However, despite initially having similar postnatal spinal cord volumes at 1 month of age, *Ppt1*$^{-/-}$ mouse spinal cords fail to grow in size to the same extent (Figure 3.1, 3.2). Interestingly, this lack of spinal cord growth was seen at all levels of the cord, and was evident in both the gray and white matter. This suggests that: a) like the other pathological phenotypes that have been already mentioned, this volume change affects all levels of the cord, and b) that this delay affects the postnatal development of both the gray and white matter and may result from the loss of PPT1 function during development, as it has been implicated in processes such as axon guidance, synaptic pruning and determining cell fate during (Chu-LaGraff et al, 2010; Fabritius et al, 2014; Isosomppi et al, 1999; Minye et al, 2016). This loss of the developmental functions of PPT1 may be more apparent in the spinal cord that undergoes significant postnatal growth cord in mice (Sakla, 1969) as compared to the forebrain. Indeed, the cerebellum, which also undergoes significant postnatal development, is also severely affected in *Ppt1*$^{-/-}$ mice (Macauley et al, 2009).

The fact that the spinal white matter is affected in these mice is also a novel finding, as various studies in the brain and cerebellum have failed to observe any significant changes in the white matter in these regions of the CNS (Bible et al, 2004; Kielar et al, 2007; Macauley et al, 2009). Further evidence for white matter involvement was observed by the pronounced microglial activation in the dorsal and ventral funiculi of the cervical and lumbar cord (Chapter 3.8). Investigation of the white matter using other markers showed that greater differences were observable in sections stained for neurofilament-H (NF) and toluidine blue, with the later showing reduced axon densities in *Ppt1*$^{-/-}$ mice, as compared to those stained for Luxol fast blue or myelin basic protein (MBP) (Chapter 3.9). This was further supported from the analysis of *Thy1-YFP/Ppt1*$^{-/-}$ mouse spinal cords, which showed significant axonal degeneration in the spinal white matter in these

mice (Figure 3.17). The fact that these changes are seen at 5 months at the earliest probably means that the observed white matter pathology is likely due to axon loss as a result of neuron loss in the gray matter (Chapter 3.3), as opposed to a primarily demyelinating pathology. Further work remains to be done with regards to the age of onset of axon degeneration, as well as to understand whether any individual white matter tracts may be affected first, similar to the selectivity of neuron loss in the gray matter. Furthermore, given the changes observed with MBP staining, it will also be of interest to stain for oligodendrocyte markers to see if they are affected in the spinal cord, even though they are not obviously thought to be involved in CLN1 disease progression (Cooper et al, 2015).

The early onset of spinal cord pathology in *Ppt1*$^{-/-}$ mice raises the possibility of disease spreading rostrally from the spinal cord to the brain. This is substantiated further by the fact that one of the earlier sites of pathology in the brain is the ventral posterior (VPM/VPL) nucleus of the thalamus where the spino-thalamic pathways synapse (Chapter 1.7) (Kielar et al, 2007). Similar data has also been shown for the dorsal lateral geniculate nucleus (LGnD) in the visual pathway following retinal degeneration (Griffey et al, 2005; Kielar et al, 2007). Together, these data suggest that the disease progresses from the periphery to the CNS and raises the possibility of the anterograde (or retrograde in the case of motor pathways) progression of the disease. This may be because the death of spinal cord neurons may lead to reduced afferent input to the postsynaptic thalamic or cortical neurons that they project to (or receive input from), causing them to, in turn, become dysfunctional. In this sense it could potentially be considered as an anterogradely spreading deafferentation along these interconnected pathways. A similar "knock-on effect" of disease propagation has been suggested in a variety of neurodegenerative conditions (Braak & Del Tredici, 2011; Fornito et al, 2015; Raj et al, 2012; Yates, 2012), and our data suggest this may also be the case in CLN1 disease. Our findings also raise the possibility that there may be significant pathology in the PNS that may have a role in initiating spinal cord pathology. Therefore, in addition to the DRG, studying the staging of pathology in the dorsal column nuclei in the brainstem

(Chapter 1.7), as well as peripheral nerves will be crucial to developing our understanding of disease progression. Analyzing the same *Thy1-YFP/Ppt1*$^{-/-}$ reporter mice that we used to reveal the loss of spinal axons (Chapter 3.9) provides robust preliminary data that the sciatic nerve undergoes a similar profound loss of axons (Cooper and Sands, personal communication). It will be important to follow up these preliminary observations to define the time course and mechanisms by which this occurs. Furthermore, the brainstem also houses the centers for cardiovascular and respiratory control (Batten & Deuchars, 2009; Coote, 2007; Dampney, 1994; Smith et al, 2007; Wong-Riley & Liu, 2005). With compromised respiratory and cardiovascular function a major clinical theme across the NCLs (Dolisca et al, 2013; Williams et al, 2006), it will also be very informative to know how much brainstem pathology contributes to these symptoms in CLN1 disease.

c) Spinal cord pathology in human CLN1 disease and mouse models of other NCLs.

There have been very few descriptions of spinal cord pathology in any form of human NCL (Anderson et al, 2013; Bruun et al, 1991). However, there was evidence of some degree of pathology in human CLN1 disease spinal cords (Haltia et al, 1973a; Santavuori et al, 1974), and we were fortunate to gain access to this original *post mortem* sample.

Our analysis revealed more profound pathology in this tissue than originally described with abundant accumulation of AFSM, microglial activation and changes in neuron morphology (Chapter 3.10). This closely resembled the pathology seen in *Ppt1*$^{-/-}$ mice, and provides evidence for the presence of similarly profound pathology in human CLN1 disease. The dearth of samples has precluded our ability to obtain quantitative data for human pathology and given our findings in murine and human CLN1 disease, the collection of spinal cords and peripheral nerves at autopsy would be recommended.

Furthermore, given the early onset of spinal cord pathology in *Ppt1*$^{-/-}$ mice and following the neuroradiological studies in human CLN1 disease brains

(Vanhanen et al, 2004), it would be interesting to revisit these imaging data sets to look for any changes in the spinal cord volumes and/or intensities in these cases. This may prove a non-invasive option as either a diagnostic tool or a prognostic measure of therapeutic efficacy.

A brief study of neuronal morphology and glial activation in mouse models for CLN2 and CLN3 disease demonstrated the existence of pathology in the spinal cords of these mice as well (Chapter 3.11). Despite visibly different pathological phenotypes in each of these forms of NCL, this serves to highlight the spinal cord as being involved in multiple forms of NCL. As such, detailing the nature and progression of spinal cord pathology will be useful in not only understanding these diseases, but also in possibly uncovering any common pathological phenotypes across the NCLs. This will likely also inform us about which therapeutic approaches may be best suited for each form of NCL.

6.2 Changes in the gait of *Ppt1*$^{-/-}$ mice

Gait is the sequential and cyclical stepping pattern used by animals for locomotion (Biewener, 1990; Takakusaki, 2013). The activity of neural circuits within the spinal cord plays a vital role in controlling gait and locomotion in mammals, acting as a "central pattern generator" that receives inputs from sensory afferents as well as descending impulses from supra-spinal centers in order to modulate motor function (Dietz, 1997; Dietz, 2003). From this description, it is easy to see that the gait is more than just the result of motor function, but rather the coordinated functioning of sensorimotor, cortical, cerebellar, vestibular and musculoskeletal systems mediated through the spinal cord and PNS (Takakusaki, 2013).

Gait abnormalities are seen in a variety of neurological disorders or as a result of spinal cord or PNS injury (Dietz, 1997; Enriquez-Algeciras et al, 2011; Hamers et al, 2006; Lin et al, 2001; Starkey et al, 2005; Vrinten & Hamers, 2003; Wooley et al, 2005; Zhou et al, 2015). Indeed Parkinsonism, a clinical syndrome that affects gait and includes resting tremors, bradykinesia, rigidity and postural instability is associated with many LSDs including GM1 and GM2 gangliosidoses, Gaucher

disease, Fabry-Anderson disease and even the major forms of NCLs, which may show some or all of these features (Shachar et al, 2011; Tuite & Krawczewski, 2007)

Ppt1$^{-/-}$ mice show a significantly reduced ability to stay on a rotarod starting at 5 months, as well as other sensorimotor and gait deficits that have been previously described (Chapter 1.5) (Dearborn et al, 2015; Griffey et al, 2006; Gupta et al, 2001). However, until recently, there was little evidence of any significant sensorimotor deficits before this age, with young *Ppt1*$^{-/-}$ mice apparently showing changes in the walking initiation test as well as their ability to climb up a 60° inclined plane (Dearborn et al, 2015). However, this reported phenotype is very different to the clinical progression of human CLN1 disease, where there is an early onset of clumsiness and motor deficits (Dolisca et al, 2013; Williams et al, 2006). Therefore, given our findings of early and profound pathology in the spinal cords of *Ppt1*$^{-/-}$ mice (Chapter 3), we decided to analyze the gait of these mice at all ages between 1-7 months using the *CatWalk XT* gait analysis system (Noldus, Wageningen, Netherlands) to further detail the sensorimotor deficits in these mice.

At 2 months, *Ppt1*$^{-/-}$ mice demonstrated a significantly altered gait with greater speed of movement, larger strides and shorter step cycles (Chapter 4.2 – 4.4). At this time, there is significant glial activation in the spinal cords of these mice, which may be associated with pain and irritation, as previously discussed (Chapter 6.1). Furthermore, it has also been shown that mice may go through a phase of "galloping" or asymmetrical gait during postnatal development before 1 month (Eilam, 1997), and while *Ppt1*$^{-/-}$ mice appear to move in a similar fashion to their wildtype counterparts at 1 month, their apparently delayed postnatal development of the spinal cord may contribute to the re-emergence of such an asymmetrical gait at this age. This increase in asymmetrical gait is evidenced by a significant increase in single, diagonal and four-limb support at 2 months (Figure 4.13).

After 5 months of age, there is not only severe neurodegeneration in the spinal cords of *Ppt1*$^{-/-}$ mice (Chapter 3), but also significant neurodegenerative

pathology in the brain and cerebellum (Kielar et al, 2007; Macauley et al, 2009). Thus, the altered gait observed is likely the result of a profoundly neurodegenerative disease, and shows a significant sensorimotor decline across various measures including, speed of movement, step cycle measures, paw intensities, stride length and step sequences (Chapter 4). There is also an increased need to use more than two limbs for support during a step cycle (Chapter 4.5). These data are in agreement with previous studies that demonstrate significant sensorimotor deficits in these mice after 5 months of age (Dearborn et al, 2015; Griffey et al, 2006; Gupta et al, 2001).

Ppt1$^{-/-}$ mice also showed an increased dependence on their forelimbs, evidenced by increased print length, width and area of the fore paws as early as 2 months. An increase in forepaw print width was also seen from 5 months of age, along with a converse decrease of hind paw print width (Figure 4.6). Meanwhile, these mice tend to place their hind paws closer to their forepaws during each step cycle, indicating a preference for support with the fore limbs, starting at 2 months and also seen consistently after 4 months (Figure 4.14). They also demonstrate an increased base of support (BOS) observed in the forepaws with age, presumably because of their increasing use of the forelimbs for stability, while the hind paws only demonstrated an increased BOS after 6 months (Figure 4.12). The phase dispersions between each set of ipsilateral limbs were significantly increased in *Ppt1*$^{-/-}$ mice after 5 months, indicating that the forepaws remained in contact with the plate (or floor) longer when moving their hind paws (Figure 4.16). *Ppt1*$^{-/-}$ mice also showed significantly higher preference for altered AA pattern step sequence, compared to the AB pattern that is more commonly seen in wildtype mice (Figure 4.15). This change has been shown to be associated with spinal cord lesions in the ventral and lateral funiculi of cats (Bem et al, 1995), and indicates that there is perhaps a differential involvement of white matter tracts during disease progression. It will require further analysis of the white matter tracts to determine how they are affected during disease progression, in order to provide histological confirmation of this.

Therefore we see that overall, starting at an early time point of 2 months, *Ppt1*$^{-/-}$ mice demonstrate a greater dependence on their forelimbs for locomotion, with reduced use of the hind limbs with age, which closely resemble the changes in hind limb mobility that were first observed in the later stages of disease progression in these mice (Gupta et al, 2001). This differential alteration in gait where the hind limbs are more affected is commonly seen in spinal cord degeneration in Parkinson and Huntington diseases (Amende et al, 2005). Nonetheless, this difference between fore and hind limb coordination in *Ppt1*$^{-/-}$ mice is juxtaposed to the generalized nature of their spinal cord pathology (Chapter 6.1), and perhaps indicates that there may either be a differential pathological involvement of the white matter tracts that we are yet to uncover and/or the peripheral nerves. As mentioned before (Chapter 6.1), initial analysis of *Thy1-YFP/Ppt1*$^{-/-}$ mouse sciatic nerves has shown that this may indeed be the case in the PNS (Cooper and Sands, personal communication).

This study has therefore demonstrated the existence of early sensorimotor phenotypes in *Ppt1*$^{-/-}$ mice that had previously not been known to exist and are possibly caused by the significant spinal cord pathology at this time point. It also served to confirm the significant and progressive decline of sensorimotor function after 5 months in these mice as a combined result of cortical, cerebellar and spinal cord pathology.

6.3 The spinal cord as a novel therapeutic target in CLN1 disease.

As previously discussed, there has only been limited success with various systemic and brain-directed therapeutic strategies for CLN1 disease (Chapter 1.6). Our research has demonstrated early and profound pathology in the spinal cord of *Ppt1*$^{-/-}$ mice (Chapter 3) that had previously not been described. We therefore hypothesized that this pathology was not ameliorated by previous brain-directed therapies approaches, and that targeting the spinal cord in *Ppt1*$^{-/-}$ mice would have a beneficial impact on disease progression.

A well-established approach for delivering therapeutic agents to the spinal cord is by means of intrathecal (IT) injections into the cerebrospinal fluid (CSF)

commonly at the level of the lumbar vertebrae. This approach is quite common in clinical practice, especially for the management of cancer-related and chronic pain (Bruel & Burton, 2016; Pope et al, 2016). IT delivery of therapeutics has also been demonstrated to be effective in delivering protein therapeutics to the CNS in a variety of disorders including stroke, brain tumors and neurodegenerative disorders including the LSDs (Calias et al, 2014). However, a disadvantage of this approach is that accurately measuring actual doses delivered to the CSF can be difficult (Follett et al, 2003). Also, IT drug delivery has been associated with the development of certain complications such as an inflammatory response along with the development of antibodies against the therapeutic agent (Follett et al, 2003), high infection rates (Aprili et al, 2009; Motta & Antonello, 2014) and granuloma formation (Duarte et al, 2012). The risk of developing these complications is directly related to the duration of intrathecal catheter placement (Fluckiger et al, 2008). Nevertheless, for severe neurodegenerative conditions such as the NCLs, the benefits of IT drug delivery may well outweigh the risks, especially via gene therapy, which is theoretically a one-time treatment.

a) IT Enzyme replacement therapy (ERT) in *Ppt1*$^{-/-}$ mice

High-dose IT ERT into the sub-arachnoid space in the lumbar region was shown to be effective in ameliorating brain pathology in mouse model of CLN2 disease (Xu et al, 2011). This promising data led us to revisit previous attempts at ERT with recombinant human PPT1 in CLN1 disease (Hu et al, 2012; Lu et al, 2010). Delivering recombinant PPT1 intrathecally resulted in significant improvements in the lifespan and motor function of *Ppt1*$^{-/-}$ mice (Lu et al, 2015). Perhaps surprisingly, histological examination of mice sacrificed 6 months after receiving the ERT revealed a significant reduction of gliosis, especially in the case of microglial activation, as well as a significant reduction of AFSM accumulation (Chapter 5.2, Lu et al, 2015). These findings were very promising for two reasons – a) given that these mice were sacrificed nearly 6 months after receiving the ERT, there was significantly prolonged activity of IT delivered PPT1 even at this late time point, and b) that delivery of the recombinant enzyme at the lumbar level of the spine resulted in a good spread of the enzyme in the CSF, as evidenced by the reduction of gliosis and AFSM in the cerebral cortex (Figures 5.2-5.7).

However, in this study IT administration of PPT1 did not have any significant effect on pathology in the deeper brain structures (thalamic nuclei) in these mice (Chapter 5.2) which may be due to the lack of penetration of the brain parenchyma by the enzyme from the CSF (Lu et al, 2015). Therefore, it is likely that the lifespan and functional improvements observed in these mice cannot solely be explained by the moderate improvements observed in brain pathology. Indeed, the histological improvements observed in the spinal cords of these mice were generally more pronounced than those seen in the brain (Chapter 5.2). From these data, we can see that not only is the IT administration of PPT1 effective in targeting the spinal cord in these mice, but that ameliorating spinal cord pathology appears to have a significant effect on functional motor deficits and lifespan in *Ppt1*$^{-/-}$ mice.

The long-lasting and widespread effects seen by early IT delivery of recombinant PPT1 may be due to a combination of factors such as the dynamics of CSF flow and reabsorption (Calias et al, 2014). These factors allow for the distribution of the enzyme to at least some brain structures, as well as the low enzyme activity required to restore normal cellular function in CLN1 disease (Griffey et al, 2006). Indeed, a low level of PPT1 activity was surprisingly observed in the brains of treated mice up to 240 days (6 months) after IT administration (Lu et al, 2015). Such a long-lasting effect of early administration of the therapy may be the result of a more protracted course of neurodegeneration, and although there was no significant neuroprotective effect of IT ERT observed at 6 months, the improved survival and motor performance of these mice suggest that they may also display delayed neurodegeneration. Furthermore, there was a clear dose-dependent improvement of IT-administered ERT upon lifespan and motor performance (Lu et al, 2015). This is also apparent in the reduction of AFSM and gliosis (Figures 5.2-5.7) (Lu et al, 2015), and demonstrates that further titration of the dose could have significantly beneficial effects.

Therefore, this study clearly provides proof of principal that IT delivery of drugs can successfully target spinal cord pathology in *Ppt1*$^{-/-}$ mice and that this route of

administration can also potentially help ameliorate disease pathology in the brain by achieving a widespread distribution of the enzyme.

b) Combination intracranial (IC) and IT gene therapy in *Ppt1*$^{-/-}$ mice.

To date the most promising of the brain-directed therapies in CLN1 disease has been the intracranial administration of gene therapy (Griffey et al, 2006; Hawkins-Salsbury et al, 2013). The efficacy of this strategy in *Ppt1*$^{-/-}$ mice has also been shown to improve when combined with other systemic therapeutic approaches (Macauley et al, 2012; Macauley et al, 2014; Roberts et al, 2012). We therefore hypothesized that IC delivery of AAV-mediated gene therapy alone may not be sufficient to impact the spinal cord pathology in these mice that we have described here (Chapter 3). Furthermore, targeting spinal cord pathology in *Ppt1*$^{-/-}$ mice by means of IT injection, which was shown to be a feasible route for administering ERT (Lu et al, 2015), with similar AAV vectors used for the IC injections could have an additional beneficial effect to the IC therapy. Furthermore, we also used a new AAV vector – AAV2/9, which was shown to have widespread distribution throughout the CNS upon IT delivery as well as better transduction capability than the AAV2/5 vector that was previously used (Dayton et al, 2012; Macauley et al, 2014; Schuster et al, 2014; Swain et al, 2014).

All treatment groups showed improved measures of lifespan and motor function, with *Ppt1*$^{-/-}$ mice that received a combination of IC and IT therapy (IC/IT mice) performing significantly better than mice receiving either treatment alone (Chapter 5.3). The fact that mice receiving IT injections only preformed significantly better than untreated *Ppt1*$^{-/-}$ mice demonstrates that targeting the spinal cord with AAV-mediated gene therapy had a significant effect on disease progression, as we had seen previously with ERT (Lu et al, 2015). Interestingly, the IC/IT mice lived for an average of 19.3 months, an increase of around 11 months from the untreated *Ppt1*$^{-/-}$ mice. This is the first study to show such a significant improvement in these parameters in these mice, and further substantiates our data for the spinal cord being crucial to disease progression in *Ppt1*$^{-/-}$ mice.

Histological examination of the brains and spinal cords of mice from the different treatment groups at 3, 5, 7 and 9 months revealed that the spinal cords of IC treated *Ppt1*$^{-/-}$ mice showed that they still displayed significant pathology including gliosis, AFSM accumulation and neuron loss similar to untreated mutant mice (Chapter 5.3). This data confirms our hypothesis that brain-directed AAV-mediated gene therapy alone did not impact spinal cord pathology. As expected, the IT only treated mice showed significant reduction in all pathological parameters in the spinal cord, with some improvements also seen in the cerebral cortex, although not to the same extent as that seen in IC only treated mice. This demonstrates that IT injection of AAV2/9 vector resulted in its distribution to structures beyond the spinal cord, as seen before with ERT (Lu et al, 2015). Interestingly, IC/IT combination treated mice showed improvements in both brain and spinal cord pathology, but in general, these were more than the sum of its parts, with spinal cord and cortical pathology almost being reduced to levels comparable to wildtype mice. This was particularly evident in the VPM/VPL nuclei of the thalamus, where neither IC nor IT therapy alone had a greatly significant impact on pathology in these mice, but IC/IT mice showed significant improvements in almost all pathological parameters.

Despite the therapies administered, all treatment groups still show a progression of pathology in the brain and spinal cord across the time points measured, with IC/IT mice again faring much better than mice receiving either IC or IT gene therapy alone. This data suggests that despite the exciting data, the mice still demonstrated progressive pathology elsewhere in the body that still needs to be treated to improve efficacy still further. Despite this, our data from this study is the first to demonstrate such significant synergistic improvements in lifespan, behavior and pathology and has further demonstrated the clinical significance of targeting the spinal cord in CLN1 disease. It will therefore be very important for future therapies to target spinal cord pathology to ensure better treatment outcomes for patients.

Taken together, both studies of IT ERT as well as combination IC/IT gene therapy have served to demonstrate the clinical significance of targeting spinal cord

pathology in *Ppt1*$^{-/-}$ mice, showing that early intervention is key to dealing with the early onset of this pathology in this region of the CNS. With growing evidence of systemic pathology in *Ppt1*$^{-/-}$ mice (Galvin et al, 2008) as well as the increasing number of systemic therapies that are available (Chapter 1.6), it is becoming more evident that the treatment of CLN1 disease will be better facilitated by early intervention and the use of combined therapeutic approaches that can successfully target the various loci of pathology.

6.4 Future directions

From the data presented in this thesis, it is evident that despite having shown the spinal cord to be severely affected in murine and human CLN1 disease, as well as it being an effective therapeutic target, there still is much work to be done towards the complete understanding of CLN1 disease pathology and to optimize therapies for clinical application.

a) Further analysis of the CLN1 spinal cord

Our data from the analysis of *Ppt1*$^{-/-}$ mouse spinal cords has revealed a novel phenotype of spinal white matter pathology (Chapter 3.9). It will therefore be important to understand the exact nature of this pathology. The development of the *Thy1-YFP/Ppt1*$^{-/-}$ mouse has been shown to be of great use in studying axonopathies, (Castelvetri et al, 2011; Feng et al, 2000) (Chapter 3.9) and further analysis of the progression of this pathology in these mice will be very informative regarding white matter pathology. Electron microscopy can also help study the thickness of the myelin sheath and axon density and morphology at various levels of the cord. It will also be helpful to track the progression of axon density loss in the different white matter tracts of the spinal cord, and see how this may relate to the onset of sensorimotor deficits (Chapter 4). It will also be important to detail the progression of pathology in the DRGs at various levels (Chapter 3.7), to study not only neuron loss, but also the possible involvement of satellite glial cells and the infiltration of peripheral lymphocytes in this region.

Our initial histological survey of synaptic markers did not reveal any significant synaptic changes in the spinal cord (Chapter 3.6), but the exact nature and cause

of any potential synaptic pathology as well as its temporal progression is yet to be detailed. We shall do this by means of western blotting of synaptosomal preparations at various time points, as was performed on the brain tissue of *Ppt1*$^{-/-}$ mice (Kielar et al, 2009).

Neuron-glial interactions have been shown to be vital to maintaining the normal functioning of the CNS (Belin & Hardin, 1991; Burda & Sofroniew, 2014; Fields & Stevens-Graham, 2002; Sofroniew & Vinters, 2010). The presence of significant glial activation that precedes neurodegeneration in *Ppt1*$^{-/-}$ mice in the brain (Kielar et al, 2007; Macauley et al, 2009) and spinal cord (Chapter 3.8) has been well established. However, the exact nature of this neuron-glia interaction and whether it may be detrimental to neuron function is poorly understood. *In-vitro* studies of neuron-glia interactions with cortical tissue from *Ppt1*$^{-/-}$ mice are currently ongoing (Lange, PhD thesis), and it will now be important to study whether similar effects exist in spinal cord tissue.

The presence of early, widespread pathology spinal cord pathology with novel phenotypes of postnatal developmental delay and white matter pathology raises the possibility of region-specific mechanisms at work in the spinal cord compared to the brain. We therefore propose proteomic profiling of brain and spinal cord tissue at early (3 months) and late (7 months) time points. This will allow us to compare and contrast the effects of Ppt1 deficiency at both these regions over the course of the disease, and will help to shed light on any region-specific functions of Ppt1 and possibly help us understand the greater vulnerability of the spinal cord in CLN1 disease.

b) Analysis of other possible pathological loci in *Ppt1*$^{-/-}$ mice.

Given the early onset and unexpected severity of disease detailed in the spinal cords of *Ppt1*$^{-/-}$ mice, we must now additionally characterize pathological changes in other regions that would have otherwise not have thought to be involved in disease progression. The early onset of disease in the spinal cord and the subsequent pathology seen in the thalamic nuclei of the brain (Chapter 3) (Kielar et al, 2007) has made us consider the antero- or retrograde transmission

of disease in a caudo-rostral fashion (Chapter 6.1). Therefore, the analysis of the brainstem and peripheral nerves in *Ppt1*$^{-/-}$ mice will be informative of the overall progression of disease in these mice. The Thy1-YFP mice (Castelvetri et al, 2011; Feng et al, 2000) will also prove a useful tool for studying the integrity of peripheral nervous tissue in greater detail. The brainstem acts as the "relay-station" for the dorsal column (Chapter 1.7) as well as housing the centers for CNS control of cardiovascular and respiratory function (Batten & Deuchars, 2009; Smith et al, 2007), which are affected in CLN1 disease (Dolisca et al, 2013; Williams et al, 2006). As such analysis of the brainstem will also provide great insight into whether these defects are caused by PNS or CNS pathology.

In addition to studying the central control centers for cardiac and respiratory function, describing any pathology that may be present in the heart and lungs of these mice will tell us whether the clinical symptoms are due to a combination of factors, or either central or peripheral pathology alone. Similarly, studying the autonomic nervous system may also help to explain the autonomic disturbances seen in human CLN1 disease (Williams et al, 2006; Wisniewski et al, 2001).

Therefore, the characterization of pathology in various loci in *Ppt1*$^{-/-}$ mice will help to provide a more comprehensive understanding of disease progression in CLN1 disease.

c) Large animal models and human CLN1 studies

Mouse models of the different forms of NCL have been very informative of disease pathology and progression (Bible et al, 2004; Kielar et al, 2007; Pontikis et al, 2004; Pontikis et al, 2005; Sleat et al, 2004). However, the recent CRISPR/Cas9 mediated generation of a PPT1 R151X sheep model, and the ongoing efforts to generate a pig model of CLN1 disease (Wishart and Cooper, personal communication), will allow us to study disease progression in animals whose CNS architecture is closer to that of humans. Indeed, it is foreseen that these models may more closely follow the disease progression seen in humans and characterizing the pathological progression of disease in them will be very

useful as it has proved in other forms of NCL (Amorim et al, 2015; Oswald et al, 2005).

From our description of spinal cord pathology in a human CLN1 disease case, it is evident that there is potentially similar pathology in humans as there is in *Ppt1*$^{-/-}$ mice. However, it must be remembered that this is just a single isolated case and that the extreme scarcity of available human CLN1 spinal tissue makes any further comparison difficult. Therefore, it is suggested that spinal cord samples also be collected routinely at *post mortem* for cases of CLN1 disease, as well as other forms of NCL. Furthermore, from the radiological changes seen in human CLN1 disease (Vanhanen et al, 2004), it will also be interesting to see whether similar studies of the spinal cord will reveal any changes, and whether this testing can help to track the progression of disease in affected cases.

d) Therapeutic implications of spinal cord pathology in CLN1 disease.

Targeting the spinal cord in *Ppt1*$^{-/-}$ mice has not only shown it to be an effective therapeutic target in CLN1 disease (Chapter 5), but that when combined with brain-directed therapies, there is a significantly greater synergistic effect than would be anticipated (Chapter 5.3). Therefore, to build on this exciting and novel data, it is likely that therapies must now be optimized in order to target multiple foci of pathology.

There is also increasing evidence for pathology outside the CNS in *Ppt1*$^{-/-}$ mice (Galvin et al, 2008) and that targeting this pathology in combination with brain directed therapies can have a positive impact on disease progression (Macauley et al, 2012; Macauley et al, 2014; Roberts et al, 2012). Therefore future therapeutic approaches may have to additionally target systemic pathology. While these separate routes of drug administration may be impractical as well as increase the risk for infections, the severity and rate of progression of CLN1 disease may allow for such clinical intervention.

A different approach to reduce the number of injections may be through the delivery of either ERT or AAV-mediated gene therapy via the ventricles as a

repeated dosing using a cannula (Katz et al, 2014), for ERT or a one-time injection for gene therapy by transducing the ependyma (Katz et al, 2015), an approach that has been shown to be useful in a canine model of CLN2 disease. Intravenous delivery of gene therapy has also been attempted in non-human primates, and while this approach showed a higher level of glial transduction as a result of having to cross the blood-brain barrier, it led to accumulation of large amounts of the vector in the liver (Gray et al, 2011). This may have toxic effects, and as it stands this approach will need much more work before being viable for therapy.

Despite the success in treating disease progression in *Ppt1*$^{-/-}$ mice, it will be important to test these therapeutic approaches in larger species (Chapter 6.4 c). As a virtue of the size and complexity of the CNS in these larger animals, there will very likely be differences in drug distribution and efficacy. Recent attempts at gene therapy in a sheep model of CLN5 disease have shown great promise (Palmer and Mitchell, personal communication) and these models will therefore serve as a crucial intermediate step before therapies for CLN1 disease can be clinically tested.

6.5 Conclusion

The research presented in this thesis serves to highlight the early and profound involvement of the spinal cord in CLN1 disease progression that adversely affects sensorimotor function, as well as revealing the spinal cord as a novel and effective therapeutic target in this disease. We have shown significant and widespread pathology in the spinal cords of *Ppt1*$^{-/-}$ mice, describing similar changes to that seen in the brains of these mice, but with an earlier onset (Figure 6.1), as well as novel disease phenotypes including postnatal developmental delay and significant white matter pathology. Similar pathological changes were also observed in a human CLN1 disease *post-mortem* sample, indicating that this pathology is not confined to the murine disease, and were also present in other mouse models of NCL, implying that spinal cord pathology may be a common feature in various forms of NCL (Chapter 3).

Automated gait analysis has revealed novel phenotypes of gait abnormalities at early time points in *Ppt1*$^{-/-}$ mice and along with the documented pathological changes in the spinal cords, has helped to better understand the sensorimotor deficits seen in these mice as well as to reconcile those observed in human CLN1 disease (Chapter 4).

We have also shown that therapeutically targeting the spinal cord with either enzyme replacement therapy or AAV-mediated gene therapy significantly and synergistically improves the lifespan, motor function and pathology in *Ppt1*$^{-/-}$ mice. Furthermore, the combination of intracranial (IC) and intrathecal (IT) administration of AAV-mediated gene therapy has shown the most improvements in these parameters of any experimental therapy for CLN1 disease to date (Chapter 5). These data serve not only to emphasize the clinical significance of targeting spinal cord pathology, but also that combination approaches that target the various pathological foci in the CNS may be the most effective approach for future CLN1 disease therapies.

Despite the success of this CNS-directed combination therapeutic strategy, the evidence for significant pathology outside the CNS in CLN1 disease (Galvin et al, 2008) and the fact that combination treated mice still do not live as long as their wildtype counterparts (Chapter 5.3) means that further work is required to elucidate the exact nature, as well as the temporal and anatomical progression of disease outside the CNS in *Ppt1*$^{-/-}$ mice. Moreover, therapeutically targeting only the CNS could lead to non-neuronal symptoms, which would have otherwise been 'masked' by the severity and rapid onset of neurological symptoms, and may still significantly contribute to disease progression.

In light of this study highlighting the spinal cord as a novel site of pathology as well as the growing body of evidence for other possible regions of pathology in these mice, a holistic therapeutic approach should be encouraged so as to allow for the greatest therapeutic effect. Therefore, there is still much work to be done in murine, as well as larger animal models (as these become available) before moving towards human clinical studies for CLN1 disease. Furthermore, despite

the success of recent clinical trials for CLN2 disease using ERT (*https://clinicaltrials.gov/show/NCT02678689*), the finding of spinal cord pathology in other forms of NCL (Chapter 3.11) could have similar implications for therapeutic strategies in these and possibly other forms of NCL as well.

This study therefore represents a significant departure from the forebrain-centric view of the NCLs, showing that CLN1 disease affects the CNS at large. Along with the evidence of other systems also being affected, this means that future therapeutic approaches must now be designed to target all these sites of pathology so as to be able to provide effective means of treating these diseases in humans.

References

Adams HR, Beck CA, Levy E, Jordan R, Kwon JM, Marshall FJ, Vierhile A, Augustine EF, de Blieck EA, Pearce DA et al (2010) Genotype does not predict severity of behavioural phenotype in juvenile neuronal ceroid lipofuscinosis (Batten disease). Dev Med Child Neurol 52**:** 637-643

Ahtiainen L, Kolikova J, Mutka AL, Luiro K, Gentile M, Ikonen E, Khiroug L, Jalanko A, Kopra O (2007) Palmitoyl protein thioesterase 1 (Ppt1)-deficient mouse neurons show alterations in cholesterol metabolism and calcium homeostasis prior to synaptic dysfunction. Neurobiology of disease 28**:** 52-64

Ahtiainen L, Van Diggelen OP, Jalanko A, Kopra O (2003) Palmitoyl protein thioesterase 1 is targeted to the axons in neurons. The Journal of comparative neurology 455**:** 368-377

Aicart-Ramos C, Valero RA, Rodriguez-Crespo I (2011) Protein palmitoylation and subcellular trafficking. Biochim Biophys Acta 1808**:** 2981-2994

Amende I, Kale A, McCue S, Glazier S, Morgan JP, Hampton TG (2005) Gait dynamics in mouse models of Parkinson's disease and Huntington's disease. J Neuroeng Rehabil 2**:** 20

Amorim IS, Mitchell NL, Palmer DN, Sawiak SJ, Mason R, Wishart TM, Gillingwater TH (2015) Molecular neuropathology of the synapse in sheep with CLN5 Batten disease. Brain Behav 5**:** e00401

Anderson GW, Goebel HH, Simonati A (2013) Human pathology in NCL. Biochim Biophys Acta 1832**:** 1807-1826

Andressen C, Blumcke I, Celio MR (1993) Calcium-binding proteins: selective markers of nerve cells. Cell Tissue Res 271**:** 181-208

Appelmans F, De Duve C (1955) Tissue fractionation studies. 3. Further observations on the binding of acid phosphatase by rat-liver particles. The Biochemical journal 59**:** 426-433

Aprili D, Bandschapp O, Rochlitz C, Urwyler A, Ruppen W (2009) Serious complications associated with external intrathecal catheters used in cancer pain patients: a systematic review and meta-analysis. Anesthesiology 111**:** 1346-1355

Araque A, Parpura V, Sanzgiri RP, Haydon PG (1999) Tripartite synapses: glia, the unacknowledged partner. Trends in Neurosciences 22**:** 208-215

Armitage JO (1994) Bone marrow transplantation. The New England journal of medicine 330**:** 827-838

Aschauer DF, Kreuz S, Rumpel S (2013) Analysis of transduction efficiency, tropism and axonal transport of AAV serotypes 1, 2, 5, 6, 8 and 9 in the mouse brain. PloS one 8**:** e76310

Autti T, Joensuu R, Aberg L (2007) Decreased T2 signal in the thalami may be a sign of lysosomal storage disease. Neuroradiology 49**:** 571-578

Ballabio A, Gieselmann V (2009) Lysosomal disorders: from storage to cellular damage. Biochim Biophys Acta 1793**:** 684-696

Bardoni R, Takazawa T, Tong CK, Choudhury P, Scherrer G, Macdermott AB (2013) Pre- and postsynaptic inhibitory control in the spinal cord dorsal horn. Ann N Y Acad Sci 1279**:** 90-96

Batten F (1903) Cerebral degeneration with symmetrical changes in the maculae in two members of a family. Trans Ophthalmol Soc UK 23**:** 386-390

Batten FE, Mayou MS (1915) Family Cerebral Degeneration with Macular Changes. Proc R Soc Med 8**:** 70-90

Batten TF, Deuchars SA (2009) How the head rules the heart: the chemical neuroanatomy of the pathways of cardiovascular regulation. J Chem Neuroanat 38**:** 143-144

Bavarsad Shahripour R, Harrigan MR, Alexandrov AV (2014) N-acetylcysteine (NAC) in neurological disorders: mechanisms of action and therapeutic opportunities. Brain Behav 4**:** 108-122

Beck M (2001) Variable clinical presentation in lysosomal storage disorders. Journal of inherited metabolic disease 24 Suppl 2**:** 47-51; discussion 45-46

Beh SC, Greenberg BM, Frohman T, Frohman EM (2013) Transverse myelitis. Neurol Clin 31**:** 79-138

Belin MF, Hardin H (1991) [Neuron-glia interactions]. Encephale 17**:** 467-473

Bem T, Gorska T, Majczynski H, Zmyslowski W (1995) Different patterns of fore-hindlimb coordination during overground locomotion in cats with ventral and lateral spinal lesions. Exp Brain Res 104**:** 70-80

Bennett MJ, Rakheja D (2013) The neuronal ceroid-lipofuscinoses. Developmental disabilities research reviews 17**:** 254-259

Bible E, Gupta P, Hofmann SL, Cooper JD (2004) Regional and cellular neuropathology in the palmitoyl protein thioesterase-1 null mutant mouse model of infantile neuronal ceroid lipofuscinosis. Neurobiology of disease 16**:** 346-359

Biewener AA (1990) Biomechanics of mammalian terrestrial locomotion. Science 250**:** 1097-1103

Bonsignore M, Tessa A, Di Rosa G, Piemonte F, Dionisi-Vici C, Simonati A, Calamoneri F, Tortorella G, Santorelli FM (2006) Novel CLN1 mutation in two Italian sibs with late infantile neuronal ceroid lipofuscinosis. Eur J Paediatr Neurol 10**:** 154-156

Bouchelion A, Zhang Z, Li Y, Qian H, Mukherjee AB (2014) Mice homozygous for c.451C>T mutation in Cln1 gene recapitulate INCL phenotype. Ann Clin Transl Neurol 1**:** 1006-1023

Boya P (2012) Lysosomal function and dysfunction: mechanism and disease. Antioxid Redox Signal 17**:** 766-774

Braak H, Del Tredici K (2011) Alzheimer's pathogenesis: is there neuron-to-neuron propagation? Acta Neuropathol 121**:** 589-595

Braakman I, Bulleid NJ (2011) Protein folding and modification in the mammalian endoplasmic reticulum. Annual review of biochemistry 80**:** 71-99

Bradman MJ, Ferrini F, Salio C, Merighi A (2015) Practical mechanical threshold estimation in rodents using von Frey hairs/Semmes-Weinstein monofilaments: Towards a rational method. J Neurosci Methods 255**:** 92-103

Braulke T, Bonifacino JS (2009) Sorting of lysosomal proteins. Biochim Biophys Acta 1793**:** 605-614

Brean A (2004) [An account of a strange instance of disease--Stengel-Batten-Spielmayer-Vogt disease]. Tidsskr Nor Laegeforen 124**:** 970-971

Bronson RT, Donahue LR, Johnson KR, Tanner A, Lane PW, Faust JR (1998) Neuronal ceroid lipofuscinosis (nclf), a new disorder of the mouse linked to chromosome 9. Am J Med Genet 77**:** 289-297

Brooks DA, Muller VJ, Hopwood JJ (2006) Stop-codon read-through for patients affected by a lysosomal storage disorder. Trends Mol Med 12**:** 367-373

Brown AG (1981) Organization in the spinal cord : the anatomy and physiology of identified neurones, Berlin ; New York: Springer-Verlag

Bruel BM, Burton AW (2016) Intrathecal Therapy for Cancer-Related Pain. Pain Med

Bruun I, Reske-Nielsen E, Oster S (1991) Juvenile ceroid-lipofuscinosis and calcifications of the CNS. Acta Neurol Scand 83**:** 1-8

Burda JE, Sofroniew MV (2014) Reactive gliosis and the multicellular response to CNS damage and disease. Neuron 81**:** 229-248

Calias P, Banks WA, Begley D, Scarpa M, Dickson P (2014) Intrathecal delivery of protein therapeutics to the brain: a critical reassessment. Pharmacol Ther 144**:** 114-122

Camp LA, Hofmann SL (1993) Purification and properties of a palmitoyl-protein thioesterase that cleaves palmitate from H-Ras. J Biol Chem 268**:** 22566-22574

Camp LA, Verkruyse LA, Afendis SJ, Slaughter CA, Hofmann SL (1994) Molecular cloning and expression of palmitoyl-protein thioesterase. J Biol Chem 269**:** 23212-23219

Carcel-Trullols J, Kovacs AD, Pearce DA (2015) Cell biology of the NCL proteins: What they do and don't do. Biochim Biophys Acta 1852**:** 2242-2255

Carri MT, Ferri A, Cozzolino M, Calabrese L, Rotilio G (2003) Neurodegeneration in amyotrophic lateral sclerosis: the role of oxidative stress and altered homeostasis of metals. Brain Res Bull 61**:** 365-374

Castelvetri LC, Givogri MI, Zhu H, Smith B, Lopez-Rosas A, Qiu X, van Breemen R, Bongarzone ER (2011) Axonopathy is a compounding factor in the pathogenesis of Krabbe disease. Acta Neuropathol 122**:** 35-48

Cearley CN, Wolfe JH (2006) Transduction characteristics of adeno-associated virus vectors expressing cap serotypes 7, 8, 9, and Rh10 in the mouse brain. Molecular therapy : the journal of the American Society of Gene Therapy 13**:** 528-537

Chang YF, Imam JS, Wilkinson MF (2007) The nonsense-mediated decay RNA surveillance pathway. Annual review of biochemistry 76**:** 51-74

Chattopadhyay S, Ito M, Cooper JD, Brooks AI, Curran TM, Powers JM, Pearce DA (2002a) An autoantibody inhibitory to glutamic acid decarboxylase in the neurodegenerative disorder Batten disease. Human molecular genetics 11**:** 1421-1431

Chattopadhyay S, Kriscenski-Perry E, Wenger DA, Pearce DA (2002b) An autoantibody to GAD65 in sera of patients with juvenile neuronal ceroid lipofuscinoses. Neurology 59**:** 1816-1817

Chen G, Li HM, Chen YR, Gu XS, Duan S (2007) Decreased estradiol release from astrocytes contributes to the neurodegeneration in a mouse model of Niemann-Pick disease type C. Glia 55**:** 1509-1518

Cho S, Dawson G (2000) Palmitoyl protein thioesterase 1 protects against apoptosis mediated by Ras-Akt-caspase pathway in neuroblastoma cells. Journal of neurochemistry 74**:** 1478-1488

Cho S, Dawson PE, Dawson G (2000) In vitro depalmitoylation of neurospecific peptides: implication for infantile neuronal ceroid lipofuscinosis. Journal of neuroscience research 59**:** 32-38

Cho SK, Hofmann SL (2004) pdf1, a palmitoyl protein thioesterase 1 Ortholog in Schizosaccharomyces pombe: a yeast model of infantile Batten disease. Eukaryotic cell 3**:** 302-310

Cho TA (2015) Spinal cord functional anatomy. Continuum (Minneap Minn) 21**:** 13-35

Chu-LaGraff Q, Blanchette C, O'Hern P, Denefrio C (2010) The Batten disease Palmitoyl Protein Thioesterase 1 gene regulates neural specification and axon connectivity during Drosophila embryonic development. PloS one 5**:** e14402

Cooper JD (2003) Progress towards understanding the neurobiology of Batten disease or neuronal ceroid lipofuscinosis. Current opinion in neurology 16**:** 121-128

Cooper JD (2010) The neuronal ceroid lipofuscinoses: the same, but different? Biochemical Society transactions 38**:** 1448-1452

Cooper JD, Messer A, Feng AK, Chua-Couzens J, Mobley WC (1999) Apparent loss and hypertrophy of interneurons in a mouse model of neuronal ceroid lipofuscinosis: evidence for partial response to insulin-like growth factor-1 treatment. The Journal of neuroscience : the official journal of the Society for Neuroscience 19**:** 2556-2567

Cooper JD, Russell C, Mitchison HM (2006) Progress towards understanding disease mechanisms in small vertebrate models of neuronal ceroid lipofuscinosis. Biochim Biophys Acta 1762**:** 873-889

Cooper JD, Tarczyluk MA, Nelvagal HR (2015) Towards a new understanding of NCL pathogenesis. Biochim Biophys Acta 1852**:** 2256-2261

Coote JH (2007) Landmarks in understanding the central nervous control of the cardiovascular system. Exp Physiol 92**:** 3-18

Cotman SL, Karaa A, Staropoli JF, Sims KB (2013) Neuronal ceroid lipofuscinosis: impact of recent genetic advances and expansion of the clinicopathologic spectrum. Current neurology and neuroscience reports 13**:** 366

Cotman SL, Vrbanac V, Lebel LA, Lee RL, Johnson KA, Donahue LR, Teed AM, Antonellis K, Bronson RT, Lerner TJ et al (2002) Cln3(Deltaex7/8) knock-in mice with the common JNCL mutation exhibit progressive neurologic disease that begins before birth. Human molecular genetics 11**:** 2709-2721

Coulthard P, Pleuvry BJ, Brewster M, Wilson KL, Macfarlane TV (2002) Gait analysis as an objective measure in a chronic pain model. J Neurosci Methods 116**:** 197-213

Coulthard P, Simjee SU, Pleuvry BJ (2003) Gait analysis as a correlate of pain induced by carrageenan intraplantar injection. J Neurosci Methods 128**:** 95-102

Cox TM, Cachon-Gonzalez MB (2012) The cellular pathology of lysosomal diseases. The Journal of pathology 226**:** 241-254

Dal Canto MC, Gurney ME (1997) A low expressor line of transgenic mice carrying a mutant human Cu,Zn superoxide dismutase (SOD1) gene develops pathological changes that most closely resemble those in human amyotrophic lateral sclerosis. Acta Neuropathol 93**:** 537-550

Dampney RA (1994) Functional organization of central pathways regulating the cardiovascular system. Physiol Rev 74**:** 323-364

Dardis A, Zampieri S, Canterini S, Newell KL, Stuani C, Murrell JR, Ghetti B, Fiorenza MT, Bembi B, Buratti E (2016) Altered localization and functionality of TAR DNA Binding Protein 43 (TDP-43) in niemann- pick disease type C. Acta Neuropathol Commun 4**:** 52

Das AK, Becerra CH, Yi W, Lu JY, Siakotos AN, Wisniewski KE, Hofmann SL (1998) Molecular genetics of palmitoyl-protein thioesterase deficiency in the U.S. J Clin Invest 102**:** 361-370

Dayton RD, Wang DB, Klein RL (2012) The advent of AAV9 expands applications for brain and spinal cord gene delivery. Expert Opin Biol Ther 12**:** 757-766

De Duve C, Pressman BC, Gianetto R, Wattiaux R, Appelmans F (1955) Tissue fractionation studies. 6. Intracellular distribution patterns of enzymes in rat-liver tissue. The Biochemical journal 60**:** 604-617

Dearborn JT, Harmon SK, Fowler SC, O'Malley KL, Taylor GT, Sands MS, Wozniak DF (2015) Comprehensive functional characterization of murine infantile Batten disease including Parkinson-like behavior and dopaminergic markers. Sci Rep 5**:** 12752

Deeg HJ, Shulman HM, Albrechtsen D, Graham TC, Storb R, Koppang N (1990) Batten's disease: failure of allogeneic bone marrow transplantation to arrest disease progression in a canine model. Clin Genet 37**:** 264-270

Defelipe J, Gonzalez-Albo MC, Del Rio MR, Elston GN (1999) Distribution and patterns of connectivity of interneurons containing calbindin, calretinin, and parvalbumin in visual areas of the occipital and temporal lobes of the macaque monkey. The Journal of comparative neurology 412**:** 515-526

Desnick RJ, Astrin KH, Bishop DF (1989) Fabry disease: molecular genetics of the inherited nephropathy. Adv Nephrol Necker Hosp 18**:** 113-127

Di Malta C, Fryer JD, Settembre C, Ballabio A (2012) Astrocyte dysfunction triggers neurodegeneration in a lysosomal storage disorder. Proceedings of the National Academy of Sciences of the United States of America 109**:** E2334-2342

Dierenfeld AD, McEntee MF, Vogler CA, Vite CH, Chen AH, Passage M, Le S, Shah S, Jens JK, Snella EM et al (2010) Replacing the enzyme alpha-L-iduronidase at birth ameliorates symptoms in the brain and periphery of dogs with mucopolysaccharidosis type I. Sci Transl Med 2**:** 60ra89

Dierich A, Kieffer BL (2004) Knockout mouse models in pain research. Methods Mol Med 99**:** 269-299

Dietz V (1997) Neurophysiology of gait disorders: present and future applications. Electroencephalogr Clin Neurophysiol 103**:** 333-355

Dietz V (2003) Spinal cord pattern generators for locomotion. Clin Neurophysiol 114**:** 1379-1389

Dodge JC, Clarke J, Treleaven CM, Taksir TV, Griffiths DA, Yang W, Fidler JA, Passini MA, Karey KP, Schuchman EH et al (2009) Intracerebroventricular infusion of acid sphingomyelinase corrects CNS manifestations in a mouse model of Niemann-Pick A disease. Experimental neurology 215**:** 349-357

Doherty GJ, McMahon HT (2009) Mechanisms of endocytosis. Annual review of biochemistry 78**:** 857-902

Dolisca SB, Mehta M, Pearce DA, Mink JW, Maria BL (2013) Batten disease: clinical aspects, molecular mechanisms, translational science, and future directions. Journal of child neurology 28**:** 1074-1100

Donsante A, Levy B, Vogler C, Sands MS (2007) Clinical response to persistent, low-level beta-glucuronidase expression in the murine model of mucopolysaccharidosis type VII. Journal of inherited metabolic disease 30**:** 227-238

Drew PD, Xu J, Storer PD, Chavis JA, Racke MK (2006) Peroxisome proliferator-activated receptor agonist regulation of glial activation: relevance to CNS inflammatory disorders. Neurochem Int 49**:** 183-189

Duarte RV, Raphael JH, Southall JL, Baker C, Ashford RL (2012) Intrathecal granuloma formation as result of opioid delivery: systematic literature review of case reports and analysis against a control group. Clin Neurol Neurosurg 114**:** 577-584

Edgley SA (2001) Organisation of inputs to spinal interneurone populations. J Physiol 533**:** 51-56

Eilam D (1997) Postnatal development of body architecture and gait in several rodent species. J Exp Biol 200**:** 1339-1350

El-Husseini AE, Craven SE, Chetkovich DM, Firestein BL, Schnell E, Aoki C, Bredt DS (2000) Dual palmitoylation of PSD-95 mediates its vesiculotubular sorting, postsynaptic targeting, and ion channel clustering. J Cell Biol 148**:** 159-172

Elliger SS, Elliger CA, Aguilar CP, Raju NR, Watson GL (1999) Elimination of lysosomal storage in brains of MPS VII mice treated by intrathecal administration of an adeno-associated virus vector. Gene therapy 6**:** 1175-1178

Enriquez-Algeciras M, Ding D, Chou TH, Wang J, Padgett KR, Porciatti V, Bhattacharya SK (2011) Evaluation of a transgenic mouse model of multiple sclerosis with noninvasive methods. Invest Ophthalmol Vis Sci 52**:** 2405-2411

Fabritius AL, Vesa J, Minye HM, Nakano I, Kornblum H, Peltonen L (2014) Neuronal ceroid lipofuscinosis genes, CLN2, CLN3 and CLN5 are spatially and temporally co-expressed in a developing mouse brain. Exp Mol Pathol 97**:** 484-491

Feng G, Mellor RH, Bernstein M, Keller-Peck C, Nguyen QT, Wallace M, Nerbonne JM, Lichtman JW, Sanes JR (2000) Imaging neuronal subsets in transgenic mice expressing multiple spectral variants of GFP. Neuron 28**:** 41-51

Fields RD, Stevens-Graham B (2002) New insights into neuron-glia communication. Science 298**:** 556-562

Filimonenko M, Stuffers S, Raiborg C, Yamamoto A, Malerod L, Fisher EM, Isaacs A, Brech A, Stenmark H, Simonsen A (2007) Functional multivesicular bodies are required for autophagic clearance of protein aggregates associated with neurodegenerative disease. J Cell Biol 179**:** 485-500

Finn R, Kovacs AD, Pearce DA (2011) Altered sensitivity of cerebellar granule cells to glutamate receptor overactivation in the Cln3(Deltaex7/8)-knock-in mouse model of juvenile neuronal ceroid lipofuscinosis. Neurochem Int 58**:** 648-655

Finn R, Kovacs AD, Pearce DA (2012) Altered glutamate receptor function in the cerebellum of the Ppt1(-/-) mouse, a murine model of infantile neuronal ceroid lipofuscinosis. Journal of neuroscience research 90**:** 367-375

Flannagan RS, Jaumouille V, Grinstein S (2012) The cell biology of phagocytosis. Annu Rev Pathol 7**:** 61-98

Florman JE, Duffau H, Rughani AI (2013) Lower motor neuron findings after upper motor neuron injury: insights from postoperative supplementary motor area syndrome. Front Hum Neurosci 7**:** 85

Fluckiger B, Knecht H, Grossmann S, Felleiter P (2008) Device-related complications of long-term intrathecal drug therapy via implanted pumps. Spinal Cord 46**:** 639-643

Follett KA, Burchiel K, Deer T, Dupen S, Prager J, Turner MS, Coffey RJ (2003) Prevention of intrathecal drug delivery catheter-related complications. Neuromodulation 6**:** 32-41

Fornito A, Zalesky A, Breakspear M (2015) The connectomics of brain disorders. Nat Rev Neurosci 16**:** 159-172

Fossale E, Wolf P, Espinola JA, Lubicz-Nawrocka T, Teed AM, Gao H, Rigamonti D, Cattaneo E, MacDonald ME, Cotman SL (2004) Membrane trafficking and mitochondrial abnormalities precede subunit c deposition in a cerebellar cell model of juvenile neuronal ceroid lipofuscinosis. BMC Neurosci 5**:** 57

Fujita K, Yamauchi M, Matsui T, Titani K, Takahashi H, Kato T, Isomura G, Ando M, Nagata Y (1998) Increase of glial fibrillary acidic protein fragments in the spinal cord of motor neuron degeneration mutant mouse. Brain Res 785**:** 31-40

Fuller M, Meikle PJ, Hopwood JJ (2006) Epidemiology of lysosomal storage diseases: an overview. In Fabry Disease: Perspectives from 5 Years of FOS, Mehta A, Beck M, Sunder-Plassmann G (eds). Oxford

Futerman AH, van Meer G (2004) The cell biology of lysosomal storage disorders. Nature reviews Molecular cell biology 5**:** 554-565

Galvin N, Vogler C, Levy B, Kovacs A, Griffey M, Sands MS (2008) A murine model of infantile neuronal ceroid lipofuscinosis-ultrastructural evaluation of storage in the central nervous system and viscera. Pediatr Dev Pathol 11**:** 185-192

Garcia-Arencibia M, Hochfeld WE, Toh PP, Rubinsztein DC (2010) Autophagy, a guardian against neurodegeneration. Semin Cell Dev Biol 21**:** 691-698

Gavin M, Wen GY, Messing J, Adelman S, Logush A, Jenkins EC, Brown WT, Velinov M (2013) Substrate Reduction Therapy in Four Patients with Milder CLN1

Mutations and Juvenile-Onset Batten Disease Using Cysteamine Bitartrate. JIMD Rep 11**:** 87-92

Geraets RD, Koh S, Hastings ML, Kielian T, Pearce DA, Weimer JM (2016) Moving towards effective therapeutic strategies for Neuronal Ceroid Lipofuscinosis. Orphanet J Rare Dis 11**:** 40

Getty AL, Pearce DA (2011) Interactions of the proteins of neuronal ceroid lipofuscinosis: clues to function. Cellular and molecular life sciences : CMLS 68**:** 453-474

Ghosh P, Dahms NM, Kornfeld S (2003) Mannose 6-phosphate receptors: new twists in the tale. Nature reviews Molecular cell biology 4**:** 202-212

Goebel HH (1995) The neuronal ceroid-lipofuscinoses. Journal of child neurology 10**:** 424-437

Goldstein JL, Brown MS, Anderson RG, Russell DW, Schneider WJ (1985) Receptor-mediated endocytosis: concepts emerging from the LDL receptor system. Annu Rev Cell Biol 1**:** 1-39

Goswami R, Ahmed M, Kilkus J, Han T, Dawson SA, Dawson G (2005) Differential regulation of ceramide in lipid-rich microdomains (rafts): antagonistic role of palmitoyl:protein thioesterase and neutral sphingomyelinase 2. Journal of neuroscience research 81**:** 208-217

Gray SJ, Matagne V, Bachaboina L, Yadav S, Ojeda SR, Samulski RJ (2011) Preclinical differences of intravascular AAV9 delivery to neurons and glia: a comparative study of adult mice and nonhuman primates. Molecular therapy : the journal of the American Society of Gene Therapy 19**:** 1058-1069

Gray SJ, Nagabhushan Kalburgi S, McCown TJ, Jude Samulski R (2013) Global CNS gene delivery and evasion of anti-AAV-neutralizing antibodies by intrathecal AAV administration in non-human primates. Gene therapy 20**:** 450-459

Griffey M, Bible E, Vogler C, Levy B, Gupta P, Cooper J, Sands MS (2004) Adeno-associated virus 2-mediated gene therapy decreases autofluorescent storage material and increases brain mass in a murine model of infantile neuronal ceroid lipofuscinosis. Neurobiology of disease 16**:** 360-369

Griffey M, Macauley SL, Ogilvie JM, Sands MS (2005) AAV2-mediated ocular gene therapy for infantile neuronal ceroid lipofuscinosis. Molecular therapy : the journal of the American Society of Gene Therapy 12**:** 413-421

Griffey MA, Wozniak D, Wong M, Bible E, Johnson K, Rothman SM, Wentz AE, Cooper JD, Sands MS (2006) CNS-directed AAV2-mediated gene therapy ameliorates functional deficits in a murine model of infantile neuronal ceroid lipofuscinosis. Molecular therapy : the journal of the American Society of Gene Therapy 13**:** 538-547

Groh J, Kuhl TG, Ip CW, Nelvagal HR, Sri S, Duckett S, Mirza M, Langmann T, Cooper JD, Martini R (2013) Immune cells perturb axons and impair neuronal survival in a mouse model of infantile neuronal ceroid lipofuscinosis. Brain 136**:** 1083-1101

Grubman A, Pollari E, Duncan C, Caragounis A, Blom T, Volitakis I, Wong A, Cooper J, Crouch PJ, Koistinaho J et al (2014) Deregulation of biometal homeostasis: the missing link for neuronal ceroid lipofuscinoses? Metallomics 6**:** 932-943

Gundersen HJ, Jensen EB (1987) The efficiency of systematic sampling in stereology and its prediction. J Microsc 147**:** 229-263

Gundersen HJ, Jensen EB, Kieu K, Nielsen J (1999) The efficiency of systematic sampling in stereology--reconsidered. J Microsc 193**:** 199-211

Gupta P, Soyombo AA, Atashband A, Wisniewski KE, Shelton JM, Richardson JA, Hammer RE, Hofmann SL (2001) Disruption of PPT1 or PPT2 causes neuronal ceroid lipofuscinosis in knockout mice. Proceedings of the National Academy of Sciences of the United States of America 98**:** 13566-13571

Hahn CN, del Pilar Martin M, Schroder M, Vanier MT, Hara Y, Suzuki K, Suzuki K, d'Azzo A (1997) Generalized CNS disease and massive GM1-ganglioside accumulation in mice defective in lysosomal acid beta-galactosidase. Human molecular genetics 6**:** 205-211

Haltia M (2006) The neuronal ceroid-lipofuscinoses: from past to present. Biochim Biophys Acta 1762**:** 850-856

Haltia M, Goebel HH (2013) The neuronal ceroid-lipofuscinoses: a historical introduction. Biochim Biophys Acta 1832**:** 1795-1800

Haltia M, Rapola J, Santavuori P (1973a) Infantile type of so-called neuronal ceroid-lipofuscinosis. Histological and electron microscopic studies. Acta Neuropathol 26**:** 157-170

Haltia M, Rapola J, Santavuori P, Keranen A (1973b) Infantile type of so-called neuronal ceroid-lipofuscinosis. 2. Morphological and biochemical studies. J Neurol Sci 18**:** 269-285

Hamers FP, Koopmans GC, Joosten EA (2006) CatWalk-assisted gait analysis in the assessment of spinal cord injury. J Neurotrauma 23**:** 537-548

Hamers FP, Lankhorst AJ, van Laar TJ, Veldhuis WB, Gispen WH (2001) Automated quantitative gait analysis during overground locomotion in the rat: its application to spinal cord contusion and transection injuries. J Neurotrauma 18**:** 187-201

Hanani M (2005) Satellite glial cells in sensory ganglia: from form to function. Brain Res Brain Res Rev 48**:** 457-476

Hausmann ON (2003) Post-traumatic inflammation following spinal cord injury. Spinal Cord 41**:** 369-378

Hawkins-Salsbury JA, Cooper JD, Sands MS (2013) Pathogenesis and therapies for infantile neuronal ceroid lipofuscinosis (infantile CLN1 disease). Biochim Biophys Acta 1832**:** 1906-1909

Helenius A, Aebi M (2001) Intracellular functions of N-linked glycans. Science 291**:** 2364-2369

Hellsten E, Vesa J, Olkkonen VM, Jalanko A, Peltonen L (1996) Human palmitoyl protein thioesterase: evidence for lysosomal targeting of the enzyme and disturbed cellular routing in infantile neuronal ceroid lipofuscinosis. The EMBO journal 15**:** 5240-5245

Hemsley KM, Luck AJ, Crawley AC, Hassiotis S, Beard H, King B, Rozek T, Rozaklis T, Fuller M, Hopwood JJ (2009) Examination of intravenous and intra-CSF protein delivery for treatment of neurological disease. Eur J Neurosci 29**:** 1197-1214

Hers HG (1965) Inborn Lysosomal Diseases. Gastroenterology 48**:** 625-633

Hickey AJ, Chotkowski HL, Singh N, Ault JG, Korey CA, MacDonald ME, Glaser RL (2006) Palmitoyl-protein thioesterase 1 deficiency in Drosophila melanogaster causes accumulation of abnormal storage material and reduced life span. Genetics 172**:** 2379-2390

Hirsch EC, Breidert T, Rousselet E, Hunot S, Hartmann A, Michel PP (2003) The role of glial reaction and inflammation in Parkinson's disease. Ann N Y Acad Sci 991**:** 214-228

Hofmann SL, Das AK, Lu JY, Wisniewski KE, Gupta P (2001) Infantile neuronal ceroid lipofuscinosis: no longer just a 'Finnish' disease. Eur J Paediatr Neurol 5 Suppl A**:** 47-51

Hollak CE, Evers L, Aerts JM, van Oers MH (1997) Elevated levels of M-CSF, sCD14 and IL8 in type 1 Gaucher disease. Blood Cells Mol Dis 23**:** 201-212

Hopwood JJ, Bunge S, Morris CP, Wilson PJ, Steglich C, Beck M, Schwinger E, Gal A (1993) Molecular basis of mucopolysaccharidosis type II: mutations in the iduronate-2-sulphatase gene. Human mutation 2**:** 435-442

Hu J, Lu JY, Wong AM, Hynan LS, Birnbaum SG, Yilmaz DS, Streit BM, Lenartowicz EM, Thompson TC, Cooper JD et al (2012) Intravenous high-dose enzyme replacement therapy with recombinant palmitoyl-protein thioesterase reduces visceral lysosomal storage and modestly prolongs survival in a preclinical mouse model of infantile neuronal ceroid lipofuscinosis. Molecular genetics and metabolism 107**:** 213-221

Isosomppi J, Heinonen O, Hiltunen JO, Greene ND, Vesa J, Uusitalo A, Mitchison HM, Saarma M, Jalanko A, Peltonen L (1999) Developmental expression of palmitoyl protein thioesterase in normal mice. Brain research Developmental brain research 118**:** 1-11

Ivy GO, Schottler F, Wenzel J, Baudry M, Lynch G (1984) Inhibitors of lysosomal enzymes: accumulation of lipofuscin-like dense bodies in the brain. Science 226**:** 985-987

Jalanko A, Braulke T (2009) Neuronal ceroid lipofuscinoses. Biochim Biophys Acta 1793**:** 697-709

Jalanko A, Vesa J, Manninen T, von Schantz C, Minye H, Fabritius AL, Salonen T, Rapola J, Gentile M, Kopra O et al (2005) Mice with Ppt1Deltaex4 mutation

replicate the INCL phenotype and show an inflammation-associated loss of interneurons. Neurobiology of disease 18**:** 226-241

Jankowska E (2001) Spinal interneuronal systems: identification, multifunctional character and reconfigurations in mammals. J Physiol 533**:** 31-40

Jarvela I, Lehtovirta M, Tikkanen R, Kyttala A, Jalanko A (1999) Defective intracellular transport of CLN3 is the molecular basis of Batten disease (JNCL). Human molecular genetics 8**:** 1091-1098

Jellinger K, Anzil AP, Seemann D, Bernheimer H (1982) Adult GM2 gangliosidosis masquerading as slowly progressive muscular atrophy: motor neuron disease phenotype. Clin Neuropathol 1**:** 31-44

Jeong SY, Crooks DR, Wilson-Ollivierre H, Ghosh MC, Sougrat R, Lee J, Cooperman S, Mitchell JB, Beaumont C, Rouault TA (2011) Iron insufficiency compromises motor neurons and their mitochondrial function in Irp2-null mice. PloS one 6**:** e25404

Jeyakumar M, Thomas R, Elliot-Smith E, Smith DA, van der Spoel AC, d'Azzo A, Perry VH, Butters TD, Dwek RA, Platt FM (2003) Central nervous system inflammation is a hallmark of pathogenesis in mouse models of GM1 and GM2 gangliosidosis. Brain 126**:** 974-987

Kalviainen R, Eriksson K, Losekoot M, Sorri I, Harvima I, Santavuori P, Jarvela I, Autti T, Vanninen R, Salmenpera T et al (2007) Juvenile-onset neuronal ceroid lipofuscinosis with infantile CLN1 mutation and palmitoyl-protein thioesterase deficiency. European journal of neurology : the official journal of the European Federation of Neurological Societies 14**:** 369-372

Katz ML, Coates JR, Sibigtroth CM, Taylor JD, Carpentier M, Young WM, Wininger FA, Kennedy D, Vuillemenot BR, O'Neill CA (2014) Enzyme replacement therapy

attenuates disease progression in a canine model of late-infantile neuronal ceroid lipofuscinosis (CLN2 disease). Journal of neuroscience research 92**:** 1591-1598

Katz ML, Tecedor L, Chen Y, Williamson BG, Lysenko E, Wininger FA, Young WM, Johnson GC, Whiting RE, Coates JR et al (2015) AAV gene transfer delays disease onset in a TPP1-deficient canine model of the late infantile form of Batten disease. Sci Transl Med 7**:** 313ra180

Kettenmann H, Hanisch UK, Noda M, Verkhratsky A (2011) Physiology of microglia. Physiol Rev 91**:** 461-553

Kettenmann H, Verkhratsky A (2011) [Neuroglia--living nerve glue]. Fortschr Neurol Psychiatr 79**:** 588-597

Khaibullina A, Kenyon N, Guptill V, Quezado MM, Wang L, Koziol D, Wesley R, Moya PR, Zhang Z, Saha A et al (2012) In a model of Batten disease, palmitoyl protein thioesterase-1 deficiency is associated with brown adipose tissue and thermoregulation abnormalities. PloS one 7**:** e48733

Kielar C, Maddox L, Bible E, Pontikis CC, Macauley SL, Griffey MA, Wong M, Sands MS, Cooper JD (2007) Successive neuron loss in the thalamus and cortex in a mouse model of infantile neuronal ceroid lipofuscinosis. Neurobiology of disease 25**:** 150-162

Kielar C, Wishart TM, Palmer A, Dihanich S, Wong AM, Macauley SL, Chan CH, Sands MS, Pearce DA, Cooper JD et al (2009) Molecular correlates of axonal and synaptic pathology in mouse models of Batten disease. Human molecular genetics 18**:** 4066-4080

Kim SJ, Zhang Z, Lee YC, Mukherjee AB (2006) Palmitoyl-protein thioesterase-1 deficiency leads to the activation of caspase-9 and contributes to rapid neurodegeneration in INCL. Human molecular genetics 15**:** 1580-1586

Kim SJ, Zhang Z, Sarkar C, Tsai PC, Lee YC, Dye L, Mukherjee AB (2008) Palmitoyl protein thioesterase-1 deficiency impairs synaptic vesicle recycling at nerve terminals, contributing to neuropathology in humans and mice. J Clin Invest 118**:** 3075-3086

Kimelberg HK, Norenberg MD (1989) Astrocytes. Sci Am 260**:** 66-72, 74, 76

Kingma SD, Bodamer OA, Wijburg FA (2015) Epidemiology and diagnosis of lysosomal storage disorders; challenges of screening. Best Pract Res Clin Endocrinol Metab 29**:** 145-157

Kiselyov K, Yamaguchi S, Lyons CW, Muallem S (2010) Aberrant Ca2+ handling in lysosomal storage disorders. Cell Calcium 47**:** 103-111

Klein AD, Futerman AH (2013) Lysosomal storage disorders: old diseases, present and future challenges. Pediatr Endocrinol Rev 11 Suppl 1**:** 59-63

Kloos AD, Fisher LC, Detloff MR, Hassenzahl DL, Basso DM (2005) Stepwise motor and all-or-none sensory recovery is associated with nonlinear sparing after incremental spinal cord injury in rats. Experimental neurology 191**:** 251-265

Kluver H, Barrera E (1953) A method for the combined staining of cells and fibers in the nervous system. J Neuropathol Exp Neurol 12**:** 400-403

Kohlschutter A, Schulz A (2009) Towards understanding the neuronal ceroid lipofuscinoses. Brain & development 31**:** 499-502

Koike M, Shibata M, Ohsawa Y, Nakanishi H, Koga T, Kametaka S, Waguri S, Momoi T, Kominami E, Peters C et al (2003) Involvement of two different cell death pathways in retinal atrophy of cathepsin D-deficient mice. Mol Cell Neurosci 22**:** 146-161

Kollmann K, Uusi-Rauva K, Scifo E, Tyynela J, Jalanko A, Braulke T (2013) Cell biology and function of neuronal ceroid lipofuscinosis-related proteins. Biochim Biophys Acta 1832**:** 1866-1881

Komine O, Yamanaka K (2015) Neuroinflammation in motor neuron disease. Nagoya J Med Sci 77**:** 537-549

Korey CA, MacDonald ME (2003) An over-expression system for characterizing Ppt1 function in Drosophila. BMC Neurosci 4**:** 30

Kornfeld S (1992) Structure and function of the mannose 6-phosphate/insulinlike growth factor II receptors. Annual review of biochemistry 61**:** 307-330

Kornfeld S, Mellman I (1989) The biogenesis of lysosomes. Annu Rev Cell Biol 5**:** 483-525

Kousi M, Lehesjoki AE, Mole SE (2012) Update of the mutation spectrum and clinical correlations of over 360 mutations in eight genes that underlie the neuronal ceroid lipofuscinoses. Human mutation 33**:** 42-63

Kovacs AD, Pearce DA (2008) Attenuation of AMPA receptor activity improves motor skills in a mouse model of juvenile Batten disease. Experimental neurology 209**:** 288-291

Kovacs AD, Weimer JM, Pearce DA (2006) Selectively increased sensitivity of cerebellar granule cells to AMPA receptor-mediated excitotoxicity in a mouse model of Batten disease. Neurobiology of disease 22**:** 575-585

Kühl TG, Dihanich S, Wong AM, Cooper JD (2013) Regional brain atrophy in mouse models of neuronal ceroid lipofuscinosis: a new rostrocaudal perspective. Journal of child neurology 28**:** 1117-1122

Lake BD, Steward CG, Oakhill A, Wilson J, Perham TG (1997) Bone marrow transplantation in late infantile Batten disease and juvenile Batten disease. Neuropediatrics 28**:** 80-81

Lane SC, Jolly RD, Schmechel DE, Alroy J, Boustany RM (1996) Apoptosis as the mechanism of neurodegeneration in Batten's disease. Journal of neurochemistry 67**:** 677-683

Larsen KE, Sulzer D (2002) Autophagy in neurons: a review. Histology and histopathology 17**:** 897-908

Lasiecka ZM, Winckler B (2011) Mechanisms of polarized membrane trafficking in neurons -- focusing in on endosomes. Mol Cell Neurosci 48**:** 278-287

Lassek AM RG (1938) A quantitative study of newborn and adult spinal cords of man. . The Journal of comparative neurology 69**:** 371-379

Lee HL, Dougherty JP (2012) Pharmaceutical therapies to recode nonsense mutations in inherited diseases. Pharmacol Ther 136**:** 227-266

Lee JA, Beigneux A, Ahmad ST, Young SG, Gao FB (2007) ESCRT-III dysfunction causes autophagosome accumulation and neurodegeneration. Curr Biol 17**:** 1561-1567

Lehtovirta M, Kyttala A, Eskelinen EL, Hess M, Heinonen O, Jalanko A (2001) Palmitoyl protein thioesterase (PPT) localizes into synaptosomes and synaptic vesicles in neurons: implications for infantile neuronal ceroid lipofuscinosis (INCL). Human molecular genetics 10**:** 69-75

Levin SW, Baker EH, Zein WM, Zhang Z, Quezado ZM, Miao N, Gropman A, Griffin KJ, Bianconi S, Chandra G et al (2014) Oral cysteamine bitartrate and N-acetylcysteine for patients with infantile neuronal ceroid lipofuscinosis: a pilot study. Lancet Neurol 13**:** 777-787

Levine B, Klionsky DJ (2004) Development by self-digestion: molecular mechanisms and biological functions of autophagy. Dev Cell 6**:** 463-477

Lim MJ, Alexander N, Benedict JW, Chattopadhyay S, Shemilt SJ, Guerin CJ, Cooper JD, Pearce DA (2007) IgG entry and deposition are components of the neuroimmune response in Batten disease. Neurobiology of disease 25**:** 239-251

Lim MJ, Beake J, Bible E, Curran TM, Ramirez-Montealegre D, Pearce DA, Cooper JD (2006) Distinct patterns of serum immunoreactivity as evidence for multiple brain-directed autoantibodies in juvenile neuronal ceroid lipofuscinosis. Neuropathol Appl Neurobiol 32**:** 469-482

Lin CH, Tallaksen-Greene S, Chien WM, Cearley JA, Jackson WS, Crouse AB, Ren S, Li XJ, Albin RL, Detloff PJ (2001) Neurological abnormalities in a knock-in mouse model of Huntington's disease. Human molecular genetics 10**:** 137-144

Lonnqvist T, Vanhanen SL, Vettenranta K, Autti T, Rapola J, Santavuori P, Saarinen-Pihkala UM (2001) Hematopoietic stem cell transplantation in infantile neuronal ceroid lipofuscinosis. Neurology 57**:** 1411-1416

Lonser RR, Walbridge S, Murray GJ, Aizenberg MR, Vortmeyer AO, Aerts JM, Brady RO, Oldfield EH (2005) Convection perfusion of glucocerebrosidase for neuronopathic Gaucher's disease. Annals of neurology 57**:** 542-548

Lu JY, Hofmann SL (2006) Inefficient cleavage of palmitoyl-protein thioesterase (PPT) substrates by aminothiols: implications for treatment of infantile neuronal ceroid lipofuscinosis. Journal of inherited metabolic disease 29**:** 119-126

Lu JY, Hu J, Hofmann SL (2010) Human recombinant palmitoyl-protein thioesterase-1 (PPT1) for preclinical evaluation of enzyme replacement therapy for infantile neuronal ceroid lipofuscinosis. Molecular genetics and metabolism 99**:** 374-378

Lu JY, Nelvagal HR, Wang L, Birnbaum SG, Cooper JD, Hofmann SL (2015) Intrathecal enzyme replacement therapy improves motor function and survival in a preclinical mouse model of infantile neuronal ceroid lipofuscinosis. Molecular genetics and metabolism 116**:** 98-105

Lucocq JM (2007) Efficient quantitative morphological phenotyping of genetically altered organisms using stereology. Transgenic Res 16**:** 133-145

Luiro K, Kopra O, Blom T, Gentile M, Mitchison HM, Hovatta I, Tornquist K, Jalanko A (2006) Batten disease (JNCL) is linked to disturbances in mitochondrial, cytoskeletal, and synaptic compartments. Journal of neuroscience research 84**:** 1124-1138

Luiro K, Yliannala K, Ahtiainen L, Maunu H, Jarvela I, Kyttala A, Jalanko A (2004) Interconnections of CLN3, Hook1 and Rab proteins link Batten disease to defects in the endocytic pathway. Human molecular genetics 13**:** 3017-3027

Luzio JP, Pryor PR, Bright NA (2007) Lysosomes: fusion and function. Nature reviews Molecular cell biology 8**:** 622-632

Luzio JP, Rous BA, Bright NA, Pryor PR, Mullock BM, Piper RC (2000) Lysosome-endosome fusion and lysosome biogenesis. J Cell Sci 113 (Pt 9)**:** 1515-1524

Lyly A, Marjavaara SK, Kyttala A, Uusi-Rauva K, Luiro K, Kopra O, Martinez LO, Tanhuanpaa K, Kalkkinen N, Suomalainen A et al (2008) Deficiency of the INCL protein Ppt1 results in changes in ectopic F1-ATP synthase and altered cholesterol metabolism. Human molecular genetics 17**:** 1406-1417

Lyly A, von Schantz C, Heine C, Schmiedt ML, Sipila T, Jalanko A, Kyttala A (2009) Novel interactions of CLN5 support molecular networking between Neuronal Ceroid Lipofuscinosis proteins. BMC cell biology 10**:** 83

Lyly A, von Schantz C, Salonen T, Kopra O, Saarela J, Jauhiainen M, Kyttala A, Jalanko A (2007) Glycosylation, transport, and complex formation of palmitoyl protein thioesterase 1 (PPT1)--distinct characteristics in neurons. BMC cell biology 8**:** 22

Macauley SL, Roberts MS, Wong AM, McSloy F, Reddy AS, Cooper JD, Sands MS (2012) Synergistic effects of central nervous system-directed gene therapy and bone marrow transplantation in the murine model of infantile neuronal ceroid lipofuscinosis. Annals of neurology 71**:** 797-804

Macauley SL, Wong AM, Shyng C, Augner DP, Dearborn JT, Pearse Y, Roberts MS, Fowler SC, Cooper JD, Watterson DM et al (2014) An anti-neuroinflammatory that targets dysregulated glia enhances the efficacy of CNS-directed gene therapy in murine infantile neuronal ceroid lipofuscinosis. The Journal of neuroscience : the official journal of the Society for Neuroscience 34**:** 13077-13082

Macauley SL, Wozniak DF, Kielar C, Tan Y, Cooper JD, Sands MS (2009) Cerebellar pathology and motor deficits in the palmitoyl protein thioesterase 1-deficient mouse. Experimental neurology 217**:** 124-135

Mallucci G, Peruzzotti-Jametti L, Bernstock JD, Pluchino S (2015) The role of immune cells, glia and neurons in white and gray matter pathology in multiple sclerosis. Prog Neurobiol 127-128**:** 1-22

Marin-Teva JL, Cuadros MA, Martin-Oliva D, Navascues J (2011) Microglia and neuronal cell death. Neuron Glia Biol 7**:** 25-40

Markiewicz I, Lukomska B (2006) The role of astrocytes in the physiology and pathology of the central nervous system. Acta Neurobiol Exp (Wars) 66**:** 343-358

Marmiroli P, Rodriguez-Menendez V, Rigamonti L, Tonoli E, Rigolio R, Cavaletti G, Tredici G, Vercelli A (2009) Neuropathological changes in the peripheral

nervous system and spinal cord in a transgenic mouse model of Niemann-Pick disease type A. Clin Neuropathol 28**:** 263-274

Martin LJ, Pan Y, Price AC, Sterling W, Copeland NG, Jenkins NA, Price DL, Lee MK (2006) Parkinson's disease alpha-synuclein transgenic mice develop neuronal mitochondrial degeneration and cell death. The Journal of neuroscience : the official journal of the Society for Neuroscience 26**:** 41-50

Meisner JG, Marsh AD, Marsh DR (2010) Loss of GABAergic interneurons in laminae I-III of the spinal cord dorsal horn contributes to reduced GABAergic tone and neuropathic pain after spinal cord injury. J Neurotrauma 27**:** 729-737

Meyer M, Kovacs AD, Pearce DA (2016) Decreased sensitivity of palmitoyl protein thioesterase 1-deficient neurons to chemical anoxia. Metab Brain Dis

Miller JN, Chan CH, Pearce DA (2013) The role of nonsense-mediated decay in neuronal ceroid lipofuscinosis. Human molecular genetics 22**:** 2723-2734

Miller JN, Kovacs AD, Pearce DA (2015) The novel Cln1(R151X) mouse model of infantile neuronal ceroid lipofuscinosis (INCL) for testing nonsense suppression therapy. Human molecular genetics 24**:** 185-196

Mink JW, Augustine EF, Adams HR, Marshall FJ, Kwon JM (2013) Classification and natural history of the neuronal ceroid lipofuscinoses. Journal of child neurology 28**:** 1101-1105

Minye HM, Fabritius AL, Vesa J, Peltonen L (2016) Data on characterizing the gene expression patterns of neuronal ceroid lipofuscinosis genes: CLN1, CLN2, CLN3, CLN5 and their association to interneuron and neurotransmission markers: Parvalbumin and Somatostatin. Data Brief 8**:** 741-749

Mitchison HM, Bernard DJ, Greene ND, Cooper JD, Junaid MA, Pullarkat RK, de Vos N, Breuning MH, Owens JW, Mobley WC et al (1999) Targeted disruption of the

Cln3 gene provides a mouse model for Batten disease. The Batten Mouse Model Consortium [corrected]. Neurobiology of disease 6**:** 321-334

Mitchison HM, Lim MJ, Cooper JD (2004) Selectivity and types of cell death in the neuronal ceroid lipofuscinoses. Brain pathology 14**:** 86-96

Mole SE, Cotman SL (2015) Genetics of the neuronal ceroid lipofuscinoses (Batten disease). Biochim Biophys Acta 1852**:** 2237-2241

Mole SE, Williams RE, Goebel HH (2005) Correlations between genotype, ultrastructural morphology and clinical phenotype in the neuronal ceroid lipofuscinoses. Neurogenetics 6**:** 107-126

Mole SE, Williams RE, Goebel HH (2011) The neuronal ceroid lipofuscinoses (Batten disease), Oxford: Oxford University Press

Molofsky AV, Krencik R, Ullian EM, Tsai HH, Deneen B, Richardson WD, Barres BA, Rowitch DH (2012) Astrocytes and disease: a neurodevelopmental perspective. Genes Dev 26**:** 891-907

Motta F, Antonello CE (2014) Analysis of complications in 430 consecutive pediatric patients treated with intrathecal baclofen therapy: 14-year experience. J Neurosurg Pediatr 13**:** 301-306

Mueller OT, Coovadia A (2010) Novel human pathological mutations. Gene symbol: PPT1. Disease: neuronal ceroid lipofuscinosis, juvenile. Human genetics 127**:** 490

Muhlau M, Engl C, Boucard CC, Schmidt P, Biberacher V, Gorsch I, Sorg C, Wohlschlager A, Zimmer C, Hemmer B et al (2014) Spinal cord atrophy in early Huntington's disease. Ann Clin Transl Neurol 1**:** 302-306

Murthy VN, Stevens CF (1998) Synaptic vesicles retain their identity through the endocytic cycle. Nature 392**:** 497-501

Nedergaard M, Ransom B, Goldman SA (2003) New roles for astrocytes: redefining the functional architecture of the brain. Trends in Neurosciences 26**:** 523-530

Neufeld EF, Fratantoni JC (1970) Inborn errors of mucopolysaccharide metabolism. Science 169**:** 141-146

Neumann M, Wang Y, Kim S, Hong SM, Jeng L, Bilgen M, Liu J (2009) Assessing gait impairment following experimental traumatic brain injury in mice. J Neurosci Methods 176**:** 34-44

Nijssen PC, Ceuterick C, van Diggelen OP, Elleder M, Martin JJ, Teepen JL, Tyynela J, Roos RA (2003) Autosomal dominant adult neuronal ceroid lipofuscinosis: a novel form of NCL with granular osmiophilic deposits without palmitoyl protein thioesterase 1 deficiency. Brain pathology 13**:** 574-581

Nimmerjahn A, Kirchhoff F, Helmchen F (2005) Resting microglial cells are highly dynamic surveillants of brain parenchyma in vivo. Science 308**:** 1314-1318

Nixon RA, Cataldo AM (1995) The endosomal-lysosomal system of neurons: new roles. Trends Neurosci 18**:** 489-496

Nixon RA, Cataldo AM (2006) Lysosomal system pathways: genes to neurodegeneration in Alzheimer's disease. J Alzheimers Dis 9**:** 277-289

Nixon RA, Yang DS (2011) Autophagy failure in Alzheimer's disease--locating the primary defect. Neurobiology of disease 43**:** 38-45

Nixon RA, Yang DS, Lee JH (2008) Neurodegenerative lysosomal disorders: a continuum from development to late age. Autophagy 4**:** 590-599

Nógrádi A, Vrbová G (2006) Anatomy and Physiology of the Spinal Cord. In Transplantation of Neural Tissue into the Spinal Cord pp 1-23. Boston, MA: Springer US

Norman RM, Wood N (1941) A Congenital Form of Amaurotic Family Idiocy. J Neurol Psychiatry 4**:** 175-190

Noskova L, Stranecky V, Hartmannova H, Pristoupilova A, Baresova V, Ivanek R, Hulkova H, Jahnova H, van der Zee J, Staropoli JF et al (2011) Mutations in DNAJC5, encoding cysteine-string protein alpha, cause autosomal-dominant adult-onset neuronal ceroid lipofuscinosis. Am J Hum Genet 89**:** 241-252

Novikoff AB, Novikoff PM, Davis C, Quintana N (1973) Studies on microperoxisomes. V. Are microperoxisomes ubiquitous in mammalian cells? The journal of histochemistry and cytochemistry : official journal of the Histochemistry Society 21**:** 737-755

O'Callaghan JP, Sriram K (2005) Glial fibrillary acidic protein and related glial proteins as biomarkers of neurotoxicity. Expert Opin Drug Saf 4**:** 433-442

Ohmi K, Greenberg DS, Rajavel KS, Ryazantsev S, Li HH, Neufeld EF (2003) Activated microglia in cortex of mouse models of mucopolysaccharidoses I and IIIB. Proceedings of the National Academy of Sciences of the United States of America 100**:** 1902-1907

Ohno K, Saito S, Sugawara K, Suzuki T, Togawa T, Sakuraba H (2010) Structural basis of neuronal ceroid lipofuscinosis 1. Brain & development 32**:** 524-530

Oswald MJ, Palmer DN, Kay GW, Shemilt SJ, Rezaie P, Cooper JD (2005) Glial activation spreads from specific cerebral foci and precedes neurodegeneration in presymptomatic ovine neuronal ceroid lipofuscinosis (CLN6). Neurobiology of disease 20**:** 49-63

Otomo A, Pan L, Hadano S (2012) Dysregulation of the autophagy-endolysosomal system in amyotrophic lateral sclerosis and related motor neuron diseases. Neurol Res Int 2012**:** 498428

Palmer DN, Oswald MJ, Westlake VJ, Kay GW (2002) The origin of fluorescence in the neuronal ceroid lipofuscinoses (Batten disease) and neuron cultures from affected sheep for studies of neurodegeneration. Archives of gerontology and geriatrics 34**:** 343-357

Pan T, Kondo S, Le W, Jankovic J (2008) The role of autophagy-lysosome pathway in neurodegeneration associated with Parkinson's disease. Brain 131**:** 1969-1978

Parkinson-Lawrence EJ, Shandala T, Prodoehl M, Plew R, Borlace GN, Brooks DA (2010) Lysosomal storage disease: revealing lysosomal function and physiology. Physiology 25**:** 102-115

Partanen S, Haapanen A, Kielar C, Pontikis C, Alexander N, Inkinen T, Saftig P, Gillingwater TH, Cooper JD, Tyynela J (2008) Synaptic changes in the thalamocortical system of cathepsin D-deficient mice: a model of human congenital neuronal ceroid-lipofuscinosis. J Neuropathol Exp Neurol 67**:** 16-29

Paxinos G, Franklin, K.B.J. (2001) The Mouse Brain in Stereotaxic Coordinates, 2nd ed.: Academic Press, San Diego.

Pearce DA (2001) Experimental models of NCL: the yeast model. Adv Genet 45**:** 205-216

Perez-Poyato MS, Mila Recansens M, Ferrer Abizanda I, Montero Sanchez R, Rodriguez-Revenga L, Cusi Sanchez V, Garcia Gonzalez MM, Domingo Jimenez R, Camino Leon R, Velazquez Fragua R et al (2011) Juvenile neuronal ceroid

lipofuscinosis: clinical course and genetic studies in Spanish patients. Journal of inherited metabolic disease 34**:** 1083-1093

Phillips SN, Muzaffar N, Codlin S, Korey CA, Taschner PE, de Voer G, Mole SE, Pearce DA (2006) Characterizing pathogenic processes in Batten disease: use of small eukaryotic model systems. Biochim Biophys Acta 1762**:** 906-919

Platt FM, Boland B, van der Spoel AC (2012) The cell biology of disease: lysosomal storage disorders: the cellular impact of lysosomal dysfunction. J Cell Biol 199**:** 723-734

Plummer J, Peterson A, Messer A (1995) Accelerated and widespread neuronal loss occurs in motor neuron degeneration (mnd) mice expressing a neurofilament-disrupting transgene. Mol Cell Neurosci 6**:** 532-543

Polazzi E, Contestabile A (2002) Reciprocal interactions between microglia and neurons: from survival to neuropathology. Rev Neurosci 13**:** 221-242

Pontikis CC, Cella CV, Parihar N, Lim MJ, Chakrabarti S, Mitchison HM, Mobley WC, Rezaie P, Pearce DA, Cooper JD (2004) Late onset neurodegeneration in the Cln3-/- mouse model of juvenile neuronal ceroid lipofuscinosis is preceded by low level glial activation. Brain Res 1023**:** 231-242

Pontikis CC, Cotman SL, MacDonald ME, Cooper JD (2005) Thalamocortical neuron loss and localized astrocytosis in the Cln3Deltaex7/8 knock-in mouse model of Batten disease. Neurobiology of disease 20**:** 823-836

Pope JE, Deer TR, Bruel BM, Falowski S (2016) Clinical Uses of Intrathecal Therapy and Its Placement in the Pain Care Algorithm. Pain Pract

Porter MY, Turmaine M, Mole SE (2005) Identification and characterization of Caenorhabditis elegans palmitoyl protein thioesterase1. Journal of neuroscience research 79**:** 836-848

Pressey SN, Smith DA, Wong AM, Platt FM, Cooper JD (2012) Early glial activation, synaptic changes and axonal pathology in the thalamocortical system of Niemann-Pick type C1 mice. Neurobiology of disease 45**:** 1086-1100

Raj A, Kuceyeski A, Weiner M (2012) A network diffusion model of disease progression in dementia. Neuron 73**:** 1204-1215

Ranta S, Zhang Y, Ross B, Lonka L, Takkunen E, Messer A, Sharp J, Wheeler R, Kusumi K, Mole S et al (1999) The neuronal ceroid lipofuscinoses in human EPMR and mnd mutant mice are associated with mutations in CLN8. Nat Genet 23**:** 233-236

Ravits J, Laurie P, Fan Y, Moore DH (2007) Implications of ALS focality: rostral-caudal distribution of lower motor neuron loss postmortem. Neurology 68**:** 1576-1582

Rexed B (1954) A cytoarchitectonic atlas of the spinal cord in the cat. The Journal of comparative neurology 100**:** 297-379

Ridet JL, Malhotra SK, Privat A, Gage FH (1997) Reactive astrocytes: cellular and molecular cues to biological function. Trends Neurosci 20**:** 570-577

Roberts MS, Macauley SL, Wong AM, Yilmas D, Hohm S, Cooper JD, Sands MS (2012) Combination small molecule PPT1 mimetic and CNS-directed gene therapy as a treatment for infantile neuronal ceroid lipofuscinosis. Journal of inherited metabolic disease 35**:** 847-857

Romanes GJ (1964) The Motor Pools of the Spinal Cord. Prog Brain Res 11**:** 93-119

Ross SE, Mardinly AR, McCord AE, Zurawski J, Cohen S, Jung C, Hu L, Mok SI, Shah A, Savner EM et al (2010) Loss of inhibitory interneurons in the dorsal spinal cord and elevated itch in Bhlhb5 mutant mice. Neuron 65**:** 886-898

Rossignol S, Dubuc R, Gossard JP (2006) Dynamic sensorimotor interactions in locomotion. Physiol Rev 86**:** 89-154

Saftig P, Klumperman J (2009) Lysosome biogenesis and lysosomal membrane proteins: trafficking meets function. Nature reviews Molecular cell biology 10**:** 623-635

Saha A, Sarkar C, Singh SP, Zhang Z, Munasinghe J, Peng S, Chandra G, Kong E, Mukherjee AB (2012) The blood-brain barrier is disrupted in a mouse model of infantile neuronal ceroid lipofuscinosis: amelioration by resveratrol. Human molecular genetics 21**:** 2233-2244

Sakla FB (1959) Postnatal growth of the cervical spinal cord of the albino mouse and the dendritic organization of its ventral horn cells. The Journal of comparative neurology 113**:** 491-507

Sakla FB (1962) Postnatal growth and change of density of the nerve fibers of the cervical spinal cord of the albino mouse. The Journal of comparative neurology 119**:** 97-103

Sakla FB (1969) Quantitative studies on the postnatal growth of the spinal cord and the vertebral column of the albino mouse. The Journal of comparative neurology 136**:** 237-247

Salmina AB (2009) Neuron-glia interactions as therapeutic targets in neurodegeneration. J Alzheimers Dis 16**:** 485-502

Salonen T, Hellsten E, Horelli-Kuitunen N, Peltonen L, Jalanko A (1998) Mouse palmitoyl protein thioesterase: gene structure and expression of cDNA. Genome Res 8**:** 724-730

Sandbank U (1968) Congenital amaurotic idiocy. Pathol Eur 3**:** 226-229

Sands MS, Davidson BL (2006) Gene therapy for lysosomal storage diseases. Molecular therapy : the journal of the American Society of Gene Therapy 13**:** 839-849

Sann S, Wang Z, Brown H, Jin Y (2009) Roles of endosomal trafficking in neurite outgrowth and guidance. Trends Cell Biol 19**:** 317-324

Santavuori P (1988) Neuronal ceroid-lipofuscinoses in childhood. Brain & development 10**:** 80-83

Santavuori P, Haltia M, Rapola J (1974) Infantile type of so-called neuronal ceroid-lipofuscinosis. Dev Med Child Neurol 16**:** 644-653

Santavuori P, Haltia M, Rapola J, Raitta C (1973) Infantile type of so-called neuronal ceroid-lipofuscinosis. 1. A clinical study of 15 patients. J Neurol Sci 18**:** 257-267

Saraste J, Kuismanen E (1992) Pathways of protein sorting and membrane traffic between the rough endoplasmic reticulum and the Golgi complex. Semin Cell Biol 3**:** 343-355

Sarkar C, Zhang Z, Mukherjee AB (2011) Stop codon read-through with PTC124 induces palmitoyl-protein thioesterase-1 activity, reduces thioester load and suppresses apoptosis in cultured cells from INCL patients. Molecular genetics and metabolism 104**:** 338-345

Schindelin J, Rueden CT, Hiner MC, Eliceiri KW (2015) The ImageJ ecosystem: An open platform for biomedical image analysis. Mol Reprod Dev 82**:** 518-529

Schmitz C, Hof PR (2005) Design-based stereology in neuroscience. Neuroscience 130**:** 813-831

Schneider CA, Rasband WS, Eliceiri KW (2012) NIH Image to ImageJ: 25 years of image analysis. Nat Methods 9**:** 671-675

Schoenen J (1982) Dendritic organization of the human spinal cord: the motoneurons. The Journal of comparative neurology 211**:** 226-247

Scholz J, Woolf CJ (2007) The neuropathic pain triad: neurons, immune cells and glia. Nat Neurosci 10**:** 1361-1368

Schultz ML, Tecedor L, Chang M, Davidson BL (2011) Clarifying lysosomal storage diseases. Trends Neurosci 34**:** 401-410

Schulz A, Kohlschutter A, Mink J, Simonati A, Williams R (2013) NCL diseases - clinical perspectives. Biochim Biophys Acta 1832**:** 1801-1806

Schuster DJ, Dykstra JA, Riedl MS, Kitto KF, Belur LR, McIvor RS, Elde RP, Fairbanks CA, Vulchanova L (2014) Biodistribution of adeno-associated virus serotype 9 (AAV9) vector after intrathecal and intravenous delivery in mouse. Front Neuroanat 8**:** 42

Scifo E, Szwajda A, Soliymani R, Pezzini F, Bianchi M, Dapkunas A, Debski J, Uusi-Rauva K, Dadlez M, Gingras AC et al (2015a) Proteomic analysis of the palmitoyl protein thioesterase 1 interactome in SH-SY5Y human neuroblastoma cells. J Proteomics 123**:** 42-53

Scifo E, Szwajda A, Soliymani R, Pezzini F, Bianchi M, Dapkunas A, Debski J, Uusi-Rauva K, Dadlez M, Gingras AC et al (2015b) Quantitative analysis of PPT1 interactome in human neuroblastoma cells. Data Brief 4**:** 207-216

Seaman MN (2004) Cargo-selective endosomal sorting for retrieval to the Golgi requires retromer. J Cell Biol 165**:** 111-122

Seehafer SS, Pearce DA (2006) You say lipofuscin, we say ceroid: defining autofluorescent storage material. Neurobiology of aging 27**:** 576-588

Seigel GM, Lotery A, Kummer A, Bernard DJ, Greene ND, Turmaine M, Derksen T, Nussbaum RL, Davidson B, Wagner J et al (2002) Retinal pathology and function in a Cln3 knockout mouse model of juvenile Neuronal Ceroid Lipofuscinosis (batten disease). Mol Cell Neurosci 19**:** 515-527

Sengul G, Watson, Charles, Tanaka, I., Paxinos, G. (2013) Atlas of the spinal cord: Mouse, rat, rhesus, marmoset and human, Waltham, MA: Academic Press

Seo JS, Leem YH, Lee KW, Kim SW, Lee JK, Han PL (2010) Severe motor neuron degeneration in the spinal cord of the Tg2576 mouse model of Alzheimer disease. J Alzheimers Dis 21**:** 263-276

Shachar T, Lo Bianco C, Recchia A, Wiessner C, Raas-Rothschild A, Futerman AH (2011) Lysosomal storage disorders and Parkinson's disease: Gaucher disease and beyond. Mov Disord 26**:** 1593-1604

Shapiro BE, Logigian EL, Kolodny EH, Pastores GM (2008) Late-onset Tay-Sachs disease: the spectrum of peripheral neuropathy in 30 affected patients. Muscle Nerve 38**:** 1012-1015

Shimada SG, LaMotte RH (2008) Behavioral differentiation between itch and pain in mouse. Pain 139**:** 681-687

Shyng C, Sands MS (2014) Astrocytosis in infantile neuronal ceroid lipofuscinosis: friend or foe? Biochemical Society transactions 42**:** 1282-1285

Siintola E, Lehesjoki AE, Mole SE (2006) Molecular genetics of the NCLs -- status and perspectives. Biochim Biophys Acta 1762**:** 857-864

Silva AL, Romao L (2009) The mammalian nonsense-mediated mRNA decay pathway: to decay or not to decay! Which players make the decision? FEBS Lett 583**:** 499-505

Simonati A, Tessa A, Bernardina BD, Biancheri R, Veneselli E, Tozzi G, Bonsignore M, Grosso S, Piemonte F, Santorelli FM (2009) Variant late infantile neuronal ceroid lipofuscinosis because of CLN1 mutations. Pediatr Neurol 40**:** 271-276

Simone C, Ramirez A, Bucchia M, Rinchetti P, Rideout H, Papadimitriou D, Re DB, Corti S (2016) Is spinal muscular atrophy a disease of the motor neurons only: pathogenesis and therapeutic implications? Cellular and molecular life sciences : CMLS 73**:** 1003-1020

Simons M, Nave KA (2015) Oligodendrocytes: Myelination and Axonal Support. Cold Spring Harb Perspect Biol 8**:** a020479

Sleat DE, El-Banna M, Sohar I, Kim KH, Dobrenis K, Walkley SU, Lobel P (2008) Residual levels of tripeptidyl-peptidase I activity dramatically ameliorate disease in late-infantile neuronal ceroid lipofuscinosis. Molecular genetics and metabolism 94**:** 222-233

Sleat DE, Wiseman JA, El-Banna M, Kim KH, Mao Q, Price S, Macauley SL, Sidman RL, Shen MM, Zhao Q et al (2004) A mouse model of classical late-infantile neuronal ceroid lipofuscinosis based on targeted disruption of the CLN2 gene results in a loss of tripeptidyl-peptidase I activity and progressive neurodegeneration. The Journal of neuroscience : the official journal of the Society for Neuroscience 24**:** 9117-9126

Sleigh JN, Gillingwater TH, Talbot K (2011) The contribution of mouse models to understanding the pathogenesis of spinal muscular atrophy. Dis Model Mech 4**:** 457-467

Smith JC, Abdala AP, Koizumi H, Rybak IA, Paton JF (2007) Spatial and functional architecture of the mammalian brain stem respiratory network: a hierarchy of three oscillatory mechanisms. J Neurophysiol 98**:** 3370-3387

Sofroniew MV, Vinters HV (2010) Astrocytes: biology and pathology. Acta Neuropathol 119**:** 7-35

Song JW, Misgeld T, Kang H, Knecht S, Lu J, Cao Y, Cotman SL, Bishop DL, Lichtman JW (2008) Lysosomal activity associated with developmental axon pruning. The Journal of neuroscience : the official journal of the Society for Neuroscience 28**:** 8993-9001

Spada M, Pagliardini S, Yasuda M, Tukel T, Thiagarajan G, Sakuraba H, Ponzone A, Desnick RJ (2006) High incidence of later-onset fabry disease revealed by newborn screening. Am J Hum Genet 79**:** 31-40

Starkey ML, Barritt AW, Yip PK, Davies M, Hamers FP, McMahon SB, Bradbury EJ (2005) Assessing behavioural function following a pyramidotomy lesion of the corticospinal tract in adult mice. Experimental neurology 195**:** 524-539

Staropoli JF, Haliw L, Biswas S, Garrett L, Holter SM, Becker L, Skosyrski S, Da Silva-Buttkus P, Calzada-Wack J, Neff F et al (2012) Large-scale phenotyping of an accurate genetic mouse model of JNCL identifies novel early pathology outside the central nervous system. PloS one 7**:** e38310

Storer JB (1966) Longevity and gross pathology at death in 22 inbred mouse strains. J Gerontol 21**:** 404-409

Stromhaug PE, Klionsky DJ (2001) Approaching the molecular mechanism of autophagy. Traffic 2**:** 524-531

Suopanki J, Lintunen M, Lahtinen H, Haltia M, Panula P, Baumann M, Tyynela J (2002) Status epilepticus induces changes in the expression and localization of endogenous palmitoyl-protein thioesterase 1. Neurobiology of disease 10**:** 247-257

Suopanki J, Tyynela J, Baumann M, Haltia M (1999a) The expression of palmitoyl-protein thioesterase is developmentally regulated in neural tissues but not in nonneural tissues. Molecular genetics and metabolism 66**:** 290-293

Suopanki J, Tyynela J, Baumann M, Haltia M (1999b) Palmitoyl-protein thioesterase, an enzyme implicated in neurodegeneration, is localized in neurons and is developmentally regulated in rat brain. Neuroscience letters 265**:** 53-56

Swain GP, Prociuk M, Bagel JH, O'Donnell P, Berger K, Drobatz K, Gurda BL, Haskins ME, Sands MS, Vite CH (2014) Adeno-associated virus serotypes 9 and rh10 mediate strong neuronal transduction of the dog brain. Gene therapy 21**:** 28-36

Takakusaki K (2013) Neurophysiology of gait: from the spinal cord to the frontal lobe. Mov Disord 28**:** 1483-1491

Tamaki S, Eckert K, He D, Sutton R, Doshe M, Jain G, Tushinski R, Reitsma M, Harris B, Tsukamoto A et al (2002) Engraftment of sorted/expanded human central nervous system stem cells from fetal brain. Journal of neuroscience research 69**:** 976-986

Tamaki SJ, Jacobs Y, Dohse M, Capela A, Cooper JD, Reitsma M, He D, Tushinski R, Belichenko PV, Salehi A et al (2009) Neuroprotection of host cells by human central nervous system stem cells in a mouse model of infantile neuronal ceroid lipofuscinosis. Cell stem cell 5**:** 310-319

Tardy C, Sabourdy F, Garcia V, Jalanko A, Therville N, Levade T, Andrieu-Abadie N (2009) Palmitoyl protein thioesterase 1 modulates tumor necrosis factor alpha-induced apoptosis. Biochim Biophys Acta 1793**:** 1250-1258

Terman A, Kurz T, Navratil M, Arriaga EA, Brunk UT (2010) Mitochondrial turnover and aging of long-lived postmitotic cells: the mitochondrial-lysosomal axis theory of aging. Antioxid Redox Signal 12**:** 503-535

Thada V, Miller JN, Kovacs AD, Pearce DA (2016) Tissue-specific variation in nonsense mutant transcript level and drug-induced read-through efficiency in the Cln1(R151X) mouse model of INCL. J Cell Mol Med 20**:** 381-385

Tikka S, Monogioudi E, Gotsopoulos A, Soliymani R, Pezzini F, Scifo E, Uusi-Rauva K, Tyynela J, Baumann M, Jalanko A et al (2016) Proteomic Profiling in the Brain of CLN1 Disease Model Reveals Affected Functional Modules. Neuromolecular Med 18**:** 109-133

Treuting PM, Dintzis SM, Frevert CW, Liggitt HD, Montine KS (2012) Comparative anatomy and histology : a mouse and human atlas, Amsterdam ; Boston: Elsevier/Academic Press

Tuite PJ, Krawczewski K (2007) Parkinsonism: a review-of-systems approach to diagnosis. Semin Neurol 27**:** 113-122

Tyynelä J, Cooper JD, Khan MN, Shemilts SJ, Haltia M (2004) Hippocampal pathology in the human neuronal ceroid-lipofuscinoses: distinct patterns of storage deposition, neurodegeneration and glial activation. Brain pathology 14**:** 349-357

Tyynela J, Palmer DN, Baumann M, Haltia M (1993) Storage of saposins A and D in infantile neuronal ceroid-lipofuscinosis. FEBS Lett 330**:** 8-12

Uchida N, Buck DW, He D, Reitsma MJ, Masek M, Phan TV, Tsukamoto AS, Gage FH, Weissman IL (2000) Direct isolation of human central nervous system stem cells. Proceedings of the National Academy of Sciences of the United States of America 97**:** 14720-14725

Unger JW (1998) Glial reaction in aging and Alzheimer's disease. Microsc Res Tech 43**:** 24-28

Valadao PA, de Aragao BC, Andrade JN, Magalhaes-Gomes MP, Foureaux G, Joviano-Santos JV, Nogueira JC, Ribeiro FM, Tapia JC, Guatimosim C (2016) Muscle atrophy is associated with cervical spinal motoneuron loss in BACHD mouse model for Huntington's disease. Eur J Neurosci

van Breemen MJ, de Fost M, Voerman JS, Laman JD, Boot RG, Maas M, Hollak CE, Aerts JM, Rezaee F (2007) Increased plasma macrophage inflammatory protein (MIP)-1alpha and MIP-1beta levels in type 1 Gaucher disease. Biochim Biophys Acta 1772**:** 788-796

Van Diggelen OP, Keulemans JL, Kleijer WJ, Thobois S, Tilikete C, Voznyi YV (2001) Pre- and postnatal enzyme analysis for infantile, late infantile and adult neuronal ceroid lipofuscinosis (CLN1 and CLN2). Eur J Paediatr Neurol 5 Suppl A**:** 189-192

Vanhanen SL, Puranen J, Autti T, Raininko R, Liewendahl K, Nikkinen P, Santavuori P, Suominen P, Vuori K, Hakkinen AM (2004) Neuroradiological findings (MRS, MRI, SPECT) in infantile neuronal ceroid-lipofuscinosis (infantile CLN1) at different stages of the disease. Neuropediatrics 35**:** 27-35

Vesa J, Hellsten E, Verkruyse LA, Camp LA, Rapola J, Santavuori P, Hofmann SL, Peltonen L (1995) Mutations in the palmitoyl protein thioesterase gene causing infantile neuronal ceroid lipofuscinosis. Nature 376**:** 584-587

Virmani T, Gupta P, Liu X, Kavalali ET, Hofmann SL (2005) Progressively reduced synaptic vesicle pool size in cultured neurons derived from neuronal ceroid lipofuscinosis-1 knockout mice. Neurobiology of disease 20**:** 314-323

Vitner EB, Farfel-Becker T, Eilam R, Biton I, Futerman AH (2012) Contribution of brain inflammation to neuronal cell death in neuronopathic forms of Gaucher's disease. Brain 135**:** 1724-1735

Vitner EB, Platt FM, Futerman AH (2010) Common and uncommon pathogenic cascades in lysosomal storage diseases. J Biol Chem 285**:** 20423-20427

Vivacqua G, Casini A, Vaccaro R, Salvi EP, Pasquali L, Fornai F, Yu S, D'Este L (2011) Spinal cord and parkinsonism: neuromorphological evidences in humans and experimental studies. J Chem Neuroanat 42**:** 327-340

von Schantz C, Kielar C, Hansen SN, Pontikis CC, Alexander NA, Kopra O, Jalanko A, Cooper JD (2009) Progressive thalamocortical neuron loss in Cln5 deficient mice: Distinct effects in Finnish variant late infantile NCL. Neurobiology of disease 34**:** 308-319

Vrinten DH, Hamers FF (2003) 'CatWalk' automated quantitative gait analysis as a novel method to assess mechanical allodynia in the rat; a comparison with von Frey testing. Pain 102**:** 203-209

Walkley SU (2009) Pathogenic cascades in lysosomal disease-Why so complex? Journal of inherited metabolic disease 32**:** 181-189

Walkley SU, March PA (1993) Biology of neuronal dysfunction in storage disorders. Journal of inherited metabolic disease 16**:** 284-287

Wei H, Kim SJ, Zhang Z, Tsai PC, Wisniewski KE, Mukherjee AB (2008) ER and oxidative stresses are common mediators of apoptosis in both

neurodegenerative and non-neurodegenerative lysosomal storage disorders and are alleviated by chemical chaperones. Human molecular genetics 17**:** 469-477

Wei H, Zhang Z, Saha A, Peng S, Chandra G, Quezado Z, Mukherjee AB (2011) Disruption of adaptive energy metabolism and elevated ribosomal p-S6K1 levels contribute to INCL pathogenesis: partial rescue by resveratrol. Human molecular genetics 20**:** 1111-1121

Weimer JM, Kriscenski-Perry E, Elshatory Y, Pearce DA (2002) The neuronal ceroid lipofuscinoses: mutations in different proteins result in similar disease. Neuromolecular Med 1**:** 111-124

Wendt KD, Lei B, Schachtman TR, Tullis GE, Ibe ME, Katz ML (2005) Behavioral assessment in mouse models of neuronal ceroid lipofuscinosis using a light-cued T-maze. Behav Brain Res 161**:** 175-182

Wenger DA, Coppola S, Liu SL (2003) Insights into the diagnosis and treatment of lysosomal storage diseases. Arch Neurol 60**:** 322-328

West MJ (1993) New stereological methods for counting neurons. Neurobiology of aging 14**:** 275-285

West MJ (2002) Design-based stereological methods for counting neurons. Prog Brain Res 135**:** 43-51

Williams RE, Aberg L, Autti T, Goebel HH, Kohlschutter A, Lonnqvist T (2006) Diagnosis of the neuronal ceroid lipofuscinoses: an update. Biochim Biophys Acta 1762**:** 865-872

Williams RE, Mole SE (2012) New nomenclature and classification scheme for the neuronal ceroid lipofuscinoses. Neurology 79**:** 183-191

Wilson SG, Mogil JS (2001) Measuring pain in the (knockout) mouse: big challenges in a small mammal. Behav Brain Res 125**:** 65-73

Winchester B, Vellodi A, Young E (2000) The molecular basis of lysosomal storage diseases and their treatment. Biochemical Society transactions 28**:** 150-154

Wirths O, Breyhan H, Marcello A, Cotel MC, Bruck W, Bayer TA (2010) Inflammatory changes are tightly associated with neurodegeneration in the brain and spinal cord of the APP/PS1KI mouse model of Alzheimer's disease. Neurobiology of aging 31**:** 747-757

Wisniewski KE, Gordon-Krajcer W, Kida E (1993) Abnormal processing of carboxy-terminal fragment of beta precursor protein (beta PP) in neuronal ceroid-lipofuscinosis (NCL) cases. Journal of inherited metabolic disease 16**:** 312-316

Wisniewski KE, Kida E, Golabek AA, Kaczmarski W, Connell F, Zhong N (2001) Neuronal ceroid lipofuscinoses: classification and diagnosis. Adv Genet 45**:** 1-34

Wisniewski KE, Kida E, Gordon-Majszak W, Saitoh T (1990) Altered amyloid beta-protein precursor processing in brains of patients with neuronal ceroid lipofuscinosis. Neuroscience letters 120**:** 94-96

Wong E, Cuervo AM (2010) Autophagy gone awry in neurodegenerative diseases. Nat Neurosci 13**:** 805-811

Wong-Riley MT, Liu Q (2005) Neurochemical development of brain stem nuclei involved in the control of respiration. Respir Physiol Neurobiol 149**:** 83-98

Wooley CM, Sher RB, Kale A, Frankel WN, Cox GA, Seburn KL (2005) Gait analysis detects early changes in transgenic SOD1(G93A) mice. Muscle Nerve 32**:** 43-50

Wraith JE (2002) Lysosomal disorders. Semin Neonatol 7**:** 75-83

Wraith JE (2004) The clinical presentation of lysosomal storage disorders. Acta Neurol Taiwan 13**:** 101-106

Wujek JR, Bjartmar C, Richer E, Ransohoff RM, Yu M, Tuohy VK, Trapp BD (2002) Axon loss in the spinal cord determines permanent neurological disability in an animal model of multiple sclerosis. J Neuropathol Exp Neurol 61**:** 23-32

Xu H, Ren D (2015) Lysosomal physiology. Annual review of physiology 77**:** 57-80

Xu S, Wang L, El-Banna M, Sohar I, Sleat DE, Lobel P (2011) Large-volume intrathecal enzyme delivery increases survival of a mouse model of late infantile neuronal ceroid lipofuscinosis. Molecular therapy : the journal of the American Society of Gene Therapy 19**:** 1842-1848

Yamashima T, Oikawa S (2009) The role of lysosomal rupture in neuronal death. Prog Neurobiol 89**:** 343-358

Yan X, Lukas J, Witt M, Wree A, Hubner R, Frech M, Kohling R, Rolfs A, Luo J (2011) Decreased expression of myelin gene regulatory factor in Niemann-Pick type C 1 mouse. Metab Brain Dis 26**:** 299-306

Yates D (2012) Neurodegenerative networking. Nat Rev Neurosci 13**:** 288

Yokoyama T, Nakamura S, Horiuchi E, Ishiyama M, Kawashima R, Nakamura K, Hasegawa K, Yagishita S (2014) Late onset GM2 gangliosidosis presenting with motor neuron disease: an autopsy case. Neuropathology 34**:** 304-308

Yoon DH, Kwon OY, Mang JY, Jung MJ, Kim DY, Park YK, Heo TH, Kim SJ (2011) Protective potential of resveratrol against oxidative stress and apoptosis in

Batten disease lymphoblast cells. Biochemical and biophysical research communications 414: 49-52

Yu J, Guo Y, Sun M, Li B, Zhang Y, Li C (2009) Iron is a potential key mediator of glutamate excitotoxicity in spinal cord motor neurons. Brain Res 1257: 102-107

Zeman W, Donahue S (1963) Fine Structure of the Lipid Bodies in Juvenile Amaurotic Idiocy. Acta Neuropathol 3: 144-149

Zeman W, Dyken P (1969) Neuronal ceroid-lipofuscinosis (Batten's disease): relationship to amaurotic family idiocy? Pediatrics 44: 570-583

Zhang L, Sheng R, Qin Z (2009) The lysosome and neurodegenerative diseases. Acta Biochim Biophys Sin (Shanghai) 41: 437-445

Zhang Z, Butler JD, Levin SW, Wisniewski KE, Brooks SS, Mukherjee AB (2001) Lysosomal ceroid depletion by drugs: therapeutic implications for a hereditary neurodegenerative disease of childhood. Nature medicine 7: 478-484

Zhang Z, Lee YC, Kim SJ, Choi MS, Tsai PC, Xu Y, Xiao YJ, Zhang P, Heffer A, Mukherjee AB (2006) Palmitoyl-protein thioesterase-1 deficiency mediates the activation of the unfolded protein response and neuronal apoptosis in INCL. Human molecular genetics 15: 337-346

Zhou M, Zhang W, Chang J, Wang J, Zheng W, Yang Y, Wen P, Li M, Xiao H (2015) Gait analysis in three different 6-hydroxydopamine rat models of Parkinson's disease. Neuroscience letters 584: 184-189

Zuchner S, Vance JM (2005) Emerging pathways for hereditary axonopathies. J Mol Med (Berl) 83: 935-943

“Blah blah blah blah blah blah blah blah blah blah blah…”

- *Alex Lifeson of Rush,*
Rock & Roll Hall of Fame acceptance speech, 2013.